



UNIVERSITY OF
BIRMINGHAM

*Extending the fundamental understanding of
detergent crystallisation and routes to improve the
low temperature stability test methods*

by

Emily Louise Summerton

A thesis submitted to
The University of Birmingham
for the degree of
DOCTOR OF ENGINEERING

School of Chemical Engineering
College of Physical and Engineering Sciences
The University of Birmingham
July 2018

UNIVERSITY OF
BIRMINGHAM

University of Birmingham Research Archive

e-theses repository

This unpublished thesis/dissertation is copyright of the author and/or third parties. The intellectual property rights of the author or third parties in respect of this work are as defined by The Copyright Designs and Patents Act 1988 or as modified by any successor legislation.

Any use made of information contained in this thesis/dissertation must be in accordance with that legislation and must be properly acknowledged. Further distribution or reproduction in any format is prohibited without the permission of the copyright holder.

ABSTRACT

The research presented in this thesis has expanded the fundamental understanding of surfactant crystallisation exhibited by dish liquid formulations under low temperature environments. With this knowledge, industries, such as P&G, can develop more robust formulation designs that do not demonstrate failures in appearance criteria. By increasing the knowledge base, this thesis provides a route to improve the stability test methods currently in place at P&G. These tests can take up to 28 days to detect crystalline failures before a definitive conclusion can be made regarding a sample's susceptibility to crystallisation. This work has identified potential routes to reduce this timescale, as well as the variability of these failures.

Studies were initially performed on model systems consisting of sodium dodecyl sulfate (SDS), N,N-dimethyldodecylamine N-oxide (DDAO) and water, where the surfactants were present at concentrations typical of commercial dish liquid. Crystals were found to be composed of SDS hydrates, with little or no DDAO present. It was shown that the SDS alcohol precursor, 1-dodecanol, was able to seed SDS crystallisation as a result of structural similarity between the two components. Differential scanning calorimetry (DSC), confocal Raman microscopy and X-ray scattering studies revealed that the presence of the non-ionic surfactant, DDAO, has a significant impact on the crystal shape, structural changes during formation and the crystallisation temperature of the solutions. In the absence of DDAO, SDS crystal formation proceeded via an intermediary structure whereas this structure was not detected in the presence of DDAO.

An extensive stability study was performed across selected dish liquid formulations to demonstrate that the conclusions drawn from the model system studies could be applied to more complex systems. Crystallisation of the dish liquid samples was monitored via time lapse photography and light transmission techniques. Sample stability was found to depend on three

factors: the amount of alkyl sulfate alcohol precursor, the amine oxide concentration and the chemical nature of the alkyl sulfate paste. Consistent with the model system findings, the greater the amount of alcohol precursor and the lower the amine oxide concentration, the more unstable the formulation with respect to crystallisation. The alkyl sulfate paste, within commercial products, contains both ethoxylated and non-ethoxylated alkyl sulfate components. Nuclear magnetic resonance (NMR) studies revealed that the crystals do not contain ethoxylated alkyl sulfates and, therefore, the presence of these surfactants were observed to improve the stability of formulations.

In enhancing the related stability test methods, the main aim was to source a method that enabled failures to be detected in a shorter time and with increased repeatability. Seeding with oven-dried dish liquid and sonication were considered as potential options, but were not pursued past initial screening due to practical limitations or repeatability issues. However, the application of mixing to a formulation afforded improvements. This method was found to reduce the time to crystal formation by increasing the rate of both primary and secondary nucleation in the system. As well as reducing both the time to failure and the variability between replicates, the application of agitation also influenced the mechanism of crystallisation. In the absence of mixing, crystallisation originated from the air-liquid interface due to the close packed conformation of the monolayer. This was further demonstrated upon addition of an oil layer to the sample. This oil layer effectively ‘freezes the interface’ by stabilising the surfactant hydrocarbon chains and reducing the drive for crystallisation. However, when mixing was introduced into the system, the crystals initially grew in the region of the stirrer blade and spread throughout the bulk. Furthermore, this method can simulate the supply chain, since formulations are subjected to varying levels of movement during distribution. A route to implement this scientific finding on a mass scale is currently being investigated by P&G.

ACKNOWLEDGEMENTS

I would like to thank my academic supervisors, Prof. Serafim Bakalis and Dr. Melanie Britton for their helpful guidance and advice throughout this EngD. I also acknowledge Dr. Georgina Zimbitas for all her support during the first two years of the project. Thanks also go to my P&G supervisors, Chris Jones and Dr. Jeanluc Bettiol, for allowing me the opportunity to undertake this project and their support during my time at P&G. Furthermore, I thank P&G, specifically the hand dish liquid department in Brussels, for allowing me to carry out some of the experimental work there. I express gratitude to P&G and EPSRC for funding this project.

In addition, I would especially like to thank Dr. Richard Greenwood for his support throughout the programme and for proof-reading some chapters of this manuscript. A special mention also goes to Kathleen Hynes and John Hooper for all their helpful advice.

In relation to the work performed at the Diamond Light Source, I would like to express my gratitude to Dr. Martin Hollamby for all his support with performing the experiments and the subsequent analysis. I am grateful to the Diamond Light Source for awarding this project a total of 64 hours on the I22 and I11 beamlines, with specific thanks to Dr. Andy Smith and Dr. Tim Snow for their support during my time there. Thanks also go to Dr. Cécile Le Duff and Dr. Louise Male for their assistance with performing NMR and XRD experiments, respectively. Furthermore, I acknowledge RISE (Research Institutes of Sweden) in Stockholm for enabling confocal Raman microscopy to be performed as part of this project.

Finally, I would really like to thank my family, specifically my parents, Ailie and Nick, and grandparents, June and Barry, for all their continued support throughout the EngD. And thanks to Adam for helping me through the tough times and always being there to make me smile! I have made many lifelong friends on the EngD so I am very grateful to them for making the time an unforgettable and great experience.

*This thesis is dedicated to my late grandpa, Dr. Ronald Butler,
who helped inspire my passion for mathematics and science.*

TABLE OF CONTENTS

Abstract	i
Acknowledgements	iii
Dedication	iv
Table of Contents	v
List of Figures	xi
List of Tables	xix
Nomenclature	xx
Publications and Conferences	xxviii
Thesis Layout	xxx
CHAPTER 1 INTRODUCTION	1
1.1 Project background	2
1.2 Project aims	4
1.3 Relevance to P&G	5
1.4 Literature review	7
1.4.1 Introduction to surfactants	7
1.4.2 Crystallisation	18
1.4.3 Surfactant crystallisation	26
1.4.4 Timescale of crystallisation	31
1.4.5 Principles of the relevant methodology	38
1.5 References	47
CHAPTER 2 CRYSTALLISATION OF SODIUM DODECYL SULFATE AND THE CORRESPONDING EFFECT OF 1-DODECANOL ADDITION	68
2.1 Abstract	69
2.2 Introduction	69
2.3 Materials and methods	73
2.3.1 Materials	73

2.3.2 Methods	74
2.4 Results and discussion	76
2.4.1 Effect of concentration on crystallisation temperature	76
2.4.2 Composition of the crystals	79
2.4.3 Dodecanol addition	80
2.4.4 1-dodecanol SDS crystallisation trigger mechanism	83
2.5 Conclusions	84
2.6 References	85
CHAPTER 3 NUCLEAR MAGNETIC RESONANCE AND SMALL-ANGLE X-RAY SCATTERING STUDIES OF MIXED SODIUM DODECYL SULFATE AND N,N- DIMETHYLDIMETHYLDODECYLAMINE N-OXIDE AQUEOUS SYSTEMS PERFORMED AT LOW TEMPERATURES	89
3.1 Abstract	90
3.2 Introduction	90
3.3 Materials and methods	93
3.3.1 Materials	93
3.3.2 Methods	94
3.4 Results and discussion	96
3.5 Conclusions	104
3.6 References	105
CHAPTER 4 THE IMPACT OF N,N-DIMETHYLDODECYLAMINE N-OXIDE (DDAO) CONCENTRATION ON THE CRYSTALLISATION OF SODIUM DODECYL SULFATE (SDS) SYSTEMS AND THE RESULTING CHANGES TO CRYSTAL STRUCTURE, SHAPE AND THE KINETICS OF CRYSTAL GROWTH	110
4.1 Abstract	111
4.2 Introduction	111
4.3 Materials and methods	114
4.3.1 Materials	114

4.3.2 Methods	114
4.4 Results and discussion	116
4.4.1 Results	116
4.4.2 Discussion.....	124
4.5 Conclusions	127
4.6 References	128
CHAPTER 5 INSIGHT INTO THE KINETICS OF CRYSTALLISATION OF SODIUM DODECYL SULFATE AND MIXED SODIUM DODECYL SULFATE AND N,N-DIMETHYLDODECYLAMINE N-OXIDE SYSTEMS UNDER BOTH ISOTHERMAL AND NON-ISOTHERMAL CONDITIONS	132
5.1 Abstract.....	133
5.2 Introduction	133
5.3 Materials and methods.....	137
5.3.1 Materials	137
5.3.2 Methods	137
5.4 Results and discussion	140
5.4.1 Isothermal SDS systems	140
5.4.2 Isothermal SDS + DDAO systems	143
5.4.3 Non-isothermal SDS systems	146
5.4.4 Non-isothermal SDS + DDAO systems.	150
5.5 Conclusions	153
5.6 References	154
CHAPTER 6 FACTORS AFFECTING THE LOW TEMPERATURE STABILITY OF COMPLEX DISH LIQUID SYSTEMS.....	158
6.1 Abstract.....	159
6.2 Introduction	159
6.3 Materials and methods.....	161
6.3.1 Materials	161

6.3.2 Methods	167
6.4 Results and discussion	171
6.4.1 Composition and structural attributes	171
6.4.2 Influences of the formulation components on low temperature stability	178
6.5 Conclusions	186
6.6 References	187
CHAPTER 7 INVESTIGATING METHODS FOR REDUCING THE TIME TO FAILURE	191
7.1 Abstract.....	192
7.2 Introduction	192
7.3 Materials and methods.....	194
7.3.1 Materials	194
7.3.2 Methods	194
7.4 Results and discussion	196
7.4.1 Oven-dried dish liquid seeding.....	196
7.4.2 Sonication	203
7.4.3 Mixing	206
7.5 Conclusions	206
7.6 References	207
CHAPTER 8 UNDERSTANDING THE CRYSTALLISATION PROCESS IN DETERGENT FORMULATIONS IN THE ABSENCE AND PRESENCE OF AGITATION.....	209
8.1 Abstract.....	210
8.2 Introduction	210
8.3 Materials and methods.....	214
8.3.1 Materials	214
8.3.2 Methods	216
8.4 Results and discussion	222

8.4.1 Mechanism without agitation	222
8.4.2 Effect of agitation	225
8.4.3 Effect of mixing speed.....	229
8.4.4 Comparison with the current test method.....	233
8.5 Conclusions	234
8.6 References	236
CHAPTER 9 CONCLUSIONS AND FUTURE WORK	241
9.1 Fundamental understanding of the failure process	242
9.1.1 Model system studies.....	243
9.1.2 Application to commercially relevant dish liquid products.....	245
9.2 Improvements to low temperature stability test methods	247
9.2.1 Screening potential methods.....	248
9.2.2 Application of mixing.....	249
9.3 Future recommendations	250
APPENDIX A OPTICAL MICROSCOPE SETTINGS	252
A.1 Microscope setup	253
APPENDIX B ¹H NMR ASSIGNMENTS	254
B.1 ¹ H NMR assignments for the individual SDS and DDAO components	255
APPENDIX C THE FITTING OF SMALL-ANGLE X-RAY SCATTERING PROFILES AND FURTHER AVRAMI PLOTS	258
C.1 Model SDS and SDS + DDAO systems	259
C.1.1 Small-angle X-ray scattering (SAXS) model fitting.....	259
C.1.2 SAXS profiles at selected time points	264
C.1.3 Time-resolved wide-angle X-ray scattering (WAXS) profiles	267
C.1.4 Avrami analysis	268
C.2 P&G dish liquid sample	275
C.3 References.....	276

APPENDIX D FURTHER INFORMATION ON THE COMPOSITION OF DISH LIQUID FORMULATIONS - SAMPLES 1-32.....	277
D.1 Samples 1-32	278
APPENDIX E TEST METHOD IMPROVEMENTS – FURTHER EXPERIMENTAL DATA.....	279
E.1 Oven-dried seeding	280
E.1.1 Seed formation	280
E.2 Application of mixing	281
E.2.1 Cooling time.....	281
E.2.2 Further time lapse images	281
E.2.3 MATLAB code for greyscale intensity.....	283
E.2.4 Fitting parameters	286

LIST OF FIGURES

CHAPTER 1

Figure 1.1. Molecular structure of sodium dodecyl sulfate (SDS)	2
Figure 1.2. Molecular structure of N,N-dimethyldodecylamine N-oxide (DDAO)	3
Figure 1.3. Two-dimensional graphical representation of a micelle.	9
Figure 1.4. Schematic illustrating how physical properties change at the CMC. Adapted from Ref. (Chakraborty, Chakraborty and Ghosh, 2011).....	10
Figure 1.5. Typical phase diagram for an aqueous surfactant systems displaying the various phases above the CMC where A = Ideal solution, B and C = Micellar solutions, D = Hexagonal phase, E = Cubic phase, F = Lamellar phase and G = Crystals in the mixture. Adapted from Ref. (Brinker <i>et al.</i> 1999).....	12
Figure 1.6. Diagram showing examples of industries requiring the use of surfactants.....	14
Figure 1.7. Solubility curve and metastable zone plotted against temperature and concentration. Adapted from Ref. (Vedantam and Ranade, 2013).	20
Figure 1.8. Transformation plot for isothermal crystallisation.....	22
Figure 1.9. Diagram showing examples of the effects of ultrasound application on crystallisation processes.	36

CHAPTER 2

Figure 2.1. DSC (a) cooling thermogram and (b) heating thermogram for a 20 wt. % SDS solution attained at a scan rate of 0.1 °C/min.	76
Figure 2.2. Plot showing the crystallisation temperatures of various SDS aqueous solutions versus the concentration of SDS.....	77
Figure 2.3. Plots of SDS concentration against the enthalpy of crystallisation in (a) J/g of surfactant solution and in (b) J/g of SDS for the various surfactant solutions.....	78
Figure 2.4. X-ray diffraction pattern for a 20 wt. % SDS solution taken at hold temperatures of 0 °C (black line) and –20 °C (red line) with the blue lines highlighting those peaks that can be matched to ice.....	79

Figure 2.5. (a) DSC thermograms for SDS, 1-dodecanol and mixed SDS + 1-dodecanol aqueous systems; (b) is an enlarged image of the area contained within the box in (a). 81

Figure 2.6. DSC thermograms for the melting transitions that occur for an aqueous solution of 20 wt. % SDS (black line), 5 wt. % 1-dodecanol (red line) and a mixed alcohol + SDS system (blue line) on heating the solution from -5°C to 40°C at a scan rate of $0.1^{\circ}\text{C}/\text{min}$ 82

Figure 2.7. Optical images for a 20 wt. % SDS + 5 wt. % 1-dodecanol aqueous solution upon cooling, taken at a selection of temperatures. 84

CHAPTER 3

Figure 3.1. ^1H NMR spectra at 500 MHz of a 20 wt. % SDS + 3 wt. % DDAO system upon cooling a pH 9 across the chemical shift range (a) 0 – 5 ppm and (b) 2.3 – 4.0 ppm. The boxed area in (a) corresponds to the chemical shift range presented in (b). Proton resonance H_1 (SDS) is at 3.67 ppm and H_a (DDAO) is at 2.83 ppm (25°C). A full spectral assignment can be found in Appendix B. 97

Figure 3.2. Plot of the peak intensity for H_1 (SDS) and H_a (DDAO) upon cooling at pH 9. The normalised intensities, for both peaks, include a slight baseline offset. 97

Figure 3.3. ^1H NMR spectra at 500 MHz of a 20 wt. % SDS + 3 wt. % DDAO system upon cooling at pH 2 across the chemical shift range (a) 0 - 6 ppm and (b) 3.0 - 4.0 ppm. The boxed area in (a) corresponds to the chemical shift range presented in (b). Proton resonance H_1 (SDS) is at 3.67 ppm and H_a (DDAO) is at 3.35 ppm (7.5°C). 98

Figure 3.4. SAXS data for 20 wt. % SDS and 20 wt. % SDS + 3 wt.% DDAO samples at (a) 24°C and (b) 0°C . In both cases, the solid lines are fits to the data as described in the text and Appendix C. 100

Figure 3.5. SAXS data for 20 wt. % SDS and 20 wt. % SDS + 3 wt. % DDAO samples at pH 2. The solid lines are fits to the data as described in the text and Appendix C. 101

Figure 3.6. WAXS data for the three samples as noted at 0°C . Concentrations of SDS and DDAO, where present, are 20 wt. % and 3 wt.% respectively. The peak at 3.15 nm^{-1} is from the polycarbonate capillary used to mount samples in the beam. All other peaks arise from the samples. From these, significant peaks are listed in Table C.3, Appendix C. 101

CHAPTER 4

Figure 4.1. Molecular structure of (a) sodium dodecyl sulfate (SDS) and (b) N,N-dimethyldodecylamine N-oxide (DDAO). 112

Figure 4.2. Plots of (a) crystallisation temperature and (b) enthalpy of crystallisation versus DDAO concentration for SDS + DDAO systems. 117

Figure 4.3. (a) DSC thermograms acquired upon cooling a 20 wt. % SDS system to -5°C across a range of cooling rates..... 118

Figure 4.4. (a) Plot showing the WAXS intensity, $I(Q)$ as a function of Q for selected time points 0 s, 600 s, 1200 s and 3600 s for a 20 wt. % SDS solution held at 0°C after being cooled from 25°C at $19^{\circ}\text{C}/\text{min}$; (b) 3D plot showing the change in $I(Q)$ vs. Q during crystallisation as a function of time for the same 20 wt. % SDS solution; (c) Plot showing the WAXS intensity, $I(Q)$ as a function of Q for selected time points 0 s, 600 s, 1200 s and 3600 s for a 20 wt. % SDS + 3 wt. % DDAO solution held at 0°C after being cooled from 25°C at $19^{\circ}\text{C}/\text{min}$; (d) 3D plot showing the change in $I(Q)$ vs. Q as a function of time during crystallisation for the same 20 wt. % SDS + 3 wt. % DDAO solution. The corresponding plots for 20 wt. % SDS + 1, 2, 4 and 5 wt. % DDAO respectively are provided in Appendix C. 119

Figure 4.5. (a) Plot of the change in maximum intensity of the primary Bragg peak (at 1.9 nm^{-1} in the SAXS) during crystallisation as a function of time for all samples containing DDAO (1 - 5 wt. %); (b) Plot showing the rate of change of peak intensity as a function of DDAO concentration. 122

Figure 4.6. Raman spectra for SDS A (red line), SDS B (green line) and DDAO (blue line); A and B refer to different forms or orientations of the SDS component. 123

Figure 4.7. (a) Location selected for the analysis of a crystalline solution of 20 wt. % SDS; (b) Confocal scans of the xy plane of the red boxed area in (a) with $z = 0\text{ }\mu\text{m}$ or (c) $z = -5\text{ }\mu\text{m}$; (d) Locations selected for the analysis of a crystalline solution of 20 wt. % SDS + 3 wt. % DDAO; (e) Confocal scan of the xy plane of the red boxed area in (d) with $z = 0\text{ }\mu\text{m}$; (f) Confocal scan of the xy plane of the blue boxed area in (d) with $z = 0\text{ }\mu\text{m}$; (g) Confocal depth scan of the yz plane attained by vertically slicing along green line in (d) with $z = -7.5$ to $+7.5\text{ }\mu\text{m}$ 124

CHAPTER 5

Figure 5.1. Avrami plot for the crystallisation of a 20 wt. % SDS solution when held at 12°C ; fitted trendline equation $y = (2.69 \pm 0.045)x - 5.54 \pm 0.092$ and $R^2 = 0.997$ 141

Figure 5.2. Bar chart showing the change in the Avrami exponent for the crystallisation of a 20 wt. % SDS solution under various isothermal temperature conditions. Standard errors were calculated from repeated measurements. 141

Figure 5.3. Time resolved SAXS profiles acquired during the crystallisation of a 20 wt. % SDS + 3 wt. % DDAO system at 0°C 144

Figure 5.4. Change in peak area upon crystallisation of a 20 wt. % SDS + 3 wt. % DDAO system when held at 0 °C with 0 s taken as the time of initial Bragg peak formation.	145
Figure 5.5. Avrami plot for the crystallisation of a 20 wt. % SDS + 3 wt. % DDAO system when held at 0 °C. Fitted trendline has equation: $y = (3.07 \pm 0.141)x - 11.47 \pm 0.488$ and $R^2 = 0.987$	145
Figure 5.6. Relative change in the crystalline fraction with temperature for crystallisation of a 20 wt. % SDS system upon cooling to -5 °C across a range of cooling rates (0.1 °C/min - 1 °C/min).	147
Figure 5.7. Relative change in the crystalline fraction with time for crystallisation of a 20 wt. % SDS system upon cooling to -5 °C across a range of cooling rates (0.1 °C/min - 1 °C/min).	148
Figure 5.8. Ozawa plot for crystallisation of a 20 wt. % SDS solution. Fitted trendline has equation: $y = -(3.05 \pm 0.091)x - 2.68 \pm 0.048$ and $R^2 = 0.996$	149
Figure 5.9. (a) Simulations of data for hard sphere of $R = 10$ nm and (b) a mix of both $R = 10$ nm and 5 nm	151
Figure 5.10. SAXS profiles acquired 600 s after the beginning of the crystallisation process occurring in the 20 wt. % SDS + 3 wt. % DDAO system, across a range of cooling rates. ..	152

CHAPTER 6

Figure 6.1. Simplified flow diagram for producing dish liquid.	162
Figure 6.2. (a) Schematic of equipment setup where the polarisers can be set parallel or perpendicular; (b) A typical 96-well microplate.	169
Figure 6.3. ^1H NMR spectrum for a typical dish liquid paste dissolved in D_2O at 25 °C.	172
Figure 6.4. ^1H NMR spectra for dish liquid surfactant paste upon cooling.	173
Figure 6.5. Change in NMR intensity for proton environments from the different surfactant structures upon cooling.	174
Figure 6.6. DSC thermograms for 20 wt. % SDS (black line) and 20 wt. % ethoxylated alkyl sulfate paste (red line) solutions acquired upon cooling from 25 °C to -5 °C.	175
Figure 6.7. SAXS profiles for Formulation A at (a) 25 °C and (b) after 64 hours at 0 °C. The red lines correspond to fits to the data as described in the text and Appendix C.	176
Figure 6.8. WAXS profile for Formulation A, acquired after 64 hours at 0 °C.	177

Figure 6.9. Screening for the presence of crystalline failures after 7 days at 0 °C across a formulation space varying by ratio of amount of alkyl sulfate (AS) to amine oxide (AO) and amount of unreacted alcohol (UnR) across a range of sodium sulfate concentrations (wt. %). A cross indicates at least one failure out of the 4 replicates A failure corresponds to a transmission intensity, detected via the microplate technique, below 150.	179
Figure 6.10. Images of formulations with differing Low T number after 7 days holding at 0 °C.	182
Figure 6.11. Change in homogeneity analysis for the three X6 replicates across a 7-day period at 0 °C.	183
Figure 6.12. Homogeneity analysis of X1, X2, X3, X5 and X6 over a 7-day period at 0 °C.	184
Figure 6.13. Greyscale images for Formulation X6 at various time points and their corresponding homogeneity index.	184
Figure 6.14. Plot of (a) rate of crystallisation and (b) induction time against the Low T number of the formulation.	185

CHAPTER 7

Figure 7. 1. Microscope images of typical oven-dried dish liquid at varying length scales where (a) and (b) are obtained the oven-dried dish liquid bulk before being moulded into seeds and (c) is a seed placed in the well of a 96-well microplate	196
Figure 7.2. SEM image illustrating the rough surface of an oven-dried dish liquid seed.	197
Figure 7.3. Seeded (left) and control (right) results for Samples 3, 7, 9 and 32 after 48 hours at 0 °C.	198
Figure 7.4. Microplate images for Samples 1-10 after 48 hours exposure to 0 °C (a) in the absence of any seeding and (b) in the presence of an oven-dried dish liquid seeding.	199
Figure 7.5. Histogram plots showing the transmission measured for Samples 1-10 (each performed in quadruplicate) after 7 days at 0 °C.	201
Figure 7.6. The effect of (a) oven dried dish liquid seeding and (b) metal ball seeding on the light transmission measured at set intervals across Samples 1-10 when held at 0 °C for total period of 48 hours. Each sample was performed in quadruplicate.....	202
Figure 7.7. Microplate optical images for the (a) control and (b) sonicated samples at the initial time point (top) and after 6 days (bottom) at 0 °C for 3 samples that are prone to failure, namely	

Samples 3, 9 and 32 (columns), each performed 4 times (rows). A second set of Sample 3 was also performed.....204

Figure 7.8. Change in the intensity of the detected light transmission for (a) Sample 3, (b) Sample 9 and (c) Sample 32 in the presence (red boxes) and absence (blue crosses) of sonication across a 6-day timescale at 0 °C.....205

CHAPTER 8

Figure 8.1. (a) Stirrer probe dimensions (b) Schematic diagram of the setup for conductivity measurements217

Figure 8.2. (a) Schematic diagram of vacuum jacketed vessel setup. Adapted from a figure supplied by Asynt Ltd. (b) Photograph of the vessel setup indicating the areas used in greyscale intensity analysis221

Figure 8.3. Time lapse images acquired during crystallisation of Formulation A at 0 °C....222

Figure 8.4. Simplified schematic diagram illustrating the different surfactant environments residing in a dish liquid sample at 25 °C and 0 °C.....223

Figure 8.5. Time lapse images of an unstable dish liquid formulation held isothermally at 0 °C over 7 days (a) in the absence and (b) in the presence of a layer of sunflower oil.224

Figure 8.6. Relation of petri dish diameter to the crystallisation area, measured after 24 and 48 hours at 0 °C.225

Figure 8.7. (a) Typical conductivity plot attained upon cooling a 20 wt. % SDS + 3 wt. % DDAO system at speed level 1 (949 rpm) (b) Plot of the time to crystallisation across the range of speed levels where the time for crystallisation is taken as the time for the conductivity of the surfactant solution to reduce to 8 mS cm⁻¹.....226

Figure 8.8. Time lapse images of the crystallisation of Formulation A in the presence of mixing. The initial colour differences in the solution are due to unavoidable light reflections from the surroundings. Circles 1, 2 and 3 indicate the growing crystalline area.....227

Figure 8.9. Box plot demonstrating the reduction in the timescale to crystallisation and statistical variability upon mixing at 0 °C, across 8 replicates of Formulation A.....227

Figure 8.10. Snapshot of the light transmission measurements acquired for Formulation A across the displayed temperature cycle (a) in the absence of mixing and (b) in the presence of mixing.....228

Figure 8.11. Time series of images, acquired at 10 minute intervals, during the crystallisation of Formulation A at a stirrer speed of 20 rpm, with the solution is held at 0 °C.229

Figure 8.12. Time resolved plot of greyscale intensity for the 4 boxed areas (A-D) when mixed at (a) 20 rpm (b) 50 rpm (c) 150 rpm (d) 300 rpm. The black line for each profile corresponding to the fit of a 4 parameter sigmoidal curve to the data.230

Figure 8.13. Variation of (a) $\frac{1}{b}$ (steepness), (b) x_0 (midpoint) and (c) induction time across the different mixing speeds and boxed areas (A-D).232

Figure 8.14. Change in homogeneity for the three X6 samples across a 7-day period at 0 °C.233

Figure 8.15. Correlation of failure times between the current and proposed low temperature stability test methods across a range of dish liquid formulations.234

APPENDIX A

Figure A.1. Screenshot of the microscope settings.253

APPENDIX B

Figure B.1. Labelling scheme for the proton environments in (a) N,N-dimethyldodecylamine N-oxide (DDAO) and (b) sodium dodecyl sulfate (SDS).255

Figure B.2. (a) ^1H NMR spectrum for a 20 wt. % SDS system and (b) ^1H NMR spectrum for 3 wt. % DDAO system dissolved in D_2O at 25 °C acquired at 500 MHz. As the NMR signals for protons H_a and H_1 are well resolved, and do not overlap with other peaks, they have been used to identify each surfactant when in a mixed system. H_1 is set to 3.67 ppm and both spectra have been adjusted relative to this calibration.256

APPENDIX C

Figure C.1. Fit deconstruction for SAXS data for a 20 wt. % SDS + 3 wt. % DDAO solution at 24 °C, showing the contributions of the prolate ellipsoid micelle $P(Q)_{\text{ellipsoid}}$ and the charged $S(Q)_{\text{RMSA}}$, described in the text. The total scattering, $I(Q)_{\text{fit}} = P(Q)_{\text{ellipsoid}} \times S(Q)_{\text{RMSA}} + I_{\text{BKG}}$, where $I_{\text{BKG}} = 0.00144$261

Figure C.2. Fit deconstruction for SAXS data for a 20 wt. % SDS + 3 wt. % DDAO solution at 0 °C, showing the contributions of the power law (PL), background (BKG), micelle population and peak intensities to the overall fit. The total modelled scattering, $I(Q)_{\text{fit}} = I(Q)_{\text{PL+BKG}} + I(Q)_{\text{Peak}} + I(Q)_{\text{Micelles}}$ 263

Figure C.3. SAXs profiles acquired at various timepoints (0 s, 120 s, 600 s, 1200 s, 1800 s, 3600 s) during crystallisation of various SDS + DDAO systems containing 20 wt. % SDS and (a) 1 wt. % DDAO (b) 2 wt. % DDAO (c) 3 wt. % DDAO (d) 4 wt. % DDAO (e) 5 wt. % DDAO.....266

Figure C.4. 3D WAXS profiles acquired during the crystallisation of SDS + DDAO systems containing 20 wt.% SDS and (a) 1 wt. % DDAO (b) 2 wt. % DDAO (c) 4 wt. % DDAO (d) 5 wt. % DDAO.267

Figure C.5. Avrami plots corresponding to crystallisation of a 20 wt. % SDS solution at (a) 12 °C (rep 2). Fitted trendline has equation $y = (2.96 \pm 0.063)x - 6.36 \pm 0.131$ and $R^2 = 0.998$; (b) 12 °C (rep 3). Fitted trendline has equation $y = (2.84 \pm 0.079)x - 7.43 \pm 0.190$ and $R^2 = 0.997$; (c) 13 °C (rep 1). Fitted trendline has equation $y = (3.43 \pm 0.088)x - 11.04 \pm 0.263$ and $R^2 = 0.995$; (d) 13 °C (rep 2). Fitted trendline has equation $y = (3.20 \pm 0.070)x - 11.65 \pm 0.234$ and $R^2 = 0.995$; (e) 13 °C (rep 3). Fitted trendline has equation $y = (3.57 \pm 0.051)x - 10.77 \pm 0.140$ and $R^2 = 0.999$; (f) 14 °C (rep 1). Fitted trendline has equation $y = (3.60 \pm 0.053)x - 10.64 \pm 0.137$ and $R^2 = 0.999$; (g) 14 °C (rep 2). Fitted trendline has equation $y = (3.69 \pm 0.185)x - 12.77 \pm 0.580$ and $R^2 = 0.983$; (g) 14 °C (rep 3). Fitted trendline has equation $y = (3.81 \pm 0.267)x - 10.81 \pm 0.666$ and $R^2 = 0.986$. ..274

APPENDIX E

Figure E.1. Relative change in the mass of a 20 g sample of dish liquid placed in an oven at 70 °C.....280

Figure E.2. Change in temperature and conductivity over time for a typical dish liquid product (Formulation A) contained within the jacketed vessel. The water bath set to 0 °C with measurements taken at the most central point of the vessel.281

Figure E.3. Time lapse images taken at 10 minute intervals ((a)-(g)) upon holding Formulation A at 0 °C and with an applied mixing speed of (a) 50 rpm (b) 150 rpm (c) 300 rpm.....282

LIST OF TABLES

Table 5.1. Parameters attained when fitting a sigmoidal function to the crystallisation profiles of a 20 wt. % SDS system attained a selection of different cooling rates (0.1 - 1 °C/min)....	148
Table 6.1. Four categories of alcohols present in blends used in the production of alkyl sulfates present in dish liquid formulations.	163
Table 6.2. Composition of Formulations X1 and X6.....	166
Table 6.3. Composition and related Low T number for Formulations X1 - X6.....	167
Table 8.1. Speed levels and corresponding rpm values.....	218
Table B.1. ¹ H NMR assignments for the individual SDS and DDAO systems at 25 °C at 500 MHz.....	257
Table B.2. T ₁ values for select proton environments acquired at 300 MHz.....	257
Table C.1. Fitting parameters for surfactant solutions at 24 °C.	260
Table C.2. Fitting parameters for surfactant solutions at 0 °C.	263
Table C.3. List of notable peaks in the WAXS data at 0 °C.	268
Table C.4. SAXS fitting parameters for various scans during crystallisation of a 20 wt. % SDS + 3 wt. % DDAO system at 0 °C.....	269
Table C.5. Avrami exponents attained for the crystallisation of a 20 wt. % SDS solution at different isothermal temperatures: 12 °C, 13 °C and 14 °C.	275
Table C.6. Fitting parameters for Formulation A at 24 °C and 0 °C.....	275
Table D.1. Compositional information for Samples 1-32.	278
Table E.1. Fitting parameters for the sigmoidal plots of greyscale intensity over time performed in triplicate at a mixing speed of (a) 20 rpm, (b) 50 rpm, (c) 150 pm and (d) 300 rpm. For each replicate, 4 greyscale plots were attained corresponding to areas A -D (provided in Figure 8.2(b)).	287

NOMENCLATURE

ABBREVIATIONS

2D	Two-dimensional
3D	Three-dimensional
Act	Active level
AS	Alkyl sulfate
AO	Amine oxide
A.U.	Arbitrary units
BBO	Broadband observe
BrA	Branched alcohol
BrAE	Branched alcohol ethoxylate
CMC	Critical micelle concentration
CTAB	Cetyltrimethylammonium bromide
DCI	Deuterium chloride
DDAO	N,N-dimethyldodecylamine N-oxide
DMSO	Dimethyl sulfoxide
DSC	Differential scanning calorimetry
FMCG	Fast-moving consumer goods

GCOM	Greyscale co-occurrence matrix
HCl	Hydrochloric acid
HPLC	High performance liquid chromatography
IR	Infra-red
LA	Linear alcohol
LAE	Linear alcohol ethoxylate
LED	Light emitting diode
Low T #	Low T number
MRI	Magnetic resonance imaging
MSZW	Metastable zone width
NaCl	Sodium chloride
NaOH	Sodium hydroxide
Na ₂ SO ₄	Sodium sulfate
NMR	Nuclear magnetic resonance
NPE	Nonylphenol ethoxylate
PEEK	Polyether ether ketone
PET	Polyethylene terephthalate
pH	Potential hydrogen
P&G	Procter & Gamble

SANS	Small-angle neutron scattering
SAS	Small-angle scattering
SAXS	Small-angle X-ray scattering
SDS	Sodium dodecyl sulfate
SEM	Scanning electron microscopy
SOBS	Sodium octylbenzene sulfonate
UnR	‘Unreacted alcohol’
UV	Ultra-violet
WAXS	Wide-angle X-ray scattering
XRD	X-ray diffraction

In the next sections parameter units are given, where appropriate. Where there is more than one option for units, the most relevant to this work is provided or, alternatively, both are given.

GENERAL

i_n	Pixel number	(-)
k	Boltzmann constant	$\text{m}^2\text{kgs}^{-2}\text{K}^{-1}$
MW	Molecular weight	gmol^{-1}
R	Gas constant	$\text{Jmol}^{-1}\text{K}^{-1}$
T	Temperature	$^{\circ}\text{C}$
t	Time	s or min

x	Mole fraction	(-)
#	Number sign	(-)
κ	Conductivity	mScm^{-1}

CRYSTALLISATION KINETICS

a	Cooling rate	$^{\circ}\text{Cmin}^{-1}$
A	Surface area of crystal	m^2
B_0	Secondary nucleation rate	s^{-1}
K_{sp}	Solubility product	(-)
k	Mass-transfer coefficient	ms^{-1}
J	Primary nucleation rate	s^{-1}
J_{Hom}	Primary homogenous nucleation rate	s^{-1}
J_{Het}	Primary heterogenous nucleation rate	s^{-1}
M_{T}	Density of crystal	kgm^{-3}
m	Ozawa exponent	(-)
n	Avrami exponent	(-)
S	Supersaturation level	(-)
T_{c}	Temperature of crystallisation	$^{\circ}\text{C}$
T_{k}	Krafft temperature	$^{\circ}\text{C}$
W	Agitation rate	rpm

$X(t)$	Crystalline fraction up to time t	(-)
$X(T)$	Crystalline fraction up to temperature T	(-)
μ_e	Chemical potential of a system at equilibrium	Jmol^{-1}
μ_s	Chemical potential of a system	Jmol^{-1}

NUCLEAR MAGNETIC RESONANCE

I	Spin	(-)
T_1	Spin-lattice relaxation time	s
T_2	Spin-spin relaxation time	s
T_2^*	Spin-spin relaxation time and magnetic inhomogeneity	s
α	Low energy spin state of ^1H nuclei	(-)
β	High energy spin state of ^1H nuclei	(-)
$\nu_{1/2}$	Line width at half maximum	Hz

X-RAY SCATTERING

A	Peak area of SAXS profile	m^{-2}
d	Distance	nm
$I(Q)$	Intensity	cm^{-1}
N_{agg}	Micelle aggregation number	(-)
$P(Q)$	Form factor	(-)
Q	Scattering vector	nm^{-1}

$S(Q)$	Structure factor	(-)
Z	Charge	eV
θ	Bragg angle	°
λ	Wavelength	nm
ρ	Scattering length density	cm ⁻²

THERMODYNAMICS

a_i	Activity coefficient for species I	(-)
a_e	Activity coefficient of a system at equilibrium	(-)
a_s	Activity coefficient of a system	(-)
$A(t)$	Area under DSC curve up to time t	Jg ⁻¹
$A(T)$	Area under DSC curve up to temperature T	J°C g ⁻¹ s ⁻¹
$A_t(\infty)$	Total area under DSC curve measured over time	Jg ⁻¹
$A_T(\infty)$	Total area under DSC curve measured over temperature	J°C g ⁻¹ s ⁻¹
C_p	Specific heat capacity	Jg ⁻¹ °C ⁻¹
ΔG	Gibbs free energy	Jmol ⁻¹
ΔH	Enthalpy (specific)	Jg ⁻¹
ΔH_{diss}	Enthalpy of dissolution	Jg ⁻¹
ΔH_{cry}	Enthalpy of crystallisation	Jg ⁻¹
q	Heat flow	Jg ⁻¹ s ⁻¹

T	Temperature	°C
T _{cry}	Temperature of crystallisation	°C
T _{diss}	Temperature of dissolution	°C
T _p	Peak temperature	°C

UNITS OF MEASUREMENT

cP	Centipoise
eV	Electronvolt
g	Gram
h	Hours
Hz	Hertz
J	Joule
K	Kelvin
L	Litre
M	Molar
m	Metre
m	Mass
min	Minute
mol	Moles
Pa	Pascal

ppm	Parts per million
rpm	Rotations per minute
S	Siemens
s	Seconds
W	Watt
wt. %	Weight percent
°C	Degrees Celsius
°	Degrees

METRIC PREFIXES

c	Centi
k	Kilo
M	Mega
m	Milli
n	Nano
μ	Micro

PUBLICATIONS AND CONFERENCES

Research contained within this manuscript has been published in journals and presented at the conferences listed below:

PUBLICATIONS

Summerton, E., Bettiol, J., Jones, C., Britton, M. M., and Bakalis, S., 2018. Understanding the crystallisation process in detergent formulations in the absence and presence of agitation, *Industrial Engineering & Chemistry Research* (in press).

Summerton, E., Hollamby, M. J., Le Duff, C. S., Thompson, E. S., Snow, T., Smith, A. J., Bettiol, J., Jones, C., Bakalis S. and Britton, M. M. 2019. Nuclear magnetic resonance and small-angle X-ray scattering of mixed sodium dodecyl sulfate and N,N-dimethyldodecylamine N-oxide aqueous systems performed at low temperatures, *Journal of Colloid and Interface Science*, **535**, p. 1-7.

Summerton, E., Hollamby, M. J., Zimbitas G., Snow, T., Smith, A. J., Sommertune, J., Bettiol, J., Jones, C., Britton, M. M. and Bakalis. S. 2018. The impact of N,N-dimethyldodecylamine N-oxide (DDAO) concentration on the crystallisation of sodium dodecyl sulfate (SDS) systems and the resulting changes to crystal structure, shape and the kinetics of crystal growth, *Journal of Colloid and Interface Science*, **527**, p. 260-266.

Summerton, E., Zimbitas, G., Britton, M. and Bakalis, S. 2017. Low temperature stability of surfactant systems, *Trends in Food Science & Technology*, **60**, p. 23-30.

Summerton, E., Zimbitas, G., Britton, M. and Bakalis, S. 2016. Crystallisation of sodium dodecyl sulfate and the corresponding effect of 1-dodecanol addition, *Journal of Crystal Growth*, **455**, p. 111-116.

ORAL PRESENTATIONS (speaker underlined)

Summerton, E., Thompson, E. S., Jones, C., Bettiol, J., Britton, M. and Bakalis, S. Understanding the crystallisation behaviour in dish liquid formulations and the corresponding effect of agitation on its mechanism, *Formula IX*, Beijing, 2017.

Summerton, E., Thompson, E. S., Britton, M., and Bakalis, S. Low temperature stability of surfactant systems, *UK Colloids*, Manchester, 2017.

POSTER PRESENTATIONS

Posters were presented by Emily Summerton (author) at the following conferences:

- SCI Formulation Forum, 2018.
- Formula VIII, Barcelona, 2016.
- International Colloids, Berlin, 2016.
- EFFOST, Athens, 2015.

THESIS LAYOUT

This thesis manuscript is composed of nine chapters including an introduction chapter, which contains the literature review, seven experimental results chapters and a conclusions and future recommendations section. The experimental chapters are provided in a self-contained paper-type format each containing an abstract, introduction, results and discussion and conclusions. Chapters 1, 2, 3, 4 and 8 are all based on papers that have either been published or submitted for publication.

Chapter 1 is the introductory chapter discussing the project objectives, the relevance of the work to the sponsor company, P&G, and background literature in this research area. Covered in the literature review is an introduction to surfactants and their applications, a discussion of surfactant crystallisation, routes documented to reduce the time to crystallisation and a background into the applicable experimental techniques.

Chapter 2 is the first results chapter which introduces crystallisation of an aqueous sodium dodecyl sulfate (SDS) system. This is the most commonly used surfactant in dish liquid applications. The effect of the alcohol precursor, 1-dodecanol, on the crystallisation process is also considered.

Chapter 3 focuses on structural and compositional studies of the crystals formed from mixed SDS and N,N-dimethyldodecylamine N-oxide (DDAO) solutions, with the surfactants present at concentrations typical of commercial dish liquid.

Chapter 4 also focuses on the crystallisation of SDS + DDAO systems. Specifically, this section considers the effect of DDAO concentration on the phase transition in terms of crystallisation kinetics, crystal shape and the structural changes occurring during crystal formation.

Chapter 5 provides an in depth kinetic analysis of the crystallisation of pure SDS and SDS + DDAO systems, under both isothermal and non-isothermal conditions.

Chapter 6 outlines the application of the learning gained from the model systems to complex dish liquid systems, with most of the work contained within this chapter carried out at the P&G Brussels Innovation Centre. Factors found to impact the stability are discussed.

Chapter 7 is a further experimental chapter that investigates potential routes to improve the low temperature stability test methods for dish liquid products. The majority of these experiments were performed at the P&G Brussels Innovation Centre.

Chapter 8, an extension of Chapter 7, is the final experimental chapter that continues to discuss possible stability test method improvements. The application of agitation as a route to improve the efficiency of these tests is explored, with particular focus on the effect of different mixing speeds and changes to the crystallisation mechanism in the presence of agitation.

Chapter 9 contains the conclusions and summarises the work completed, in addition to providing recommendations for next steps in the investigations.

CHAPTER 1

INTRODUCTION

Some discussions contained within this chapter have been published within: Summerton, E., Zimbitas, G., Britton, M. and Bakalis, S. 2017. Low temperature stability of surfactant systems, *Trends in Food Science & Technology*, **60**, p. 23-30.

1.1 Project background

Over recent decades, the detergent industry has continued to grow and expand its product portfolio. Since the introduction of the soap bar in the 1800s (Spitz, 2016), this industry has diversified to include a range of products, such as liquid detergents, dishwasher tablets, washing powders and shampoos. All these formulations have complex compositions and aim to provide the optimal physical, sensory and chemical attributes for consumers. The key active ingredients incorporated within all these products are chemical components called surfactants, which are responsible for removing any soils. More specifically, anionic surfactants are most prevalent in the cleaning industry (Scheibel, 2004), in comparison to other surfactant types, which is largely driven by their ability to clean, their foaming properties and their relatively low economic cost.

This project focuses on the detergent surfactant system known as dish liquid, which is used daily by consumers across the globe. As well as containing a high proportion of anionic surfactants, dish liquid also contains amphoteric surfactants in a lower proportion. In past studies, it has been demonstrated that mixed surfactant systems display more suitable characteristics than one containing a single surfactant (Yangxin *et al.*, 2008). This is also true for other homecare and personal care products. In typical dish liquid formulations, the anionic surfactants tend to be alkyl sulfates such as sodium dodecyl sulfate (SDS), depicted in Figure 1.1. Other alkyl sulfates arise from variations in chain length, the presence of ethoxy groups or branching off the main hydrocarbon chain.

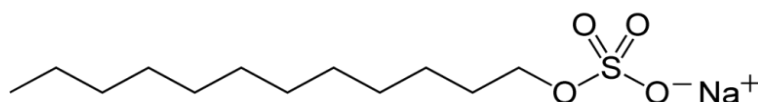


Figure 1.1. Molecular structure of sodium dodecyl sulfate (SDS).

An example of an amphoteric surfactant frequently used in dish liquid formulations is displayed in Figure 1.2. Although N,N-dimethyldodecylamine N-oxide (DDAO) is an amphoteric surfactant, it exhibits non-ionic properties when present in dish liquid, due to the surrounding alkaline pH environment (Búcsi *et al.*, 2014).

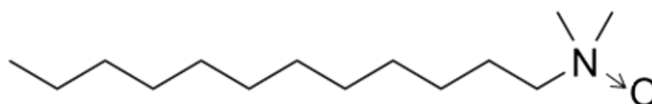


Figure 1.2. Molecular structure of N,N-dimethyldodecylamine N-oxide (DDAO).

Dish liquid also contains other ingredients, including dyes, perfumes, preservatives, water and ethanol, which are added at specific concentrations in order to attain the required physical and chemical properties of the formulation (Lai, 1996).

Formulation development of homecare products, such as dish liquid, continues to play a prominent role in industry. The cost of the raw materials is susceptible to fluctuations and there are also ongoing changes in consumer demands. As a result of these factors, new formulations must be introduced, or the existing ones refined, in order to satisfy market demand and maximise profit. When designing formulations, it is important to expose the product to extensive chemical testing, such as foam stability or viscosity measurements. Furthermore, the stability of a product must be monitored across the shelf life at a range of different temperatures and humidity environments (Porter, 2013). This has become especially important in recent years as formulations are being supplied to continents exhibiting widely varying climates. Unfortunately, these stability tests often have long timescales, with up to a month of testing required in some cases. In addition, there is a high degree of variability arising from existence of environmental factors that are difficult to control. For example, dust particles can act as nucleation sites and promote the onset of crystalline failures in some products at low temperatures.

Stability issues can arise in dish liquid under low and sub-zero temperature environments. There is a risk that crystalline entities may appear in the formulation and result in the surfactant system failing appearance criteria. Other failure modes may include a complete phase change or phase split. The behaviour of this detergent formulation at low temperatures is not well understood and there are significant gaps in the knowledge base. It is important to minimise crystallisation and, therefore, a fundamental chemical understanding of this failure process is necessary to improve product development and the efficiency of the associated stability test methods.

1.2 Project aims

The fundamental understanding surrounding the crystallisation process occurring at low temperatures in some homecare products was highlighted as an area requiring further research if product stability is to be improved. Specifically, this project focuses on the crystallisation behaviour of dish liquid. Current research into surfactant crystallisation is mainly focused on binary and single surfactant systems, with relatively few publications focused on the surfactants relevant to the dish liquid industry or at surfactant concentrations that are representative of commercial products.

A key objective of the work is to generate a broader knowledge base of this crystallisation process and understand the composition and structure of crystals that form in this surfactant system. To achieve such an objective, simple binary and single surfactant systems are used to provide an initial understanding before performing studies on commercial dish liquid products.

Compositional and structural attributes of the crystals are explored using data acquired from variable temperature nuclear magnetic resonance (NMR) and small-angle X-ray scattering (SAXS), with the 62 hours of beamtime at the Diamond Light Source, Oxfordshire, UK providing a key opportunity to characterise the crystals. Examples of some other techniques that are used throughout the thesis include optical microscopy and differential scanning

calorimetry (DSC), from which information about the kinetics and thermodynamics of the process can be inferred. The impact of the formulation composition on the product stability is also discussed, after performing a series of stability tests at P&G.

Using the acquired knowledge, a further aim of the project is to improve the reliability and reproducibility of the accompanying stability test methods, which can demonstrate high statistical variability and long timescales to failure. Furthermore, the current stability tests monitor the stability of stationary formulations, which is not necessarily representative of the supply chain. In this work, methods that not only reduce the failure timescales, but also more closely simulate transportation, are investigated and tested over a wide formulation space using a selection of light transmission techniques.

1.3 Relevance to P&G

P&G, the industrial sponsor for this project, proposed that work undertaken in this project would provide key scientific understanding behind stability issues that can arise at low temperatures in their dish liquid formulations. P&G originated in Cincinnati, where it was founded by William Procter and James Gamble. They originally had separate roles as a candle maker and soap maker respectively but, through family connections, the two men formed the P&G collaboration in 1837 at which point the company began to grow in employee numbers and diversify in product range. P&G is a dominant player in the fast-moving consumer goods (FMCG) industry with leading brands in several market segments such as haircare, personal care and homecare (P&G, 2017).

During product development, stability testing must be performed before a formulation can be launched to market. Product stability is important due to the strong global presence of P&G products, which comes with an increased probability of the formulations being exposed to a wide range of temperatures and climates. Currently P&G serves more than 180 countries and

employs over 95,000 people. P&G places a large emphasis on the R&D sector spending 1.9 billion dollars in the last financial year. To continue to be a market leader and fulfil their mission statement, it is important that P&G maintain a strong focus on scientific research. The chemical and physical stability of their products is at the forefront of this research.

A fundamental understanding of the crystallisation failures exhibited by detergent formulations in cold climates will be valuable when designing new formulations. Stability issues not only incur costs to P&G, but also cause wastage and product recalls resulting in a negative environmental impact as well as reducing brand loyalty. Reducing its environmental footprint and improving sustainability are at the centre of P&G's business aims so it is important to minimise the occurrence of these crystalline failures.

To detect crystalline failures, low temperature stability testing is performed on detergent products at temperatures ranging from $-3\text{ }^{\circ}\text{C}$ to $10\text{ }^{\circ}\text{C}$ with a high proportion of the testing carried out at $0\text{ }^{\circ}\text{C}$. Unfortunately, the timescales of the tests are long requiring up to 28 days to determine if a formulation meets the necessary success criteria, with much of this testing performed via visual inspection. There are also significant discrepancies in failure times, even between samples from the same batch, that may originate from external factors that are difficult to control, such as the existence of dust particles or temperature and pressure fluctuations. An approach capable of determining stability failures within a reduced timescale and with minimal variability is key for improving the efficiency of the business. Furthermore, there is a requirement for an approach that more closely simulates the supply chain, since the current method does not account for any movement that the formulations may experience during distribution.

1.4 Literature Review

1.4.1 Introduction to surfactants

1.4.1.1 Surfactant classification

Surfactants, also termed surface-active agents, have a distinct molecular structure and can be classified as amphiphilic compounds since they possess both hydrophobic and hydrophilic properties (Rosen, 2004). The basic chemical structure is composed of a hydrophobic hydrocarbon chain attached to a hydrophilic head group (Farn, 2008). The hydrocarbon chain typically comprises of 10 - 16 carbon atoms (Porter, 2013). Depending on the strength and polarity of the functional head group, surfactants can be further sub-classified into four distinct categories; cationic, anionic, zwitterionic and non-ionic (Zhang *et al.*, 2006; Kronberg *et al.*, 2014). Examples of cationic surfactants include amine and quaternary ammonium salts, both of which have positively charged head groups. Sulfonate and sulfate salts, such as sodium dodecyl sulfate (SDS), are examples of anionic surfactants. Amphoteric surfactants, such as some amine oxides, contain both negative and positively charged head groups, with their net head group charge dependent on the pH of the system (Friedli, 2001). Finally, non-ionic surfactants possess neutral head groups.

1.4.1.2 Micelle formation

When present at low concentrations in aqueous solution, surfactants exist as monomers that have a preference to accumulate at the air-liquid interface (Goodwin, 2009). By forming a monolayer at the surface, unfavourable interactions between the hydrophobic surfactant chains and water are minimised (Gil and Lacks, 2016). The monomers will displace some surface water molecules reducing the intermolecular forces between the water and thus lowering the surface tension (Holmberg, 2002).

Surfactants aggregate when the surfactant concentration exceeds a specific value called the critical micelle concentration (CMC). The CMC depends on a variety of factors, with the most important being the nature of the surfactant(s) involved in the system. An increase in alkyl chain length lowers the CMC due to an increasing hydrophobic character of the micelle core (Lomax, 1996). The surrounding environmental conditions, such as temperature and ionic strength, can also have an impact on the CMC (Rosen and Kunjappu, 2012). Typically, increasing the temperature of the system causes an initial decrease in the CMC followed by a subsequent increase (Chen *et al.*, 1998). A decrease in the hydrogen bonding between the solvent and head group is responsible for the initial decrease. Secondly, as the temperature rises, water surrounding the alkyl chains in the micellar core becomes increasingly disordered resulting in the subsequent increase in the CMC.

These micelle aggregates form due to the hydrophobic effect (Maibaum *et al.*, 2004; Southall *et al.*, 2002). Such a phenomenon results in a surfactant arrangement in which the degree of unfavourable contact between the hydrophobic surfactant tail and the polar water molecules is minimised (McClements, 2015). These aggregates can adopt a variety of molecular arrangements such as micelles, vesicles, bilayers and reverse micelles (Menger *et al.*, 1998). A two-dimensional (2D) image of a cross-section of a spherical micelle is illustrated in the schematic in Figure 1.3 and shows the hydrocarbon tails residing in the core of the structure (Hunter, 2001).

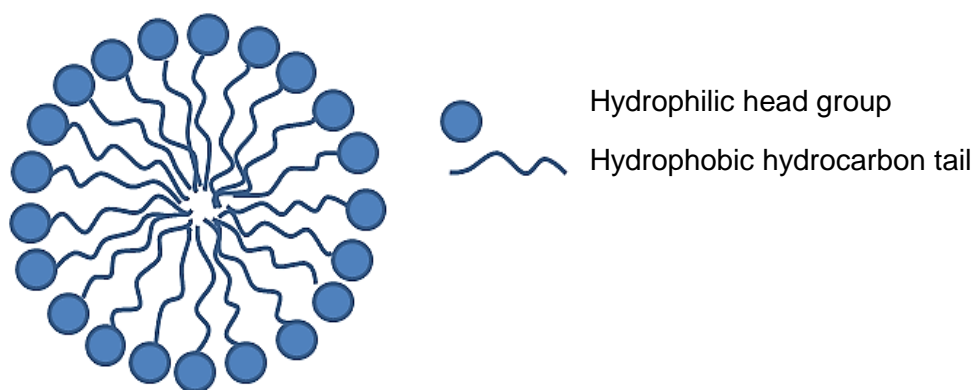


Figure 1.3. Two-dimensional graphical representation of a micelle.

These micelles can also adopt various different shapes, such as spherical, rod-like and disk-like (Dong and Gao, 2015). The change in micellar shape with surfactant concentration has been studied by computational simulation to further understand the mechanism when transitioning between different forms (Gao *et al.*, 2005).

The structures of micelles have been extensively studied by small-angle X-ray scattering (SAXS) (Lipfert *et al.*, 2007) where it is possible to attain parameters such as their size and shape. For example, calcium dodecyl sulfate micelles were found to be ellipsoidal (Mahapatra *et al.*, 2015). Various parameters, such as core radius and micellar charge, were also obtained for these micelles by fitting relevant models to the SAXS profiles. With small-angle neutron scattering (SANS) it is possible, through contrast variation, to selectively observe characteristics of the shell and core of aggregates (Hollamby, 2013).

1.4.1.3 Measuring the critical micelle concentration (CMC)

During recent decades, numerous methods have been reported for measuring the CMC of a solution, ranging from optical to spectroscopic and conductive methods (Kissa, 2001). A selection of the commonly used approaches are described in the next section.

Figure 1.4 illustrates how some key physical properties change at the point of the CMC.

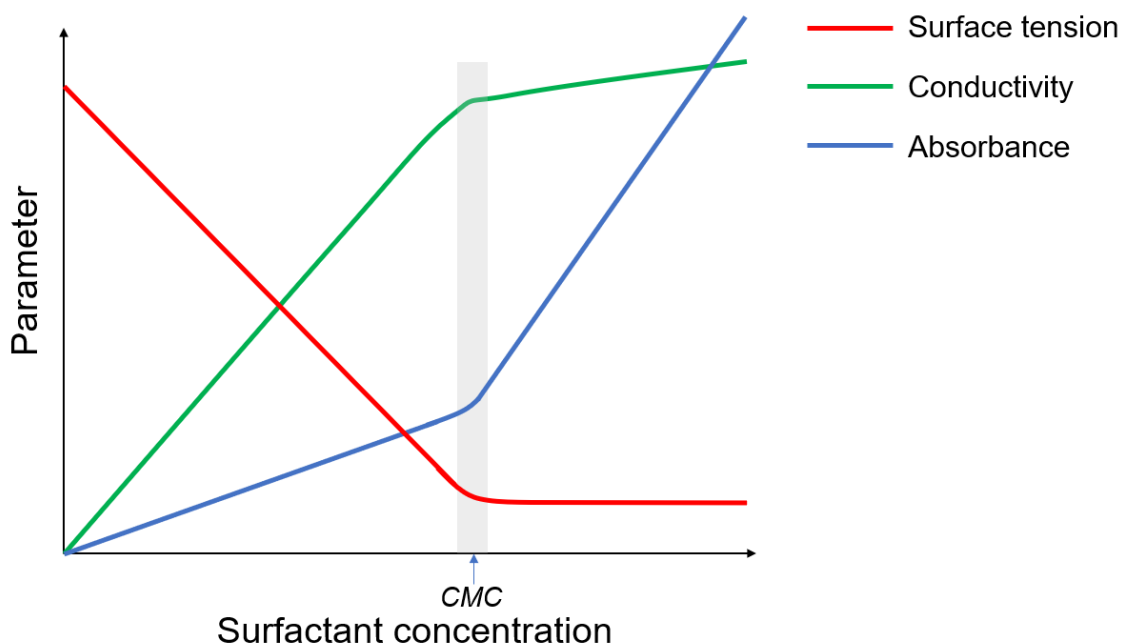


Figure 1.4. Schematic illustrating how physical properties change at the CMC. Adapted from Ref. (Chakraborty, Chakraborty and Ghosh, 2011).

1.4.1.3.1 Surface tension

The most common method for determining the CMC is through measuring the change in surface tension with surfactant concentration (Lin *et al.*, 1999; Chu, 2014; Patist *et al.*, 2000). As illustrated by Figure 1.4, the surface tension of a surfactant system decreases with addition of surfactant until the CMC is reached, after which the surface tension then remains constant. When surfactant monomers adsorb at the interface, they disrupt the hydrogen bonding packing of the water molecules in that region, thus reducing the surface tension (Chakraborty *et al.*, 2011). The initial lowering of the surface tension upon surfactant addition is important for many applications, including the enhancement of foam stability and thin films which, in the absence of any surfactants, would collapse (Zimbitas *et al.*, 2017). Upon reaching the CMC, any further surfactant goes into micelles in the bulk, rather than accumulating at the surface, so the surface tension remains unchanged. Although this method can be used for both ionic and non-ionic surfactants, a previous study revealed that the surface tension method is not always suitable for

non-ionic surfactants (Patist *et al.*, 2000). There is not always a distinct change in surface tension, which they attribute to a wide molecular weight distribution. This implies molecules with varying degrees of ethoxylation are present, leading to a range of CMC values within one sample.

1.4.1.3.2 Conductivity

A plot of solution conductivity versus surfactant concentration can yield the CMC at the break point (Figure 1.4) (Shirahama and Kashiwabara, 1971; Dominguez *et al.*, 1997). This change in conductivity can be explained by the ability of micelles to carry charge, compared to monomers. Since micelles are larger and less mobile than monomers, they are less efficient charge carriers. Below the CMC an increase in surfactant concentration yields an increase in monomers and counterions and hence an increase in the number of charge carriers in the bulk. Above the CMC the monomer concentration no longer changes, and further surfactant molecules form micelles. Furthermore, the counterions bind to the micelles and therefore become less available to carry charge through the system.

1.4.1.3.3 Solubility of dyes

The absorbance of water insoluble dyes, such as pyrene, can also be used to determine the CMC of a system (Patist *et al.*, 2000; Topel *et al.*, 2013). Some dye molecules exhibit an increase in their solubility at the CMC (Figure 1.4). The dye molecules become incorporated into the micelles and, therefore, become increasingly soluble (Nasiru *et al.*, 2011). This change in the environment results in an increase in absorbance of the solution, which can be used to attain the CMC.

1.4.1.4 Further surfactant phases

The micellar structure adopted by surfactants enables them to dissolve hydrophobic molecules, such as fats and oils, in aqueous solution and provide cleaning and emulsifying properties (Rosen, 2004). Additionally, surfactants have foaming properties as well as acting as wetting and solubilising agents (Attwood, 2012). Upon an increase in surfactant concentration in aqueous solution other surfactant phases can form (Yan and Texter, 2006). A typical phase diagram as a function of surfactant concentration is shown in Figure 1.5 (Brinker *et al.*, 1999; Miller *et al.*, 2016).

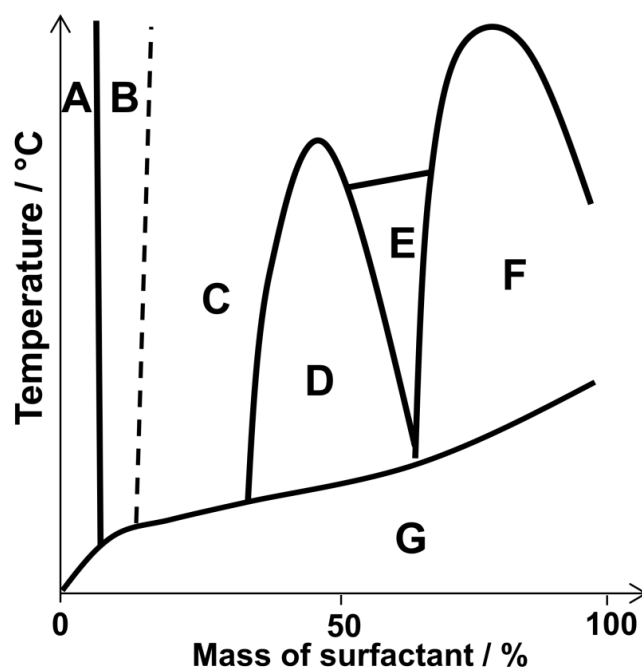


Figure 1.5. Typical phase diagram for an aqueous surfactant systems displaying the various phases above the CMC where A = Ideal solution, B and C = Micellar solutions, D = Hexagonal phase, E = Cubic phase, F = Lamellar phase and G = Crystals in the mixture. Adapted from Ref. (Brinker *et al.*, 1999).

An increase in surfactant concentration favours the formation of liquid crystal phases (Rosevear, 1968). These liquid crystal phases can have various forms, namely hexagonal, cubic and lamellar phases, with the latter forming at higher concentrations. The hexagonal phase is

formed by hexagonal close packing of the rod-shaped cylindrical micelles whereas the cubic form originates from spherical micelles cubic close packing (Tiddy, 1980). When P&G produce their cleaning products, the surfactant paste is initially supplied in the concentrated, hexagonal liquid crystal form. Before supplying to market, significant dilution and application of high-shear mixing is required to attain the isotropic micellar phase. The hexagonal form displays anisotropic properties, as detected by a polarising microscopy (Rosen, 2004). Other liquid crystal forms also exhibit this property but, conversely, micelle solutions display isotropic characteristics. Aside from forming micelles, monomers and the liquid crystal phases, hydrated crystals can also form at low temperatures. However, this particular phase transition is not well understood, despite resulting in appearance failures in industrial formulations.

1.4.1.5 Use of surfactants in industry

Due to their chemical properties, surfactants are extensively used in a variety of industries on a global scale. These industries include those of homecare, food, personal care, textiles, plastic and cleaning (Azarmi, 2015; Farn, 2008; Salager, 2002; Rosen, 2004) with further examples illustrated in Figure 1.6.



Figure 1.6. Diagram showing examples of industries requiring the use of surfactants.

Due to the widespread use of surfactants within industry, the global surfactant market is increasing in size especially with the introduction of synthetic surfactants in recent years. The compound annual growth rate for the period from 2015 to 2020 is forecasted as 5.3% with an estimated end value of \$39.86 billion in the year 2021 (Markets, 2016).

The different categories of surfactants, namely anionic, cationic, non-ionic and amphoteric, are used to varying extents within industry, with anionic surfactants accounting for the majority (Salager, 2002). This is attributed to the ubiquitous nature of this type of surfactant within the detergent and laundry industries. Anionic surfactants are extremely effective at removing soils from surfaces as well as exhibiting a large amount of foaming. Cationic surfactants derived from ammonium salts are commonly present in hair conditioning products because of their capability to attract negatively charged fibrous materials (Gavazzoni Dias, 2015). This is especially important after use with a shampoo in which the surfactants are negatively charged.

Zwitterionic surfactants are often found in toiletries and creams because of their milder behaviour (Farn, 2008). Surfactant use in the detergent industry is expanded in more detail in the next section.

Aside from the detergent industry, many products in the food sector contain surfactants for their emulsifying properties (Sharma, 2014). Emulsions consist of at least one immiscible liquid dispersed as droplets throughout a continuous phase with examples including mayonnaise, milk, butter, margarine and salad dressing (Guzey and McClements, 2006). In addition to providing emulsifying properties, the presence of surfactants in food products is also important for attaining the desired microstructure and rheological properties, as well as improved consistency, shelf life and stabilisation (Nitschke and Costa, 2007). The naturally occurring surfactant lechitin is present in egg yolk and milk proteins (Kralova and Sjoblom, 2009). The presence of lecithin in chocolate production is responsible for bringing about the desired structural changes relating to the viscosity and moisture level (Ziegler *et al.*, 2003; Afoakwa *et al.*, 2007). The reduction in viscosity is necessary in order to obtain a homogeneous suspension of chocolate mixture. As another example, addition of rhamnolipid surfactants to bakery products results in further control of the stability, texture, volume and conservation (Van Haesendonck, 2004). In addition to structural benefits, there have been experimental investigations into the capability of biosurfactants to control the presence of bacterial surface colonies which can impact health and affect food quality (Nitschke and Costa, 2007).

1.4.1.6 Surfactants in dish liquid

The detergent industry utilises surfactants in the majority of their products ranging from shampoos and fabric conditioners to washing powder and kitchen cleaning products. This sector accounts for at least 50 % of the industrial demand for surfactants (Yangxin *et al.*, 2008), with anionic surfactants being the most widely used due to their low cost and associated chemical

properties. Dish liquid is one product which contains a relatively high concentration of this surfactant type.

Despite the introduction of automatic dishwashers, dish liquid still maintains a significant market share across the world, especially in regions where automatic dishwashing is not common, so the formulation development of this product continues to be important. New variants are regularly developed to account for changes in the costs of the raw materials and to meet new consumer demands. This is also true for many other detergent products.

The first manual dishwashing liquid was introduced in the 1940s with a non-ionic surfactant as the active ingredient (Lai, 1996). However, this formulation did not provide a sufficient amount of foaming upon cleaning so anionic surfactants were considered in the next stage of the product development. Although there was more foaming with this formulation, stability issues arose and it was discovered that a multiple surfactant system, containing both anionic and non-ionic surfactants, provides an improved performance (Yangxin *et al.*, 2008). The current P&G dish liquid formulation contains a mixture of alkyl sulfates (anionic), ethoxylated alkyl sulfates (anionic) and amine oxides (amphoteric) as the key surfactant ingredients. Branching is incorporated in some of the alkyl sulfates at P&G to improve the robustness of the formulation (Scheibel, 2004). In more recent years, preservatives and different variants of dyes and perfumes have been introduced. There is an ongoing consumer demand for the product to be low cost, high performance and relatively environmentally friendly (Ivanković and Hrenović, 2010).

Surfactants provide the cleaning capability of these formulations. The mechanism of soil removal from hard surfaces is proposed to be a multi stage process whereby the surfactant first inserts into the soil causing subsequent swelling which then enables removal of the soil through emulsification or agitation (Zoller, 2008; Cox, 1986). The hydrophobic nature of the

hydrocarbon surfactant tails favours their binding to the soil. The mechanism employed by dish liquid is the same as that employed by shampoos and soaps. Hard water can present issues when the ions in the water bind to surfactants reducing their cleaning capability, for which chelating agents are often added to formulations.

Detergent products must be supplied to industries across the globe. At all product scales it is an essential requirement that the formulation demonstrates stability during all stages of manufacture, transport and subsequent shelf life (Chantraine *et al.*, 2006; Lai, 1996). In some areas of the world the formulations are subjected to extreme climates. When dish liquid products are exposed to high temperatures there is a risk of discolouration since dyes contained within the formulation may degrade (Bechtold and Mussak, 2009) or react with other species. At low and sub-zero temperatures there is also a risk of stability failure through the appearance of crystalline entities in the system. These can occur when the formulations are under static conditions, where no external shear or agitation is applied. Aside from failures under stationary conditions, flow-induced crystallisation can also result in phase transitional failures (Somani *et al.*, 2000). For example, upon application of shear, polymers can form orientated lamellar crystals.

In order to minimise the risk of crystallisation in product distribution, industries have stability tests in place, typically involving the storage of formulations at varying temperature conditions for defined time periods (Porter, 2013). However, the test methods can be time-consuming with some formulations requiring up to a month of testing before a definitive conclusion can be reached. Due to the increasing global demand and product portfolio, there is a requirement for a method which more closely simulates the supply chain and has the capability of detecting failures in a reduced timescale. In order to source an improved test method, it is important that knowledge of the mechanism of this crystallisation is further understood. Despite the strong

application to industrial products, few studies exist in this area of scientific research. Before examining surfactant crystallisation, a general understanding of crystallisation is required.

1.4.2 Crystallisation

1.4.2.1 Introduction to crystallisation

The main thermodynamic driving force for crystallisation is the difference in the chemical potential of the solute, compared to its equilibrium state (Vedantam and Ranade, 2013; Himawan *et al.*, 2006).

$$\Delta\mu = \mu_s - \mu_e = RT \ln \frac{a_s}{a_e} \quad (1.1)$$

where μ_s and μ_e are the chemical potentials of the system and its equilibrium state, a_s and a_e are the related activities, R is the gas constant and T is the temperature.

It is often challenging to attain the potential difference between such states and, therefore, it is generally accepted to use the concentration difference instead (Vedantam and Ranade, 2013; Boistelle and Astier, 1988). A solution is assumed to thermodynamically favour the formation of crystals if it is supersaturated. A supersaturated solution is one in which the concentration of the solute molecules exceeds that of the concentration at saturation (Mullin, 1993). The existence of supersaturation in a system, which depends on the temperature and the solute concentration, can be determined from a solubility diagram (Figure 1.7). The point at which the maximum amount of solute remains dissolved in solution is the equilibrium solubility or solubility limit. As well as determining whether crystallisation is a thermodynamic possibility, the degree of supersaturation can also impact which polymorphs form in the system (Teychené and Biscans, 2008). Aside from cooling a system to induce supersaturation, and promote crystallisation, other methods can also induce this property (Mullin, 1993). Evaporation of the

solvent will result in high local supersaturation. Furthermore, the addition of another solvent can cause the solute to crystallise out.

There is also a region of supersaturation where nucleation is negligible, known as the metastable zone, (Dincer *et al.*, 2014; Myerson, 2002) as shown in Figure 1.7. It is important to determine this section of the solubility curve for industrial crystallisation processes in order to obtain a high quality of product at minimal expense (Mersmann and Bartosch, 1998). The metastable zone is influenced by the applied cooling rate, agitation, impurities, hysteresis and the surrounding temperature (Nývlt, 1985). Once the metastable limit is reached, nucleation becomes spontaneous and the rate increases. The metastable zone can be measured isothermally by detecting the onset of crystallisation at a certain temperature condition through turbidity or conductivity measurements (Zhang *et al.*, 2015).

However, it is not only the presence of supersaturation that will determine a solution's susceptibility to crystallisation because any kinetic effects must also be accounted for. Kinetically driven processes include nucleation and crystal growth and it is these processes that tend to determine the size distribution of the crystals (Vedantam and Ranade, 2013).

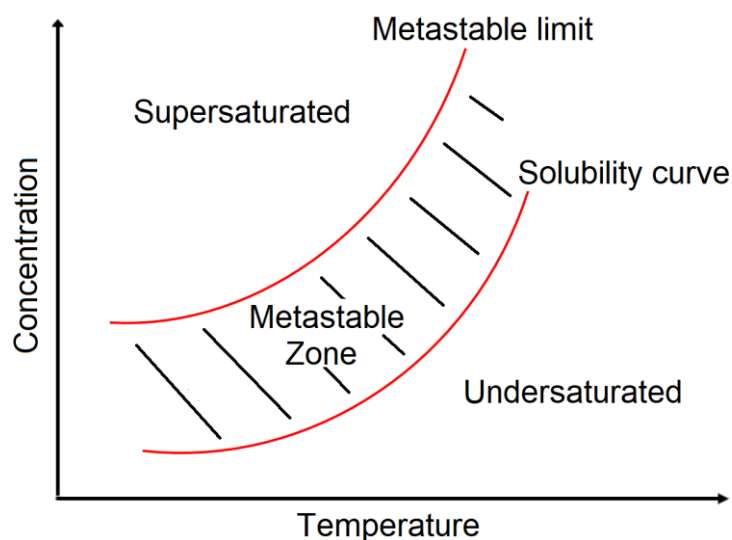


Figure 1.7. Solubility curve and metastable zone plotted against temperature and concentration. Adapted from Ref. (Vedantam and Ranade, 2013).

1.4.2.2 Nucleation

Nucleation can be subdivided into primary and secondary nucleation (Mullin, 1993; Myerson, 2002). Primary nucleation occurs in supersaturated solutions that do not contain crystalline entities. This process can be classified as either homogeneous and heterogeneous nucleation, where the former is nucleation occurring in a bulk solution that is absent from dust or other foreign matter. Homogeneous nucleation relies on collisions between the solute molecules, which have a low probability of occurring (Sear, 2006; Mullin, 1993). Conversely, heterogeneous nucleation uses foreign objects as nucleation sites for crystallisation. Most nucleation processes adopt the latter route. During nucleation, solute molecules form clusters via bimolecular addition. If a cluster exceeds a critical radius, it can form a stable nucleus where the attractive forces between the molecules outweigh those exerted from the surrounding solvent molecules (Mullin, 1993). These clusters, typically comprised of tens to thousands of solute molecules, proceed to grow into crystals (Mullin, 1993).

Contrary to primary nucleation, secondary nucleation occurs in solutions that already contain crystalline entities (Botsaris, 1976; Agrawal and Paterson, 2015). There are various mechanisms by which this process can occur (Kadam *et al.*, 2011) including crystals breaking apart, collisions of existing crystals with other surfaces or crystals and shear removal of the crystal surface, all of which result in further crystal fragments being distributed throughout the solution. The rate of secondary nucleation can be described by Myerson (2002):

$$B_0 = kSM_TW \quad (1.2)$$

where B_0 is the rate of secondary nucleation, k is the mass transfer coefficient, S is supersaturation, M_T is the density of the crystals and W is the agitation rate in rpm.

Initially, nucleation tends to begin in the region of highest supersaturation, such as a cold surface or the surface of the solution. This area may have a high supersaturation due to temperature effects or evaporation, respectively (Boistelle and Astier, 1988). Many techniques are used to detect the onset of nucleation including turbidity, microscopy and conductivity.

1.4.2.3 Crystal growth

Stable nuclei, corresponding to those which exceed some critical radii, begin to grow into larger crystalline entities. Berthoud (1921) and Valetton (1924) proposed crystal growth to be a two-step process consisting of mass transfer of the solute molecules to the crystal interface followed by inclusion of the molecules into the structure (Berthoud, 1912; Valetton, 1924; Valetton, 1924; Karpiński, 1985). This first step follows equation 1.3:

$$\frac{dm}{dt} = kA\Delta c \quad (1.3)$$

where m is mass, k is mass-transfer coefficient, A is the surface area of the crystals and Δc is change in concentration from the equilibrium state. The mass transfer coefficient depends on

the diffusivity and the film thickness of the boundary layer of the crystal. After mass transfer of the solute molecules to the crystal, the second step involves the incorporation of molecules into the structure, which form subsequent layers (Mullin, 1993; Tachibana, 2017). The rate of the crystal growth can be dependent on either of the two steps (Vedantam and Ranade, 2013). When a form of agitation is introduced into the system, the rate of mass transfer increases and, therefore, it is likely that the second step becomes rate determining. The shape of the crystals is controlled by both thermodynamic and kinetic effects. These include the cooling rate, supersaturation and amount of impurities in the system.

1.4.2.4 Kinetics of crystallisation

Before crystallisation can be detected in a system, there is an induction period. This is the sum of the time required to achieve steady state in the system, the nucleation time and the time to observable crystallisation (Mullin, 1993).

The rate profile for isothermal crystallisation exhibits an S-shape, as displayed in Figure 1.8 (Tiller, 1991; Yang *et al.*, 2005; Himawan *et al.*, 2006)

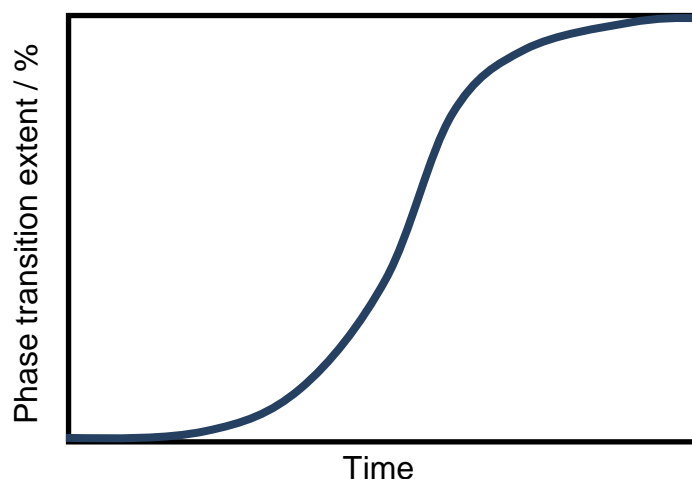


Figure 1.8. Transformation plot for isothermal crystallisation.

The initial stage of the transformation is slow and limited by the formation of nuclei. As the number of nuclei increase, the rate of the phase transformation also increases. The rate subsequently reduces towards the conclusion of the process. The slower growth rate at the end is a result of the increasing amount of the newly crystallised phase providing a boundary to further growth.

This isothermal crystallisation can be described by the Avrami equation (Michell *et al.*, 2013):

$$\ln [-\ln (1 - X(t))] = \ln K + n \ln t \quad (1.4)$$

where K and n are constants and $X(t)$ corresponds to the normalised crystalline constant at time t . The Avrami exponent, n , typically takes a value from 1 to 3 and is a sum of two terms, namely n_d and n_n (Müller *et al.*, 2005; Balsamo *et al.*, 2004). The former, n_d , relates to the dimensionality of the crystal growth: one-dimensional ($n_d=1$), two-dimensional ($n_d=2$) or three-dimensional ($n_d=3$) (Pei *et al.*, 2010). Whether there is one-dimensional, two-dimensional or three-dimensional growth influences the type of crystal, forming rod-shaped, disc-shaped or spherical crystal structures respectively. The second constant, n_n , is related to the time dependence of nucleation exhibiting a value of 1 for sporadic nucleation and 0 for instantaneous nucleation.

Although the Avrami equation is suitable for isothermal crystallisation, non-isothermal data cannot be fitted to such a model. Various alternate models have been suggested, such as the Ozawa and combined Avrami-Ozawa models (Bianchi *et al.*, 2008; Kuo *et al.*, 2006; Bandyopadhyay *et al.*, 2008). The Ozawa equation is provided in equation 1.5:

$$\log [-\log (1 - X(T))] = \log K - m \log a \quad (1.5)$$

where $X(T)$ is the crystalline fraction at temperature T , K is a cooling function depending on the overall crystallisation rate, a is the cooling rate and m is the Ozawa exponent which depends on the dimensionality of the crystal growth.

A plot of $\log [-\log (1 - X(T))]$ versus $\log a$ provides a value for the crystallisation parameters, m and K . However, non-isothermal crystallisation does not always fit this Ozawa model. For example, no linear fit was achieved during an investigation into the crystallisation of polyether ether ketone (PEEK) and nanoparticle-filled PEEK composites (Kuo *et al.*, 2006). The basis of the Ozawa model is quasi-isothermal crystallisation, therefore, it is not possible to use this method to describe all systems (Qu *et al.*, 2004). Under non-isothermal crystallisation, the crystallisation rate depends on both time and cooling rate and as a result there are deviations from the model. However, the same PEEK substrates were successfully described by the Ozawa-Avrami model described in equation 1.6:

$$\log a = \log F - b \log t \quad (1.6)$$

where a is cooling rate, t is time to achieve a specific degree of crystallinity, $b = \frac{n}{m}$ where n and m are the Avrami and Ozawa exponents respectively and F describes the necessary cooling rate to achieve a specific degree of relative crystallinity in a given time.

1.4.2.5 Crystallisation in industry

Although crystallisation is an unfavourable occurrence in dish liquid and other homecare products, there are many applications where crystallisation is an important part of the production process, such as in the food and cosmetic sectors. For example, table salt and sugar, when supplied to consumers, must exhibit a specific crystal size distribution (Beckmann, 2013). The chemical properties of chocolate are largely dictated by the type of crystal that the cocoa butter forms. Several polymorphs are possible and depend on the processing conditions (Schenk

and Peschar, 2004; Afoakwa *et al.*, 2007). Le Révérend *et al.* developed a model to predict structural changes occurring during the chocolate manufacture across a range of temperature profiles (Le Révérend *et al.*, 2009).

The process of crystallisation is also very important in the pharmaceutical industry where it is extensively used to attain the purest possible form of active ingredients (James, 1998; Chen *et al.*, 2011). The crystal attributes, such as size, morphology and crystal form, are dictated by experimental conditions such as the temperature and pH. The type of crystal influences the properties of the resulting active ingredient, so it is crucial to optimise processing conditions for the required component.

There are also situations where it is preferable to minimise any crystallisation occurrence. One example is the formation of wax crystals in diesel fuel upon exposure to cold environments (Leube *et al.*, 2000). Problems arise when these crystals cause blockages in diesel engines. In recent years polymeric additives, such as polyethylene-co-vinyl acetate, have been added to fuels in an attempt to combat this problem (Dunn, 2011; Machado *et al.*, 2001). These modifiers function by co-crystallising with the wax, due to the structural similarity between the two components, and, by doing so, disrupt the packing and growth of the wax crystals (Wei, 2015). Similarly, the occurrence of water crystallisation within jet fuel can become a risk if not properly controlled (Baena-Zambrana *et al.*, 2013). Crystallisation can also occur in dish liquid products under these low temperature environments. Unlike the issues described with diesel fuels, the existence of these crystals does not affect the functionality of the product. However, they can be detrimental for the long-term stability since the product fails appearance criteria.

1.4.3 Surfactant crystallisation

1.4.3.1 Krafft temperature

Having discussed the basic theory and stages of crystallisation, the occurrence of this phase transition in single and mixed surfactant systems will now be considered. The minimum temperature required for micelle formation in surfactant solutions is termed the Krafft temperature. Below this point there is no value for the CMC and a risk of surfactant crystallisation (Manojlovic, 2012). The Krafft temperature T_k is the crossover between the solubility curve of the solution and the critical micelle concentration curve (Bales *et al.*, 2002). Therefore, dissolution of the crystals occurs if the temperature is raised or the surfactant concentration reduced.

The concept of the Krafft temperature dates back to the late 19th century when Freidrich Krafft, a chemist, observed a phase transition upon cooling a surfactant solution (Krafft, 1895). All solutions of ionic surfactants have a corresponding Krafft temperature (Vautier-Giongo and Bales, 2003) but, conversely, non-ionic surfactants tend to exhibit the opposite relationship between solubility and temperature. Their solubility decreases with temperature to the cloud point, at which the solution becomes turbid (Delgado *et al.*, 2004; Sharma *et al.*, 2003). Upon a temperature increase, there comes a point at which the hydration of the head group of the non-ionic surfactant is not sufficient to solubilise the surfactant molecules (Kartal, 2006; Al-Sabagh *et al.*, 2011). In an attempt to stabilise the system, the micelles become larger and subsequently a turbid solution develops.

In the previous section, supersaturation was introduced as the thermodynamic driving force for crystallisation. In an aqueous solution of the ionic surfactant SDS, the supersaturation can be described by Myerson (2002):

$$S = \frac{a_{DS^-} a_{Na^+}}{K_{sp}}, \text{ where } K_{sp} = a_{DS^-,eqm} a_{Na^+,eqm} \quad (1.7)$$

where a_{DS^-} and a_{Na^+} are the activities of DS^- and Na^+ in the solution respectively and K_{sp} is the solubility product given by the product of the equilibrium activities of DS^- and Na^+ . S is the supersaturation, which must have a value over 1 for crystallisation to take place. Crystals form from surfactant monomers and counterions (Stellner and Scamehorn, 1989; Shiau *et al.*, 1994).. The solubility product, and therefore the supersaturation, depends on the temperature of the system.

Surfactant crystallisation can occur below the Krafft temperature T_k , which is influenced by numerous factors including the structure of the surfactant, the presence of other components, the ionic strength, and the surrounding pH environment, some of which are explored in the following sub-sections.

1.4.3.1.1 Effect of surfactant structure

An increase in the length of the carbon chain of the surfactant results in stronger Van der Waals forces between the hydrophobic tails. This interaction increases the thermodynamic stability of the crystal phase and promotes its formation, resulting in the system displaying a higher Krafft temperature (Gu and Sjoblom, 1992; Islam *et al.*, 2015). A linear relationship between chain length and T_k has been documented for various surfactant systems, including alkyl sulfates (Gu and Sjoblom, 1991) and betaine surfactants (Chu and Feng, 2011).

When quantifying the relationship between chain length and T_k , the number of ethoxy units must also be taken into account (Gu and Sjoblom, 1992). The existence of an ethoxy group can suppress the drive for crystallisation because the larger head group disrupts the packing of the crystals. Similarly, the presence of branching on the hydrocarbon chain also tends to disrupt the packing and disfavour crystal formation. Cripe *et al.* (P&G) investigated how the stability

of an alkyl sulfate solution changes with addition of methyl branches to the main chain (Scheibel, 2004). As expected, these branched surfactants decreased the Krafft temperature of the system, compared its linear form.

1.4.3.1.2 Influence of alcohol precursors

It is also important to consider the effect of short and long chain alcohols on T_k . The reasoning for this interest is attributed to the fact that the sulfate and sulfonate surfactants in detergent formulations are produced *in situ* from their corresponding alcohols (Dierker and Schafer, 2010). As such, it is important to understand the effect of any remnant alcohol on product stability. Typically, the amount of remaining alcohol in detergent formulations can range from trace amounts to 3 %.

A paper dating back to the 1960s (Nakayama *et al.*, 1966) outlines the effect of medium chain alcohols on SDS crystallisation where they hypothesise that the alcohols insert into the micelles and reduce the headgroup repulsion. As a result, there is an increased tendency for micellisation and the monomer concentration is lowered. Since the crystals are formed from surfactant monomers, the tendency for crystallisation and the Krafft temperature of the system also reduce. The alcohols of interest in this investigation were heptanol and hexanol. The behaviour cannot be considered to be the same for the SDS alcohol precursor, 1-dodecanol, since heptanol and hexanol are slightly soluble in water at ambient temperature, which is not true for 1-dodecanol.

1.4.3.1.3 Influence of multiple surfactants

The Krafft temperature of an anionic surfactant system can be lowered upon addition of a second anionic or non-ionic surfactant. In the case of a bi-anionic surfactant solution, the more dissimilar the structures, the greater reduction in T_k (Scamehorn, 1986). As with addition of hexanol and heptanol, the decrease in the Krafft temperature can also be explained by a lower

concentration of monomers available for crystallisation. This is due to an increased tendency to form micelles (Fan *et al.*, 1988; Stellner and Scamehorn, 1986) since the second surfactant inserts into the micelles between the anionic surfactants and reduces the repulsion between the negatively charged head groups. Further counterions need to be added or the temperature of the surfactant mixture lowered to induce supersaturation in the system so crystallisation can occur (equation 1.7) (Tsuji *et al.*, 1980). Salinity tolerance can be used to show the effect of a non-ionic surfactant on anionic surfactant crystallisation (Stellner and Scamehorn, 1989). When SDS is in the presence of a non-ionic surfactant, an additional cation source is required for crystallisation.

There have been relatively few studies looking into the nature of the crystals formed in these mixed non-ionic and anionic surfactant systems, with some high performance liquid chromatography (HPLC) and X-ray diffraction (XRD) studies concluding that the crystals were 99.98 % pure anionic surfactant (Soontravanich, 2007; Stellner and Scamehorn, 1986). There is the potential for other techniques to provide insight into the crystal composition, such as low temperature nuclear magnetic resonance (NMR) or Raman spectroscopy.

It is also important to note that anionic and cationic surfactant mixtures do not follow the same trends as those of a mixed ionic and non-ionic nature. An anionic surfactant system becomes more prone to crystallisation on addition of a cationic surfactant. There is electrostatic attraction between the two oppositely charged surfactants. Ions pairs form and crystallise out of solution (Shiau *et al.*, 1994).

1.4.3.2 Crystallisation studies of surfactant systems

Despite the importance of low temperature stability with respect to detergent products, crystallisation of surfactants has received relatively little interest. In various publications, Smith *et al.* studied aqueous sodium, potassium and rubidium dodecyl sulfate crystallisation (Smith

et al., 2001; Smith *et al.*, 2004; Smith *et al.*, 2000). Turbidity was used as the measurement of choice for the temperature of crystallisation and that of dissolution. Furthermore, the metastable zone width (MSZW) was calculated as the difference between the temperature of dissolution and that of crystallisation, as described in equation 1.8 below. The metastable zone width can be defined as the temperature difference between the saturation point and the temperature of crystal formation upon exposure to a constant cooling rate (Kadam *et al.*, 2012).

$$MSZW = T_{diss} - T_{cryst} \quad (1.8)$$

A plot of the logarithm of the cooling rate against the logarithm of the MSZW was used to obtain the order of the reaction. Thermodynamic quantities, such as enthalpy and entropy, were determined assuming ideal solution behaviour and application of the Van't Hoff isotherm in equation 1.9:

$$\ln(x) = \frac{\Delta H_{diss}}{RT} + \frac{\Delta S_{diss}}{R} \quad (1.9)$$

where x is the mole fraction of the solute in the solvent. ΔH_{diss} and ΔS_{diss} are the enthalpy and entropy of dissolution, respectively. A notable conclusion drawn from this study indicated a linear increase in the enthalpy of dissolution upon an increase in ionic radii. Since all the metal ions are equally charged, a larger ionic radius will result in a lower charge density. Decreasing the charge density will reduce the attractive forces between the ions and surrounding water molecules, increasing the enthalpy of dissolution of the system.

Also focused on the surfactant SDS, Miller *et al.* reported how the applied isothermal or non-isothermal conditions can impact the crystal form or shape (Miller *et al.*, 2016; Miller *et al.*, 2017). For example, the shape of the crystals was found to depend on the holding temperature, for isothermal crystallisation, or the cooling rate, for non-isothermal studies. The crystals changed from platelets to needles when a higher cooling rate was applied to the system. The

effect of cooling rate and the surrounding temperature are critical for product stability, especially during transportation and shelf life, when the formulation may experience sudden temperature changes as well as smaller, local environmental fluctuations.

Broadening the field to include crystallisation of other single surfactant systems yields relatively few studies in this area; Fu-Gen Wu *et al.* looked into the crystallisation of the cationic surfactant cetyltrimethylammonium bromide (CTAB) on cooling in order to better understand the various metaphases that occur throughout the phase transition pathway (Wu *et al.*, 2012). In their study crystal growth kinetics and mechanisms are examined via the use of optical microscopy and differential scanning calorimetry (DSC). Image analysis was required in order to determine a crystallisation mechanism and associated morphological changes in the structural conformation. This technique was also employed by De Anda *et al.* during a study into the crystallisation of glutamic acid (De Anda *et al.*, 2005).

The crystallisation of mixed anionic and non-ionic surfactant systems has received some attention (Soontravanich and Scamehorn, 2009; Soontravanich *et al.*, 2009; Soontravanich, 2007; Stellner and Scamehorn, 1986; Shiau *et al.*, 1994). However, the crystallisation of SDS + DDAO systems is yet to be reported, prior to this thesis, despite its application to detergent products.

1.4.4 Timescale of crystallisation

1.4.4.1 Industry stability test methods

Within the detergent industry, the timescales of the tests used detect crystalline failures at low temperatures can be extremely long, with up to a month of testing required to conclude the stability outcome of some formulations. This can incur high costs and an increased probability of failures after distribution. Furthermore, there is statistical variability in the time to failure

between samples from the same batch. This is likely to be due to factors that influence the rate nucleation and crystal growth and are difficult to control, which may include the existence of dust, trace impurities particles (Cacciuto *et al.*, 2004) or temperature and pressure fluctuations (Himawan *et al.*, 2006). As a result, there is industry interest in sourcing a method capable of reducing the timescale and variability. A common way to reduce the timescale of crystallisation is by reducing the duration of the nucleation step. The remainder of this section outlines routes to reduce the time to crystallisation which have the potential to be used in both the stability testing and processing of surfactant systems.

1.4.4.2 Seeding

Seeding is the process whereby small parent crystal, or other heterogeneous surface, is inserted into a supersaturated solution to provide a base from which crystal growth can originate (Cacciuto *et al.*, 2004). As a result, the addition of seed particles decreases the timescale of the nucleation process. Various seeding methods for the introduction of the parent crystal have been reported but, in recent years, there has been an increasing focus towards heterogeneous seeding. The capability for seeding to reduce the time to protein crystallisation is reported in various studies (Gerdtz *et al.*, 2006; Stura and Wilson, 1991; D'Arcy *et al.*, 2003). This is a particularly difficult process since the seed crystals must be added at specific times in the crystal growth cycle. The established method for seeding uses previously formed crystals as the seeds for further crystallisation of the same bulk mixture. This particular method can be subcategorised into two separate techniques, namely microseeding and macroseeding whereby the latter utilises a single crystal and the former a transfer of sub microscopic seeds (Bergfors, 2003). For the majority of experimental cases, microseeding is preferable to that of the macroseeding process. The transfer of a single crystal can be a difficult process from a laboratory preparation perspective. Seeding is frequently used in industrial crystallisers to maintain a level crystal size distribution.

There are various methods for introducing microcrystals into a solution. Seed crystals can be added directly after reducing the crystals to the necessary size via sonication and homogenisation. Alternatively, a seed stock solution can be used which allows for control of the degree of seeding. Aside from these methods, another option is to use a 'seeding wand' that involves the parent crystal being streaked with a 'wand' and inserted into the solution. Various materials have been used as the wand, namely glass rods and wires and needles. However, animal hair or whiskers have been found to provide optimum characteristics due to the ability of their structural features to capture and trap the seeds effectively.

Aside from using hair as a means for streak seeding from a parent crystal, hair itself has also been demonstrated to initiate crystallisation in biological protein studies (D'Arcy *et al.*, 2003). Protein crystallisation is a difficult procedure when using protein-specific seed crystals since they must be added at a certain time point in order to be effective. However, horse hair is stable and can be inserted at any stage eliminating the time dependence factor.

In recent years, other types of heterogeneous seeds for protein crystallisation have been investigated (McPherson and Gavira, 2014). McPherson and Shlichta used an inorganic crystalline material to act as a heterogeneous nucleation surface for protein crystallisation (McPherson and Shlichta, 1988). Porous silicon has been successfully used to induce protein crystallisation, attributed to the specific pore size of this inorganic material (Chayen *et al.*, 2001). Polymeric films have also been tested as a means for heterogeneous nucleation. The concluding results suggest polymeric film surfaces can be particularly useful for the crystallisation of proteins present in low concentrations (Fermani *et al.*, 2001).

1.4.4.3 Application of mixing and shear

The presence of agitation or mixing is a crucial factor during product manufacture and transportation when formulations are exposed to varying degrees of vibration and movement.

In systems where it is thermodynamically possible to form crystalline entities, mixing can impact the time to crystallisation as well as properties of the crystals themselves. Although the application of mixing has not been specifically reported for surfactant systems, it has been documented to reduce the time to crystallisation for other systems (Mullin and Raven, 1962; Liu and Rasmuson, 2013; Liu *et al.*, 2014; McLeod *et al.*, 2016; Li *et al.*, 2015).

There is debate as to whether the application of mixing to a system affects both primary and secondary nucleation. Primary nucleation depends on the rates of homogeneous and heterogeneous nucleation (Mullin, 1993). Classical nucleation theory states that:

$$J = Ae^{-\frac{\Delta G}{kT}} \quad (1.10)$$

where J is the rate of primary nucleation, T is the temperature, k is the Boltzmann constant, ΔG is the energy barrier to nucleation and the pre-exponential factor A is dependent on the frequency of collisions between the solute molecules (McLeod *et al.*, 2016). The total rate of primary nucleation is a sum of the heterogeneous J_{Hom} and heterogeneous J_{Het} contributions.

For both types of primary nucleation, the probability of molecular collisions increases upon inducing kinetic turbulence in the mixture. The fluid motion is highest in the region surrounding the central point of the mixing head, with the areas above and below the mixing head subjected to the lowest. The increased collision frequency results in an increased pre-exponential factor yielding higher values of J_{Het} and J_{Hom} . In addition, the rough surface of agitator blade can act as a base for heterogeneous nucleation (Liang *et al.*, 2004), thus lowering the energy barrier for this type of nucleation. This also contributes to increasing the rate of primary nucleation.

The majority of crystallisation in industry proceeds via secondary crystallisation since crystallites tend to be present in the bulk. There is ongoing debate regarding the mechanism by which mixing impacts the rate of secondary nucleation. When crystals form, there tends to be a region of low solute concentration around the crystals and stirrer blade. Upon mixing, this

concentration gradient is reduced, and the rate of secondary nucleation and crystal growth from these points consequently increases (Liang *et al.*, 2004; Callahan and Ni, 2014). Furthermore, crystals caught in the mixer blade can break apart into many separate entities increasing the number of available nucleation sites for crystal growth. Increased fluid motion and shear also increases the probability of crystal-blade and crystal-crystal collisions, both of which result in the dispersion of crystal entities that can act as nuclei for further crystallisation. Application of fluid shear may also cause the molecules to align and transition towards a close packed crystal structure.

Aside from affecting the kinetics of nucleation, mixing also has also been reported to influence the crystal size distribution, types of polymorphs and the morphology and, therefore, is often used in crystallisation processes to attain a specific crystal form (Herrera and Hartel, 2000). As part of a study into the crystallisation of *m*-hydroxybenzoic acid, conducted by Liu *et al.*, it was found that the speed of mixing determined the distribution between the two possible crystalline polymorphs (Liu *et al.*, 2014). An intermediate agitation rate (200-400 rpm) resulted in predominately one crystal form.

1.4.4.4 Application of ultrasound

Ultrasound waves refer to sound waves in excess of 20 kHz, which are outside the hearing limit of humans (Kadam *et al.*, 2015). This technique has yet to be reported for surfactant crystallisation. The application of ultrasound has been demonstrated to have various advantages during crystallisation processes, which are displayed in Figure 1.9.

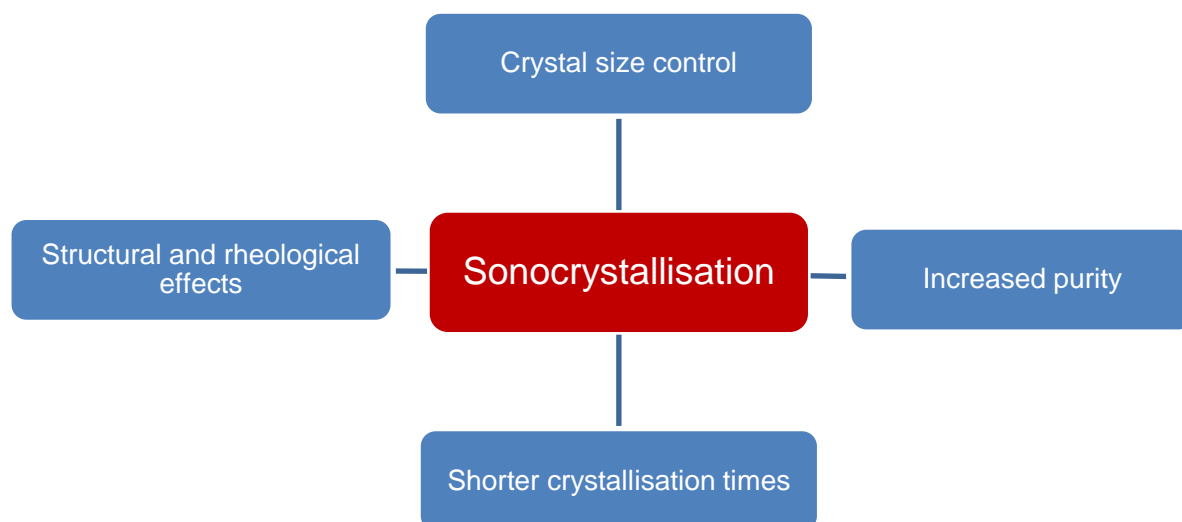


Figure 1.9. Diagram showing examples of the effects of ultrasound application on crystallisation processes.

Through ultrasonication it is possible to reduce the nucleation time of crystallisation (Lee *et al.*, 2014). The mechanism by which the application of these waves can reduce the induction time is still not yet fully understood. The induction time can be defined as the time between formation of a supersaturated solution and crystal formation. One explanation states that the ultrasound waves result in a low to high pressure cycle whereby small bubbles are formed at the low pressure state. At a specific volume, the bubbles collapse and result in further nucleation sites for crystal growth (Higaki *et al.*, 2001; Lee *et al.*, 2014).

In addition to facilitating nucleation, the metastable zone is also reduced upon sonication. The metastable zone can be defined as the difference between the solubility curve limit and spontaneous solidification (de Castro and Priego-Capote, 2007). The reduction of this phenomenon can influence crystal size distribution, purity and structure. The crystallisation of sorbital hexaacetate not only occurs at a higher temperature in the presence of a short burst of ultrasound, but also demonstrates larger crystals with more regularity in their structure. When crystallisation was initiated at a lower supersaturation level, slow controlled crystal growth was favoured (Sander *et al.*, 2014).

Depending on specific requirements, the crystal size distribution can be significantly altered by the application of ultrasound. Continuous sonication during the phase transition facilitates the production of small crystals. This is attributed to the continuous application resulting in a high degree of nucleation sites as well as a result of the breakages of large agglomerates (Ruecroft *et al.*, 2005). A short burst of ultrasound can favour the growth of large and regular crystals in comparison to a sample without applied sonication. The application of sonication also highly affects the crystal morphology such as the size and number of crystal entities.

Compared to conventional seeding techniques, sonocrystallisation does not require addition of external bodies (Luque de Castro and Priego-Capote, 2007). Therefore, there is the potential for it to be utilised for sterile products which can be difficult to crystallise using seeding methods. In 1927, the first use of sonocrystallisation was reported (Richards and Loomis, 1927) with further reports in the 1950s to 1970s. These were all on a small scale, with one example being the preparation of crystals of progesterone through ultrasonication (Principe and Skauen, 1962). Although the use of ultrasound to trigger crystallisation is well established (Zamanipoor and Mancera, 2014), it is still in early stages with regards to any scale up that would allow for it to be used extensively in industry testing.

During the manufacture of food products, ultrasound has been reported as a valuable tool with the potential to scale up in future developments (Deora *et al.*, 2013). During the manufacture of chocolate, the contained fats are required to crystallise at a specific size and polymorph, which can be tailored through ultrasonication. When exposed to ultrasonication the crystallisation process of these fats has a reduced timescale, an effect which can also be demonstrated with other fat-containing products such as butter and margarine. Ultrasonication is also advantageous in food freezing preservation (Chemat *et al.*, 2011). Application of ultrasound can result in a more homogeneous and rapid cooling of a food product and improve preservation. Sonication can also be used to break up crystalline entities and liquefy honey

(Kabbani *et al.*, 2011). Honey is a sugar-based product that displays a tendency for undesired sugar crystallisation at room temperature. Studies have shown that sonication minimises the presence of crystals and prolongs the timescale of their formation (Deora *et al.*, 2013). In addition to the processing stage, there is also potential for ultrasound to be used in the stability tests of some surfactant products. By decreasing the nucleation time, crystallisation failures in surfactant systems would be determined in a shorter timescale.

1.4.5 Principles of the relevant methodology

Understanding the crystallisation process occurring within detergents is vital for future formulation development. In addition, the resulting knowledge may have application to other industries where crystallisation is important. A variety of techniques have been used to study crystallisation including differential scanning calorimetry (DSC), nuclear magnetic resonance (NMR), confocal Raman microscopy, small-angle X-ray scattering (SAXS), wide-angle X-ray scattering (WAXS), microscopy, turbidity and other light transmission techniques. Although this list is not exhaustive, further details are provided for these methods since they are used throughout the thesis.

1.4.5.1 Differential scanning calorimetry (DSC)

DSC is an analytical technique that can be used to determine phase transitions through thermal analysis (Thomas, 2005; Borchardt and Daniels, 1957). The ease of the sample preparation, fast acquisition of data and the need for only a small sample size are key advantages of this method (Jain *et al.*, 2008; Thomas, 2005). DSC monitors the difference in heat flow rate, defined as the heat q supplied per unit time, between the reference and sample cells (Gill *et al.*, 2010) through a selected temperature region. Since both cells are exposed to the same temperature cycle, any change in the two heat flows implies the occurrence of a phase transition.

Thermodynamics of micelle formation have been extensively studied by calorimetry (Chatterjee *et al.*, 2001). Changes in the heat capacity C_p for micelle formation at different temperatures can be used to infer how the CMC depends on temperature (Kresheck, 2006; Kresheck, 2001). Heat capacity C_p can be related to the heat flow and the heating rate of the sample (Morintale, 2013) as indicated in equation 1.11.

$$C_p = \frac{\frac{\Delta q}{t}}{\frac{\Delta T}{t}} = \frac{\Delta q}{\Delta T} \quad (1.11)$$

where Δq is the change in heat flow and ΔT is the change in temperature.

Changes in heat flow have been used to detect the onset of crystallisation (Wu *et al.*, 2012), melting, decomposition (Kissinger, 1957) and glass transition points (Jain *et al.*, 2008). Peak maxima and the onset and offset points of nucleation can provide insight into the kinetics of the crystallisation. Furthermore, the peak area can be related to the enthalpy of the transition.

Both non-isothermal and isothermal crystallisation can be studied using this analytical technique (Zhou *et al.*, 2011). As discussed in the previous section, isothermal crystallisation can be described by the Avrami equation (Yang *et al.*, 2005). In order to apply this equation, the crystalline content at various timepoints $X(t)$ is attained from DSC thermograms (Pei *et al.*, 2010).

$$X(t) = \frac{A(t)}{A_t(\infty)} \quad (1.12)$$

where $A(t)$ is the area of the cooling thermogram from the start of the crystallisation until time t and $A_t(\infty)$ is the total area of the crystallisation peak.

Non-isothermal crystallisation can also be studied by DSC, most commonly through application of Ozawa or Avrami-Ozawa theories (Hao *et al.*, 2010; Rigg *et al.*, 2017; Bianchi *et al.*, 2008). For these investigations the cooling rate is assumed to remain constant throughout each thermal

profile. In addition to considering the effect of different cooling rates, DSC can also be used to understand the effect of sample concentration on crystallisation (Kekicheff *et al.*, 1989) and to detect any hysteresis effects. Furthermore, activation energies for isothermal and non-isothermal crystallisation can be attained using the Arrhenius equation and the Kissinger or Ozawa methods, respectively (Frączyk, 2011; Ozawa, 1970; Kissinger, 1957). The Kissinger method is provided in equation 1.13:

$$\frac{d[\ln(\frac{a}{T_p^2})]}{d(\frac{1}{T_p})} = \frac{-\Delta E}{R} \quad (1.13)$$

where a is the cooling rate, T_p is peak temperature, ΔE is activation energy and R is the gas constant.

Extensive information can be extracted from DSC thermograms, with applications to many research areas (Biliaderis, 1983). This technique is often used in combination with microscopy to attain an overall picture of crystallisation processes.

1.4.5.2 Microscopy

The use of microscopy dates back to the 1600s when Robert Hooke's compound microscope was at the forefront of scientific inventions (Bradbury, 2014). Leeuwenhoek, a Dutch businessman, also contributed a significant amount to the field with his advances in lens-making (Yount, 2008). The aim of microscopy is to view the system of interest at a small scale in detail that cannot be achieved by the naked eye to observe structural features such as crystal shape, crystal size and the distribution of nucleation sites (Allen, 2015). A study focused on the crystallisation of aqueous SDS solutions used microscopy to observe the changes in crystal shape, from platelets to needles, upon a change in cooling rate or the surrounding isothermal environment (Miller *et al.*, 2016; Miller *et al.*, 2017). Both magnification and enhanced

resolution are equally important with this technique. A light source passes through the sample and subsequently through the objective lenses to the eyepiece lenses, with magnification of the image occurring at each stage (Allen, 2015). Each time that an image at a different magnification is captured, a calibration is performed. Optical microscopy can be either reflective or transmissive and, as a result, can be applied to both opaque and transparent samples.

Simple optical microscopy is employed in some of the research contained in this thesis, but polarised microscopy is also a useful technique for observing crystallisation. Polarised microscopy functions on the principle that crystals demonstrate birefringent properties (Stoiber and Morse, 1994). Light is emitted from the source and passes through a polariser to produce waves that oscillate in a single plane. The sample crystals then refract the light and splits into two perpendicular components. The light then passes through a second polariser placed at right angles to the first polariser. When the polarisers are perpendicular, only birefringent samples, such as crystals, illuminate the field of view. The colour distribution of the image can assist in determining the nature of unknown samples via the Michel Levy chart (Carlton, 2011). The use of polarised microscopy has been a valuable asset in many studies. For example, it has been used to understand the phase behaviour of ethoxylated non-ionic surfactant mixtures (Vitiello *et al.*, 2014). In this particular study, polarised microscopy was used to distinguish between different liquid crystalline phases.

There are also other types of microscopy such as fluorescence, electron and confocal. Fluorescence microscopy is especially important in biological studies where fluorescence stains have been developed that bind to targets to different extents (Renz, 2013; Wayne, 2014). A fluorescence microscope uses ultra-violet (UV) light to illuminate the sample which gives increased sample resolution, compared to optical microscopy, due to the reduced wavelength. This is also the case with scanning electron microscopy (SEM) which is used to determine

surface topology when an electron beam is moved across a sample. It is also possible to build 3D images of a samples through confocal microscopy (Webb, 1996) and indicate the locations of different components.

1.4.5.3 Turbidity

A solid suspension or crystals increases the level of turbidity in the solution (Smith *et al.*, 2001). The amount of light that can pass through a sample is reduced. This property is the principle behind Crystalline8, where a reduction in light transmission corresponds to the presence of crystals.

1.4.5.4 Nuclear magnetic resonance (NMR)

NMR has been employed across many branches of science, in particular organic chemistry, as a means to identify or confirm the structural arrangement of molecules (Clayden, 2001; Richards and Hollerton, 2010). There are many aspects of NMR, including 2D NMR and magnetic resonance imaging (MRI), but the focus of this overview is purely on ^1H NMR, which is utilised in some of the studies contained within this thesis.

^1H NMR relies on the magnetic properties of ^1H nuclei, which have a spin of $\frac{1}{2}$. In the absence of an external magnetic field, all spins reside at the same energy state. Upon an application of an external magnetic field, the spins will tend to align with the external field (Duer, 2008) and can take one of two different energy states: α (lower energy) or β (higher energy) (Akitt and Mann, 2000). Typically, nuclei with spin I can take $2I + 1$ different states. An electromagnetic radiation pulse is applied which enables nuclei to attain resonance and flip between the two energy states (James, 1998). The amount of energy absorbed is detected and, via Fourier transformation, the resultant NMR spectrum is obtained (Günther, 2013). The difference between the energy states determines the chemical shift of the signal and is highly dependent

on the shielding effects of surrounding nuclei. As a result, NMR is capable of distinguishing between the different proton environments. The signal intensity relates to the relative number of protons in that particular environment and the peak splitting indicates coupling with other protons.

The molecular tumbling rate of components within a system can dictate characteristics of the resultant NMR spectrum, including the degree of line broadening. Environmental and physical factors, such as temperature and viscosity, can reduce or increase the molecular tumbling within a solution. Slower molecular motion will decrease the spin-spin relaxation time, responsible for line broadening (James, 1998; Foster *et al.*, 2007). Line broadening can be related to the spin-spin relaxation time by equation 1.14:

$$\nu_{\frac{1}{2}} = \frac{1}{\pi T_2^*} \quad (1.14)$$

where $\nu_{\frac{1}{2}}$ is line width at half maximum and T_2^* is the ‘observed’ spin-spin relaxation time which depends on magnetic inhomogeneity.

Since NMR is a non-invasive technique (Hammer, 1998), it is extensively used across different industrial sectors. The food industry uses NMR for determining the water and fat content in samples, including the relative proportions of unsaturated or saturated fat, and understanding structural changes during shelf life (Marcone *et al.*, 2013; Todt *et al.*, 2006). Through using a similar approach, there is the possibility to use this spectroscopic technique to detect the onset of surfactant crystallisation.

1.4.5.5 X-ray scattering

Small-angle scattering (SAS), using both neutron and X-rays, is an important technique in the field of crystallography, where it has been used to study crystal shape, crystallisation kinetics, degree of crystallinity, polydispersity, size and porosity (Tabor *et al.*, 2009; Bots *et al.*, 2012).

Solutions of micelles have been extensively studied via the scattering techniques, SANS and SAXS, to determine micelle shape and confirmation (Lucena *et al.*, 2012; Hammouda, 2013; Bergstrom and Pedersen, 1999; Lipfert *et al.*, 2007). For example, Vitiello *et al.* used both scattering techniques and polarising microscopy to understand the phase diagram of a multi non-ionic surfactant system that has relevance to the detergent industry (Vitiello *et al.*, 2014).

To perform a SAXS measurement, a monochromatic X-ray beam is first directed at the sample (Kikhney and Svergun, 2015). Similarly, SANS functions by a similar method, but uses neutrons as the beam source with the scattering relating to atomic number, rather than electron density. These techniques complement one another (Blazek and Gilbert, 2011). Scattering from X-rays tends to have a greater signal to noise ratio and shorter experimental runtimes, compared to neutron techniques (Hollamby, 2013). However, SANS enables isotopes to be differentiated, such as hydrogen and deuterium, which is not possible with X-ray scattering. By selectively deuterating certain components, SANS can be used to gain a detailed insight into structures (Brasher and Kaler, 1996; Heller, 2010).

During a SAXS experiment, the X-rays released from the source cause the electrons in the sample to oscillate at the same wavelength. A scattered beam with the same energy as the incident beam forms a diffraction pattern on the 2D detector (Boldon *et al.*, 2015). The points are converted to their respective scattering vector, Q , before being radially averaged and plotted on a 1D plot against intensity (Li *et al.*, 2016). The scattering vector, Q , is related to the scattering angle, θ and wavelength λ such that:

$$Q = \frac{4\pi\sin\theta}{\lambda} \quad (1.15)$$

The use of the Q function removes the dependency on wavelength, such that a sample which has been exposed to beams with differing wavelengths should display the same intensity across the measured Q range in both cases. In the small angle region 2θ is scattered between 0° and

5°. Q is inversely proportional to the distance, d , as displayed in equation 1.16, and this relationship which is derived from Bragg's law.

$$Q = \frac{2\pi}{d} \quad (1.16)$$

The measured intensity is described by the scattering law (equation 1.17) and contains contributions from the form factor $P(Q)$ and structure factor $S(Q)$ (Cosgrove, 2010).

$$I(Q) = \Delta\rho * N * V^2 * P(Q) * S(Q) \quad (1.17)$$

where $\Delta\rho$ is the difference in scattering length density between particle and matrix, V is volume of sample, N is the number of particles, $P(Q)$ is the form factor and $S(Q)$ is the structure factor.

$P(Q)$ is an oscillatory function that depends on the scattering from individual particles and the corresponding dimensions of the particles. The polydispersity of the particles changes the maximum and minimum of the oscillations with a greater degree of oscillation observed for heavily monodispersed samples (Cosgrove, 2010). The shape of the particles also has a strong influence on the form factor. At high Q , and therefore short distances, Porod's law states that the surface fractal dimension dictates the gradient of the slope which ranges between Q^{-3} and Q^{-4} , with Q^{-3} and Q^{-4} arising from rough and smooth surfaces, respectively. When $x < 3$ for Q^{-x} , a mass fractal is present in the system (Cherny *et al.*, 2014). Below the high Q region, the slope is characteristic of the internal structure.

The structure factor $S(Q)$ arises from the scattering of the beam from different particles and is used to understand the particle-particle interactions. However, in dilute suspensions these interactions are not significant and $S(Q) = 1$ (Lipfert *et al.*, 2007). In concentrated suspensions, $S(Q)$ depends on the degree of order in the sample.

Fitting software can be used to determine parameters such as the micelle radii and charge, from the resulting SAXS profiles (Bressler *et al.*, 2015). In dilute solutions, the radius can be directly calculated with Guinier's law without relying on prior knowledge of the shape of the aggregate. Guinier's law calculates the particle radius from the gradient of the profile in the low Q region.

Before the 1970s, all SAXS experiments were performed at lab scale where there are limitations in the resolution. More recently, sources of high energy radiation are provided by synchrotron facilities, such as the Diamond Light Source, Oxfordshire, UK or ISIS, Oxfordshire, UK (Svergun *et al.*, 2013). At such sites, the data collection is rapid, ranging from minutes to milliseconds, so phase transitions can be monitored *in situ*. Time resolved SAS can be used to follow transitions over a set period and determine the existence of any intermediate structures (Tabor *et al.*, 2009). Like NMR, SAS is not a destructive technique (Bréchnac *et al.*, 2008) and can be used to study samples in different physical states or chemical environments. Resulting data can be used to detect structural changes occurring during crystallisation and understand the kinetics of the process.

Further structural insight into crystals can be attained from wide-angle X-ray scattering (WAXS), also performed at synchrotron sources. With this technique, it is possible to probe information about the inter-atomic structure including the d -spacing between the crystalline planes (Blazek and Gilbert, 2011). Time resolved WAXS can be used to understand the mechanism of the crystallisation and identify intermediary structures (Bots *et al.*, 2012).

1.4.5.6 Comparison between techniques

The techniques outlined in this section are often used in parallel to complement one another, as is the case with the work presented in this manuscript. All techniques have both advantages and limitations which may result in one technique being more suitable than another when investigating a particular property or characteristic. For example, extensive information on

crystal structure can be acquired from SAXS at length scales that is not possible with other techniques. Both SAXS and DSC are capable of providing an insight into the kinetics of a crystallisation process and, in the case of isothermal transitions, the phase change can subsequently be described by the Avrami equation once the crystalline content has been calculated from peak area or slices. Furthermore, the effect of different cooling rates and isothermal temperature conditions can be attained by DSC measurements and SAXS can provide complementary information regarding changes to the structure or polydispersity of the crystals. Fast data collection is possible with both these techniques, particularly important when following phase transitions that have a short timescale.

Studying crystallisation with NMR is not as widely reported as the other techniques. A novel approach using NMR to determine crystal composition is the focus of Chapter 3. In combination with SAXS, a detailed insight into the nature of the crystals can be attained. Microscopy complements these methods since crystallisation can be observed at higher length scales, typically outside of the range possible with SAXS. Furthermore, it is also possible to observe the distribution of nucleation sites, which would be challenging with other, non-visual techniques.

These techniques are used throughout this EngD project to develop an understanding of the crystallisation process occurring at low temperatures in detergent products, specifically dish liquid.

1.5 References

- Afoakwa, E. O., Paterson, A. & Fowler, M. 2007. Factors influencing rheological and textural qualities in chocolate - a review. *Trends in Food Science & Technology*, 18, 290-298.
- Agrawal, S. G. & Paterson, A. H. J. 2015. Secondary Nucleation: Mechanisms and Models. *Chemical Engineering Communications*, 202, 698-706.

- Akitt, J. W. & Mann, B. E. 2000. *NMR and Chemistry: An Introduction to Modern NMR Spectroscopy*, CRC Press.
- Al-Sabagh, A. M., Nasser, N. M., Migahed, M. A. & Kandil, N. G. 2011. Effect of chemical structure on the cloud point of some new non-ionic surfactants based on bisphenol in relation to their surface active properties. *Egyptian Journal of Petroleum*, 20, 59-66.
- Allen, T. 2015. *Microscopy: A Very Short Introduction*, Oxford University Press.
- Attwood, D. 2012. *Surfactant systems: their chemistry, pharmacy and biology*, Springer Science & Business Media.
- Azarmi, R. 2015. Type and application of some common surfactants. *Journal of Chemical and Pharmaceutical Research*, 7, 632-640.
- Baena-Zambrana, S., Repetto, S., Lawson, C. P. & Lam, J.-W. 2013. Behaviour of water in jet fuel—A literature review. *Progress in Aerospace Sciences*, 60, 35-44.
- Bales, B. L., Benrraou, M. & Zana, R. 2002. Krafft temperature and micelle ionization of aqueous solutions of cesium dodecyl sulfate. *The Journal of Physical Chemistry B*, 106, 9033-9035.
- Balsamo, V., Urdaneta, N., Pérez, L., Carrizales, P., Abetz, V. & Müller, A. J. 2004. Effect of the polyethylene confinement and topology on its crystallisation within semicrystalline ABC triblock copolymers. *European Polymer Journal*, 40, 1033-1049.
- Bandyopadhyay, J., Ray, S. S. & Bousmina, M. 2008. Nonisothermal crystallization kinetics of poly(ethylene terephthalate) nanocomposites. *Journal of Nanoscience and Nanotechnology*, 8, 1812-1822.
- Bechtold, T. & Mussak, R. 2009. *Handbook of Natural Colorants*, Wiley.
- Beckmann, W. 2013. *Crystallization: Basic Concepts and Industrial Applications*, Wiley.
- Bergfors, T. 2003. Seeds to crystals. *Journal of Structural Biology*, 142, 66-76.

- Bergstrom, M. & Pedersen, J. S. 1999. Structure of pure SDS and DTAB micelles in brine determined by small-angle neutron scattering (SANS). *Physical Chemistry Chemical Physics*, 1, 4437-4446.
- Berthoud, A. 1912. Théorie de la formation des faces d'un cristal. *Journal de Chimie Physique*, 10, 624-635.
- Bianchi, O., Oliveira, R. V. B., Fiorio, R., Martins, J. D. N., Zattera, A. J. & Canto, L. B. 2008. Assessment of Avrami, Ozawa and Avrami–Ozawa equations for determination of EVA crosslinking kinetics from DSC measurements. *Polymer Testing*, 27, 722-729.
- Biliaderis, C. G. 1983. Differential scanning calorimetry in food research - A review. *Food Chemistry*, 10, 239-365.
- Blazek, J. & Gilbert, E. P. 2011. Application of small-angle X-ray and neutron scattering techniques to the characterisation of starch structure: A review. *Carbohydrate Polymers*, 85, 281-293.
- Boistelle, R. & Astier, J. P. 1988. Crystallization mechanisms in solution. *Journal of Crystal Growth*, 90, 14-30.
- Boldon, L., Laliberte, F. & Liu, L. 2015. Review of the fundamental theories behind small angle X-ray scattering, molecular dynamics simulations, and relevant integrated application. *Nano reviews*, 6, 25661.
- Borchardt, H. J. & Daniels, F. 1957. The Application of Differential Thermal Analysis to the Study of Reaction Kinetics¹. *Journal of the American Chemical Society*, 79, 41-46.
- Bots, P., Benning, L. G., Rodriguez-Blanco, J.-D., Roncal-Herrero, T. & Shaw, S. 2012. Mechanistic insights into the crystallization of amorphous calcium carbonate (ACC). *Crystal Growth & Design*, 12, 3806-3814.
- Botsaris, G. D. 1976. Secondary Nucleation — A Review. In: Mullin, J. W. (ed.) *Industrial Crystallization*. Boston, MA: Springer US.

- Bradbury, S. 2014. *The Evolution of the Microscope*, Elsevier Science.
- Brasher, L. L. & Kaler, E. W. 1996. A Small-Angle Neutron Scattering (SANS) Contrast Variation Investigation of Aggregate Composition in Catanionic Surfactant Mixtures. *Langmuir*, 12, 6270-6276.
- Bréchnignac, C., Houdy, P. & Lahmani, M. 2008. *Nanomaterials and Nanochemistry*, Springer Berlin Heidelberg.
- Bressler, I., Kohlbrecher, J. & Thunemann, A. F. 2015. SASfit: a tool for small-angle scattering data analysis using a library of analytical expressions. *Journal of Applied Crystallography*, 48, 1587-1598.
- Brinker, C. J., Lu, Y., Sellinger, A. & Fan, H. 1999. Evaporation-Induced Self-Assembly: Nanostructures Made Easy. *Advanced Materials*, 11, 579-585.
- Búcsi, A., Karlovská, J., Chovan, M., Devínsky, F. & Uhríková, D. 2014. Determination of pKa of N-alkyl-N,N-dimethylamine-N-oxides using ^1H NMR and ^{13}C NMR spectroscopy. *Chemical Papers*, 68, 842-846.
- Cacciuto, A., Auer, S. & Frenkel, D. 2004. Onset of heterogeneous crystal nucleation in colloidal suspensions. *Nature*, 428, 404-406.
- Callahan, C. J. & Ni, X.-W. 2014. An investigation into the effect of mixing on the secondary nucleation of sodium chlorate in a stirred tank and an oscillatory baffled crystallizer. *CrystEngComm*, 16, 690-697.
- Carlton, R. A. 2011. *Pharmaceutical Microscopy*, Springer New York.
- Chakraborty, T., Chakraborty, I. & Ghosh, S. 2011. The methods of determination of critical micellar concentrations of the amphiphilic systems in aqueous medium. *Arabian Journal of Chemistry*, 4, 265-270.
- Chantraine, F., Viana, M., Brielles, N., Mondain-Monval, O., Pouget, C., Branlard, P., Rubinstenn, G. & Chulia, D. 2006. Parametric study of surfactant effect on mechanical

- and dissolution properties of detergent tablets. *Journal of Surfactants and Detergents*, 9, 267-277.
- Chatterjee, A., Moulik, S. P., Sanyal, S. K., Mishra, B. K. & Puri, P. M. 2001. Thermodynamics of Micelle Formation of Ionic Surfactants: A Critical Assessment for Sodium Dodecyl Sulfate, Cetyl Pyridinium Chloride and Dioctyl Sulfosuccinate (Na Salt) by Microcalorimetric, Conductometric, and Tensiometric Measurements. *The Journal of Physical Chemistry B*, 105, 12823-12831.
- Chayen, N. E., Saridakis, E., El-Bahar, R. & Nemirovsky, Y. 2001. Porous silicon: an effective nucleation-inducing material for protein crystallization. *Journal of Molecular Biology*, 312, 591-595.
- Chemat, F., Zill E, H. & Khan, M. K. 2011. Applications of ultrasound in food technology: Processing, preservation and extraction. *Ultrasonics Sonochemistry*, 18, 813-835.
- Chen, J., Sarma, B., Evans, J. M. B. & Myerson, A. S. 2011. Pharmaceutical Crystallization. *Crystal Growth & Design*, 11, 887-895.
- Chen, L.-J., Lin, S.-Y., Huang, C.-C. & Chen, E.-M. 1998. Temperature dependence of critical micelle concentration of polyoxyethylenated non-ionic surfactants. *Colloids and Surfaces A: Physicochemical and Engineering Aspects*, 135, 175-181.
- Cherny, A. Y., Anitas, E., Osipov, V. & Kuklin, A. 2014. Small-angle scattering from multiphase fractals. *Journal of Applied Crystallography*, 47, 198-206.
- Chu, H. M. 2014. *Surfactants in Household Detergents: Detergents*.
- Chu, Z. & Feng, Y. 2011. Empirical correlations between Krafft temperature and tail length for amidosulfobetaine surfactants in the presence of inorganic salt. *Langmuir*, 28, 1175-1181.
- Clayden, J. 2001. *Organic Chemistry*, Oxford University Press.
- Cosgrove, T. 2010. *Colloid Science: Principles, Methods and Applications*, John Wiley & Sons.

- Cox, M. F. 1986. Surfactants for hard-surface cleaning - mechanisms of solid soil removal. *Journal of the American Oil Chemists' Society*, 63, 559-565.
- D'arcy, A., Mac Sweeney, A. & Haber, A. 2003. Using natural seeding material to generate nucleation in protein crystallization experiments. *Acta Crystallographica Section D-Biological Crystallography*, 59, 1343-1346.
- De Anda, J. C., Wang, X. Z., Lai, X. & Roberts, K. J. 2005. Classifying organic crystals via in-process image analysis and the use of monitoring charts to follow polymorphic and morphological changes. *Journal of Process Control*, 15, 785-797.
- De Castro, M. D. L. & Priego-Capote, F. 2007. Ultrasound-assisted crystallization (sonocrystallization). *Ultrasonics Sonochemistry*, 14, 717-724.
- Delgado, B., Pino, V., Ayala, J. H., González, V. & Afonso, A. M. 2004. Nonionic surfactant mixtures: a new cloud-point extraction approach for the determination of PAHs in seawater using HPLC with fluorimetric detection. *Analytica Chimica Acta*, 518, 165-172.
- Deora, N. S., Misra, N. N., Deswal, A., Mishra, H. N., Cullen, P. J. & Tiwari, B. K. 2013. Ultrasound for Improved Crystallisation in Food Processing. *Food Engineering Reviews*, 5, 36-44.
- Dierker, M. & Schafer, H. J. 2010. Surfactants from oleic, erucic and petroselinic acid: Synthesis and properties. *European Journal of Lipid Science and Technology*, 112, 122-136.
- Dincer, T. D., Zisu, B., Vallet, C., Jayasena, V., Palmer, M. & Weeks, M. 2014. Sonocrystallisation of lactose in an aqueous system. *International Dairy Journal*, 35, 43-48.

- Dominguez, A., Fernandez, A., Gonzalez, N., Iglesias, E. & Montenegro, L. 1997. Determination of Critical Micelle Concentration of Some Surfactants by Three Techniques. *Journal of Chemical Education*, 74, 1227.
- Dong, B. & Gao, Y. 2015. Various Self-Assembly Behaviors of Amphiphilic Molecules in Ionic Liquids. *Ionic Liquids-Current State of the Art*. InTech.
- Duer, M. J. 2008. *Solid state NMR spectroscopy: principles and applications*, Wiley.
- Dunn, R. O. 2011. Improving the cold flow properties of biodiesel by fractionation. *Soybean-Applications and Technology*. InTech.
- Fan, X. J., Stenius, P., Kallay, N. & Matijevic, E. 1988. Precipitation of surfactant salts. 2. The effect of nonionic surfactants on precipitation of calcium dodecyl-sulfate. *Journal of Colloid and Interface Science*, 121, 571-578.
- Farn, R. J. 2008. *Chemistry and Technology of Surfactants*, Oxford, Blackwell Publishing Ltd.
- Fermani, S., Falini, G., Minnucci, M. & Ripamonti, A. 2001. Protein crystallization on polymeric film surfaces. *Journal of Crystal Growth*, 224, 327-334.
- Foster, M. P., Mcelroy, C. A. & Amero, C. D. 2007. Solution NMR of large molecules and assemblies. *Biochemistry*, 46, 331-340.
- Frączyk, A. 2011. The activation energy of primary crystallization of Fe₉₅Si₅ metallic glass. *Technical Sciences/University of Warmia and Mazury in Olsztyn*, 93-100.
- Friedli, F. 2001. *Detergency of Specialty Surfactants*, Taylor & Francis.
- Gao, J., Ge, W. & Li, J. 2005. Effect of concentration on surfactant micelle shapes - A molecular dynamics study. *Science in China Series B: Chemistry*, 48, 470-475.
- Gavazzoni Dias, M. F. R. 2015. Hair Cosmetics: An Overview. *International Journal of Trichology*, 7, 2-15.
- Gerds, C. J., Tereshko, V., Yadav, M. K., Dementieva, I., Collart, F., Joachimiak, A., Stevens, R. C., Kuhn, P., Kossiakoff, A. & Ismagilov, R. F. 2006. Time-Controlled Microfluidic

- Seeding in nL-Volume Droplets To Separate Nucleation and Growth Stages of Protein Crystallization. *Angewandte Chemie International Edition*, 45, 8156-8160.
- Gil, P. S. & Lacks, D. J. 2016. Effect of surfactant shape on solvophobicity and surface activity in alcohol-water systems. *The Journal of Chemical Physics*, 145, 204705.
- Gill, P., Moghadam, T. T. & Ranjbar, B. 2010. Differential scanning calorimetry techniques: applications in biology and nanoscience. *Journal of Biomolecular Techniques : JBT*, 21, 167-93.
- Goodwin, J. 2009. *Colloids and Interfaces with Surfactants and Polymers*, Wiley.
- Gu, T. & Sjtjblomt, J. 1991. Empirical Relationships between the Krafft Points and the. *Acta Chemica Scandinavica*, 45, 762-765.
- Gu, T. R. & Sjoblom, J. 1992. Surfactant structure and its relation to the Krafft point, cloud point and micellization - some empirical relationships. *Colloids and Surfaces*, 64, 39-46.
- Günther, H. 2013. *NMR Spectroscopy: Basic Principles, Concepts and Applications in Chemistry*, Wiley.
- Guzey, D. & Mcclements, D. J. 2006. Formation, stability and properties of multilayer emulsions for application in the food industry. *Advances in Colloid and Interface Science*, 128, 227-248.
- Hammer, B. E. 1998. Industrial applications of nuclear magnetic resonance. *Sensor Review*, 18, 245-251.
- Hammouda, B. 2013. Temperature Effect on the Nanostructure of SDS Micelles in Water. *Journal of Research of the National Institute of Standards and Technology*, 118, 151-167.
- Hao, W., Yang, W., Cai, H. & Huang, Y. 2010. Non-isothermal crystallization kinetics of polypropylene/silicon nitride nanocomposites. *Polymer Testing*, 29, 527-533.

- Heller, W. T. 2010. Small-angle neutron scattering and contrast variation: a powerful combination for studying biological structures. *Acta Crystallographica Section D: Biological Crystallography*, 66, 1213-1217.
- Herrera, M. L. & Hartel, R. W. 2000. Effect of processing conditions on crystallization kinetics of a milk fat model system. *Journal of the American Oil Chemists' Society*, 77, 1177-1188.
- Higaki, K., Ueno, S., Koyano, T. & Sato, K. 2001. Effects of ultrasonic irradiation on crystallization behavior of tripalmitoylglycerol and cocoa butter. *Journal of the American Oil Chemists Society*, 78, 513-518.
- Himawan, C., Starov, V. M. & Stapley, A. G. F. 2006. Thermodynamic and kinetic aspects of fat crystallization. *Advances in Colloid and Interface Science*, 122, 3-33.
- Hollamby, M. J. 2013. Practical applications of small-angle neutron scattering. *Physical Chemistry Chemical Physics*, 15, 10566-10579.
- Holmberg, K. E. A. 2002. *Surfactants and Polymers in Aqueous Solution*, Wiley.
- Hunter, R. J. 2001. *Foundations of Colloid Science*, Oxford University Press.
- Islam, M. N., Sarker, K. C. & Sharker, K. K. 2015. Influence of Some Hofmeister Anions on the Krafft Temperature and Micelle Formation of Cetylpyridinium Bromide in Aqueous Solution. *Journal of Surfactants and Detergents*, 18, 9-16.
- Ivanković, T. & Hrenović, J. 2010. Surfactants in the environment. *Archives of Industrial Hygiene and Toxicology*, 61, 95-110.
- Jain, P. K., Deepika, K. & Saxena, N. 2008. Phase transformation and crystallization kinetics of Se₉₀In₈Sb₂ chalcogenide glass. *Chalcogenide Letters*, 5, 126-136.
- James, T. L. 1998. Fundamentals of NMR. *Online Textbook: Department of Pharmaceutical Chemistry, University of California, San Francisco*, 1-31.

- Kabbani, D., Sepulcre, F. & Wedekind, J. 2011. Ultrasound-assisted liquefaction of rosemary honey: Influence on rheology and crystal content. *Journal of Food Engineering*, 107, 173-178.
- Kadam, S. S., Kramer, H. J. M. & Ter Horst, J. H. 2011. Combination of a Single Primary Nucleation Event and Secondary Nucleation in Crystallization Processes. *Crystal Growth & Design*, 11, 1271-1277.
- Kadam, S. S., Kulkarni, S. A., Coloma Ribera, R., Stankiewicz, A. I., Ter Horst, J. H. & Kramer, H. J. M. 2012. A new view on the metastable zone width during cooling crystallization. *Chemical Engineering Science*, 72, 10-19.
- Kadam, S. U., Tiwari, B. K., Alvarez, C. & O'donnell, C. P. 2015. Ultrasound applications for the extraction, identification and delivery of food proteins and bioactive peptides. *Trends in Food Science & Technology*, 46, 60-67.
- Karpiński, P. H. 1985. Importance of the two-step crystal growth model. *Chemical Engineering Science*, 40, 641-646.
- Kartal, Ç. 2006. Study of the cloud point of nonionic surfactant and nonionic-cationic surfactant mixture: Effect of electrolytes. *Scientific Papers*, 34, 41-42.
- Kekicheff, P., Grabiellémadelmont, C. & Ollivon, M. 1989. Phase-diagram of sodium dodecyl-sulfate water-system .1. A calorimetric study. *Journal of Colloid and Interface Science*, 131, 112-132.
- Kikhney, A. G. & Svergun, D. I. 2015. A practical guide to small angle X-ray scattering (SAXS) of flexible and intrinsically disordered proteins. *FEBS Letters*, 589, 2570-2577.
- Kissa, E. 2001. *Fluorinated Surfactants and Repellents, Second Edition*, Taylor & Francis.
- Kissinger, H. E. 1957. Reaction Kinetics in Differential Thermal Analysis. *Analytical Chemistry*, 29, 1702-1706.
- Krafft, F., Wiglow, H. 1895. *Chemische Berichte.*, 28, 2566.

- Kralova, I. & Sjoblom, J. 2009. Surfactants Used in Food Industry: A Review. *Journal of Dispersion Science and Technology*, 30, 1363-1383.
- Kresheck, G. C. 2001. Comparison of the DSC Curves Obtained for Aqueous Solutions of Nonionic and Ionic Surfactants. *The Journal of Physical Chemistry B*, 105, 4380-4385.
- Kresheck, G. C. 2006. The temperature dependence of the heat capacity change for micellization of nonionic surfactants. *Journal of Colloid and Interface Science*, 298, 432-440.
- Kronberg, B., Holmberg, K. & Lindman, B. 2014. *Surface Chemistry of Surfactants and Polymers*, Wiley.
- Kuo, M. C., Huang, J. C. & Chen, M. 2006. Non-isothermal crystallization kinetic behavior of alumina nanoparticle filled poly(ether ether ketone). *Materials Chemistry and Physics*, 99, 258-268.
- Lai, K. Y. 1996. *Liquid Detergents*, CRC Press.
- Le Révérend, B., Fryer, P. & Bakalis, S. 2009. Modelling crystallization and melting kinetics of cocoa butter in chocolate and application to confectionery manufacturing. *Soft Matter*, 5, 891-902.
- Lee, J., Ashokkumar, M. & Kentish, S. E. 2014. Influence of mixing and ultrasound frequency on antisolvent crystallisation of sodium chloride. *Ultrasonics Sonochemistry*, 21, 60-68.
- Leube, W., Monkenbusch, M., Schneiders, D., Richter, D., Adamson, D., Fetters, L., Dounis, P. & Lovegrove, R. 2000. Wax-crystal modification for fuel oils by self-aggregating partially crystallizable hydrocarbon block copolymers. *Energy & Fuels*, 14, 419-430.
- Li, J., Shu, Q. & Chou, K. 2015. Effect of agitation on crystallization behavior of CaO-Al₂O₃-SiO₂-Na₂O-CaF₂ mold fluxes with varying basicity. *Metallurgical and Materials Transactions B*, 46, 1555-1563.

- Li, T., Senesi, A. J. & Lee, B. 2016. Small Angle X-ray Scattering for Nanoparticle Research. *Chemical Reviews*, 116, 11128-11180.
- Liang, K., White, G., Wilkinson, D., Ford, L. J., Roberts, K. J. & Wood, W. M. L. 2004. Examination of the process scale dependence of L-glutamic acid batch crystallized from supersaturated aqueous solutions in relation to reactor hydrodynamics. *Industrial & Engineering Chemistry Research*, 43, 1227-1234.
- Lin, S.-Y., Lin, Y.-Y., Chen, E.-M., Hsu, C.-T. & Kwan, C.-C. 1999. A Study of the Equilibrium Surface Tension and the Critical Micelle Concentration of Mixed Surfactant Solutions. *Langmuir*, 15, 4370-4376.
- Lipfert, J., Columbus, L., Chu, V. B., Lesley, S. A. & Doniach, S. 2007. Size and Shape of Detergent Micelles Determined by Small-Angle X-ray Scattering. *The Journal of Physical Chemistry B*, 111, 12427-12438.
- Liu, J. & Rasmuson, Å. C. 2013. Influence of Agitation and Fluid Shear on Primary Nucleation in Solution. *Crystal Growth & Design*, 13, 4385-4394.
- Liu, J., Svärd, M. & Rasmuson, Å. C. 2014. Influence of Agitation and Fluid Shear on Nucleation of m-Hydroxybenzoic Acid Polymorphs. *Crystal Growth & Design*, 14, 5521-5531.
- Lomax, E. G. 1996. *Amphoteric Surfactants, Second Edition*, Taylor & Francis.
- Lucena, I., Canuto, J., Caroni, A., Fonseca, J., Neto, A. D. & Dantas, T. C. 2012. Characterization of nonionic surfactant micellar structures in organic solvents by small angle X-ray scattering (SAXS). *Colloids and Surfaces A: Physicochemical and Engineering Aspects*, 408, 48-56.
- Luque De Castro, M. D. & Priego-Capote, F. 2007. Ultrasound-assisted crystallization (sonocrystallization). *Ultrasonics Sonochemistry*, 14, 717-724.

- Machado, A. L. C., Lucas, E. F. & González, G. 2001. Poly(ethylene-co-vinyl acetate) (EVA) as wax inhibitor of a Brazilian crude oil: oil viscosity, pour point and phase behavior of organic solutions. *Journal of Petroleum Science and Engineering*, 32, 159-165.
- Mahapatra, P., Rasheed, A. A., Goyal, P. & Bellare, J. R. 2015. Structure of Micelles Calcium Didodecyl Sulfate: A SAXS Study. *Journal of Nanomedicine & Nanotechnology*, 2015.
- Maibaum, L., Dinner, A. R. & Chandler, D. 2004. Micelle formation and the hydrophobic effect. *Journal of Physical Chemistry B*, 108, 6778-6781.
- Manojlovic, J. Z. 2012. The krafft temperature of surfactant solutions. *Thermal Science*, 16, S631-S640.
- Marcone, M. F., Wang, S., Albabish, W., Nie, S., Somnarain, D. & Hill, A. 2013. Diverse food-based applications of nuclear magnetic resonance (NMR) technology. *Food Research International*, 51, 729-747.
- Markets, M. A. 2016. *Surfactants Market by Type, Substrate, Application - Global Forecast to 2021* [Online]. Available: <http://www.marketsandmarkets.com/Market-Reports/biosurfactants-market-493.html> [Accessed 13/06/2018].
- Mcclements, D. J. 2015. *Food emulsions: principles, practices, and techniques*, CRC Press.
- Mcleod, J. S., Paterson, A. H. J., Bronlund, J. E. & Jones, J. R. The effect of agitation on the nucleation of α -lactose monohydrate. *International Dairy Journal*.
- Mcpherson, A. & Gavira, J. A. 2014. Introduction to protein crystallization. *Acta Crystallographica Section F-Structural Biology Communications*, 70, 2-20.
- Mcpherson, A. & Shlichta, P. 1988. Heterogeneous and epitaxial nucleation of protein crystals on mineral surfaces. *Science*, 239, 385-387.
- Menger, F. M., Zana, R. & Lindman, B. 1998. Portraying the structure of micelles. *Journal of Chemical Education*, 75, 115-115.

- Mersmann, A. & Bartosch, K. 1998. How to predict the metastable zone width. *Journal of Crystal Growth*, 183, 240-250.
- Michell, R. M., Blaszczyk-Lezak, I., Mijangos, C. & Müller, A. J. 2013. Confinement effects on polymer crystallization: From droplets to alumina nanopores. *Polymer*, 54, 4059-4077.
- Miller, R. M., Ces, O., Brooks, N. J., Robles, E. S. J. & Cabral, J. T. 2017. Crystallization of Sodium Dodecyl Sulfate-Water Micellar Solutions under Linear Cooling. *Crystal Growth & Design*, 17, 2428-2437.
- Miller, R. M., Poulos, A. S., Robles, E. S. J., Brooks, N. J., Ces, O. & Cabral, J. T. 2016. Isothermal Crystallization Kinetics of Sodium Dodecyl Sulfate–Water Micellar Solutions. *Crystal Growth and Design*, 16, 3379-3388.
- Morintale, E. 2013. Use of heat flows from DSC curve for calculation of specific heat of the solid materials. *Physics AUC*, 23, 89-94.
- Müller, A. J., Balsamo, V. & Arnal, M. L. 2005. Nucleation and crystallization in diblock and triblock copolymers. *Block Copolymers II*. Springer.
- Mullin, J. W. 1993. *Crystallization*, Butterworth-Heinemann.
- Mullin, J. W. & Raven, K. D. 1962. Influence of Mechanical Agitation on the Nucleation of Some Aqueous Salt Solutions. *Nature*, 195, 35-38.
- Myerson, A. 2002. *Handbook of Industrial Crystallization*, Butterworth-Heinemann.
- Nakayama, H., Shinoda, K. & Hutchins.E 1966. Effect of added alcohols on solubility and Krafft point of sodium dodecyl sulfate. *Journal of Physical Chemistry*, 70, 3502-3504.
- Nasiru, T., Avila, L. & Levine, M. 2011. Determination of critical micelle concentrations using UV-visible spectroscopy. *Journal of High School Research*, 2, 1-5.
- Nitschke, M. & Costa, S. 2007. Biosurfactants in food industry. *Trends in Food Science & Technology*, 18, 252-259.

- Nývlt, J. 1985. *The Kinetics of Industrial Crystallization*, Elsevier.
- Ozawa, T. 1970. Kinetic analysis of derivative curves in thermal analysis. *Journal of Thermal Analysis*, 2, 301-324.
- P&G 2017. P&G Annual Report 2017.
- Patist, A., Bhagwat, S. S., Penfield, K. W., Aikens, P. & Shah, D. O. 2000. On the measurement of critical micelle concentrations of pure and technical-grade nonionic surfactants. *Journal of Surfactants and Detergents*, 3, 53-58.
- Pei, A., Zhou, Q. & Berglund, L. A. 2010. Functionalized cellulose nanocrystals as biobased nucleation agents in poly(L-lactide) (PLLA) - Crystallization and mechanical property effects. *Composites Science and Technology*, 70, 815-821.
- Porter, M. R. 2013. *Handbook of Surfactants*, Springer US.
- Principe, J. R. & Skauen, D. M. 1962. Preparation of Microcrystalline Progesterone Using Ultrasound. *Journal of Pharmaceutical Sciences*, 51, 389-390.
- Qu, X., Ding, H., Lu, J., Wang, Y. & Zhang, L. 2004. Isothermal and nonisothermal crystallization kinetics of MC nylon and polyazomethine/MC nylon composites. *Journal of Applied Polymer Science*, 93, 2844-2855.
- Renz, M. 2013. Fluorescence microscopy—A historical and technical perspective. *Cytometry Part A*, 83, 767-779.
- Richards, S. A. & Hollerton, J. C. 2010. *Essential Practical NMR for Organic Chemistry*, Wiley.
- Richards, W. T. & Loomis, A. L. 1927. The chemical effects of high frequency sound waves I. A preliminary survey. *Journal of the American Chemical Society*, 49, 3086-3100.
- Rigg, A., Duff, A., Nie, Y., Somuah, M., Tetteh, N. & Hesp, S. a. M. 2017. Non-isothermal kinetic analysis of reversible ageing in asphalt cements. *Road Materials and Pavement Design*, 1-26.

- Rosen, M. J. 2004. *Surfactants and Interfacial Phenomena*, Wiley.
- Rosen, M. J. & Kunjappu, J. T. 2012. *Surfactants and Interfacial Phenomena*, Wiley.
- Rosevear, F. 1968. Liquid crystals: the mesomorphic phases of surfactant compositions. *Journal of the Society of Cosmetic Chemists*, 19, 581-594.
- Ruecroft, G., Hipkiss, D., Ly, T., Maxted, N. & Cains, P. W. 2005. Sonocrystallization: The use of ultrasound for improved industrial crystallization. *Organic Process Research & Development*, 9, 923-932.
- Salager, J.-L. 2002. Surfactants types and uses. *FIRP Booklet E300. Merida Venezuela*, 2, 3.
- Sander, J. R. G., Zeiger, B. W. & Suslick, K. S. 2014. Sonocrystallization and sonofragmentation. *Ultrasonics Sonochemistry*, 21, 1908-1915.
- Scamehorn, J. F. 1986. An Overview of Phenomena Involving Surfactant Mixtures. *Acs Symposium Series*, 311, 1-27.
- Scheibel, J. J. 2004. The evolution of anionic surfactant technology to meet the requirements of the laundry detergent industry. *Journal of Surfactants and Detergents*, 7, 319-328.
- Schenk, H. & Peschar, R. 2004. Understanding the structure of chocolate. *Radiation Physics and Chemistry*, 71, 829-835.
- Sear, R. P. 2006. Heterogeneous and Homogeneous Nucleation Compared: Rapid Nucleation on Microscopic Impurities. *The Journal of Physical Chemistry B*, 110, 4985-4989.
- Sharma, K. S., Patil, S. R. & Rakshit, A. K. 2003. Study of the cloud point of C12En nonionic surfactants: effect of additives. *Colloids and Surfaces A: Physicochemical and Engineering Aspects*, 219, 67-74.
- Sharma, R. K. 2014. Surfactants: Basics and Versatility in Food Industries. *PharmaTutor*, 2, 17-29.

- Shiau, B. J., Harwell, J. H. & Scamehorn, J. F. 1994. Precipitation of mixtures of anionic and cationic surfactants. 3. Effect of added nonionic surfactant. *Journal of Colloid and Interface Science*, 167, 332-345.
- Shirahama, K. & Kashiwabara, T. 1971. The CMC-decreasing effects of some added alcohols on the aqueous sodium dodecyl sulfate solutions. *Journal of Colloid and Interface Science*, 36, 65-70.
- Smith, L. A., Duncan, A., Thomson, G. B., Roberts, K. J., Machin, D. & Mcleod, G. 2004. Crystallisation of sodium dodecyl sulphate from aqueous solution: phase identification, crystal morphology, surface chemistry and kinetic interface roughening. *Journal of Crystal Growth*, 263, 480-490.
- Smith, L. A., Hammond, R. B., Roberts, K. J., Machin, D. & Mcleod, G. 2000. Determination of the crystal structure of anhydrous sodium dodecyl sulphate using a combination of synchrotron radiation powder diffraction and molecular modelling techniques. *Journal of Molecular Structure*, 554, 173-182.
- Smith, L. A., Roberts, K. J., Machin, D. & Mcleod, G. 2001. An examination of the solution phase and nucleation properties of sodium, potassium and rubidium dodecyl sulphates. *Journal of Crystal Growth*, 226, 158-167.
- Somani, R. H., Hsiao, B. S., Nogales, A., Srinivas, S., Tsou, A. H., Sics, I., Balta-Calleja, F. J. & Ezquerro, T. A. 2000. Structure Development during Shear Flow-Induced Crystallization of i-PP: In-Situ Small-Angle X-ray Scattering Study. *Macromolecules*, 33, 9385-9394.
- Soontravanich, S. 2007. *Formation and Dissolution of Surfactant Precipitates*. PhD Thesis, University of Oklahoma.

- Soontravanich, S. & Scamehorn, J. F. 2009. Use of a Nonionic Surfactant to Inhibit Precipitation of Anionic Surfactants by Calcium. *Journal of Surfactants and Detergents*, 13, 13.
- Soontravanich, S., Walsh, S., Scamehorn, J. F., Harwell, J. H. & Sabatini, D. A. 2009. Interaction between an anionic and an amphoteric surfactant. Part II: Precipitation. *Journal of Surfactants and Detergents*, 12, 145-154.
- Southall, N. T., Dill, K. A. & Haymet, A. D. J. 2002. A view of the hydrophobic effect. *Journal of Physical Chemistry B*, 106, 521-533.
- Spitz, L. 2016. *Soap Manufacturing Technology*, Elsevier Science.
- Stellner, K. L. & Scamehorn, J. F. 1986. Surfactant precipitation in aqueous-solutions containing mixtures of anionic and nonionic surfactants. *Journal of the American Oil Chemists' Society*, 63, 566-574.
- Stellner, K. L. & Scamehorn, J. F. 1989. Hardness tolerance of anionic surfactant solutions. 2. Effect of added nonionic surfactant. *Langmuir*, 5, 77-84.
- Stoiber, R. E. & Morse, S. A. 1994. *Crystal Identification with the Polarizing Microscope*, Springer US.
- Stura, E. A. & Wilson, I. A. 1991. Applications of the streak seeding technique in protein crystallization. *Journal of Crystal Growth*, 110, 270-282.
- Svergun, D. I., Koch, M. H. J., Timmins, P. A. & May, R. P. 2013. *Small Angle X-Ray and Neutron Scattering from Solutions of Biological Macromolecules*, OUP Oxford.
- Tabor, R. F., Eastoe, J. & Grillo, I. 2009. Time-resolved small-angle neutron scattering as a lamellar phase evolves into a microemulsion. *Soft Matter*, 5, 2125-2129.
- Tachibana, M. 2017. *Beginner's Guide to Flux Crystal Growth*, Tokyo, Springer Japan : Imprint: Springer.

- Teychené, S. & Biscans, B. 2008. Nucleation Kinetics of Polymorphs: Induction Period and Interfacial Energy Measurements. *Crystal Growth & Design*, 8, 1133-1139.
- Thomas, L. C. 2005. An introduction to the techniques of differential scanning calorimetry (DSC) and modulated DSC. *Publicationes de la Universidade da Coruna, Coruna*, 9-25.
- Tiddy, G. J. T. 1980. Surfactant-water liquid crystal phases. *Physics Reports*, 57, 1-46.
- Tiller, W. A. 1991. *The Science of Crystallization: Macroscopic Phenomena and Defect Generation*, Cambridge University Press.
- Todt, H., Guthausen, G., Burk, W., Schmalbein, D. & Kamlowski, A. 2006. Water/moisture and fat analysis by time-domain NMR. *Food Chemistry*, 96, 436-440.
- Topel, O., Cakir, B. A., Budama, L. & Hoda, N. 2013. Determination of critical micelle concentration of polybutadiene-block-poly(ethyleneoxide) diblock copolymer by fluorescence spectroscopy and dynamic light scattering. *Journal of Molecular Liquids*, 177, 40-43.
- Tsujii, K., Saito, N. & Takeuchi, T. 1980. Krafft points of anionic surfactants and their mixtures with special attention to their applicability in hard water. *The Journal of Physical Chemistry*, 84, 2287-2291.
- Valeton, J. J. P. 1924. Growth and dissolution of crystals. II. *Zeitschrift Fur Kristallographie*, 59, 335-365.
- Valeton, J. J. P. 1924. Growth and dissolution of crystals. III. *Zeitschrift Fur Kristallographie*, 60, 1-38.
- Van Haesendonck, I. P. H., & Vanzeveren, E. C. A. 2004. *Rhamnolipids in bakery products*.
- Vautier-Giongo, C. & Bales, B. L. 2003. Estimate of the ionization degree of ionic micelles based on Krafft temperature measurements. *Journal of Physical Chemistry B*, 107, 5398-5403.

- Vedantam, S. & Ranade, V. V. 2013. Crystallization: Key thermodynamic, kinetic and hydrodynamic aspects. *Sadhana-Academy Proceedings in Engineering Sciences*, 38, 1287-1337.
- Vitiello, G., Mangiapia, G., Romano, E., Lavorgna, M., Guido, S., Guida, V., Paduano, L. & D'errico, G. 2014. Phase behavior of the ternary aqueous mixtures of two polydisperse ethoxylated nonionic surfactants. *Colloids and Surfaces A: Physicochemical and Engineering Aspects*, 442, 16-24.
- Wayne, R. 2014. Chapter 11 - Fluorescence Microscopy. *Light and Video Microscopy (Second Edition)*. San Diego: Academic Press.
- Webb, R. H. 1996. Confocal optical microscopy. *Reports on Progress in Physics*, 59, 427.
- Wei, B. 2015. Recent advances on mitigating wax problem using polymeric wax crystal modifier. *Journal of Petroleum Exploration and Production Technology*, 5, 391-401.
- Wu, F.-G., Wang, N.-N., Zhang, Q.-G., Sun, S.-F. & Yu, Z.-W. 2012. Crystallization from the micellar phase of imidazolium-based cationic surfactants. *Journal of Colloid and Interface Science*, 374, 197-205.
- Yan, F. & Texter, J. 2006. Polymerization of and in mesophases. *Advances in Colloid and Interface Science*, 128–130, 27-35.
- Yang, J., McCoy, B. J. & Madras, G. 2005. Distribution kinetics of polymer crystallization and the Avrami equation. *Journal of Chemical Physics*, 122.
- Yangxin, Y., Jin, Z. & Bayly, A. E. 2008. Development of surfactants and builders in detergent formulations. *Chinese Journal of Chemical Engineering*, 16, 517-527.
- Yount, L. 2008. *Antoni Van Leeuwenhoek: First to See Microscopic Life*, Enslow Publishers.
- Zamanipoor, M. H. & Mancera, R. L. 2014. The emerging application of ultrasound in lactose crystallisation. *Trends in Food Science & Technology*, 38, 47-59.

- Zhang, J., Wang, Z.-L., Liu, J., Chen, S. & Liu, G.-Y. 2006. *Self-Assembled Nanostructures*, Springer Science & Business Media.
- Zhang, Y., Jiang, Y., Zhang, D., Qian, Y. & Wang, X. Z. 2015. Metastable zone width, crystal nucleation and growth kinetics measurement in anti-solvent crystallization of β -artemether in the mixture of ethanol and water. *Chemical Engineering Research and Design*, 95, 187-194.
- Zhou, W. Y., Duan, B., Wang, M. & Cheung, W. L. 2011. Isothermal and Non-isothermal Crystallization Kinetics of Poly (L-Lactide)/Carbonated Hydroxyapatite Nanocomposite Microspheres. *Advances in Diverse Industrial Applications of Nanocomposites*. InTech.
- Ziegler, G. R., Garbolino, C. & Coupland, J. N. The influence of surfactants and moisture on the colloidal and rheological properties of model chocolate dispersions. 3rd International symposium on food rheology and structure, 2003. 335.
- Zimbitas, G., Fryer, P. J., Zhang, Z. & Bakalis, S. 2017. Free-standing thin film interactions with small particles. *Innovative Food Science & Emerging Technologies*, 40, 18-26.
- Zoller, U. 2008. Handbook of Detergents, Part E. CRC Press.

CHAPTER 2

CRYSTALLISATION OF SODIUM DODECYL SULFATE AND THE CORRESPONDING EFFECT OF 1-DODECANOL ADDITION

Discussions contained in this chapter have been published within: Summerton, E., Zimbitas, G., Britton, M. and Bakalis, S. 2016. Crystallisation of sodium dodecyl sulfate and the corresponding effect of 1-dodecanol addition, *Journal of Crystal Growth*, **455**, p. 111-116. Additional details have been introduced to the methodology chapter.

2.1 Abstract

Sodium dodecyl sulfate (SDS) exhibits crystallisation upon exposure to low temperatures, which can pose a problem in terms of product stability. In this study, non-isothermal crystallisation of SDS is investigated via differential scanning calorimetry (DSC) at concentrations that are typical of those present in many industrial liquid detergents. At different low temperatures, the crystal structures are analysed with X-ray diffraction (XRD) and it is concluded that ice formation during the surfactant crystallisation process occurs below 0 °C. The capability of the alcohol precursor, 1-dodecanol, as a seeding material for SDS crystallisation is also investigated through the use of DSC and optical microscopy. These results show that 1-dodecanol can successfully act as a seed for SDS crystallisation. Upon cooling an SDS aqueous system, the crystallisation peak in the DSC thermogram shifts to a higher temperature in the presence of 1-dodecanol. Therefore, any remnant alcohol precursor in surfactant-based formulations could have a negative impact on the product stability upon exposure to cold climates.

2.2 Introduction

The leading players in the fast-moving consumer goods (FMCG) industry provide over 400 brands worldwide and involve products being sold on a short timescale at a relatively low cost. The FMCG industry can be further subcategorised into separate sectors including food and beverages, personal care, homecare and beauty care. New products are added to the portfolios on a regular basis in order to maintain market leadership. The forecasted revenue for 2021 for the laundry care and detergent sector is \$39. 86 billion (Markets, 2016) with a compound growth rate of 5.3 %, illustrating the sheer size of this particular industry. Within this sector, each brand is manufactured to specific consumer requirements in terms of supply volume and packaging material. Depending on the product formulation and nature of the local consumer

market, the volume supplied can range from millilitres to litres. However, at all product scales it is an essential requirement that the formulation demonstrates stability during the stages of manufacture, transport and the subsequent shelf life (Chantraine *et al.*, 2006), with a two year shelf life period commonly expected for the majority of homecare brands. This is particularly challenging for liquid products in regions where there is potential exposure to cold climates. Under such temperature conditions, there can be a risk of surfactant crystallisation, which, in turn, can affect product appearance. Within the detergent industry there are stability test methods in place to predict and minimise crystallisation failures (Lai, 1996). Since the detergent and laundry care industry continues to expand globally, there is a need to further broaden knowledge of surfactant crystallisation. This understanding will enable product stability and the accompanying test methods to be further optimised.

Typical liquid detergent formulations have a complex composition, with surfactants and water as the major components, alongside other additives such as perfumes, dyes and preservatives. The surfactants are essential in providing the necessary functions of detergent products through their cleaning and foaming properties. These formulations tend to contain a variety of different surfactants, with some of anionic nature and others that exhibit non-ionic behaviour at the pH of liquid detergents. It is this combination that provides the optimum characteristics. The major component is the anionic surfactants, which exhibit excellent soil removal properties and come at a relatively low cost (Lai, 1996). However, the minor presence of non-ionic surfactants is also important due to their foaming ability and low temperature stability properties. Sodium dodecyl sulfate (SDS) (Amante *et al.*, 1991; Stellner *et al.*, 1988) and N, N-dimethyldodecylamine N-oxide (DDAO) (Kume *et al.*, 2008) are examples of widely used anionic and non-ionic surfactants, respectively.

Above the critical micelle concentration (CMC), surfactant and mixed surfactant systems can form micellar aggregates. This concentration can be determined by conductivity and surface

tension measurements (Mandavi, 2008). Aside from concentration, temperature also plays an important role in the process. The minimum temperature that is required for micelle formation is termed the Krafft temperature. Below this point, aggregates cannot form and there is a risk of surfactant crystallisation. The Krafft temperature of an aqueous ionic surfactant system can be lowered upon addition of a non-ionic surfactant (Stellner and Scamehorn, 1989; Stellner and Scamehorn, 1986). The non-ionic surfactant inserts into the aggregates and reduces the repulsion between the charged head groups, resulting in non-ideal micelles. Thus, the degree of micellisation increases and the CMC is reduced. The solubility product of the surfactant salt no longer equals the product of surfactant monomer concentration and counterion concentration. As a result, a lower temperature is required for crystallisation to occur. Aside from the addition of non-ionic surfactants, the structural features of the surfactant can also influence its Krafft temperature. In 1991, Gu *et al.* investigated the structural variability relationship with Krafft temperature, providing an empirical formula for the Krafft temperature dependency (Gu and Sjoblom, 1992).

The crystallisation of surfactants consists of two processes: nucleation and crystal growth (Vedantam and Ranade, 2013). Nucleation can be defined as the start of the phase transition where surfactant molecules aggregate into clusters constituting the nuclei. (Vedantam and Ranade, 2013) Crystals will only grow from nuclei above a critical radius. The rate of nucleation is the limiting factor at the beginning of the crystallisation process. As the amount of nuclei increase, the rate of the phase transition also increases and then subsequently slows towards the end of the phase transition as the newly crystallised phase provides a boundary for the further growth. A S-shaped rate profile is typical for such systems (Tiller, 1991).

In the literature, there are relatively few reports regarding the crystallisation of SDS solutions, despite the importance of sulfated surfactants in the detergent industry. In 2001, Smith *et al.* reported the crystallisation transitions for a SDS solutions over a range of concentrations up to

a maximum of 20 wt. % SDS. This investigation employed various techniques, including differential scanning calorimetry (DSC) and turbidity measurements (Smith *et al.*, 2001; Smith *et al.*, 2004). Their work also considered the morphology of the SDS crystals. This was further investigated by Chantraine *et al.* using X-ray diffraction (XRD), Raman spectroscopy and scanning electron microscopy (SEM) (Chantraine *et al.*, 2007). Crystallisation studies of other single surfactant systems are limited in the literature; Fu-Gen Wu *et al.* investigated the cooling crystallisation of the cationic surfactant cetyltrimethylammonium bromide (CTAB) to provide further knowledge regarding the various metaphases (Wu *et al.*, 2012). The mechanism and accompanying kinetics of the crystallisation were examined via the use of optical microscopy and DSC. The work of De Anda *et al.* on the crystallisation of glutamic acid emphasises the importance of image analysis when determining a mechanism and associated morphological changes in the structural conformation (De Anda *et al.*, 2005). In addition to single surfactant systems, crystallisation of anionic and non-ionic surfactant mixtures is also a field with few publications (Stellner and Scamehorn, 1986; Stellner *et al.*, 1988; Shiau *et al.*, 1994).

Aside from additional surfactants, other components can affect the crystallisation of an ionic surfactant. For example, the presence of short and long chain alcohols can influence crystallisation behaviour. SDS is manufactured from its alcohol precursor, 1-dodecanol, through sulfation under a selected set of conditions (Dierker and Schafer, 2010). During the manufacturing process, incomplete conversion results in some 1-dodecanol remaining in the solution. Investigations into SDS and 1-dodecanol mixtures are limited with one example being a study into the development of a model distinguishing between the presence of SDS and 1-dodecanol via surface tension isotherms (Kralchevsky *et al.*, 2003). Earlier studies have focused on the structural effects that short chain alcohols and phenols have on SDS complexes. These investigations used small angle neutron scattering (SANS), XRD and pulsed field nuclear magnetic resonance (NMR) (Forland *et al.*, 1998; Hirata and Iimura, 1998). In a separate study,

the thermodynamic properties of SDS solutions mixed with various short chain alcohols were used to support the hypothesis of a hydrogen bonding interaction between the two components (Motin *et al.*, 2015). Longer chain alcohol addition to SDS solutions results in a lowering of the Krafft temperature upon dissolution of small quantities of hexanol, heptanol and octanol (Nakayama *et al.*, 1966). However, an investigation into Krafft temperature variation for an SDS solution upon addition of 1-dodecanol does not seem to appear in the literature, despite it being the alcohol precursor.

In this chapter, SDS crystallisation will be discussed for a range of aqueous SDS concentrations which are typical of dish liquid products supplied by industrial manufacturers. An understanding of surfactant crystallisation is vital when controlling and improving the low temperature stability test methods for detergent products. The understanding of SDS + alcohol aqueous systems is the focus for the second part of the study where the effect of 1-dodecanol addition on SDS crystallisation will be reported.

2.3 Materials and methods

Experimental work involved initial preparation of the surfactant solutions followed by exposure to cooling and heating cycles to enable crystallisation and subsequent melting to occur. These processes were monitored through a variety of techniques, which are described below.

2.3.1 Materials

SDS was purchased from Fischer Scientific (> 97.5 %). Aqueous solutions of SDS in the concentration range 10 - 30 wt. % were used throughout the study with 20 wt. % as the main system of interest. All solutions were freshly prepared with distilled water so as to minimise deviations due to hydrolysis.

1-dodecanol was purchased from Sigma Aldrich (> 98 %). Its melting point is approximately 24 °C so it exhibits extremely low aqueous solubility at room temperature. 1-dodecanol was present in a 5 wt. % concentration in the surfactant solutions.

2.3.2 Methods

2.3.2.1 Differential scanning calorimetry

Thermograms of the SDS solutions were obtained through use of a Sentaram micro DSC with distilled water as the reference sample. For each sample run, approximately 70 mg of the sample and reference were measured into their respective cells and placed into the DSC furnace chamber. The instrument measures the difference in heat flow between the two respective cells (Thomas, 2005). Each experiment was repeated a minimum of two times.

The lowest available cooling and subsequent heating scan rate of 0.1 °C/min was utilised throughout the non-isothermal DSC studies. The upper temperature was in the range 30 °C to 40 °C with the lower limit being –5 °C. A 20-minute holding time was applied at the maximum and minimum temperature points.

Having investigated the crystallisation kinetics of SDS aqueous systems, the addition of 1-dodecanol into the system was then studied via DSC. Due to its low solubility, 1-dodecanol was added directly into the DSC furnace cell. DSC thermograms of SDS, 1-dodecanol and SDS + 1-dodecanol aqueous systems were compared. Shifts in crystallisation and melting temperatures were recorded, with the results being discussed in terms of the characteristics of the alcohol surfactant system. The scan rate used for these experiments was also 0.1 °C/min. Thermal analysis of the data was performed using the Calisto processing software package.

2.3.2.2 Optical microscopy

An optical microscope, model Leica Z16 APOA, was coupled with a Linkam LTS120 Peltier stage and used to observe the crystallisation phase transition of a 3 g sample of a 20 wt. % SDS solution in the absence and presence of 1- dodecanol addition. A 1 °C/min cooling rate was used. Limitations in the microscope and Peltier stage equipment meant that it was not possible to venture below this cooling rate with this method. Despite the differences in experimental cooling rates between DSC and optical microscopy measurements, comparisons could still be made between the two techniques as to the overall effect of 1-dodecanol addition. A petri dish was used to contain the samples. After calibration, the image sequence was optimised using Image J. Microscope settings were selected using the software platform Micro-Manager and are captured in Appendix A.

2.3.2.3 X-ray diffraction (XRD)

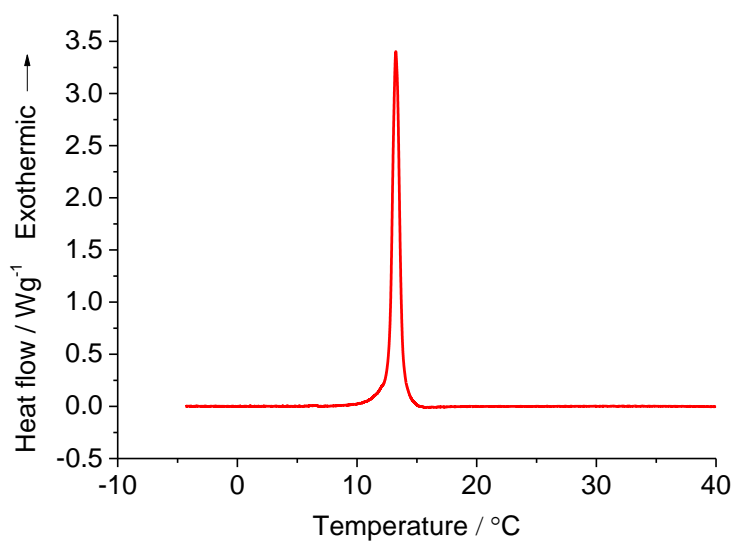
A powder diffractometer, model Siemens D5000, was used in combination with a cyropad to obtain diffraction patterns for 20 wt. % SDS solutions upon crystallisation at various low temperatures, namely 0 °C and –20 °C. 1.5 mm borosilcate glass capillaries were filled with the respective solution to a level of approximately 4 cm. The capillary was then attached to the base and aligned before being inserted into the diffractometer. Subsequently, the capillary solution was cooled consecutively to the selected temperatures at the maximum cooling rate of 8 °C/min. At each temperature, a hold time of 15 minutes was programmed prior to measurement. A step of 0.015° and a step time of 0.4 seconds were used. 2θ was investigated between 5° and 30°. The resulting diffraction pattern was viewed using EVA software.

2.4 Results and discussion

Characteristics of SDS and SDS + 1-dodecanol systems at low temperatures were investigated. Particular areas of interest include the variation of crystallisation temperature with concentration and the nature of the crystals.

2.4.1 Effect of concentration on crystallisation temperature

(a)



(b)

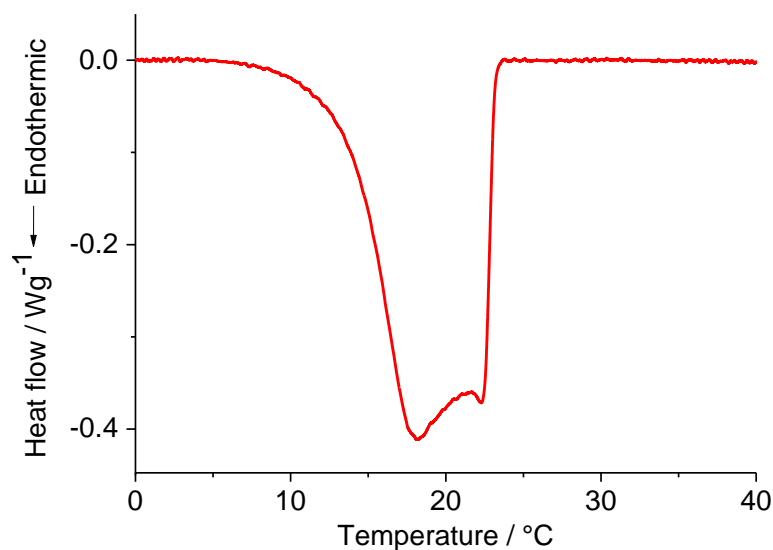


Figure 2.1. DSC (a) cooling thermogram and (b) heating thermogram for a 20 wt. % SDS solution attained at a scan rate of 0.1 °C/min.

Figures 2.1(a) and (b) display typical DSC thermograms for a 20 wt. % SDS solution when exposed to a cooling and a subsequent heating cycle. Upon cooling one exothermic peak is observed for all concentrations, with the peak maxima relating to the crystallisation temperature and the area to the enthalpy in J/g. With regards to the heating cycle, a broad peak is typically observed at all concentrations.

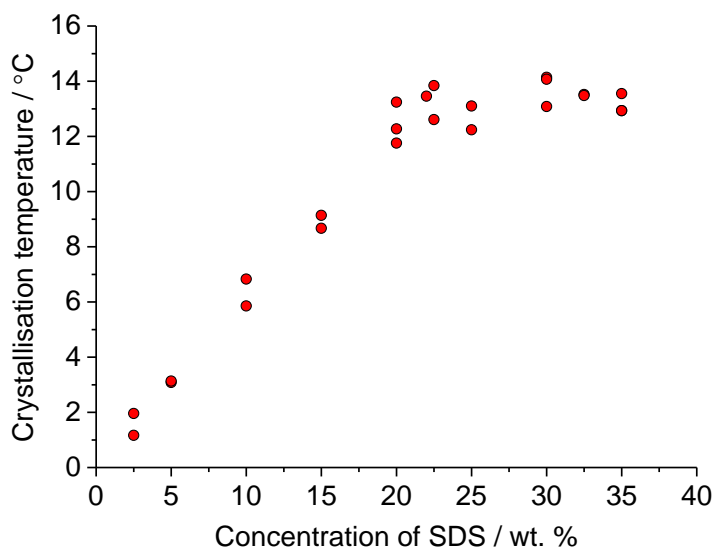
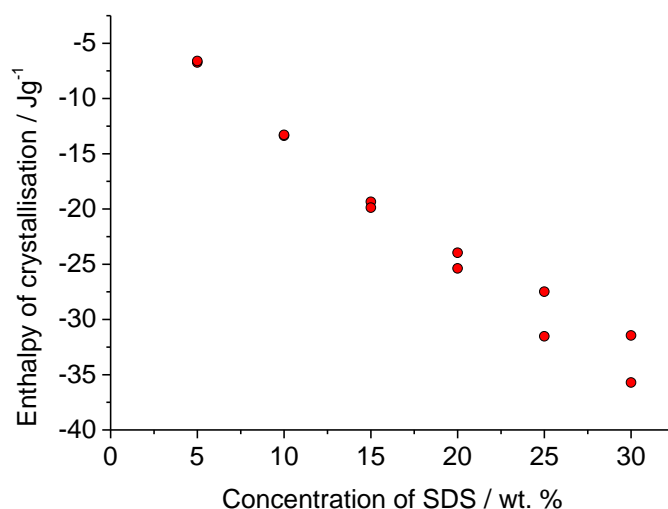


Figure 2.2. Plot showing the crystallisation temperatures of various SDS aqueous solutions versus the concentration of SDS.

Figure 2.2 displays the variation in crystallisation temperature with SDS aqueous concentration. Up to 20 wt. % - 23 wt. %, a linear correlation between SDS concentration and crystallisation temperature is attained. Beyond this concentration range, the variability in crystallisation temperature is minimal. The temperature that crystallisation can occur in such a system can be affected by both kinetic and thermodynamic effects. Melting transitions are largely driven by an entropic thermodynamic effect whereas nucleation and crystal growth are more likely dependent on kinetic effects. The rate of the crystallisation, and hence the temperature of phase transition, is governed by the nucleation and subsequent crystal growth (Vedantam and Ranade, 2013). During nucleation surrounding surfactant molecules collide and form clusters. If these clusters exceed a critical radius, they can then grow into crystals. When the SDS concentration

is below 20 - 23 wt. % the limitation factor is likely the collision frequency. As the concentration is increased the collision frequency increases, and hence the nucleation time is reduced. However, beyond a 20 - 23 wt. % concentration the crystallisation temperature remains approximately constant, indicating that crystallisation only occurs below 15 °C. This is known as the Krafft temperature (Vautier-Giongo and Bales, 2003). Beyond this temperature, the solution can form micellar aggregates eliminating any possibility for crystallisation.

(a)



(b)

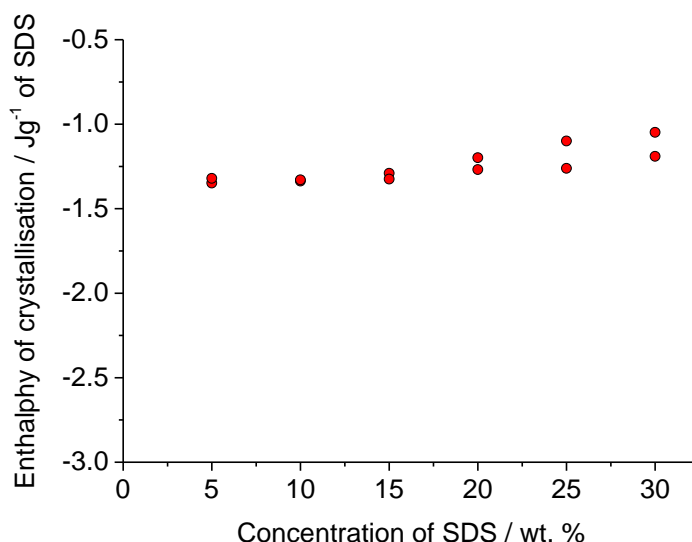


Figure 2.3. Plots of SDS concentration against the enthalpy of crystallisation in (a) J/g of surfactant solution and in (b) J/g of SDS for the various surfactant solutions.

Figures 2.3(a) and (b) display plots for the enthalpy in J/g of solution and in J/g of SDS for the various aqueous systems. As deduced from Figure 2.3(a), the enthalpy of the overall system increases with concentration of surfactant. This is attributed to the amount of SDS per gram of solution. This is further evident from the plot in Figure 2.3(b) where the enthalpy remains approximately constant.

2.4.2 Composition of the crystals

The crystallisation of a 20 wt. % SDS solution was further investigated by XRD, which enables one to infer information about the crystal structure. In Figure 2.4, the black line and red line correspond to XRD patterns obtained at the sample temperatures of 0 °C and –20 °C respectively.

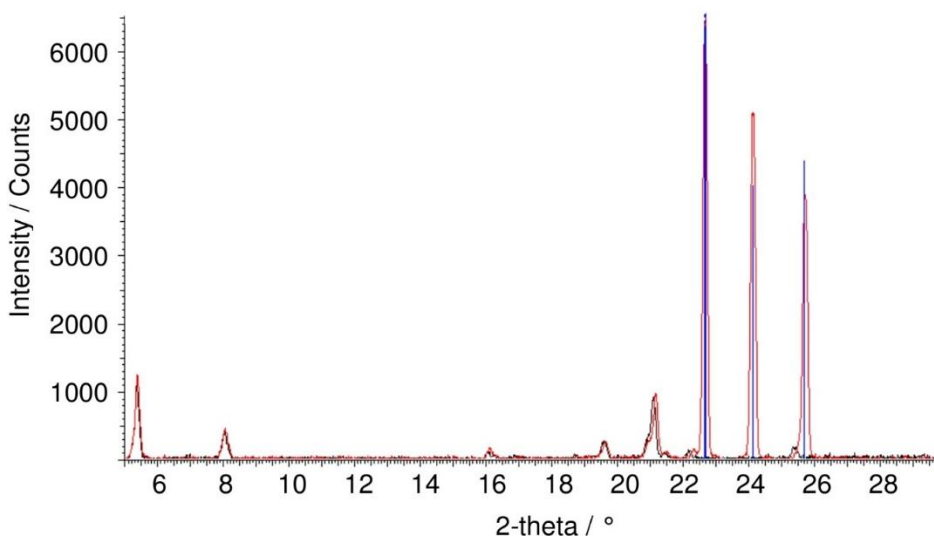


Figure 2.4. X-ray diffraction pattern for a 20 wt. % SDS solution taken at hold temperatures of 0 °C (black line) and –20 °C (red line) with the blue lines highlighting those peaks that can be matched to ice.

The powder diffraction patterns at the two respective temperatures overlap with each other, with the exception of three additional peaks in the –20 °C pattern. These additional peaks are matched to ice and assigned the blue lines in Figure 2.4 (Malkin *et al.*, 2012). Hence, it is

possible to deduce that ice does not appear at 0 °C but it is present when the sample temperature is lowered to –20 °C. DSC measurements agree with this finding since no ice formation is evident when the lower temperature limit is –5 °C. However, if the cooling cycle is taken to lower temperatures, the DSC thermogram displays a peak for water freezing at –10 °C. Aside from the ice peaks the remaining peaks in the two XRD patterns match, indicating there is no structural change between the two SDS crystal structures.

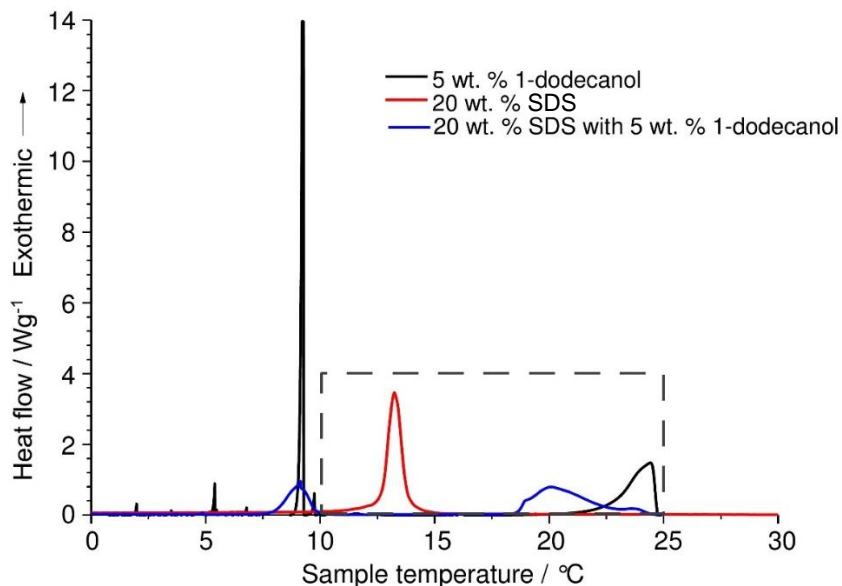
2.4.3 Dodecanol addition

Having discussed non-isothermal SDS crystallisation, the presence of its alcohol precursor on the kinetics will now be considered. Remnant alcohol precursors may be present in some detergent products as a result of incomplete conversion to their respective sulfated surfactants. Although the percentage of this impurity will be minimal, the 1-dodecanol used in this investigation was set at a 5 wt. % concentration as a result of practical laboratory limitations. Despite being at a slightly higher concentration than found in industry, the behaviour in this system is expected to be indicative of the influence of 1-dodecanol.

It is possible to determine the change in crystallisation and subsequent melting temperatures upon addition of 1-dodecanol through the appearance of any peak shifting in the DSC thermogram. From the red line in Figure 2.5 it can be deduced that SDS crystallises at 13 °C when no other excipients, except water, are present. The black line is for an aqueous solution of 1-dodecanol in the absence of SDS. A crystallisation temperature of 24.4 °C and a lower peak at 9.2 °C is observed for this solution (Zuo *et al.*, 2011). The peak at 24.4 °C has a distinctly different shape to other peaks in the same region which can be attributed to the order of the phase transition. The peak at 24.4 °C can be related to the crystallisation of the alcohol alone (Zuo *et al.*, 2011), but the lower peak must relate to an alcohol-water phase, since these are the only two components present. Finally, the blue line is for a mixed SDS + 1-dodecanol

aqueous system. In the mixed system there are also peaks below 10 °C that may also correspond to the water-alcohol phase for in the 1-dodecanol aqueous system.

(a)



(b)

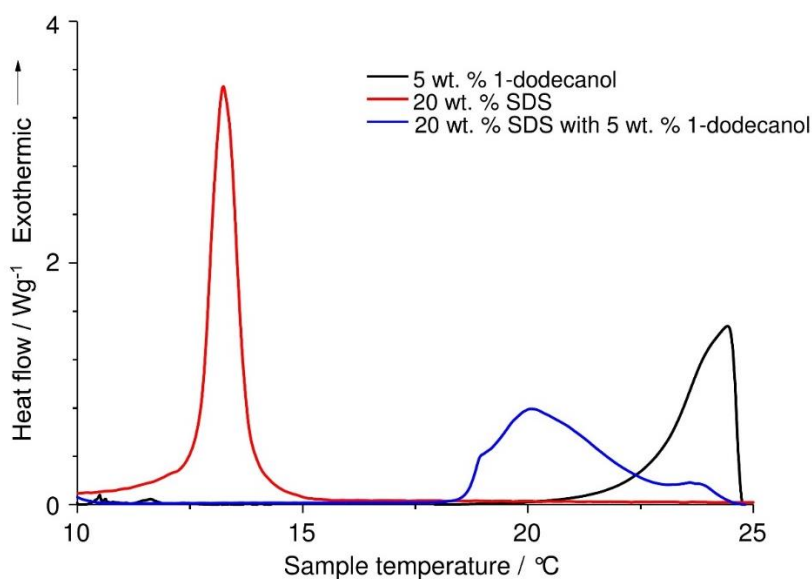


Figure 2.5. (a) DSC thermograms for SDS, 1-dodecanol and mixed SDS + 1-dodecanol aqueous systems; (b) is an enlarged image of the area contained within the box in (a).

At the higher temperature end, the SDS + 1-dodecanol system displays two overlapping peaks located at 20.2 °C and 23.5 °C. The hypothesis is that 1-dodecanol acts as a seed for the

crystallisation of SDS. Seeds tend to be effective if they are of the correct size and have a similar chemical composition or structure to the sample to be crystallised *in situ*, as is the case of SDS with 1-dodecanol (Cacciuto *et al.*, 2004). The existence of two peaks may likely be due to a SDS + alcohol polymorph and the subsequent higher peak can be attributed to excess 1-dodecanol. Repeated cycles eliminate the additional higher peak with the remaining overall peak shifting to the right. Upon repeat of the cycle the system has more time to pack into an optimum structure so as to incorporate the added 1-dodecanol in a co-crystal formation. Co-crystal formation is attributed to the similar structural properties between the two components.

Although the focus of this paper has been on the crystallisation phase transitions of SDS and SDS + 1-dodecanol systems it is important to include the effect of 1-dodecanol on the melting transition, as acquired by DSC studies. Figure 2.6 displays the melting transition for a 5 wt. % aqueous solution of 1-dodecanol (black line), 20 wt. % SDS (red line) and a combined SDS + 1-dodecanol system (blue line) as they are exposed to a heating cycle from -5°C at a consistent scan rate of $0.1^{\circ}\text{C}/\text{min}$.

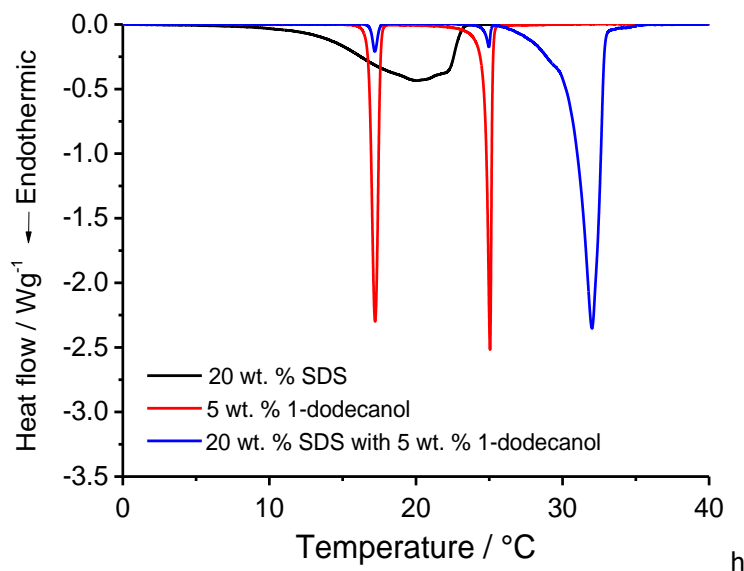


Figure 2.6. DSC thermograms for the melting transitions that occur for an aqueous solution of 20 wt. % SDS (black line), 5 wt. % 1-dodecanol (red line) and a mixed alcohol + SDS system (blue line) on heating from -5°C to 40°C at a scan rate of $0.1^{\circ}\text{C}/\text{min}$.

Aqueous 1-dodecanol exhibits two sharp melting peaks upon heating. From data previously reported (Zuo *et al.*, 2011), it is known that a pure 1-dodecanol system exhibits only one melting peak at 17.6 °C, as matched to one of the peaks in Figure 2.6. Appearing at approximately 25 °C, the other peak for the aqueous 1-dodecanol system is attributed to a 1-dodecanol + water phase since these are the only components present. The two peaks from the aqueous 1-dodecanol system demonstrate a sharp overlap with two from the mixed alcohol + SDS system. Hence, these peaks in the mixed system can be assigned to the same phases. The remaining peak in the SDS + 1-dodecanol system has a maximum in excess of 30 °C. It can be concluded that the SDS aqueous system melts over a wider and lower temperature range when 1-dodecanol is not present. In addition to facilitating the crystallisation of SDS at a higher temperature, 1-dodecanol also stabilises the crystal, enabling it to remain in crystalline form to a higher temperature point.

2.4.4 1-dodecanol SDS crystallisation trigger mechanism

From DSC studies, it is inferred that the 1-dodecanol facilitates the crystallisation of SDS. It has been hypothesised that such a phenomenon is due to the low solubility of 1-dodecanol. Short chain alcohols have been reported to insert into, and stabilise, micelles (Nakayama *et al.*, 1966) . However, 1-dodecanol is immiscible in an SDS aqueous solution. Insoluble globules are only observed when 1-dodecanol is added to the surfactant solution, suggesting the composition of these features is 1-dodecanol. These insoluble 1-dodecanol globules can act as seeds for crystallisation due to the similarity in the structure between 1-dodecanol and SDS. The size of these globules (1 -2 mm) is similar to impurities such as other remnant alcohols or foreign matter that may reside in the final dish liquid product. Through optical microscopy, it is possible to further determine the mechanism by which this occurs, as in the image sequence provided in Figure 2.7.

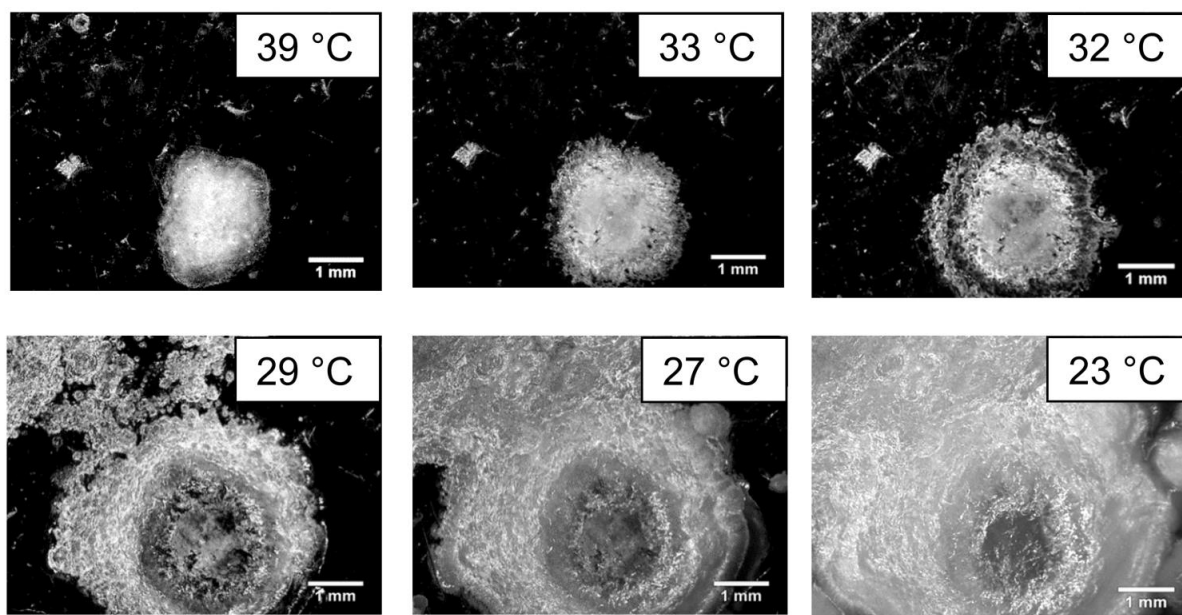


Figure 2.7. Optical images for a 20 wt. % SDS + 5 wt. % 1-dodecanol aqueous solution upon cooling, taken at a selection of temperatures.

On cooling the mixed system, crystallisation of the globules themselves is initially observed with subsequent crystallisation of the surrounding SDS. These images clearly demonstrate the seeding capability of 1-dodecanol on SDS solution. Further experiments are also in agreement. The crystallisation appearing in the top left of the images is a result of crystallisation surrounding another globule. On further cooling, complete crystallisation of the system is observed at approximately 23 °C. When examining 20 wt. % SDS systems without the addition of 1-dodecanol and at the same cooling rate and system volume, crystallisation is not observed until 7 °C with complete crystallisation occurring at 0 °C.

2.5 Conclusions

The crystallisation of aqueous SDS systems upon cooling was observed via DSC and optical microscopy. Results indicate the crystallisation temperature is dependent on SDS concentration, specifically for concentrations below 20 wt. % where a linear increase in crystallisation temperature with concentration is observed. This linear relationship is likely to

be due to an increased nucleation rate. At higher SDS concentrations, crystallisation occurs immediately as the Krafft temperature is reached. XRD studies further support the existence of crystallisation of the SDS system and suggests ice is formed in this anionic surfactant system upon further cooling of the system below 0 °C.

Knowledge of the effect of 1-dodecanol on SDS crystallisation provides understanding for the potential of unsulfonated material for inducing crystallisation. Due to the seeding potential of 1-dodecanol, shifts in the phase transition temperature are observed during both the cooling and subsequent melting process.

Understanding the phase transitional behaviour in SDS has allowed for an increased understanding in one of the most widely used surfactants in the detergent industry. For the first time, the effect of its alcohol precursor is demonstrated to have a profound effect on the crystallisation and subsequent melting in such systems. This is of specific industry importance when there is a risk of some remnant alcohol precursor remaining in a surfactant system that could have a negative effect on stability.

2.6 References

- Amante, J. C., Scamehorn, J. F. & Harwell, J. H. 1991. Precipitation of mixtures of anionic and cationic surfactants. 2. Effect of surfactant structure, temperature and pH. *Journal of Colloid and Interface Science*, 144, 243-253.
- Cacciuto, A., Auer, S. & Frenkel, D. 2004. Onset of heterogeneous crystal nucleation in colloidal suspensions. *Nature*, 428, 404-406.
- Chantraine, F., Viana, M., Brielles, N., Mondain-Monval, O., Pouget, C., Branlard, P., Rubinstenn, G. & Chulia, D. 2006. Parametric study of surfactant effect on mechanical and dissolution properties of detergent tablets. *Journal of Surfactants and Detergents*, 9, 267-277.

- Chantraine, F., Viana, M., Cazalbou, S., Brielles, N., Mondain-Monval, O., Pouget, C., Branlard, P., Rubinstenn, G. & Chulia, D. 2007. From compressibility to structural investigation of sodium dodecyl sulphate - Part 2: A singular behavior under pressure. *Powder Technology*, 177, 41-50.
- De Anda, J. C., Wang, X. Z., Lai, X. & Roberts, K. J. 2005. Classifying organic crystals via in-process image analysis and the use of monitoring charts to follow polymorphic and morphological changes. *Journal of Process Control*, 15, 785-797.
- Dierker, M. & Schafer, H. J. 2010. Surfactants from oleic, erucic and petroselinic acid: Synthesis and properties. *European Journal of Lipid Science and Technology*, 112, 122-136.
- Forland, G. M., Samseth, J., Gjerde, M. I., Hoiland, H., Jensen, A. O. & Mortensen, K. 1998. Influence of alcohol on the behavior of sodium dodecylsulfate micelles. *Journal of Colloid and Interface Science*, 203, 328-334.
- Gu, T. R. & Sjoblom, J. 1992. Surfactant structure and its relation to the Krafft point, cloud point and micellization - some empirical relationships. *Colloids and Surfaces*, 64, 39-46.
- Hirata, H. & Iimura, N. 1998. The surfactant molecular complex formation (III): Systems of anionic surfactants and various phenols and some other materials. *Journal of Colloid and Interface Science*, 199, 111-122.
- Kralchevsky, P. A., Danov, K. D., Kolev, V. L., Broze, G. & Mehreteab, A. 2003. Effect of nonionic admixtures on the adsorption of ionic surfactants at fluid interfaces. 1. Sodium dodecyl sulfate and dodecanol. *Langmuir*, 19, 5004-5018.
- Kume, G., Gallotti, M. & Nunes, G. 2008. Review on anionic/cationic surfactant mixtures. *Journal of Surfactants and Detergents*, 11, 1-11.
- Lai, K. Y. 1996. *Liquid Detergents*, CRC Press.

- Malkin, T. L., Murray, B. J., Brukhno, A. V., Anwar, J. & Salzmann, C. G. 2012. Structure of ice crystallized from supercooled water. *Proceedings of the National Academy of Sciences*, 109, 1041-1045.
- Mandavi, R., Sar, S. K. Rathore, N. 2008. Critical micelle concentration of surfactant, mixed-surfactant and polymer by different method at room temperature and its importance. *Oriental Journal of Chemistry*, 24, 559-564.
- Markets, M. A. 2016. *Surfactants Market by Type, Substrate, Application - Global Forecast to 2021* [Online]. Available: <http://www.marketsandmarkets.com/Market-Reports/biosurfactants-market-493.html> [Accessed 03/01/2018].
- Motin, M. A., Mia, M. a. H. & Islam, A. K. M. N. 2015. Thermodynamic properties of Sodium Dodecyl Sulfate aqueous solutions with Methanol, Ethanol, n-Propanol and iso-Propanol at different temperatures. *Journal of Saudi Chemical Society*, 19, 172-180.
- Nakayama, H., Shinoda, K. & Hutchins.E 1966. Effect of added alcohols on solubility and Krafft point of sodium dodecyl sulfate. *Journal of Physical Chemistry*, 70, 3502-3504.
- Shiau, B. J., Harwell, J. H. & Scamehorn, J. F. 1994. Precipitation of mixtures of anionic and cationic surfactants. 3. Effect of added nonionic surfactant. *Journal of Colloid and Interface Science*, 167, 332-345.
- Smith, L. A., Duncan, A., Thomson, G. B., Roberts, K. J., Machin, D. & Mcleod, G. 2004. Crystallisation of sodium dodecyl sulphate from aqueous solution: phase identification, crystal morphology, surface chemistry and kinetic interface roughening. *Journal of Crystal Growth*, 263, 480-490.
- Smith, L. A., Roberts, K. J., Machin, D. & Mcleod, G. 2001. An examination of the solution phase and nucleation properties of sodium, potassium and rubidium dodecyl sulphates. *Journal of Crystal Growth*, 226, 158-167.

- Stellner, K. L., Amante, J. C., Scamehorn, J. F. & Harwell, J. H. 1988. Precipitation phenomena in mixtures of anionic and cationic surfactants in aqueous-solutions. *Journal of Colloid and Interface Science*, 123, 186-200.
- Stellner, K. L. & Scamehorn, J. F. 1986. Surfactant precipitation in aqueous-solutions containing mixtures of anionic and nonionic surfactants. *Journal of the American Oil Chemists' Society*, 63, 566-574.
- Stellner, K. L. & Scamehorn, J. F. 1989. Hardness tolerance of anionic surfactant solutions. 2. Effect of added nonionic surfactant. *Langmuir*, 5, 77-84.
- Thomas, L. C. 2005. An introduction to the techniques of differential scanning calorimetry (DSC) and modulated DSC. *Publicationes de la Universidade da Coruna, Coruna*, 9-25.
- Tiller, W. A. 1991. *The Science of Crystallization: Macroscopic Phenomena and Defect Generation*, Cambridge University Press.
- Vautier-Giongo, C. & Bales, B. L. 2003. Estimate of the ionization degree of ionic micelles based on Krafft temperature measurements. *Journal of Physical Chemistry B*, 107, 5398-5403.
- Vedantam, S. & Ranade, V. V. 2013. Crystallization: Key thermodynamic, kinetic and hydrodynamic aspects. *Sadhana-Academy Proceedings in Engineering Sciences*, 38, 1287-1337.
- Wu, F.-G., Wang, N.-N., Zhang, Q.-G., Sun, S.-F. & Yu, Z.-W. 2012. Crystallization from the micellar phase of imidazolium-based cationic surfactants. *Journal of Colloid and Interface Science*, 374, 197-205.
- Zuo, J., Li, W. & Weng, L. 2011. Thermal performance of caprylic acid/1-dodecanol eutectic mixture as phase change material (PCM). *Energy and Buildings*, 43, 207-210.

CHAPTER 3

NUCLEAR MAGNETIC RESONANCE AND SMALL-ANGLE X-RAY SCATTERING STUDIES OF MIXED SODIUM DODECYL SULFATE AND N,N- DIMETHYLDODECYLAMINE N-OXIDE AQUEOUS SYSTEMS PERFORMED AT LOW TEMPERATURES

Discussions contained in this chapter have been published within: Summerton, E., Hollamby, M. J., Le Duff, C. S., Thompson, E. S., Snow, T., Smith, A. J., Bettiol, J., Jones, C., Bakalis S. and Britton, M. M. 2019. Nuclear magnetic resonance and small-angle X-ray scattering studies of mixed sodium dodecyl sulfate and N,N-dimethyldodecylamine N-oxide performed at low temperatures, *Journal of Colloid and Interface Science*, **535**, p. 1-7.

3.1 Abstract

With the rising global demand for homecare products, understanding the factors that influence formulation stability is of increasing importance. At low and sub-zero temperatures ($< 10\text{ }^{\circ}\text{C}$) there is a risk of surfactant crystallisation in dish liquid products, resulting in a turbid solution that fails appearance criteria. To enable industry to build more robust formulations, it is important to understand the underlying chemistry of the crystallisation process. Here, a model system containing anionic (sodium dodecyl sulfate, SDS) and amphoteric (N,N-dimethyldodecylamine N-oxide, DDAO) surfactants, at concentrations typical of dish liquid products, is studied. Variable temperature ^1H nuclear magnetic resonance (NMR) spectroscopy and small-angle X-ray scattering (SAXS) are used to probe the compositional and structural properties of this system, as a function of pH. On cooling, at pH 9, a mixture of hydrated crystals, predominately composed of SDS, and micelles containing both surfactants, have been observed prior to complete freezing. At pH 2, both surfactants appear to undergo a simultaneous phase transition, resulting in the removal of micelles and the formation of hydrated crystals of mixed composition.

3.2 Introduction

Home and personal care products are used on a daily basis by consumers across the globe. Consequently, they are exposed to a variety of different environmental climates that can cause problems with product stability. In particular, low temperatures cause stability issues for liquid detergent products that are prone to surfactant crystallisation. While crystallisation is reversible, it is considered a product failure. Such failures can occur at any point during the product lifecycle, including transport and shelf life stages. To improve the formulation stability and to

minimise the failure rate, it is important to build an improved understanding of surfactant crystallisation in these systems.

Common liquid detergents typically contain a mixture of anionic and amphoteric surfactants in an aqueous formulation (Kume *et al.*, 2008) to optimise soil removal and foaming characteristics. Anionic surfactants are the major surfactant component and are cheap, efficient at removing soils and are largely responsible for the high foaming characteristics of the detergent (Holmberg *et al.*, 2003). The most commonly used anionic surfactant in liquid detergents is sodium dodecyl sulfate (SDS) (Dierker and Schafer, 2010). While amphoteric surfactants comprise the minor surfactant component, they also play an important role by increasing the tolerance of the detergent to increased water hardness (Stellner and Scamehorn, 1989). Common amphoteric surfactants found in liquid detergents are those based around the amine oxide functional group. One example of this is N,N-dimethyldodecylamine N-oxide (DDAO). At $\text{pH} < 5$, DDAO is protonated and behaves as a cationic surfactant, whereas at $\text{pH} > 5$ it is non-ionic (Rathman and Christian, 1990; Herrmann, 1962). In hand-dishwashing detergent products, commonly referred to as dish liquid, the typical pH is sufficiently high that amine oxide-based surfactants exhibit non-ionic surfactant-like behaviour.

In mixed micelles containing SDS and DDAO, the surfactant headgroups strongly interact, leading to a reduction in the critical micelle concentration, CMC, versus that of either surfactant alone (Goloub *et al.*, 2000). Ion pairs form between the two surfactants which stabilise the mixed micelles through a shielding of the electrostatic repulsion between the SDS headgroups by those of DDAO (Goloub *et al.*, 2000). Moreover, it is believed that the presence of SDS causes DDAO protonation to occur at a higher pH than that of pure DDAO (Soontravanich *et al.*, 2008; Goloub *et al.*, 2000). Combining these surfactants is also expected to lower the Krafft temperature, T_K , in comparison to a pure SDS solution. This reduction in T_K can be attributed

to the lower CMC (Fan *et al.*, 1988) of the system and the formation of non-ideal mixed micelles (Scamehorn, 1986). With DDAO present in the solution there is an increased tendency for micellisation, resulting in a decrease in the concentration of SDS monomers and unbound counterions and consequently a decreased tendency for crystallisation.

Studies into the crystallisation of mixed surfactant systems have been carried out to some extent, but there remains limited literature reporting the nature of the precipitate (Stellner and Scamehorn, 1989; Soontravanich, 2007). For example, HPLC was used to determine the composition of the precipitate formed when the non-ionic surfactant nonylphenol ethoxylate (NPE) was added to SDS and found that NPE was not present in the precipitate (Stellner and Scamehorn, 1989). Furthermore, the composition of the precipitant from a bi-anionic surfactant system containing the surfactants SDS and sodium octylbenzene sulfonate (SOBS) has also been investigated via X-ray diffraction (XRD) (Soontravanich, 2007). In the mixed sample, two sets of peaks were observed with 2θ values corresponding to pure SDS and SOBS crystals, suggesting that mixed crystals were not formed. Aside from these studies, there are few reports regarding the composition of the precipitant formed from mixed surfactant systems below T_K .

Two techniques which can provide further compositional and structural insight into the crystallisation of mixed surfactant systems are temperature-resolved nuclear magnetic resonance (NMR) and small-angle X-ray scattering (SAXS). While there are few NMR studies of surfactant crystallisation from micelles, it has been used to follow the nucleation and freezing of individual components during the crystallisation of some emulsions (Hindmarsh *et al.*, 2004) and food materials (Gallo *et al.*, 2003; Kolz *et al.*, 2010) by monitoring the change in individual NMR signals as a function of time. On the other hand, several studies have used SAXS or small-angle neutron scattering (SANS) to provide structural insight into various phase transitions, (Hollamby, 2013; Tabor *et al.*, 2009; Wu *et al.*, 2010) and to probe the structure and

composition of micelles in dilute systems of both pure and mixed SDS and DDAO (Kakitani *et al.*, 1995; Hammouda, 2013).

In this paper, NMR has been used to observe the crystallisation of a mixed micelle system, comprising SDS and DDAO surfactants, in water. NMR parameters for the two surfactants were monitored as the solution was cooled from 25 °C to –3 °C, at pH 9. By comparing the change in relative peak intensity for the two surfactants, it was possible to identify the crystal composition formed in this mixed micelle system. SAXS was used to probe the structure of the systems at room temperature and at 0 °C. Furthermore, a difference in the behaviour was observed upon lowering the pH of the system. By combining results from these complimentary techniques, it has been possible to build a clearer picture of both the structure and composition of the phases that form in these systems under both pH environments.

3.3 Materials and methods

3.3.1 Materials

Surfactant solutions were prepared from DDAO (Sigma Aldrich, 30 wt. % in water) and SDS (Fisher Scientific, 97.5 %) which were used without further purification. Binary surfactant solutions were prepared with 20 wt. % SDS and 3 wt. % DDAO in distilled water, for SAXS and WAXS measurements, and in D₂O (Sigma Aldrich, 99.9 %), for NMR measurements. A correction has been made to account for the density difference between D₂O and H₂O so that the molar surfactant concentration remains the same. A pure solution of 20 wt. % SDS solution was also prepared. Solutions were stirred for 15 minutes at ambient temperature and then left for 24 hours. The pH of both the 20 wt. % SDS + 3 wt. % DDAO solution and 20 wt. % SDS solution were approximately pH 9. A second binary solution of 20 wt. % SDS + 3 wt. % DDAO solution was also prepared at pH 2 using a solution of 35 wt. % DCl in D₂O, for NMR

measurements, or 0.5 M HCl in H₂O, for SAXS measurements. The pH was measured using a Meter Toledo pH meter.

3.3.2 Methods

3.3.2.1 Variable temperature NMR

NMR measurements were performed using Wilmad Precision 5 mm NMR tubes and a Bruker AVANCE spectrometer equipped with a 9.4 T vertical bore magnet, operating at a ¹H resonance frequency of 400.13 MHz and fitted with a 5 mm BBO probe. Sample temperature was controlled using BVT3200 and low temperatures were obtained using evaporating liquid N₂ and a heater inside the probe. Samples were allowed to equilibrate at each temperature for a minimum of 30 minutes. Spectra at each temperature were acquired using a 90° pulse sequence, [90°-acq]. A spectral width of 8 kHz was used and 32k complex data points were acquired. 64 signal averages were acquired with a repetition time of 15 s. The repetition time used was greater than 5*T*₁ for the protons in the SDS and DDAO surfactants. *T*₁ values are provided in Appendix B.

At pH 9, ¹H NMR spectra were acquired at the following temperatures: 25 °C, 20 °C, 15 °C, 13 °C, 10 °C, 5 °C, 0 °C and –3 °C. Under a pH 2 environment ¹H NMR spectra were acquired at 7.5 °C, 5 °C, 0 °C, –3 °C, –5 °C, –8 °C and –10 °C, corresponding to the range over which the phase transition occurs. Spectra were processed using TopSpin (v.3.5). The NMR spectra for the individual SDS and DDAO systems, at pH 9, were acquired at 25 °C and the respective ¹H NMR signals assigned to the proton environments of the two surfactants (see Appendix B). H₁ (SDS) was set at 3.7 ppm at 25 °C, determined from SDS in DMSO-d₆ (SDBS, 2018), and remaining spectra were adjusted with respect to this. The NMR signals for the SDS and DDAO surfactants were determined using the peak intensities for the H₁ and H_a protons, respectively.

Changes in intensity were plotted in Origin (v.9.0) with error bars determined from repeated measurements.

3.3.2.2 Small angle X-ray scattering

Small angle scattering (SAXS) data was obtained using the I22 beamline at Diamond Light Source. Samples were loaded into 1.8 mm (internal diameter) and 2.0 mm (external diameter) polycarbonate capillaries and mounted in the beam within the Linkam DSC600 capillary stage, which also provided temperature control (at 24 °C and 0 °C, with an applied cooling rate of 19 °C/min). A 12.3989 keV ($\lambda = 0.099987$ nm) beam was used with a sample-detector distance of 6702.56 mm, providing a detectable Q -range on the SAXS detector of order $0.02 - 2.5 \text{ nm}^{-1}$ and $1.51 - 60.57 \text{ nm}^{-1}$ on the WAXS detector. Data processing was performed using the DAWN package (van der Veen, 2015; Filik *et al.*, 2017) and a set of pipelines developed at Diamond Light Source. Before processing, uncertainty estimates based on Poisson counting statistics were added to all measurement data, which were subsequently propagated through the image correction steps. Each raw background measurement was corrected for the following in order: masking pixels, time, incident beam flux, and transmission. Each sample file was corrected for the following in order: masking pixels, time, incident beam flux, transmission, background, thickness, and scaled to absolute units. The scaling factor for scaling to absolute units was determined using a calibrated glassy carbon sample (Zhang *et al.*, 2010). After this correction, the data was azimuthally averaged, with the resulting uncertainty assuming the largest of: 1) the propagated uncertainties, 2) the standard error of the mean for the data points comprising a bin, or 3) 1% of the mean intensity in the bin.

The data at 24 °C was analysed using the SASfit software package (Bressler *et al.*, 2015). There is some discussion in the literature concerning whether SDS micelles are oblate or prolate ellipsoids (Kakitani *et al.*, 1995; Bergstrom and Pedersen, 1999; Vass *et al.*, 2008; Garg *et al.*,

2005; Hammouda, 2013). The two options are difficult to distinguish using scattering techniques, but the prolate model is considered to be more appropriate in denser systems (Vass *et al.*, 2008). Several small-angle scattering studies, including one that focused on mixed micelles comprising SDS and DDAO (Kakitani *et al.*, 1995) have favoured the prolate shape. Consequently, a model comprising a delta distribution of charged core-shell prolate ellipsoids, as outlined in the supporting information, was used to analyse the data. A breakdown of the $S(Q)$ and $P(Q)$ contributions to the overall fit is shown in Appendix C, Figure C.1 and the analysis parameters are provided in Table C.1.

The data at 0 °C for both the pure SDS solution and the mixed SDS + DDAO system was also analysed using SASfit (Bressler *et al.*, 2015) in both cases using a simple model comprising contributions from one or more Bragg peak(s), the power law and the background scattering (see details in Appendix C). For the 20 wt. % SDS + 3 wt. % DDAO sample, an additional contribution of delta distribution of charged core-shell prolate ellipsoids was added, to account for the increased $I(Q)$ at high Q .

3.4 Results and discussion

Figure 3.1 displays a series of ^1H NMR spectra acquired from 25 °C to –3 °C, with an expansion of the region between 2.6 - 4.0 ppm, for the mixed SDS + DDAO system at pH 9. The change in peak intensity as a function of temperature for the protons H_1 (SDS) and H_a (DDAO) under this pH environment is presented in Figure 3.2.

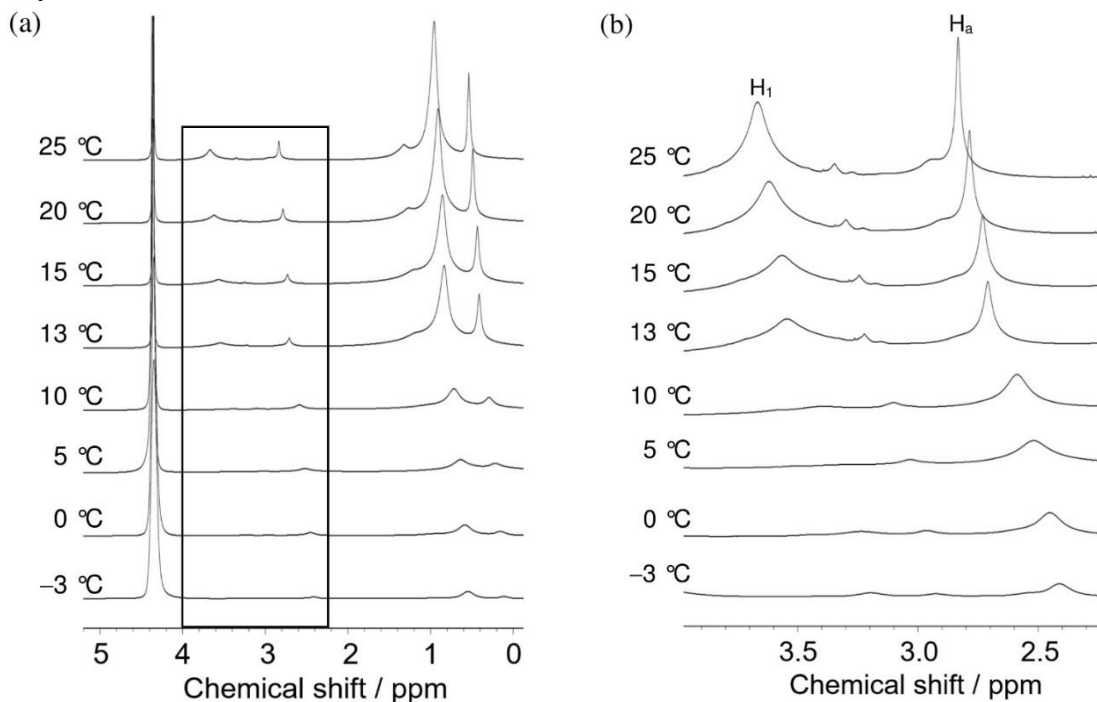


Figure 3.1. ^1H NMR spectra at 500 MHz of a 20 wt. % SDS + 3 wt. % DDAO system upon cooling at pH 9 across the chemical shift range (a) 0 - 5 ppm and (b) 2.3 - 4.0 ppm. The boxed area in (a) corresponds to the chemical shift range presented in (b). Proton resonance H_1 (SDS) is at 3.67 ppm and H_a (DDAO) is at 2.83 ppm (25 °C). A full spectral assignment can be found in Appendix B.

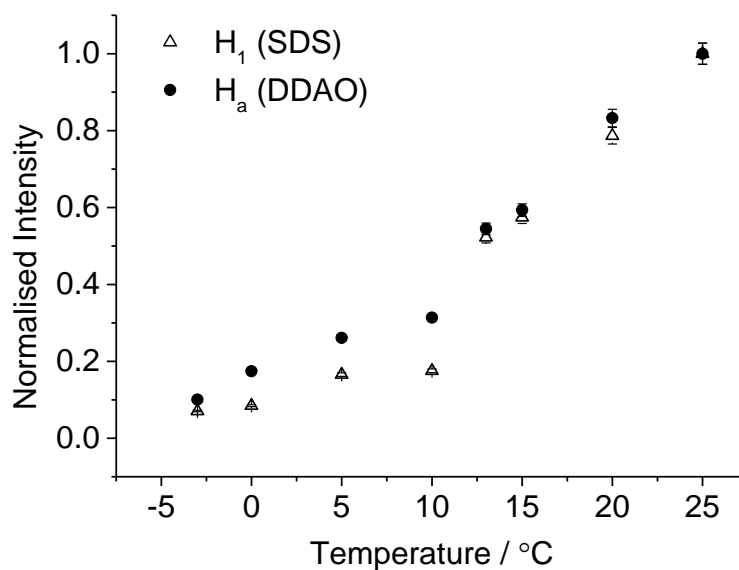


Figure 3.2. Plot of the peak intensity for H_1 (SDS) and H_a (DDAO) upon cooling at pH 9. The normalised intensities, for both peaks, include a slight baseline offset.

At pH 9, there is a significant drop in the peak intensity of the ^1H NMR signal of H_1 (SDS) between 10 °C and 13 °C. A similar trend is not observed for H_a in DDAO. Although the peak intensity of the H_a (DDAO) also exhibits a reduction in peak intensity, the drop between 10 °C and 13 °C is not as significant as H_1 (SDS). Instead, the intensity tends to decrease at consistent rate. In contrast, at pH 2, both surfactants display a sharp drop intensity between –5 °C and –3 °C (Figure 3.3). There is a change in the chemical shifts for the H_a (DDAO) peak, compared to the H_1 (SDS) peak at pH 2, because of the change in environment experienced by these protons when the headgroup is protonated (Vijay *et al.*, 2009; Gaikar *et al.*, 2008; Bhat and Gaikar, 1999). In addition, at pH 2, there are a greater number of peaks in the region of interest, attributed to interaction between the two charged surfactant species resulting in further proton environments.

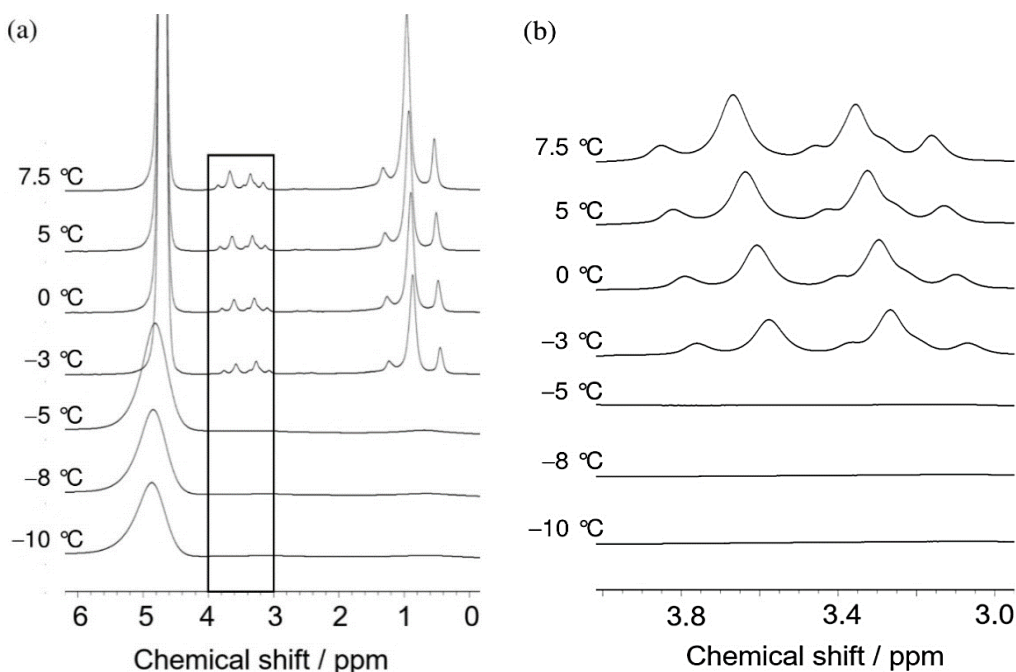


Figure 3.3. ^1H NMR spectra at 500 MHz of a 20 wt. % SDS + 3 wt. % DDAO system upon cooling at pH 2 across the chemical shift range (a) 0 - 6 ppm and (b) 3.0 - 4.0 ppm. The boxed area in (a) corresponds to the chemical shift range presented in (b). Proton resonance H_1 (SDS) is at 3.67 ppm and H_a (DDAO) is at 3.35 ppm (7.5 °C).

In Figure 3.4, the SAXS profiles, at 24 °C and 0 °C, for the mixed system are compared to the corresponding profiles for a pure SDS system. In Figure 3.4(a), a cropped Q -range is shown due to the high error in the low Q ($< 0.8 \text{ nm}^{-1}$) part of the data arising from the weak sample scattering versus background compounded by a high sample volume fraction. The data, collected at 24 °C, is characterised by two merged maxima resulting from a form factor, $P(Q)$ corresponding to the electron-dense micelle shell and a structure factor, $S(Q)$ arising from the Q micelle charge. The addition of DDAO causes a shift in the low Q maxima to a lower Q . Cooling both samples to 0 °C results in a notable change in the SAXS data, shown in Figure 3.4(b). For the 20 wt. % SDS sample, an increase in $I(Q)$ at low Q is observed followed by a region over which $I(Q) \propto Q^{-4}$ and a Bragg peak at $Q = 1.9 \text{ nm}^{-1}$. The 20 wt. % SDS + 3 wt. % DDAO data at 0 °C is similar to that for the pure SDS sample, except for an increased $I(Q)$ in the region $0.7 < Q < 2.5 \text{ nm}^{-1}$, which has a similar shape to that presented in Figure 3.4(a).

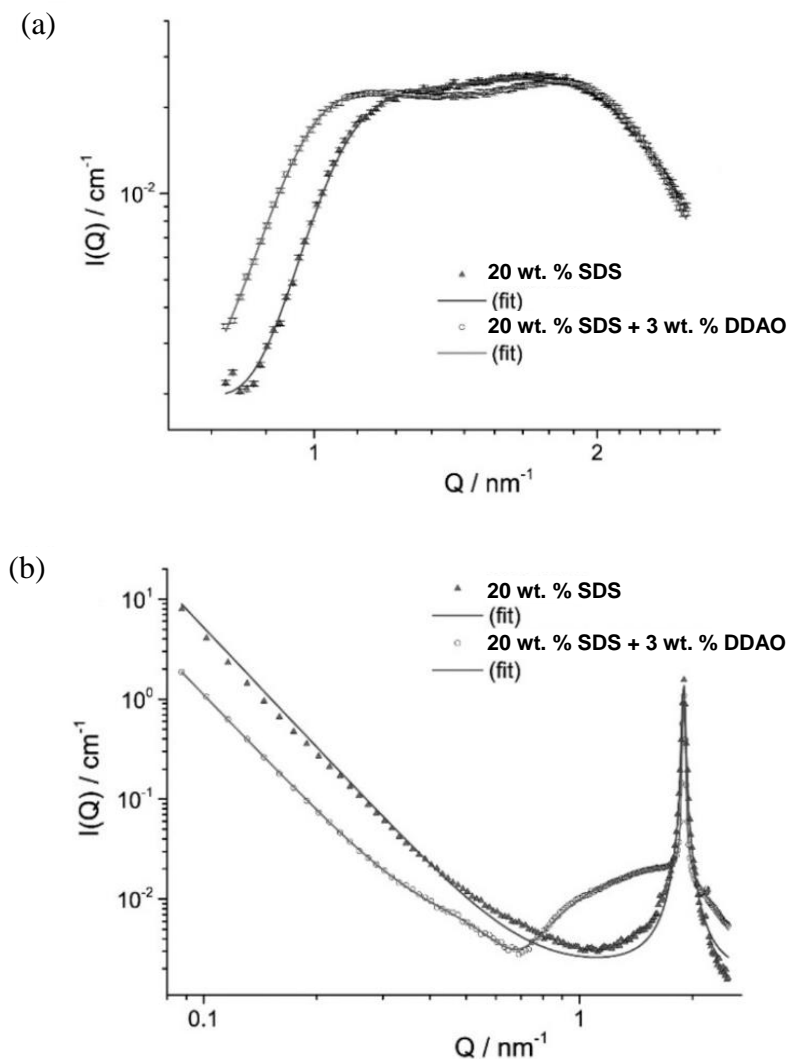


Figure 3.4. SAXS data for 20 wt. % SDS and 20 wt. % SDS + 3 wt. % DDAO samples at (a) 24 °C and (b) 0 °C. In both cases, the solid lines are fits to the data as described in the text and Appendix C.

At pH 2, the profile acquired at 0 °C exhibits two Bragg peaks (Figure 3.5) with neither peak matching the Bragg peak previously observed (Figure 3.4(b)) in the pure SDS and mixed SDS + DDAO systems at pH 9. The corresponding peak shift values for the three systems (20 wt. % SDS, 20 wt. % SDS + DDAO (pH 9) and 20 wt. % + 3 wt. % DDAO (pH 2)) at 0 °C are provided in Appendix C. Further comparisons regarding the crystal structure can also be drawn from the WAXS for the three different systems, as depicted in Figure 3.6.

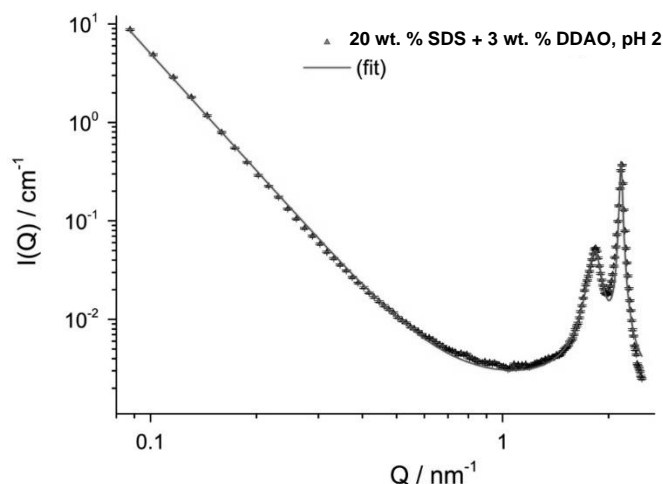


Figure 3.5. SAXS data for 20 wt. % SDS and 20 wt. % SDS + 3 wt. % DDAO samples at pH 2.

The solid lines are fits to the data as described in the text and Appendix C.

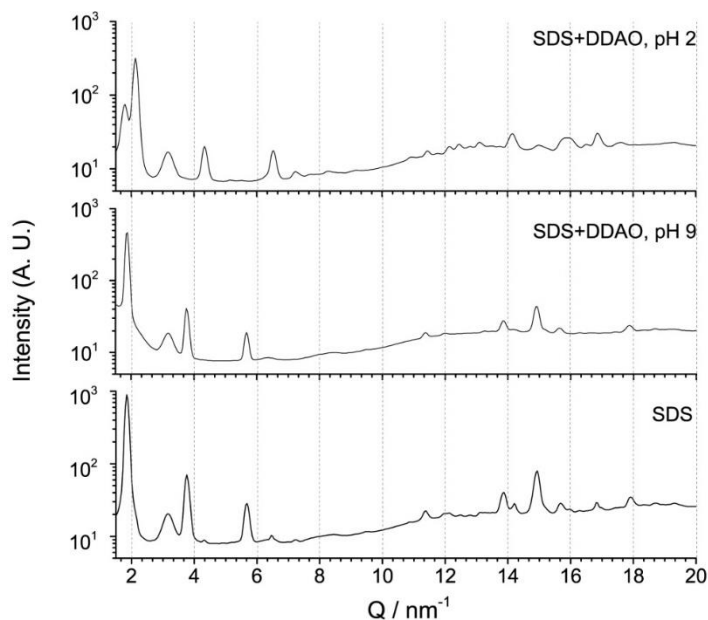


Figure 3.6. WAXS data for the three samples as noted at 0 °C. Concentrations of SDS and DDAO, where present, are 20 wt. % and 3 wt. % respectively. The peak at 3.15 nm^{-1} is from the polycarbonate capillary used to mount samples in the beam. All other peaks arise from the samples. From these, significant peaks are listed in Table C.3, Appendix C.

At pH 9, the ^1H NMR data suggests that SDS crystallises first, before the system fully solidifies. The drop in NMR signal for the SDS and DDAO protons is expected to be associated with an

increase in viscosity and a reduction in the mobility of the monomers and micelles, leading to a reduction in their T_2^* NMR relaxation time and an increase in the width of their peaks (James, 1998). There is a sudden drop in SDS signal between 10 °C and 13 °C, which indicates SDS is undergoing a phase transition. However, not all of the SDS signal disappears at the lower temperature, indicating a proportion of the SDS remains in solution. The DDAO does not display a sudden drop in the signal, suggesting it is not residing in the crystal itself, yet, there is a decrease indicating that the DDAO surfactant is affected by the SDS crystal formation between 10 °C and 13 °C. In another study (Chapter 4), confocal Raman microscopy indicated a tendency for DDAO to surround the SDS hydrated crystals and, therefore, is influenced by their formation, which potentially explains the decrease in the DDAO signal (Summerton *et al.*, 2018).

SAXS data at 24 °C suggests that pure SDS micelles and mixed SDS + DDAO micelles co-exist in the system. The differences between profiles obtained for a pure SDS and a mixed SDS + DDAO system indicate there is an increase in micelle size when DDAO is present, which is in line with previous observations (Kakitani *et al.*, 1995). By adding 3 wt. % DDAO, to a solution of SDS, the micelle aggregation number, N_{agg} , increases from 170 to 190 and the ellipsoid aspect ratio, a/b , from 1.8 to 2.2. Conversely, the proportional charge per headgroup, Z/N_{agg} falls from 0.12 to 0.11. This reduction in charge is in agreement with the literature, (Kakitani *et al.*, 1995) and is expected to reduce repulsions between the SDS head-groups in the interphase. Consequently, the shell curvature is able to decrease, allowing a more elongated structure to form.

The formation of a Bragg peak in the pure SDS system at 0 °C indicates the growth of SDS crystallites (Hammouda, 2013). The calculated d -spacing, $d = 3.3$ nm, is closer to the values expected for the mono- or hemi-hydrated crystal forms (2.9 or 3.1 nm respectively), but lower

than that of the 1/8 hydrate (3.9 nm) (Miller *et al.*, 2016). For the mixed SDS + DDAO system, the Bragg peak position is the same as the pure SDS system, indicating SDS is the dominant component of the crystals in both samples. This is in agreement with the drop in NMR signal observed for the SDS protons (H_1) (Figure 3.2). Aside from the Bragg peak, there is an additional contribution in the SAXS profile for the mixed system, which can be fitted to the remaining micelle phase. For the remaining micelles, $N_{agg} = 240$ and $a/b = 2.4$, which is more in line with data reported for mixed SDS + DDAO micelles than that for DDAO micelles alone (Kakitani *et al.*, 1995). Moreover, the micelles remain charged, albeit with a lower Z/N_{agg} than the values reported at 24 °C. Put together, the scattering data and associated analysis provides compelling evidence that the crystallites formed in the mixed SDS + DDAO system contain predominantly SDS, in agreement with NMR data. Unlike in the pure SDS system, not all SDS crystallises and some remains within a mixed micelle population, as is also observed in the NMR data. Thus, the remaining NMR signal originates from micelles containing DDAO and any uncrystallised SDS. By adding DDAO, the energy to form micelles is reduced, consequently diminishing the energetic driving force for crystallisation, consequently leading to a shift in the equilibrium towards micelles remaining in solution.

At pH 2, both SAXS and NMR studies suggest a simultaneous change in the phase behaviour of each surfactant. The NMR data shows the SDS and DDAO surfactants crystallise at the same time. This observation is expected to be because of the formation of the protonated form of DDAO, which can ion pair with SDS and counterions (Búcsi *et al.*, 2014; Goloub *et al.*, 2000). This is further supported by peaks at differing shifts in the corresponding SAXS profile, compared to that of the pure SDS and the mixed pH 9 system.

Further detail into the structure of the SDS crystallites can be drawn from WAXS data (Figure 3.6), with comparisons for notable peaks given in Table C.3 (supplementary). After holding at

0 °C for 45 minutes, at pH 9, the peaks in the mixed system can be matched, within error, to those observed in the pure SDS system, further indicating the formation of the same SDS phase. Peaks at 1.87, 3.76, 5.68 and 11.35 nm⁻¹ are assigned as first, second, third and sixth-order lamellar *d*-spacings (*d* = 3.34 nm) while peaks at higher *Q* (e.g. at 13.9, 14.9, 15.7 and 17.9 nm⁻¹) may arise from the head-head and alkyl peaks (Hyde, 2001). In the pure SDS system, more peaks are apparent in this region. However, as the peak intensities for this sample are approximately 2-3 times more intense, over the entire *Q*-range, this is more likely to be an observational artefact arising from a low peak intensity versus background. In contrast, at pH 2, a different structure forms, with first, second and third order lamellar *d*-spacings shifted to higher *Q* (at 2.13, 4.33 and 6.52 nm⁻¹ respectively) giving *d* = 2.95 nm. This suggests the formation of crystals containing both surfactants.

3.5 Conclusions

By combining variable temperature ¹H NMR and SAXS measurements it has been possible, for the first time, to determine the compositional and structural changes in a mixed SDS + DDAO surfactant system, which is of particular interest in the fast moving consumer goods (FMCG) industry (Summerton *et al.*, 2016). Crystals formed as the mixed SDS + DDAO system is cooled, at pH 9, are observed to be predominately SDS hydrated crystals, with little or no DDAO. At pH 2, the protonated DDAO, and its subsequent ion pairing behaviour, results in both surfactants crystallising simultaneously. While dish liquid is a highly complex system, this research provides important insight into the crystallisation process of liquid detergent systems upon exposure to cold climates. In turn, this understanding will assist in building more robust formulations and improvements to their accompanying test methods.

3.6 References

- Bergstrom, M. & Skov Pedersen, J. 1999. Structure of pure SDS and DTAB micelles in brine determined by small-angle neutron scattering (SANS). *Physical Chemistry Chemical Physics*, 1, 4437-4446.
- Bhat, M. & Gaikar, V. G. 1999. Characterization of Interaction between Butyl Benzene Sulfonates and Cetyl Trimethylammonium Bromide in Mixed Aggregate Systems. *Langmuir*, 15, 4740-4751.
- Bressler, I., Kohlbrecher, J. & Thunemann, A. F. 2015. SASfit: a tool for small-angle scattering data analysis using a library of analytical expressions. *Journal of Applied Crystallography*, 48, 1587-1598.
- Búcsi, A., Karlovská, J., Chovan, M., Devínsky, F. & Uhríková, D. 2014. Determination of pKa of N-alkyl-N,N-dimethylamine-N-oxides using ^1H NMR and ^{13}C NMR spectroscopy. *Chemical Papers*, 68, 842-846.
- Dierker, M. & Schafer, H. J. 2010. Surfactants from oleic, erucic and petroselinic acid: Synthesis and properties. *European Journal of Lipid Science and Technology*, 112, 122-136.
- Fan, X. J., Stenius, P., Kallay, N. & Matijevic, E. 1988. Precipitation of surfactant salts. 2. The effect of nonionic surfactants on precipitation of calcium dodecyl-sulfate. *Journal of Colloid and Interface Science*, 121, 571-578.
- Filik, J., Ashton, A. W., Chang, P. C. Y., Chater, P. A., Day, S. J., Drakopoulos, M., Gerring, M. W., Hart, M. L., Magdysyuk, O. V., Michalik, S., Smith, A., Tang, C. C., Terrill, N. J., Wharmby, M. T. & Wilhelm, H. 2017. Processing two-dimensional X-ray diffraction

Chapter 3 Nuclear magnetic resonance and small-angle X-ray scattering studies of mixed sodium dodecyl sulfate and N,N-dimethyldodecylamine N-oxide aqueous systems performed at low temperatures

- and small-angle scattering data in DAWN 2. *Journal of Applied Crystallography*, 50, 959-966.
- Gaikar, V. G., Padalkar, K. V. & Aswal, V. K. 2008. Characterization of mixed micelles of structural isomers of sodium butyl benzene sulfonate and sodium dodecyl sulfate by SANS, FTIR spectroscopy and NMR spectroscopy. *Journal of Molecular Liquids*, 138, 155-167.
- Gallo, A., Mazzobre, M. F., Buera, M. P. & Herrera, M. L. 2003. Low resolution ^1H -Pulsed NMR for sugar crystallization studies. *Latin American applied research*, 33, 97-102.
- Garg, G., Hassan, P. A., Aswal, V. K. & Kulshreshtha, S. K. 2005. Tuning the Structure of SDS Micelles by Substituted Anilinium Ions. *The Journal of Physical Chemistry B*, 109, 1340-1346.
- Goloub, T. P., Pugh, R. J. & Zhmud, B. V. 2000. Micellar Interactions in Nonionic/Ionic Mixed Surfactant Systems. *Journal of Colloid and Interface Science*, 229, 72-81.
- Hammouda, B. 2013. Temperature Effect on the Nanostructure of SDS Micelles in Water. *Journal of Research of the National Institute of Standards and Technology*, 118, 151-167.
- Herrmann, K. W. 1962. Non-ionic-cationic micellar properties of dimethyldodecylamine oxide. *Journal of Physical Chemistry*, 66, 295-300.
- Hindmarsh, J. P., Hollingsworth, K. G., Wilson, D. I. & Johns, M. L. 2004. An NMR study of the freezing of emulsion-containing drops. *Journal of Colloid and Interface Science*, 275, 165-171.

- Chapter 3 Nuclear magnetic resonance and small-angle X-ray scattering studies of mixed sodium dodecyl sulfate and N,N-dimethyldodecylamine N-oxide aqueous systems performed at low temperatures*
- Hollamby, M. J. 2013. Practical applications of small-angle neutron scattering. *Physical Chemistry Chemical Physics*, 15, 10566-10579.
- Holmberg, K., Jönsson, B., Kronberg, B. & Lindman, B. 2003. *Surfactants and polymers in aqueous solution*, Wiley Online Library.
- Hyde, S. T. 2001. Identification of lyotropic liquid crystalline mesophases. *Handbook of Applied Surface & Colloid Chemistry*. Wiley.
- James, T. L. 1998. Fundamentals of NMR. *Online Textbook: Department of Pharmaceutical Chemistry, University of California, San Francisco*, 1-31.
- Kakitani, M., Imae, T. & Furusaka, M. 1995. Investigation of Mixed Micelles of Dodecyldimethylamine Oxide and Sodium Dodecyl Sulfate by SANS: Shape, Size, Charge, and Interaction. *Journal of Physical Chemistry*, 99, 16018-16023.
- Kolz, J., Yarovoy, Y., Mitchell, J., Johns, M. L. & Gladden, L. F. 2010. Interactions of binary liquid mixtures with polysaccharides studied using multi-dimensional NMR relaxation time measurements. *Polymer*, 51, 4103-4109.
- Kume, G., Gallotti, M. & Nunes, G. 2008. Review on anionic/cationic surfactant mixtures. *Journal of Surfactants and Detergents*, 11, 1-11.
- Miller, R. M., Poulos, A. S., Robles, E. S. J., Brooks, N. J., Ces, O. & Cabral, J. T. 2016. Isothermal Crystallization Kinetics of Sodium Dodecyl Sulfate–Water Micellar Solutions. *Crystal Growth and Design*, 16, 3379-3388.
- Rathman, J. F. & Christian, S. D. 1990. Determination of surfactant activities in micellar solutions of dimethyldodecylamine oxide. *Langmuir*, 6, 391-395.

Scamehorn, J. F. 1986. An Overview of Phenomena Involving Surfactant Mixtures. ACS Symposium Series, 311, 1-27.

Soontravanich, S. 2007. *Formation and Dissolution of Surfactant Precipitates*. PhD Thesis, University of Oklahoma.

Soontravanich, S., Munoz, J. A., Scamehorn, J. F., Harwell, J. H. & Sabatini, D. A. 2008. Interaction Between an Anionic and an Amphoteric Surfactant. Part I: Monomer–Micelle Equilibrium. *Journal of Surfactants and Detergents*, 11, 251-261.

Spectral database for organic compounds SDBS [Online]. Available: http://sdb.sdb.aist.go.jp/sdb/cgi-bin/direct_frame_top.cgi [Accessed 13/06/2018].

Stellner, K. L. & Scamehorn, J. F. 1989. Hardness tolerance of anionic surfactant solutions. 2. Effect of added nonionic surfactant. *Langmuir*, 5, 77-84.

Summerton, E., Hollamby, M. J., Zimbitas, G., Snow, T., Smith, A. J., Sommertune, J., Bettiol, J., Jones, C., Britton, M. M. & Bakalis, S. 2018. The impact of N,N-dimethyldodecylamine N-oxide (DDAO) concentration on the crystallisation of sodium dodecyl sulfate (SDS) systems and the resulting changes to crystal structure, shape and the kinetics of crystal growth. *Journal of Colloid and Interface Science*, 527, 260-266.

Summerton, E., Zimbitas, G., Britton, M. & Bakalis, S. 2016. Crystallisation of sodium dodecyl sulfate and the corresponding effect of 1-dodecanol addition. *Journal of Crystal Growth*, 455, 111-116.

Tabor, R. F., Eastoe, J. & Grillo, I. 2009. Time-resolved small-angle neutron scattering as a lamellar phase evolves into a microemulsion. *Soft Matter*, 5, 2125-2129.

Van Der Veen, J. F. 2015. JSR - XFELs, DLSRs and beamline articles. *Journal of Synchrotron Radiation*, 22, 1-2.

Vass, S., Pedersen, J. S., Pleštil, J., Laggner, P., Rétfalvi, E., Varga, I. & Gilányi, T. 2008. Ambiguity in Determining the Shape of Alkali Alkyl Sulfate Micelles from Small-Angle Scattering Data. *Langmuir*, 24, 408-417.

Vijay, R., Singh, J., Baskar, G. & Ranganathan, R. 2009. Amphiphilic Lauryl Ester Derivatives from Aromatic Amino Acids: Significance of Chemical Architecture in Aqueous Aggregation Properties. *Journal of Physical Chemistry B*, 113, 13959-13970.

Wu, F.-G., Wang, N.-N., Yu, J.-S., Luo, J.-J. & Yu, Z.-W. 2010. Nonsynchronicity Phenomenon Observed during the Lamellar– Micellar Phase Transitions of 1-Stearoyllysophosphatidylcholine Dispersed in Water. *Journal of Physical Chemistry B*, 114, 2158-2164.

Zhang, F., Ilavsky, J., Long, G. G., Quintana, J. P. G., Allen, A. J. & Jemian, P. R. 2010. Glassy Carbon as an Absolute Intensity Calibration Standard for Small-Angle Scattering. *Metallurgical and Materials Transactions A*, 41, 1151-1158.

CHAPTER 4

THE IMPACT OF N,N-DIMETHYLDODECYLAMINE N- OXIDE (DDAO) CONCENTRATION ON THE CRYSTALLISATION OF SODIUM DODECYL SULFATE (SDS) SYSTEMS AND THE RESULTING CHANGES TO CRYSTAL STRUCTURE, SHAPE AND THE KINETICS OF CRYSTAL GROWTH

Discussions contained in this chapter have been published within: Summerton, E., Hollamby, M. J., Zimbitas G., Snow, T., Smith, A. J., Sommertune, J., Bettiol, J., Jones, C., Britton, M. M. and Bakalis. S. 2018. The impact of N,N-dimethyldodecylamine N-oxide (DDAO) concentration on the crystallisation of sodium dodecyl sulfate (SDS) systems and the resulting changes to crystal structure, shape and the kinetics of crystal growth, *Journal of Colloid and Interface Science*, **527**, p. 260-266.

4.1 Abstract

At low temperatures stability issues arise in commercial detergent products, such as dish liquid, when surfactant crystallisation occurs, a process which is not currently well-understood. An understanding of the phase transition can be obtained using a simple binary SDS (sodium dodecyl sulfate) + DDAO (N,N-dimethyldodecylamine N-oxide) aqueous system. It is expected that the crystallisation temperature of an SDS system can be lowered with addition of DDAO, thus providing a route to improve detergent stability. Detergent systems are typically comprised of anionic surfactants, amphoteric surfactants and water. This study explores the crystallisation of a three component system consisting of sodium dodecyl sulfate (SDS), N,N-dimethyldodecylamine N-oxide (DDAO), and water using wide-angle X-ray scattering (WAXS), differential scanning calorimetry (DSC) and confocal Raman microscopy. The presence of DDAO lowered the crystallisation temperature of a 20 wt. % SDS system. For all aqueous mixtures of SDS + DDAO at low temperatures, SDS hydrated crystals, $\text{SDS} \cdot 1/2\text{H}_2\text{O}$ or $\text{SDS} \cdot \text{H}_2\text{O}$, formed. SDS hydrates comprise of layers of SDS separated by water layers. DDAO tended to reside in the vicinity of these SDS crystals. In the absence of DDAO an additional intermediary hydrate structure, $\text{SDS} \cdot 1/8\text{H}_2\text{O}$, formed whereas for mixed SDS + DDAO systems no such structure was detected during crystallisation.

4.2 Introduction

Home and personal care products are primarily composed of water and surfactants, with the total surfactant concentration ranging from 10 to 50 wt. % (Summerton *et al.*, 2017; Lai, 1996). Two surfactants that reside in typical dish liquid formulations include the anionic surfactant sodium dodecyl sulfate (SDS) (Summerton *et al.*, 2016) and the amphoteric surfactant N,N-dimethyldodecylamine N-oxide (DDAO), which behaves as a non-ionic surfactant at the pH of

interest (Búcsi *et al.*, 2014) (Figure 4.1). Due to the increasing global demand for these products, the SDS market is growing with an estimated value of \$700 million by 2024 (Global Market Insights, 2017).

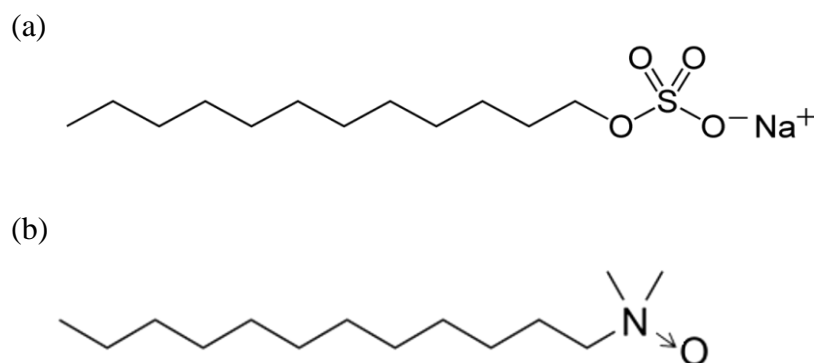


Figure 4.1. Molecular structure of (a) sodium dodecyl sulfate (SDS) and (b) *N,N*-dimethyldodecylamine *N*-oxide (DDAO).

Commercial surfactant systems are used worldwide and therefore need to be supplied to many different regions, so they must demonstrate chemical and physical stability across a wide temperature range. At ambient temperature, the surfactants in the products aggregate to form mixed micelles. However, upon exposure to low temperatures, surfactant crystallisation may occur in the products. Although the change is reversible and does not affect the performance, the change in appearance makes it unacceptable to consumers. Manufacturers have developed a range of methods to evaluate the stability of formulations at low temperatures, typically involving the storage of formulations at controlled temperature conditions. To improve both product stability and the method for testing for failures, it is critical to understand the crystallisation process.

Despite the industrial significance of SDS and DDAO surfactants, due to their extensive use in detergents products, the crystallisation of mixed SDS + DDAO systems has received little attention. Smith *et al.* considered the crystallisation of the surfactant SDS at concentrations

ranging from 5 to 20 wt. % (Smith *et al.*, 2001; Smith *et al.*, 2000). A decrease in the applied cooling rate was found to increase the temperature of crystallisation and reduce the width of the metastable zone. They also report the structure of anhydrous SDS for the first time and compare the findings to SDS hydrates. More recently, Miller *et al.* observed the effect of different isothermal and non-isothermal conditions on the morphology of crystals forming from a 20 wt. % SDS solution (Miller *et al.*, 2016; Miller *et al.*, 2017). The temperature and the cooling rate were found to dictate whether the crystals form needles or platelets.

The majority of the literature for the crystallisation of mixed surfactant systems date back to the 1980s and 1990s. The Krafft temperature, T_k , for some binary surfactant mixtures is found to be lower than their respective single components (Rodriguez and Scamehorn, 1999). The decrease in T_k of an anionic surfactant system upon the addition of a second anionic or non-ionic surfactant has been demonstrated for binary surfactant solutions comprising of two different sulfates or sulfonates (Tsujii *et al.*, 1980). Furthermore, the addition of the non-ionic surfactant, nonylphenol ethoxylate, to a solution of SDS caused the precipitation boundary to reduce in size (Shiau *et al.*, 1994). In these mixed surfactant systems micelle formation becomes increasingly favoured, lowering the CMC and reducing the monomer concentration that is able to form crystals (Soontravanich and Scamehorn, 2009).

To the best of our knowledge there is a distinct lack of research into the crystallisation of mixed SDS + DDAO systems, despite its application to commercial products. There are unanswered questions surrounding the influence that DDAO has on SDS crystallisation in terms of the crystallisation kinetics, crystal shape and the structure of the crystals, for which this paper aims to address. In this study SDS and DDAO are present at concentrations typical of those in dish liquid formulations, which are much higher than those previously presented for similar mixed surfactant studies. Crystallisation is initiated by lowering the temperature of the system, in order

to replicate conditions that formulations may experience during the supply chain. It is expected that the acquired knowledge from this study will enable industries to gain a greater understanding of the behaviour of their dish liquid formulations at low temperatures. In turn, this will result in improvements to product stability and the accompanying stability test methods.

4.3 Materials and methods

4.3.1 Materials

Aqueous surfactant solutions containing 20 wt. % SDS (ionic) and various amounts of the amphoteric surfactant DDAO (0 - 5 wt. %) at pH 9 were used throughout this study. SDS was purchased at a purity of 97.5 % from Fischer Scientific. DDAO was purchased from Sigma Aldrich in aqueous form at a concentration of 30 wt. %. Both surfactants were used without further purification. All solutions were freshly prepared to minimise deviations due to hydrolysis of SDS. The solution was mixed for 15 minutes at 25 °C and then left for 12 hours to release any entrapped air.

4.3.2 Methods

4.3.2.1 Differential scanning calorimetry (DSC)

DSC (Differential scanning calorimetry) thermograms of a pure SDS system and various mixed SDS + DDAO systems were acquired using a Sentaram micro DSC. Distilled water was used as the reference sample. For each run approximately 70 mg of the sample was measured into the sample cell and placed into the DSC furnace chamber.

20 wt. % SDS aqueous solutions, with varying amounts of DDAO (0.5 - 5 wt. %), were cooled and subsequently heated at a rate of 0.1 °C/min. Additionally, a pure 20 wt. % SDS system was cooled across a selection of cooling rates (0.1 - 1 °C/min). The upper temperature was in the range of 30 to 40 °C with the lower limit being -10 °C, at which there was a 20-minute hold time before heating the system. A thermal analysis software package, Calisto processing, was used to acquire enthalpies and peak temperatures from the thermograms.

4.3.2.2 Confocal Raman microscopy

Confocal Raman microscopy was performed on a WITec alpha 300 system applying a 532 nm excitation laser. Spectra were recorded using a x60 magnification water-immersion objective. The surfactant solutions were applied on a microscopy slide with a recess, with the slide being placed on top of a Linkam PE 94 Peltier cooling stage, set to 0 °C. A cover slip was placed over the sample and subsequently covered with distilled water which the objective was then immersed into. Typical integration times were in the range of 0.1 s with a resolution of 4 pixels/ μm^2 . The data was analysed using WITec Project Plus 4.1 software. Cluster analysis followed by de-mixing was subsequently performed in order to distinguish different chemical components. Raman spectra of the pure surfactants were also recorded. This allowed one to plot distribution maps of the components.

4.3.2.3 X-ray scattering

Small-angle X-ray scattering (SAXS) and wide-angle X-ray scattering (WAXS) data was obtained using the I22 beamline at Diamond Light Source, Oxfordshire, UK. Samples were loaded into 1.8 mm (internal diameter) and 2.0 mm (external diameter) polycarbonate capillaries and mounted in the beam within the Linkam DSC600 capillary stage, which also provided temperature control (at 25 °C and 0 °C, with an applied cooling rate = 19 °C/min). A

12.3989 keV ($\lambda = 0.099987$ nm) beam was used with a sample-detector distance of 6702.56 mm, providing a detectable Q -range on the SAXS detector of order $0.02 - 2.50 \text{ nm}^{-1}$ and $1.51 - 60.57 \text{ nm}^{-1}$ on the WAXS detector. Data processing was performed using the DAWN software package (van der Veen, 2015; Filik *et al.*, 2017) and a set of pipelines developed at Diamond Light Source. Before processing uncertainty estimates based on Poisson counting statistics were added to all measurement data, which were subsequently propagated through the image correction steps. Each raw background measurement was corrected for the following: masking pixels, time, incident beam flux, and transmission. Each sample file was corrected for the following: masking pixels, time, incident beam flux, transmission, background, thickness, and scaled to absolute units. The scaling factor for scaling to absolute units was determined using a calibrated glassy carbon sample (Zhang *et al.*, 2010). After this correction the data was azimuthally averaged, with the resulting uncertainty assuming the largest of: 1) the propagated uncertainties, 2) the standard error of the mean for the data points comprising a bin, or 3) 1% of the mean intensity in the bin. Two-dimensional (2D) plots of the acquired SAXS and WAXs data were displayed as stacked graphs at selected timepoints using OriginPro(v.9.0) graphical software. Time resolved three-dimensional (3D) plots of the WAXS data were produced in MATLAB R2016b.

4.4 Results and discussion

4.4.1 Results

4.4.1.1 Crystallisation temperature

DSC thermograms for the SDS + DDAO systems were acquired upon cooling the system and inducing crystallisation. One main exothermic peak, corresponding to the crystallisation of SDS, was observed for all solutions. Figure 4.2 shows how the crystallisation temperatures,

corresponding to the peak maxima, and the enthalpy of crystallisation, related to the peak area, change with DDAO concentration. Both factors demonstrate strong linear correlation with the amount of DDAO, as anticipated from pre-existing studies (Summerton *et al.*, 2016). A low cooling rate, 0.1 °C/min, was used since it is representative of typical environmental changes that formulation may experience (Miller *et al.*, 2016; Miller *et al.*, 2017). There are two types of nucleation, homogenous and heterogenous, and, in most industrial systems, the latter occurs. Here, the DSC cell walls provide a surface where heterogenous nucleation can occur.

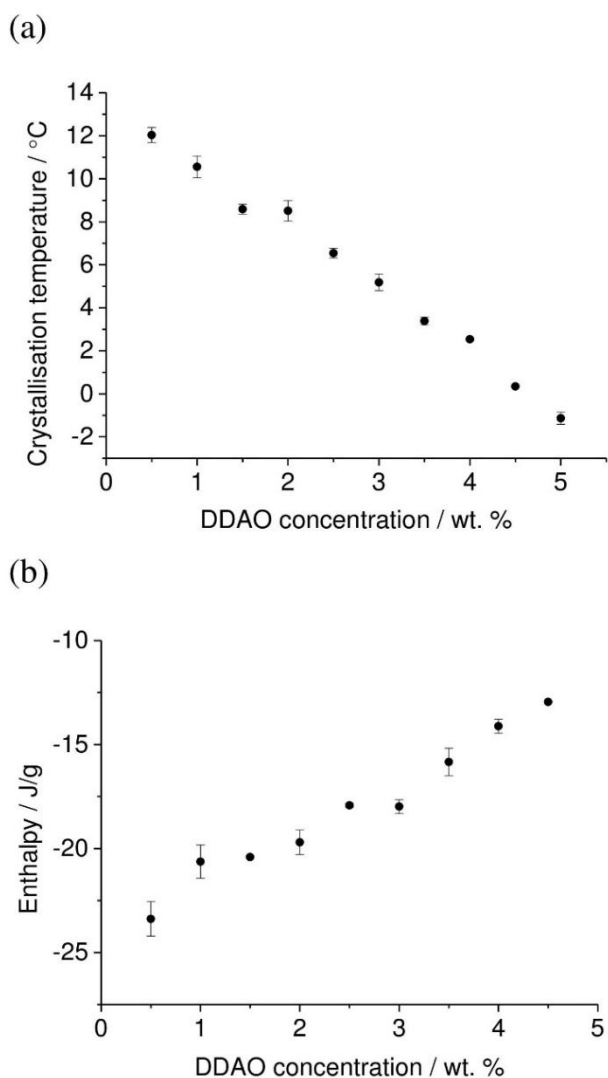


Figure 4.2. Plots of (a) crystallisation temperature and (b) enthalpy of crystallisation versus DDAO concentration for SDS + DDAO systems.

It is also important to consider the effect that the cooling rate has on the crystallisation process since formulations can be exposed to various temperature fluctuation. When the cooling rate was varied between 0.1 and 1 °C/min, a change in the crystallisation temperature was observed. The higher the cooling rate, the lower the crystallisation temperature attained from the DSC thermogram (Figure 4.3).

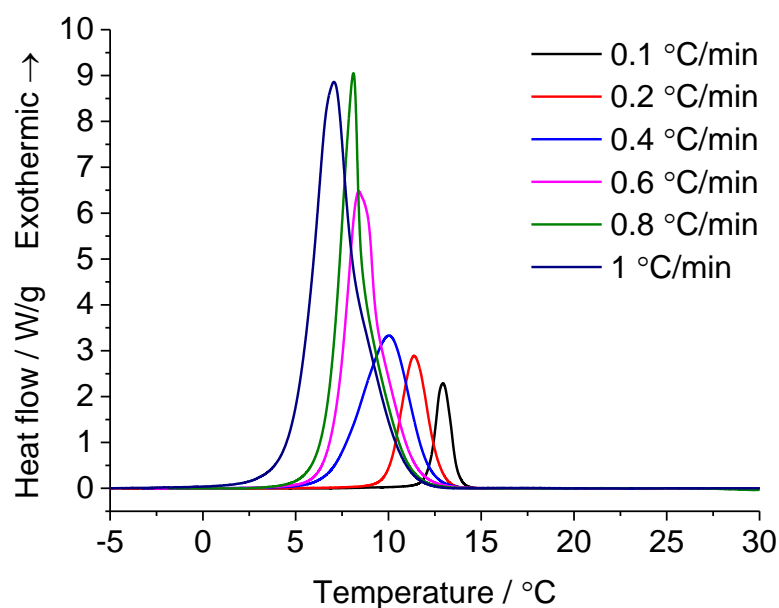


Figure 4.3. DSC thermograms acquired upon cooling a 20 wt. % SDS system to -5 °C across a range of cooling rates.

4.4.1.2 Crystal structure and kinetics

4.4.1.2.1 Crystal Structure

WAXS was used to follow the crystallisation of the pure SDS and SDS + DDAO systems *in situ*. The 2D and 3D WAXS profiles, acquired when holding the systems at 0 °C, are presented in Figure 4.4.

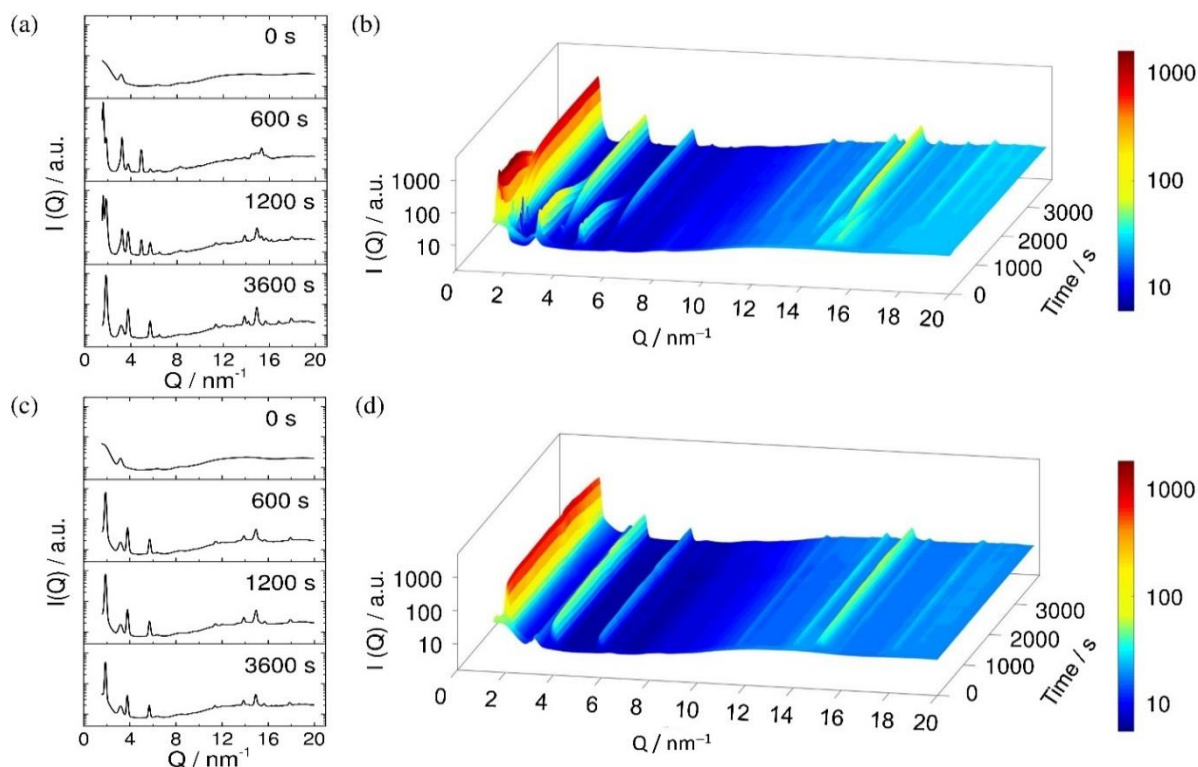


Figure 4.4. (a) Plot showing the WAXS intensity, $I(Q)$ as a function of Q for selected time points 0 s, 600 s, 1200 s and 3600 s for a 20 wt. % SDS solution held at 0 °C after being cooled from 25 °C at 19 °C/min; (b) 3D plot showing the change in $I(Q)$ vs. Q during crystallisation as a function of time for the same 20 wt. % SDS solution; (c) Plot showing the WAXS intensity, $I(Q)$ as a function of Q for selected time points 0 s, 600 s, 1200 s and 3600 s for a 20 wt. % SDS + 3 wt. % DDAO solution held at 0 °C after being cooled from 25 °C at 19 °C/min; (d) 3D plot showing the change in $I(Q)$ vs. Q as a function of time during crystallisation for the same 20 wt. % SDS + 3 wt. % DDAO solution. The corresponding plots for 20 wt. % SDS + 1, 2, 4 and 5 wt. % DDAO respectively are provided in Appendix C.

In the pure SDS system, approximately 40 s after reaching 0 °C, a peak initially starts to develop at 1.65 nm^{-1} and the intensity of this peak increases for 20 seconds. This corresponds to a structure with a d -spacing of $3.86 \pm 0.03 \text{ nm}$. Second and third reflections of this primary peak are visible at 3.24 and 4.91 nm^{-1} . The d -spacing values implies a SDS:1/8H₂O hydrated crystal

(Coiro *et al.*, 1987) (Smith *et al.*, 2004). Hydrated SDS crystal structures are comprised of layers of SDS molecules closely aligned to one another, with the SDS layers separated by water-rich regions. The d -spacing corresponds to the distance between the SDS layers. Other notable peaks at 14.5, 14.8 and 15.4 nm⁻¹ are likely to arise from the spacing between the head-groups and alkyl chains of SDS. The most intense of these is likely to be the head-head peak, which is found to be at 15.4 nm⁻¹ ($d = 0.41$ nm).

Approximately 400 s after reaching 0 °C, there is a change in structure, as shown by a reduction in intensity of the peaks at 1.65, 3.24, 4.91, 14.5, 14.8 and 15.4 nm⁻¹ and an increase in intensity in peaks at 1.85, 3.76, 5.67, 11.37, 13.89, 14.95, 15.70, 17.96 nm⁻¹. This transition takes approximately 2000 s to complete. The first four peaks are likely to be the 1st, 2nd, 3rd and 6th reflections and the d -spacing of structure is 3.32 nm. This value is close to that of the SDS·1/2H₂O or SDS·H₂O hydrates reported in the literature (Smith *et al.*, 2004; Coiro *et al.*, 1987). The inclusion of more water into the headgroup region results in the alkyl chains becoming tilted, leading to a reduction in the d -spacing. The higher Q peaks are again likely to arise from the spacing between the head-groups and alkyl chains of SDS. The most intense of these, again likely to be the head-head peak, is now found at 14.95 nm⁻¹ ($d = 0.42$ nm).

In contrast, the WAXS data for the SDS + DDAO systems points to the existence of just one crystal structure throughout the crystallisation process. There are significant peaks detected at 1.87, 3.76, 5.68, 11.35, 13.9, 14.9, 15.7 and 17.9 nm⁻¹, in clear similarity to the data for the second crystalline phase formed by the 20 wt. % SDS solution. As with the 20 wt. % SDS solution, the crystal is therefore likely to be the SDS·1/2H₂O or SDS·H₂O hydrate, implying no DDAO resides in the crystal.

4.4.1.2.2 Kinetics of the phase transition

In addition to understanding the structural changes, X-ray scattering can also provide information on the kinetics of the crystallisation process. The primary Bragg peak is detected at 1.9 nm^{-1} in the SAXS profiles for all SDS + DDAO systems. SAXS profiles for the systems are provided in the supplementary information at various timepoints (Appendix C). Figure 4.5(a) shows the increase in peak intensity as a function of time for 20 wt. % SDS systems with different amounts of added DDAO. Upon increasing the amount of DDAO there are two notable changes in the plot. Firstly, there is an increase in the lag-time until the peak is first observed and, secondly, the rate at which the peak grows decreases in the trend shown in Figure 4.5(b). The gradient of the linear increase can be related to the rate of growth and the time lag indicates the induction time. The R^2 values for the linear fits are all in excess of 0.96. The drop in the signal of the 1 wt. % DDAO system after crystallisation may be due to a decline in underlying signal or a change in density.

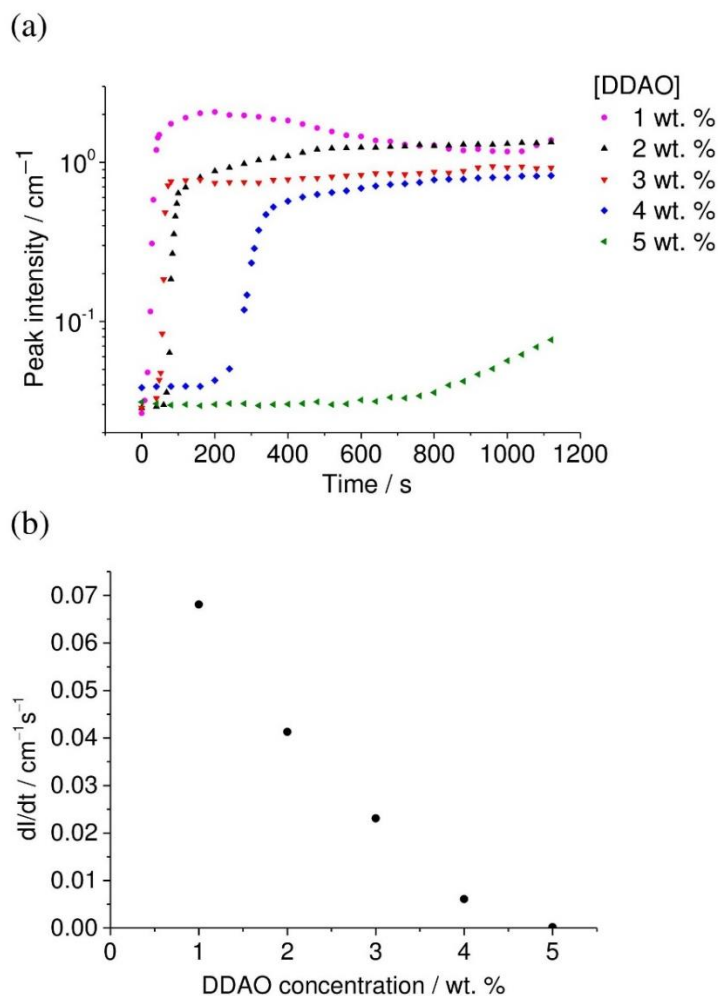


Figure 4.5. (a) Plot of the change in maximum intensity of the primary Bragg peak (at 1.9 nm^{-1} in the SAXS) during crystallisation as a function of time for all samples containing DDAO (1 - 5 wt. %); (b) Plot showing the rate of change of peak intensity during crystallisation as a function of DDAO concentration.

4.4.1.3 Crystal shape and growth characteristics

The Raman spectra for the three individual surfactant components are displayed in Figure 4.6. DDAO can be clearly distinguished from the SDS contributions by the peak above 3000 cm^{-1} and the peak below 800 cm^{-1} . Furthermore, there are two SDS contributions that can be distinguished by their differences in the peak profile around 800 cm^{-1} . The two SDS

contributions arise from the orientation of SDS to the laser beam. Although there are few reports in this area, one study uses Raman spectroscopy to investigate changes observed during SDS crystallisation, including increased peak splitting and an increased degree of trans conformers (Picquart, 1986).

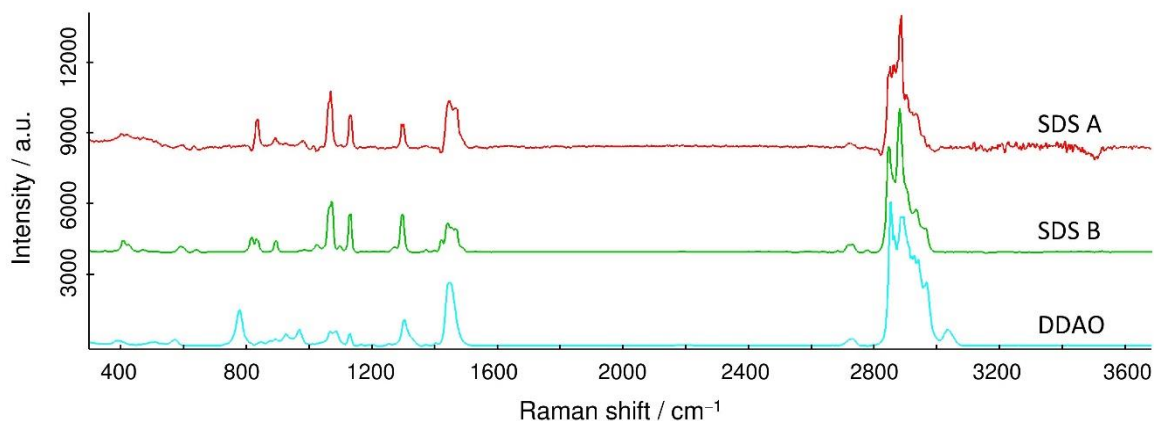


Figure 4.6. Raman spectra for SDS A (red line), SDS B (green line) and DDAO (blue line); A and B refer to different forms or orientation of the SDS component.

Figure 4.7 displays confocal Raman microscopy images for crystals formed from 20 wt. % SDS and 20 wt. % + 3 wt. % DDAO solution. In the pure SDS system both SDS contributions are present and exist as platelets, with a considerable number orientated on their side. From Figure 4.7(b), the crystals initially appear needle-shaped. However, a second image (Figure 4.7(c)) acquired at a 5 μm height difference, gave a similar profile, indicating the existence of side-on platelets. This is due to local supersaturation at the point of contact between the cooling stage and the surfactant solution, where crystals begin growing upwards.

When DDAO is added, at a level of 3 wt. %, the resultant crystals are ring shaped and grow on a much smaller scale (Figure 4.7(e)-(g)). Due to the absence of any red-coloured regions, only one SDS contribution exists in the mixed surfactant system. Furthermore, the green-coloured

area, corresponding to DDAO, is concentrated in the same region as SDS, implying a tendency of DDAO to surround the SDS crystals.

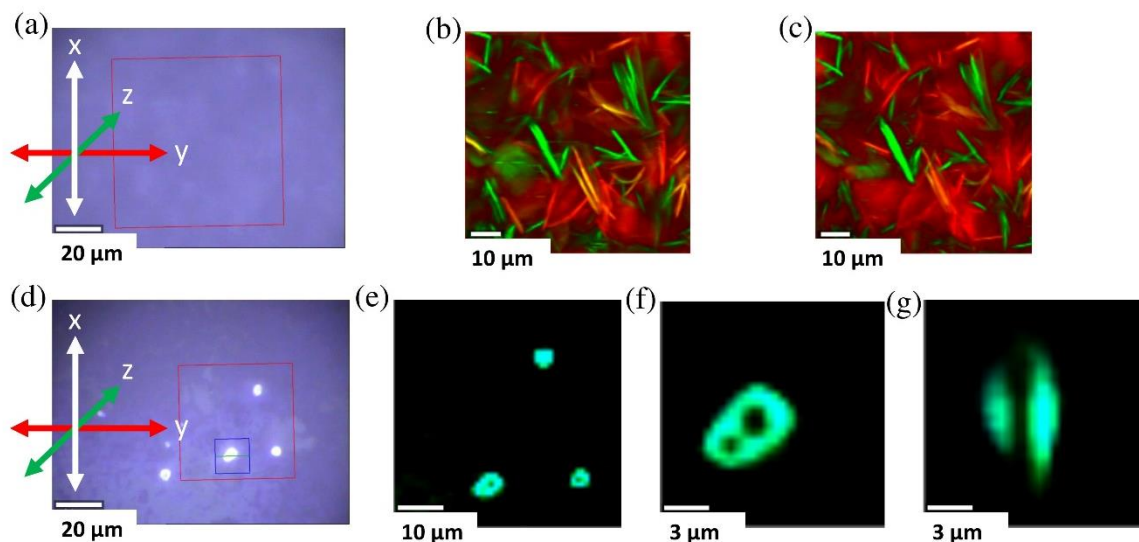


Figure 4.7. (a) Location selected for the analysis of a crystalline solution of 20 wt. % SDS; (b) Confocal scans of the xy plane of the red boxed area in (a) with $z = 0 \mu\text{m}$ or (c) $z = +5 \mu\text{m}$; (d) Locations selected for the analysis of a crystalline solution of 20 wt. % SDS + 3 wt. % DDAO; (e) Confocal scan of the xy plane of the red boxed area in (d) with $z = 0 \mu\text{m}$; (f) Confocal scan of the xy plane of the blue boxed area in (d) with $z = 0 \mu\text{m}$; (g) Confocal depth scan of the yz plane attained by vertically slicing along green line in (d) with $z = -7.5$ to $+7.5 \mu\text{m}$.

4.4.2 Discussion

Non-ideal mixed micelles form in SDS + DDAO systems (Scaemhorn, 1986) and the deviation from ideality lowers the critical micelle concentration (CMC), in comparison to that of a pure SDS solution. The existence of DDAO enhances micelle formation in the system, consequently reducing the concentration of SDS monomers, which is the driving force for crystallisation (Stellner and Scaemhorn, 1989; Stellner and Scaemhorn, 1986; Soontravanich and Scaemhorn, 2009). This increased favourability to form micelles is a result of reduced repulsion energy

between the SDS groups in mixed SDS + DDAO micelles, compared to pure SDS micelles. In order for SDS to precipitate out of solution the supersaturation level, S (equation 4.1), must be greater than 1 (Soontravanich, 2007; Thanh *et al.*, 2014).

$$S = \frac{a_{DS^-} a_{Na^+}}{K_{sp}}, \text{ where } K_{sp} = a_{DS^-,eqm} a_{Na^+,eqm} \quad (4.1)$$

where a_{DS^-} and a_{Na^+} are the activities of DS^- and Na^+ in the solution and K_{sp} is the solubility product, which is given by the product of the equilibrium activities of DS^- and Na^+ and exhibits temperature dependency. Upon addition of DDAO, the temperature must be lowered to induce supersaturation so SDS crystals can form. In addition to reducing the crystallisation temperature, the enthalpy of crystallisation is also found to decrease with increasing DDAO concentration.

Larger, less easily-flowing aggregates (Akbas and Sidim, 2005) form when DDAO is present, compared to a pure SDS system. This, in turn, results in an increase in the viscosity of the system with DDAO concentration. Alongside the effects of a reduced SDS monomer concentration, a high solution viscosity can also hinder SDS crystal growth since it can affect both the growth rate and the crystallisation temperature. The effect of viscosity on crystal growth has been reported in a previous study (Murray, 2008) in which ice crystallisation was inhibited when contained within an ultra-viscous solution.

Zero-shear viscosity measurements of SDS + DDAO systems show an increase with DDAO concentration. For example, 20 wt. % SDS + 3 wt. % DDAO solution has a zero-shear viscosity of 0.424 Pa.s whereas addition of 5 wt. % DDAO provides a viscosity of 9.62 Pa.s. Measurements were not possible below 2.5 wt. % DDAO due to the inherent low viscosity of the system. In the pure SDS system the viscosity is low, similar to water, and molecular mobility

is not restricted. Crystal growth is fast and spreads through the solution, forming many platelets. The mixed 20 wt. % SDS + 3 wt. % DDAO system, being at a higher viscosity (0.424 Pa.s), demonstrates slower growth. There is a resultant tendency for crystals to dissolve from the centre, forming ring-shaped crystals (Mandal *et al.*, 2012). Furthermore, the DDAO surfactant surrounds the SDS crystals which also contributes to the reduced rate of growth. Further insight into how DDAO concentration influences the rate of crystallisation and induction time can also be obtained from the time resolved plots of the intensity of the first Bragg peak in the SAXS profiles. The time lapsed until the peak begins to grow and the gradient of the peak growth correspond to the induction time and rate, respectively. As to be expected, the rate of crystal formation decreases and the time to crystallisation increases with an increase in the amount of DDAO.

Aside from DDAO affecting the crystallisation temperature, rate of formation, shape and viscosity, this surfactant also influences the structural changes that occur during SDS crystal formation at 0 °C. The crystals formed from both SDS and SDS + DDAO systems are SDS hydrates, composed of SDS-rich layers separated by water layers, with the ratio of water to SDS varying between the different possible hydrates. WAXS data acquired from SDS + DDAO systems points to the crystal structure being either the SDS·1/2H₂O or SDS·H₂O hydrate, which matches the final structure formed from a pure SDS sample. However, the pure SDS system initially forms the SDS·1/8H₂O hydrate, which then gradually transitions to the SDS·1/2H₂O or SDS·H₂O hydrate. When DDAO is present, SDS is trapped in micelles for a longer period of time. Such a feature is responsible for more controlled crystal growth in the SDS + DDAO system, enabling the final structure to form directly rather than proceeding via an intermediary. Furthermore, confocal Raman microscopy investigations indicate that, upon SDS crystal

formation, DDAO is concentrated on the surface of the SDS crystals where it is able to influence both the mechanism and rate of formation.

4.5 Conclusions

Increasing the amount of DDAO lowers the concentration of SDS monomers, due to mixed micelle formation, and consequently reduces the drive for SDS crystallisation. In the presence of DDAO, the crystallisation temperature is lowered, compared to that of a pure SDS system. Furthermore, the presence of DDAO was found to significantly increase the induction time to crystallisation, as well as reduce the rate of crystal growth. In the final part of the study, X-ray scattering techniques demonstrate the structural differences and similarities between those of a pure SDS system versus a SDS + DDAO system. Both systems result in the same final structure, where the *d*-spacing and peak assignments are matched to those of SDS·1/2H₂O or SDS·H₂O hydrate structures, comprised of layers of SDS separated by water layers. The pure SDS system proceeds via the SDS·1/8H₂O hydrate structure but, conversely, this intermediary is not detected in the mixed system. DDAO surrounds the crystals and consequently affects the mechanism of their formation.

Through this work a detailed insight has been gained into the nature of the SDS crystallisation process occurring in SDS + DDAO systems under low temperature conditions. SDS and DDAO were chosen as the core surfactants for this study due to their extensive use in industry, especially in dish liquid formulations. It is important to reiterate that, in this study, both surfactants are at concentrations typical of commercial detergent products. DDAO was found to influence the crystallisation temperature, crystal shape, structure and kinetics of SDS solutions. The reported results have furthered the understanding of dish liquid systems at low temperatures, which is important when improving the stability of such formulations. Future

work would involve applying the understanding to other surfactant systems of significance in the detergent industry, such as those containing dimethyl laurylaminoacetate betaine and branched sulfated surfactants.

4.6 References

- Akbas, H. & Sidim, T. 2005. The viscous properties of anionic/cationic and cationic/nonionic mixed surfactant systems. *Colloid Journal*, 67, 525-530.
- Búcsi, A., Karlovská, J., Chovan, M., Devínsky, F. & Uhríková, D. 2014. Determination of pKa of N-alkyl-N,N-dimethylamine-N-oxides using ^1H NMR and ^{13}C NMR spectroscopy. *Chemical Papers*, 68, 842-846.
- Coiro, V. M., Manigrasso, M., Mazza, F. & Pochetti, G. 1987. Structure of a triclinic phase of sodium dodecyl sulfate monohydrate. A comparison with other sodium dodecyl sulfate crystal phases. *Acta Crystallographica Section C*, 43, 850-854.
- Filik, J., Ashton, A. W., Chang, P. C. Y., Chater, P. A., Day, S. J., Drakopoulos, M., Gerring, M. W., Hart, M. L., Magdysyuk, O. V., Michalik, S., Smith, A., Tang, C. C., Terrill, N. J., Wharmby, M. T. & Wilhelm, H. 2017. Processing two-dimensional X-ray diffraction and small-angle scattering data in DAWN 2. *Journal of Applied Crystallography*, 50, 959-966.
- Global Market Insights. 2017. *Sodium Lauryl Sulfate (SLS) Market to exceed \$700 Million by 2024* [Online]. Available: <https://globenewswire.com/newsrelease/2017/04/24/970119/0/en/Sodium-Lauryl-Sulfate-SLS-Market-to-exceed-700-Million-by-2024-Global-Market-Insights-Inc.html> [Accessed 17/05/2018].
- Lai, K. Y. 1996. *Liquid Detergents*, CRC Press.

- Mandal, P. K., Chandrasekaran, A. R., Madhanagopal, B. R., Venkadesh, S. & Gautham, N. 2012. Ring crystals of oligonucleotides: Growth stages and X-ray diffraction studies. *Journal of Crystal Growth*, 354, 20-26.
- Miller, R. M., Ces, O., J Brooks, N., Robles, E. & Cabral, J. 2017. *Crystallization of Sodium Dodecyl Sulfate–Water Micellar Solutions under Linear Cooling*.
- Miller, R. M., Poulos, A. S., Robles, E. S. J., Brooks, N. J., Ces, O. & Cabral, J. T. 2016. Isothermal Crystallization Kinetics of Sodium Dodecyl Sulfate–Water Micellar Solutions. *Crystal Growth and Design*, 16, 3379-3388.
- Murray, B. J. 2008. Inhibition of ice crystallisation in highly viscous aqueous organic acid droplets. *Atmospheric Chemistry and Physics*, 8, 5423-5433.
- Picquart, M. 1986. Vibrational-mode behavior of SDS aqueous solutions studied by Raman scattering. *Journal of Physical Chemistry*, 90, 243-250.
- Rodriguez, C. H. & Scamehorn, J. F. 1999. Modification of Krafft temperature or solubility of surfactants using surfactant mixtures. *Journal of Surfactants and Detergents*, 2, 17-28.
- Scamehorn, J. F. 1986. An Overview of Phenomena Involving Surfactant Mixtures. *ACS Symposium Series*, 311, 1-27.
- Shiau, B. J., Harwell, J. H. & Scamehorn, J. F. 1994. Precipitation of mixtures of anionic and cationic surfactants. 3. Effect of added nonionic surfactant. *Journal of Colloid and Interface Science*, 167, 332-345.
- Smith, L. A., Duncan, A., Thomson, G. B., Roberts, K. J., Machin, D. & Mcleod, G. 2004. Crystallisation of sodium dodecyl sulphate from aqueous solution: phase identification, crystal morphology, surface chemistry and kinetic interface roughening. *Journal of Crystal Growth*, 263, 480-490.
- Smith, L. A., Hammond, R. B., Roberts, K. J., Machin, D. & Mcleod, G. 2000. Determination of the crystal structure of anhydrous sodium dodecyl sulphate using a combination of

- synchrotron radiation powder diffraction and molecular modelling techniques. *Journal of Molecular Structure*, 554, 173-182.
- Smith, L. A., Roberts, K. J., Machin, D. & Mcleod, G. 2001. An examination of the solution phase and nucleation properties of sodium, potassium and rubidium dodecyl sulphates. *Journal of Crystal Growth*, 226, 158-167.
- Soontravanich, S. 2007. *Formation and Dissolution of Surfactant Precipitates*. PhD Thesis, University of Oklahoma.
- Soontravanich, S. & Scamehorn, J. F. 2009. Use of a Nonionic Surfactant to Inhibit Precipitation of Anionic Surfactants by Calcium. *Journal of Surfactants and Detergents*, 13, 13.
- Stellner, K. L. & Scamehorn, J. F. 1986. Surfactant precipitation in aqueous-solutions containing mixtures of anionic and nonionic surfactants. *Journal of the American Oil Chemists Society*, 63, 566-574.
- Stellner, K. L. & Scamehorn, J. F. 1989. Hardness tolerance of anionic surfactant solutions. 2. Effect of added nonionic surfactant. *Langmuir*, 5, 77-84.
- Summerton, E., Zimbitas, G., Britton, M. & Bakalis, S. 2016. Crystallisation of sodium dodecyl sulfate and the corresponding effect of 1-dodecanol addition. *Journal of Crystal Growth*, 455, 111-116.
- Summerton, E., Zimbitas, G., Britton, M. & Bakalis, S. 2017. Low temperature stability of surfactant systems. *Trends in Food Science & Technology*, 60, 23-30.
- Thanh, N. T. K., Maclean, N. & Mahiddine, S. 2014. Mechanisms of Nucleation and Growth of Nanoparticles in Solution. *Chemical Reviews*, 114, 7610-7630.
- Tsujii, K., Saito, N. & Takeuchi, T. 1980. Krafft points of anionic surfactants and their mixtures with special attention to their applicability in hard water. *The Journal of Physical Chemistry*, 84, 2287-2291.

Chapter 4 The impact of N,N-dimethyldodecylamine N-oxide (DDAO) concentration on the crystallisation of sodium dodecyl sulfate (SDS) systems and the resulting changes to crystal structure, shape and kinetics of crystal growth

Van Der Veen, J. F. 2015. JSR - XFELs, DLSRs and beamline articles. *Journal of Synchrotron Radiation*, 22, 1-2.

Zhang, F., Ilavsky, J., Long, G. G., Quintana, J. P. G., Allen, A. J. & Jemian, P. R. 2010. Glassy Carbon as an Absolute Intensity Calibration Standard for Small-Angle Scattering. *Metallurgical and Materials Transactions A*, 41, 1151-1158.

CHAPTER 5

INSIGHT INTO THE KINETICS OF CRYSTALLISATION OF SODIUM DODECYL SULFATE AND MIXED SODIUM DODECYL SULFATE AND N,N- DIMETHYLDODECYLAMINE N-OXIDE SYSTEMS UNDER BOTH ISOTHERMAL AND NON-ISOTHERMAL CONDITIONS

5.1 Abstract

Sodium dodecyl sulfate (SDS) and N,N-dimethyldodecylamine N-oxide (DDAO) are key components in detergent formulations. This chapter explores the kinetics of crystallisation for SDS and SDS + DDAO aqueous systems under isothermal and non-isothermal low temperature environments with the surfactants present at concentrations typical of commercial products. Differential scanning calorimetry (DSC) and X-ray scattering are used, with the latter performed with awarded beamtime at the Diamond Light Source, Oxfordshire, UK.

For crystallisation of pure SDS systems, the Avrami exponent (Avrami, 1939; Marangoni, 1998), which dictates the order of crystallisation, is found to be positively correlated to the isothermal holding temperature. Under non-isothermal conditions, pure SDS systems are fitted to the Ozawa model (Ozawa, 1971) with an Ozawa exponent of approximately 3, indicating the existence of three-dimensional (3D) crystal growth. Spherulite 3D crystallisation, or 2D crystallisation with sporadic nucleation, of SDS occurs with the SDS + DDAO system on holding at 0 °C. Small-angle X-ray scattering (SAXS) profiles are attained during the crystallisation of SDS + DDAO systems at a variety of cooling rates (0.5 - 10 °C/min). Changes in the form factor $P(Q)$ across the different temperature profiles indicate that a higher cooling rate increases the degree of polydispersity of the crystals.

5.2 Introduction

The difference in chemical potential between the liquid and crystalline state dictates whether crystallisation is thermodynamically possible. However, the rate and occurrence of this phase transformation, as well as the resulting shape and morphology, are dictated by kinetic processes such as nucleation and crystal growth (Di Lorenzo and Silvestre, 1999; Vedantam and Ranade, 2013).

The Avrami equation has been used to describe the isothermal kinetics of crystallisation across a variety of systems. Michael Avrami (Avrami, 1941; Avrami, 1939; Avrami, 1940) first proposed the Avrami equation in the 1930s in order to describe the change in the crystallite content over time, which typically follows a sigmoidal curve. In recent years, many transformations have been described by fitting data to a linear form (equation 5.1) of the Avrami equation (Marangoni, 1998).

$$\ln[-\ln(1 - X(t))] = n \ln t + \ln k \quad (5.1)$$

where $X(t)$ is the crystalline fraction, k is a rate constant, n is the Avrami exponent and t is the crystallisation time.

The Avrami exponent (n) is a sum of two terms, n_d and n_n (Lorenzo *et al.*, 2007). The former, n_d , is the dimensionality part of the exponent and therefore depends on whether the growth is one dimensional ($n_d = 1$), two dimensional ($n_d = 2$) or three dimensional ($n_d = 3$) (Pei *et al.*, 2010; Torrens-Serra *et al.*, 2011). The latter constant, n_n , is related to the type of nucleation. Values of 1 and 0 are attained for sporadic nucleation and instantaneous nucleation, respectively (Monasse and Haudin, 1986). During sporadic nucleation there are a limited number of nucleation sites and further sites continue to form throughout the phase transition (Özcan *et al.*, 2003).

Non-isothermal kinetics are probably more relevant to industry but are covered by a smaller body of research due to the difficulties inherent in their study. For example, during polymer production the cooling rate was found to impact the crystalline fraction and the temperature of crystallisation (Di Lorenzo and Silvestre, 1999; Supaphol *et al.*, 2004). There have been attempts to modify the Avrami equation to describe non-isothermal kinetics. For example, Ziabicki proposed that a non-isothermal crystallisation process could be represented by a sequence of isothermal sections, each described by the Avrami equation (Ziabicki, 1974). In

the 1970s, Ozawa extended the Avrami equation to describe the non-isothermal study of polyethylene terephthalate crystallisation (Ozawa, 1971; Durmus *et al.*, 2010). From this work, the Ozawa equation (equation 5.2) was introduced:

$$\log [-\ln(1 - X(T))] = \log K - m \log a \quad (5.2)$$

where $X(T)$ is the crystalline fraction at temperature T , m is Ozawa exponent, a is the cooling rate and K is a constant relating to the cooling. In order to apply the Ozawa equation to a system, it is necessary to know the degree of crystallisation at a specific temperature and across a range of cooling rates, potentially limiting its application. In some systems an acceptable fit is not achieved, likely due to secondary crystallisation not being taken into account (Chen *et al.*, 2016). Furthermore, this theory also assumes that a constant cooling rate is present (Monasse and Haudin, 1986), which may not necessarily be the case.

In 1998, Lui and co-workers proposed a further modification by combining both the Ozawa and Avrami equations (An *et al.*, 1998) to give equation 5.3:

$$\log a = \log F - b \log t \quad (5.3)$$

where t is the crystallisation time, a is the cooling rate, $b = \frac{m}{n}$ and F is a cooling rate function. As previously, m and n are the Ozawa and Avrami exponents, respectively. Values for b and F can be attained from a plot of the cooling rate against the time taken to reach a specific percent of crystallinity. Crystallisation of polyether ether ketone (PEEK) has successfully been described by this model, for which the Ozawa model was not appropriate (Kuo *et al.*, 2006). Furthermore, the Ozawa-Avrami model was used for studying the isothermal crystallisation of polypropylene/silicon nitride nanocomposites (Hao *et al.*, 2010).

Differential scanning calorimetry (DSC) is often used to perform crystallisation studies and understand the kinetics of processes (Xu *et al.*, 2009; Hao *et al.*, 2010). This analytical

technique detects phase transitions by measuring the difference in the heat flow between the reference and sample cell upon application of the same temperature profile. Both isothermal and non-isothermal studies can be performed on this instrument and the proportion of crystalline material formed can be determined (Lorenzo *et al.*, 2007; Jeziorny, 1978). A study performed by Ratta *et al.* on polyimide crystallisation stated that the normalised crystallised content at time t , $X(t)$, can be given by the enthalpy of crystallisation up to time t as a fraction of the total enthalpy of the phase transition (Ratta *et al.*, 2000). It is possible to relate the peak area of a phase transition directly to $X(t)$ (equation 5.4) since peak area and enthalpy are proportional (Brittain and Bruce, 2006). The thermograms

$$X(t) = \frac{A(t)}{A_t(\infty)} \quad (5.4)$$

where $A(t)$ is the area of the peak up to time t and $A_t(\infty)$ is the total area of the peak.

In recent years, X-ray scattering has been increasingly used to observe crystallisation due to the high resolution and fast data acquisition possible at synchrotron sources. For example, X-rays were used to study the C49 to C54 phase transformation that occurs in titanium disulfide thin films. The change in area under the Bragg peaks over time was used to deduce rate of crystal growth and attain an Avrami plot (Özcan *et al.*, 2003).

The intensity of a small-angle X-ray scattering profile has contributions from both the form factor $P(Q)$ and the structure factor $S(Q)$, with the latter resulting from inter-particle scattering (Cosgrove, 2010). The form factor, $P(Q)$, is dependent on the distribution of particle radii. When there is variation in the radii of individual particles, the oscillations average out to a smooth slope (Cosgrove, 2010). Although the gradient of the slope is not affected by polydispersity, the maximum and minimum are more prominent with monodispersed samples.

This chapter focuses on understanding the kinetics of crystallisation of sodium dodecyl sulfate (SDS) and mixed SDS and N,N-dimethyldodecylamine N-oxide (DDAO) surfactant systems where the surfactant concentration is comparable to that of commercial products (Lai, 1996). DSC is used to investigate isothermal and non-isothermal crystallisation of SDS systems and SAXS is used for investigating the kinetics of crystallisation of SDS + DDAO surfactant systems. This blend of surfactants are of significant importance in the detergent industry where they are extensively used because of their high cleaning and foaming properties, as well as their relatively low cost and high commercial availability (Zoller, 2008).

5.3 Materials and methods

5.3.1 Materials

20 wt. % SDS and 20 wt. % SDS + 3 wt. % DDAO aqueous solutions were used for the DSC and SAXS measurements, respectively. SDS was purchased from Fischer Scientific at a purity level greater than 97.5 %. DDAO was purchased from Sigma Aldrich in aqueous form at a concentration of 30 wt. %. Both surfactants were used without further purification. The solutions were formulated 24 hours in advance to minimise hydrolysis. The solutions were prepared at 25 °C by the addition of distilled water to the surfactants followed by mixing with a magnetic stirrer for 15 minutes. The solutions were then left undisturbed overnight to be used the next day.

5.3.2 Methods

5.3.2.1 Differential scanning calorimetry (DSC)

DSC thermograms of the solutions during cooling were acquired with a Sentaram microDSC, with a ± 0.1 °C accuracy. Approximately 70 mg of the sample, contained within a cell, was

placed into the furnace along with a reference cell filled with 70 mg of distilled water. A software package, Calisto processing, was used to input the required cooling profile. Each DSC experiment was repeated in triplicate. OriginPro (v.9.0) software was used to slice the peaks and attain values for the peak area, and therefore crystalline content, over time. With this data, Avrami plots could subsequently be produced using this graphical package.

5.3.2.1.1 Isothermal studies using DSC

The maximum available cooling rate, 1 °C/min, was used throughout the isothermal studies in order to minimise the possibility of crystallisation during cooling. 12 °C, 13 °C and 14 °C were selected as the different isothermal conditions. After cooling to the required temperature, the SDS system was held for 20 minutes, after which the crystallisation process was complete. Isothermal analysis was not possible at temperatures below this narrow range due to immediate, unmeasurable crystallisation, whereas temperatures exceeding 14 °C did not result in a reproducible phase transition.

5.3.2.1.2 Cooling rate studies using DSC

Cooling rates were investigated in the range 0.1 - 1 °C/min. The system was cooled from 25 °C at the various cooling rates (0.1, 0.2, 0.4, 0.6, 0.8 and 1 °C/min) to an end temperature of -5 °C. The system was held for 20 minutes at this temperature before heating back to 25 °C.

5.3.2.2 Small angle X-ray scattering (SAXS)

SAXS data was obtained using the I22 beamline at the Diamond Light Source, Oxfordshire, UK. Samples were loaded into 1.8 mm (internal diameter) polycarbonate capillaries and mounted in the beam within the Linkam DSC600 capillary stage, which also provided temperature control. A 12.3989 keV ($\lambda = 0.099987$ nm) beam was used with a sample-detector distance of 6702.56 mm, providing a detectable Q -range on the SAXS detector of order 0.02 –

2.5 nm⁻¹. Data processing was performed using the DAWN package (Filik *et al.*, 2017; van der Veen, 2015), and a set of pipelines developed at Diamond Light Source. Before processing, uncertainty estimates based on Poisson counting statistics were added to all measurement data, which were subsequently propagated through the image correction steps. Each raw background measurement was corrected for the following in order: masking pixels, time, incident beam flux, and transmission. Each sample file was corrected for the following: masking pixels, time, incident beam flux, transmission, background, thickness, and scaled to absolute units. The scaling factor for scaling the scattering intensity $I(Q)$ to absolute units was determined using a calibrated glassy carbon sample (Zhang *et al.*, 2010). After this correction, the data was azimuthally averaged, with the resulting uncertainty assuming the largest of: 1) the propagated uncertainties, 2) the standard error of the mean for the data points comprising a bin, or 3) 1% of the mean intensity in the bin.

5.3.2.2.1 Isothermal studies using SAXS

The surfactant solution was cooled to 0 °C at the maximum cooling rate of 19 °C/min. Scans were collected every 4 seconds across a maximum period of 60 minutes. The software package SASfit (Bressler *et al.*, 2015) was used to fit the profiles attained during crystallisation with a simple model comprising of contributions from a Bragg peak, a power law and background scattering and an additional contribution arising from a delta distribution of charged core-shell prolate ellipsoids, corresponding to micelles remaining in solution, to account for the observed signal at high Q (see details in Appendix C). By fitting the profiles, the change in area of the Bragg peak at 1.91 nm⁻¹ over time (see Figure 5.3) could be attained. Corresponding plots were produced in OriginPro (v.9.0) and Sigmaplot was used for fitting sigmoidal models.

5.3.2.2.2 Cooling rate studies using SAXS

Crystallisation of SDS + DDAO systems was studied at the following cooling rates: 0.5, 2.5, 5 and 10 °C/min. Samples were cooled to 0 °C and SAXS profiles acquired every 4 seconds. The SAXS profiles attained 600 seconds after crystallisation started were plotted in OriginPro (v.9.0) for the different cooling rates.

5.4 Results and discussion

5.4.1 Isothermal SDS systems

Using equation 5.4, the crystalline fraction was calculated at various time points during the crystallisation process. The data was used to obtain Avrami plots. The Avrami exponent can be determined from the gradient of the respective Avrami plot, with the corresponding plot for 12 °C provided in Figure 5.1. The plots corresponding to 13 °C and 14 °C along with the replicates are provided in Appendix C. The bar chart in Figure 5.2 displays the change in the value of the Avrami exponent with isothermal holding temperature.

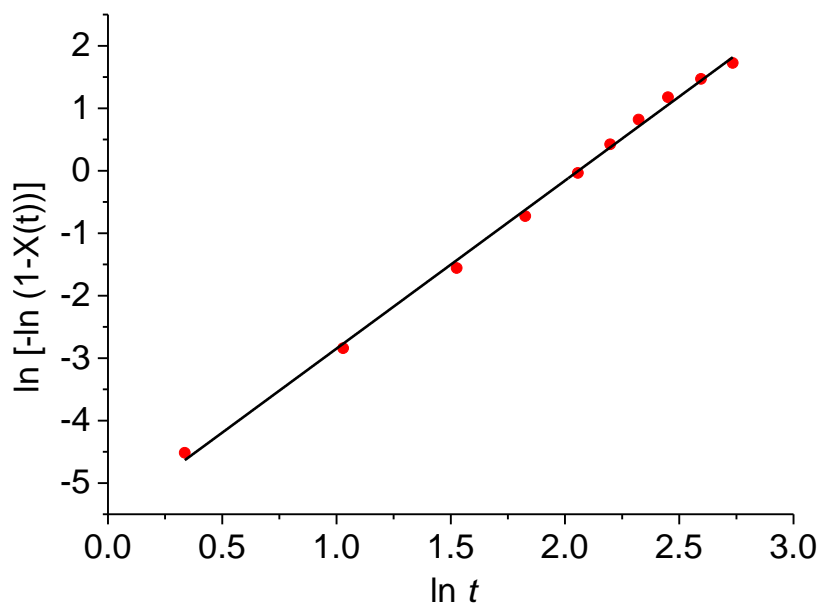


Figure 5.1. Avrami plot for crystallisation of a 20 wt. % SDS solution when held at 12 °C.

Fitted trendline has equation: $y = (2.69 \pm 0.045)x - 5.54 \pm 0.092$ and $R^2 = 0.997$.

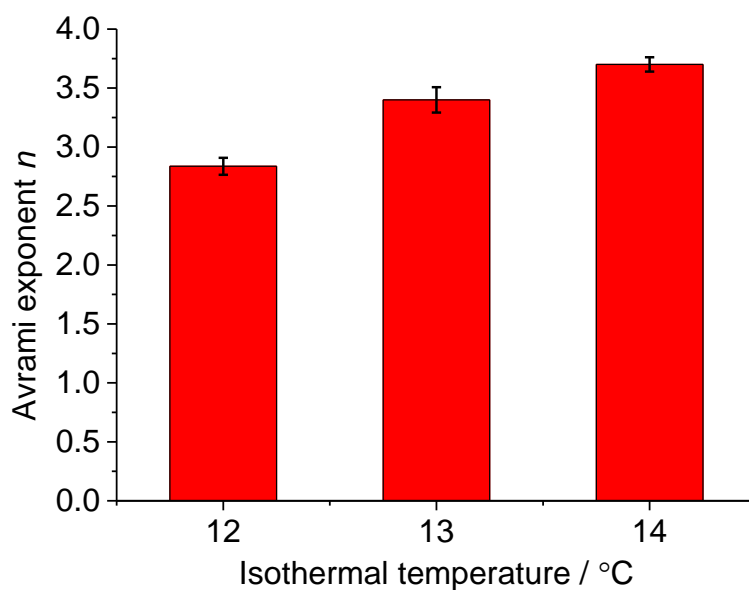


Figure 5.2. Bar chart showing the change in the Avrami exponent for crystallisation of a 20 wt. % SDS solution under various isothermal temperature conditions. Standard errors were calculated from repeated measurements.

An Avrami exponent of approximately 3 was attained when the system crystallised at 12 °C. This indicates the occurrence of 3D spherulite crystal growth and instantaneous nucleation

within the bulk. However, 2D growth and sporadic nucleation would also yield a value of 3. Work performed by Miller *et al.* on SDS crystallisation provided Avrami exponents of 2.9 and 2.3, attained by using DSC and optical microscopy, respectively (Miller *et al.*, 2016). In their study, it was concluded that platelets and needles were forming. Platelets were also observed as part of the confocal Raman study contained in Chapter 4. However, the cooling rates used was considerable larger than the 1 °C/min applied here. Here, as the isothermal temperature increases, the Avrami exponent also increases and tends towards a value of 4 at 14 °C. A value of 4 is only achieved with 3D growth and sporadic nucleation. It is hypothesised that either the nucleation mechanism transitions from instantaneous to a sporadic where the nucleation occurs as a function time, or the dimensionality of the growth increases. In the case of the former, the increase in the Avrami exponent with isothermal temperature is attributed to a decrease in supersaturation of the solution, resulting in the nucleation sites continuing to form during the phase transition (sporadic nucleation). Özcan *et al.* performed a similar study where they reported a change in the type of nucleation when titanium disulphide films transformed from the C49 to C54 phase (Özcan *et al.*, 2003). In their study, the Avrami exponent decreased from 3 to 2 upon a decrease in the isothermal holding temperature. However, since SDS is known to form 2D platelets, from previous isothermal studies at lower temperatures and with higher cooling rates, it is possible that the dimensionality could be progressively changing rather than the nucleation mode.

An isothermal study of a 20 wt. % SDS solution was also performed using small-angle X-ray scattering (SAXS), to provide evidence that the two techniques were comparable. As indicated in Chapter 4, a change in the hydrate structure is observed when studying the crystallisation of a pure SDS system at 0 °C. The structure of interest is the final one that forms, which matches that detected in SDS + DDAO systems. Avrami analysis of this crystal form was attempted using the pure SDS SAXS data. However, it proved challenging to determine the exact point at

which the Bragg peak of this phase started to grow, since the peak was present at very low amplitude for a prolonged period. This time point has an impact on the resultant Avrami exponent. The time that the peak growth began was narrowed to a range between 400 and 500 s after reaching 0 °C. Taking $t = 0$ as 400 s and 500 s gave Avrami exponents of 2.9 and 4.3, respectively. Although a wide range, this is in line with the Avrami exponents acquired from DSC, which range between 3 and 4. This indicates that the SAXS is comparable with DSC, despite the difference in cooling rates. This is important since Avrami analysis of the SDS + DDAO system was performed using SAXS, rather than DSC.

5.4.2 Isothermal SDS + DDAO systems

Isothermal crystallisation of a mixed SDS + DDAO system was investigated using an alternative technique, SAXS, where the change in peak area was related to the progression of the phase transition. Scans acquired across the 60 minute runtime are provided in Appendix C. However, the scans of interest are those acquired between 50 s and 120 s, when the Bragg peak forms. The phase transition began at 52 seconds and a snapshot of SAXS profiles acquired during crystallisation are depicted in Figure 5.3. However, when producing an Avrami plot, $t = 0$ s is taken as the start of the phase transition (52 s after the start of the run). This is evident in Figures 5.4 and 5.5.

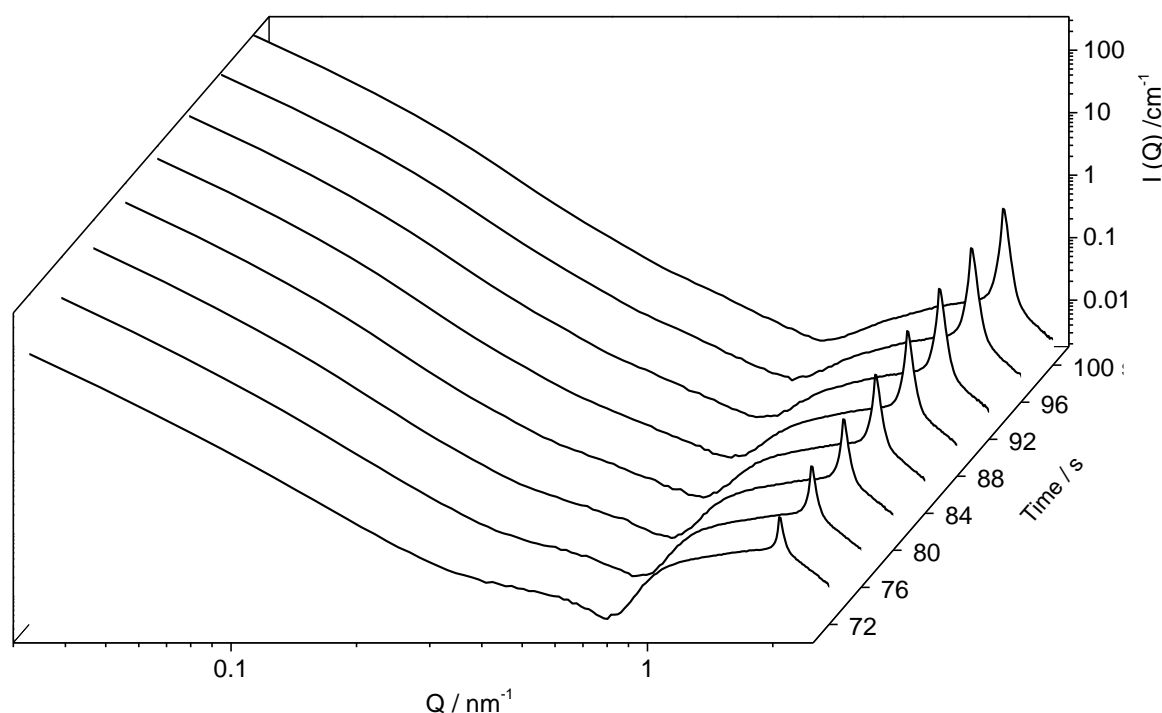


Figure 5.3. Time resolved SAXS profiles acquired during the crystallisation of a 20 wt. % SDS + 3 wt. % DDAO system at 0 °C.

The change in peak area over time for this phase transition is plotted in Figure 5.4, where a typical sigmoidal transformation is observed (Avrami, 1940). The crystal growth can be described by the Avrami equation (equation 5.1). An Avrami plot for the SDS + DDAO system is depicted in Figure 5.5 and the dataset is fitted with a linear trendline with a gradient of 3.07. This gradient indicates an Avrami exponent of 3 which suggests the occurrence of a 3D crystal growth with instantaneous nucleation or, alternately, 2D crystal growth and sporadic nucleation. From previous work, DDAO was found to have a significant effect on both the induction time and the rate of the process (see Chapter 4). Furthermore, in the presence of DDAO, ring-shaped crystals were observed, indicating the presence of 3D growth. The Avrami exponents of both the pure SDS system, at 14 °C, and the mixed SDS + DDAO system suggest the presence of 3D growth. This is most likely because SDS is the major component of the crystals in both systems.

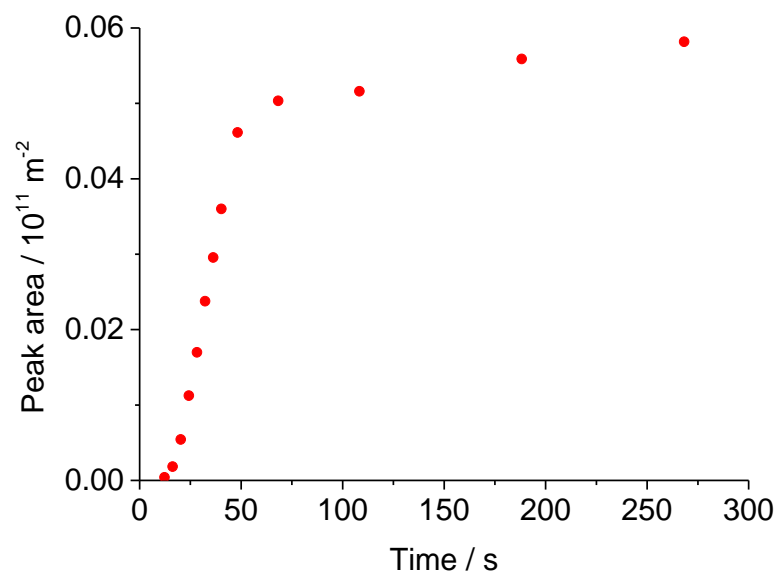


Figure 5.4. Change in peak area upon crystallisation of a 20 wt. % SDS + 3 wt. % DDAO system when held at 0 °C with 0 s taken as the time of initial Bragg peak formation.

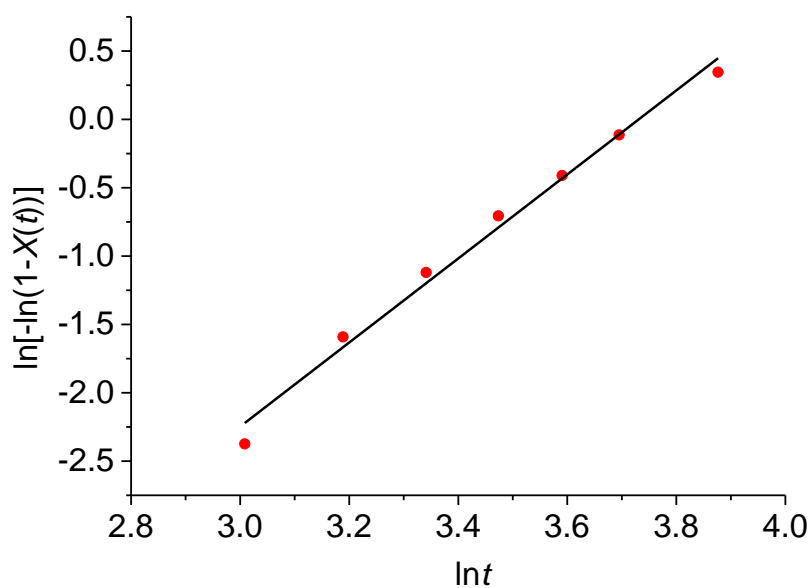


Figure 5.5. Avrami plot for the crystallisation of a 20 wt. % SDS + 3 wt. % DDAO system when held at 0 °C. Fitted trendline has equation: $y = (3.07 \pm 0.141)x - 11.47 \pm 0.488$ and $R^2 = 0.987$.

5.4.3 Non-isothermal SDS systems

DSC thermograms were attained during the crystallisation of a pure SDS aqueous system at different cooling rates (see Chapter 4, Figure 4.3). Despite the limited range of cooling rates, differences are observed between the thermograms. A higher cooling rate resulted in a lowering of the system's crystallisation temperature, corresponding to the peak maxima. Although the crystallisation temperatures and the associated onset and offset temperatures vary between the different cooling rates, the total enthalpy ΔH remains consistent. The cooling thermograms are expressed as heat flow, in $\text{Jg}^{-1}\text{s}^{-1}$, as a function of temperature, in $^{\circ}\text{C}$. Hence the peak area has units of $\text{J}^{\circ}\text{Cg}^{-1}\text{s}^{-1}$. To acquire the enthalpy of crystallisation, in Jg^{-1} , the peak area must be divided by the corresponding cooling rate.

Since the cooling rate is constant for each experimental run, the enthalpy and peak area are directly proportional (Kuo *et al.*, 2006). Therefore, the normalised crystalline content of a sample at temperature T can be expressed as:

$$X(T) = \frac{A(T)}{A_T(\infty)} \quad (5.5)$$

where $X(T)$ is the relative normalised crystalline content at temperature T , $A(T)$ is the area of the cooling thermogram from the start of the crystallisation until temperature T and $A_T(\infty)$ is the total area of the crystallisation peak (Shapaan and Shaaban, 2010). The plot in Figure 5.6 illustrates the change in $X(T)$ with temperature at different cooling rates, where all rates display a sigmoidal curve of crystal formation. Initially the growth is limited by the probability of nucleation. Once nuclei of a critical radii have formed, the growth then proceeds at a faster rate before slowing towards the end of the phase transition when the new phase can act as a boundary to any further solid formation.

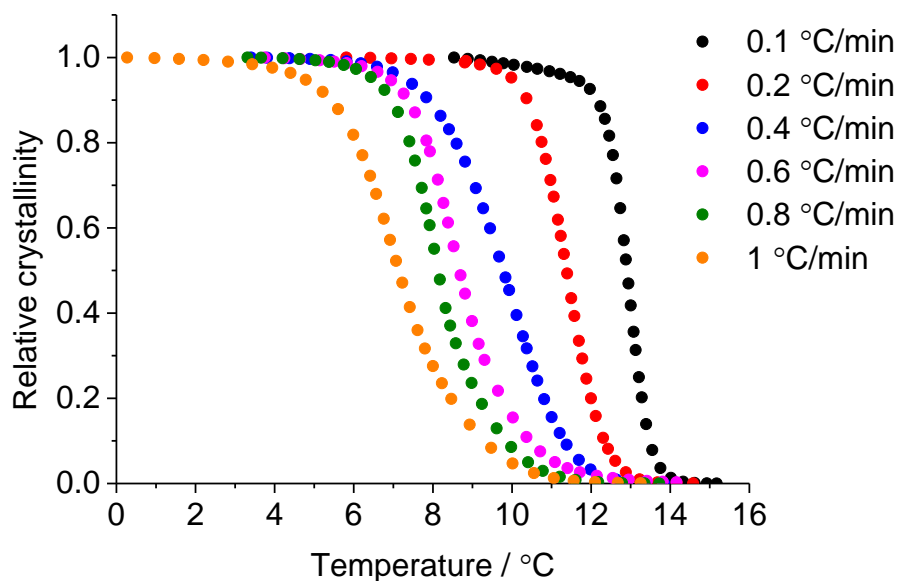


Figure 5.6. Relative change in the crystalline fraction with temperature for crystallisation of a 20 wt. % SDS system upon cooling to -5°C across a range of cooling rates (0.1°C/min - 1°C/min).

It is commonplace in crystallisation studies for the half life time of crystallisation to be reported and compared across a range of conditions. This crystallisation half life, $t_{1/2}$, is defined as the time taken to achieve a relative crystallinity of 0.5. A plot of relative crystallinity versus time is provided in Figure 5.7 where time, Δt , is calculated using equation 5.6:

$$\Delta t = \frac{T - T_0}{a} \quad (5.6)$$

where T is the temperature, T_0 is the starting temperature and a is the cooling rate.

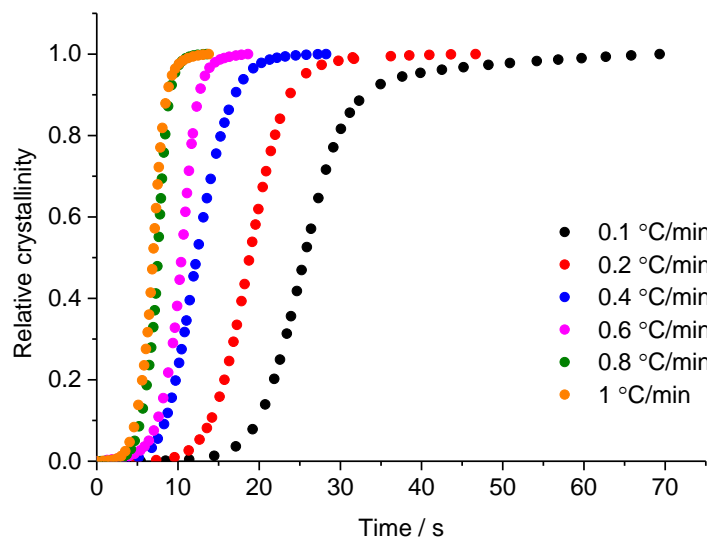


Figure 5.7. Relative change in the crystalline fraction with time for crystallisation of a 20 wt. % SDS system upon cooling to -5°C across the range of cooling rates (0.1°C/min - 1°C/min).

Using SigmaPlot, the best fit for the plots in Figure 5.7 can be achieved with the sigmoidal function (equation 5.7):

$$f = a[1 + e^{-\left(\frac{x-x_0}{b}\right)}]^{-1} \quad (5.7)$$

where f is the degree of relative crystallinity, x is the time from the start of crystallisation and x_0 , a and b are all constants. The values of x_0 , a and b that provide the best sigmoidal fit are listed in Table 5.1. $t_{1/2}$ was obtained on substitution of $f = 0.5$ into equation 5.7.

Table 5.1. Parameters attained when fitting a sigmoidal function to the crystallisation profiles of a 20 wt. % SDS system attained at a selection of different cooling rates (0.1 - 1°C/min).

Cooling rate / $^{\circ}\text{C/min}$	a	x_0	b	$t_{1/2}$ / s
0.1	0.9776	25.50	2.771	25.63
0.2	0.9948	18.79	2.214	18.82
0.4	0.9933	12.36	1.943	12.39
0.6	1.007	10.39	1.140	10.37
0.8	1.007	7.467	0.7808	7.457
1	1.002	6.887	0.8499	6.884

If $t_{1/2}$ is short, as occurs at the higher cooling rates, the crystal formation process is fast. Upon exposure to higher cooling rates the solution becomes increasingly supersaturated after a given time, compared to lower cooling rates, resulting in faster nucleation throughout the solution. Although it may be possible to describe the primary stage of the non-isothermal crystallisation with the Avrami equation, other models, such as the Ozawa model, are required to fully describe the process.

5.4.3.1 Ozawa model

Applying the Ozawa model requires the presence of a temperature at which crystallisation is occurring across all investigated cooling rates. 12 °C was selected as an appropriate temperature condition for the pure SDS system and the crystalline fraction $X(T)$ at this temperature for each cooling rate was calculated using equation 5.6.

The gradient of the plot of $\log a$ against $\log[-\ln(1 - X(T))]$ gives the Ozawa exponent, from which it is possible to gain further insight into the nature of the crystal growth (Figure 5.8).

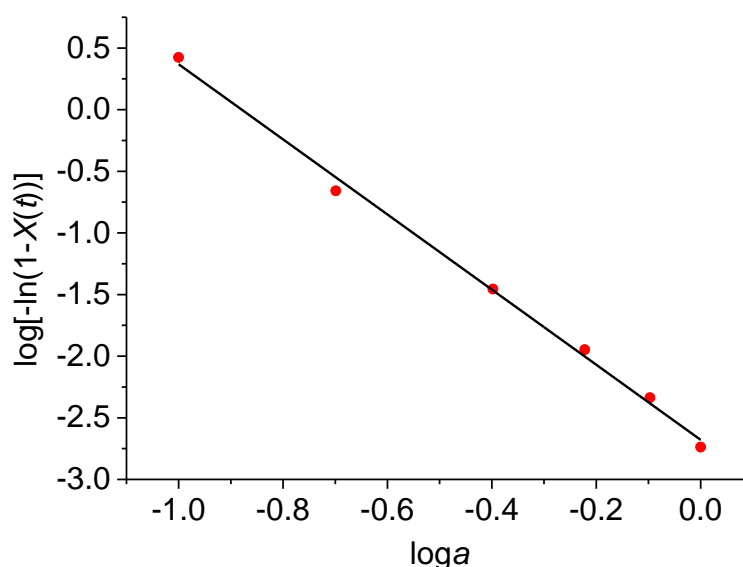


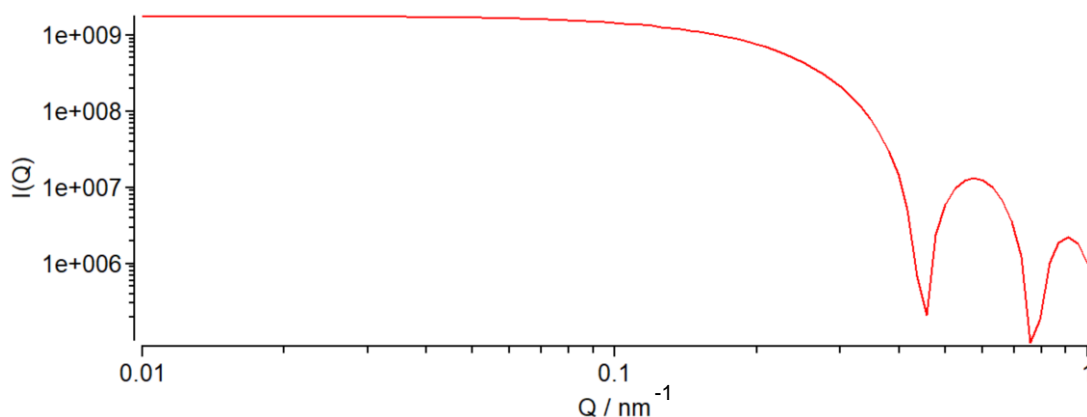
Figure 5.8. Ozawa plot for crystallisation of a 20 wt. % SDS solution. Fitted trendline has equation: $y = -(3.05 \pm 0.091)x - 2.68 \pm 0.048$ and $R^2 = 0.996$.

The trendline $\log[-\ln(1 - X(T))] = -3.05 \log a - 2.68$ was fitted to the data set. The Ozawa constant, m , was 3.05 and a K value of 2.68 was obtained. This m value implies that 3D growth occurs. Non-isothermal crystallisation of pure SDS systems was previously studied using optical microscopy and DSC (Miller *et al.*, 2017). A value of 2.6 was attained for the Avrami exponent, varying from the Ozawa exponent value calculated in this study. However, Miller *et al.* utilised the Avrami equation which is not necessarily valid for non-isothermal studies. As evident from the low standard errors in the slope in Figure 5.8, the non-isothermal crystallisation of SDS can be successfully described by the Ozawa equation.

5.4.4 Non-isothermal SDS + DDAO systems

The influence of the cooling rate on the crystallisation of the SDS + DDAO system was explored, using SAXS, across a wider range than for the pure SDS system. The cooling rate was found to influence the degree of polydispersity in the system. All profiles have a $P(Q)$, represented by an oscillatory function caused by the scattering from crystallites during initial formation. However, the oscillations are smoothed over by the presence of polydispersity. There are different types of polydispersity, including shape, size and conformational dispersity. For the purpose of this work the focus is size polydispersity when particles bear the same shape but differ in radii, a common occurrence in colloidal systems. Highly monodispersed systems have more prominent oscillations, whereas a distribution of particle radii results in a smoothing of the slope (Hollamby, 2013). This can be shown by simulations of hard spheres in SASfit, provided in Figures 5.9 (a) and (b). As the distribution of radii increases, the oscillations in the slope begin to smooth out.

(a)



(b)

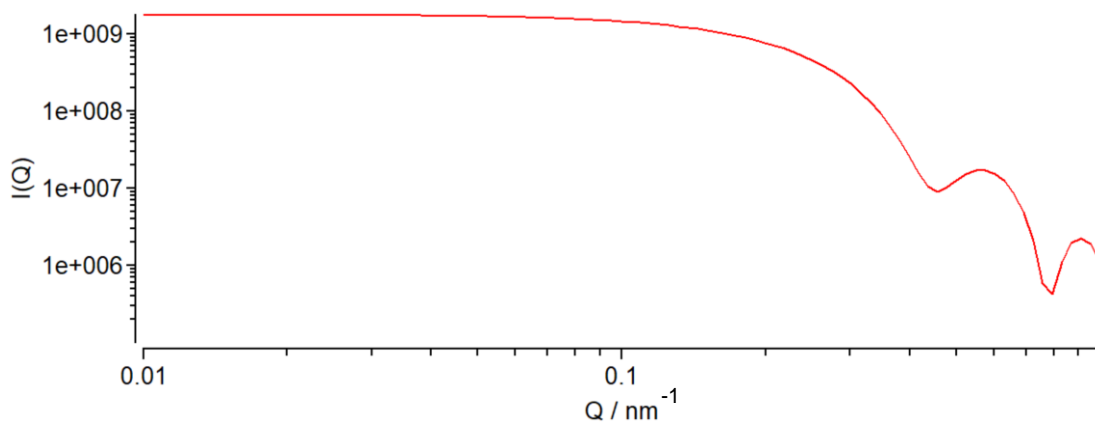


Figure 5.9 (a) Simulation of data for hard spheres of $R = 10$ nm and (b) a mix of both $R = 10$ nm and $R = 5$ nm.

For the SDS + DDAO systems, differences in polydispersity across the different cooling rates are evident from the resulting scattering profiles, shown in Figure 5.10.

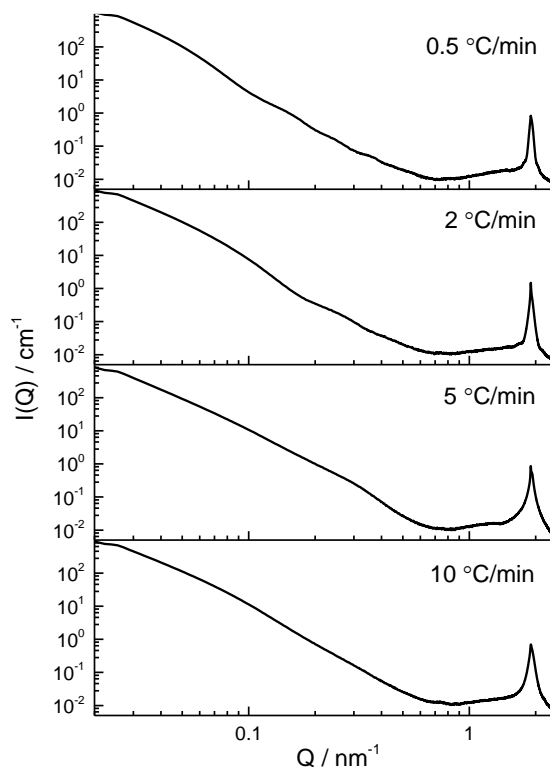


Figure 5.10. SAXS profiles acquired 600 s after the beginning of the crystallisation process occurring in a 20 wt. % SDS + 3 wt. % DDAO system, across a range of cooling rates.

Oscillations appear in the slope at low Q at the lower cooling rates (0.5 and 2 °C/min) but, conversely, are not observed at the higher cooling rates. It is evident from Figure 5.10 that increasing the cooling rate increases the degree of polydispersity of the nuclei. The maximum and minimum of the form factor are only visible in the samples with lower cooling rates: 0.5 and 2 °C/min. Variations in polydispersity has been previously documented in other systems, including the crystallisation of mefenamic acid in ethyl acetate (Mudalip *et al.*, 2017), where the narrowest crystal size distribution was found to result at the lower cooling rates. When a solution is cooled slowly the rate of nucleation is lower than at a higher cooling rate, resulting in the controlled formation of similarly sized crystals. At higher cooling rates the system nucleates rapidly producing a wider crystal size distribution.

5.5 Conclusions

Isothermal crystallisation of a 20 wt. % SDS system was described with the Avrami equation. An increase in the Avrami exponent from 3 to 4 was observed upon increasing the holding temperature from 12 °C to 14 °C. This indicated a change in the nucleation mode from instantaneous to sporadic or a transition in dimensionality from 2 to 3, both with sporadic nucleation. Previous studies, including those presented in Chapter 4, indicate 2D growth, in the form of platelets and needles (Miller *et al.*, 2016). However, the range of cooling rates used varies from those applied in this study. With the mixed SDS + DDAO system, an Avrami exponent of 3 was acquired upon holding at 0 °C indicating 2D or 3D growth occurs, depending on the mode of nucleation. However, it is likely that the latter, 3D growth, is occurring, since ring-shaped crystals have been observed by confocal Raman microscopy (Chapter 4).

Non-isothermal crystallisation of the SDS system across a range of cooling rates, from 0.1 to 1 °C/min, was successfully described using the Ozawa equation. An Ozawa exponent of 3 was obtained, indicating 3D crystal growth. A prior non-isothermal study attained a value of 2.6 for the Avrami exponent, but the Avrami equation is not necessarily valid for non-isothermal studies (Miller *et al.*, 2017). Crystallisation of the SDS + DDAO system was investigated across a wider range of cooling rates with X-ray scattering and it was possible to infer about changes in the polydispersity of the crystals. As the cooling rate decreased the polydispersity of the crystallites also decreased, which is attributed to the slower nucleation rate at the lower cooling rates thus enabling for more controlled crystal growth.

There are few studies discussing the crystallisation of surfactants, despite the importance of surfactant solutions and their stability within the homecare, food and personal care industries. In this study, insight into the crystallisation kinetics of 20 wt. % SDS and 20 wt. % SDS + 3 wt. % DDAO systems has been presented from both an isothermal and a non-isothermal

perspective which will help further the understanding of the crystallisation process responsible for stability issues in some detergents. It is anticipated that this knowledge will help industry to improve product stability and test methods as part of their ongoing research and development.

5.6 References

- An, Y., Dong, L., Mo, Z., Liu, T. & Feng, Z. 1998. Nonisothermal crystallization kinetics of poly(β -hydroxybutyrate). *Journal of Polymer Science Part B: Polymer Physics*, 36, 1305-1312.
- Avrami, M. 1939. Kinetics of phase change. I General theory. *The Journal of Chemical Physics*, 7, 1103-1112.
- Avrami, M. 1940. Kinetics of phase change. II Transformation-time relations for random distribution of nuclei. *The Journal of Chemical Physics*, 8, 212-224.
- Avrami, M. 1941. Granulation, phase change, and microstructure kinetics of phase change. III. *The Journal of chemical physics*, 9, 177-184.
- Bressler, I., Kohlbrecher, J. & Thunemann, A. F. 2015. SASfit: a tool for small-angle scattering data analysis using a library of analytical expressions. *Journal of Applied Crystallography*, 48, 1587-1598.
- Brittain, H. G. & Bruce, R. D. 2006. Chapter 4 Thermal analysis. *Comprehensive Analytical Chemistry*. Elsevier.
- Chen, Z., Hay, J. N. & Jenkins, M. J. 2016. The effect of secondary crystallization on crystallization kinetics – Polyethylene terephthalate revisited. *European Polymer Journal*, 81, 216-223.
- Cosgrove, T. 2010. *Colloid Science: Principles, Methods and Applications*, Wiley.
- Di Lorenzo, M. & Silvestre, C. 1999. Non-isothermal crystallization of polymers. *Progress in Polymer Science*, 24, 917-950.

- Durmus, A., Ercan, N., Soyubol, G., Deligöz, H. & Kaşgöz, A. 2010. Nonisothermal crystallization kinetics of poly(ethylene terephthalate)/clay nanocomposites prepared by melt processing. *Polymer Composites*, 31, 1056-1066.
- Filik, J., Ashton, A. W., Chang, P. C. Y., Chater, P. A., Day, S. J., Drakopoulos, M., Gerring, M. W., Hart, M. L., Magdysyuk, O. V., Michalik, S., Smith, A., Tang, C. C., Terrill, N. J., Wharmby, M. T. & Wilhelm, H. 2017. Processing two-dimensional X-ray diffraction and small-angle scattering data in DAWN 2. *Journal of Applied Crystallography*, 50, 959-966.
- Hao, W., Yang, W., Cai, H. & Huang, Y. 2010. Non-isothermal crystallization kinetics of polypropylene/silicon nitride nanocomposites. *Polymer Testing*, 29, 527-533.
- Hollamby, M. J. 2013. Practical applications of small-angle neutron scattering. *Physical Chemistry Chemical Physics*, 15, 10566-10579.
- Jeziorny, A. 1978. Parameters characterizing the kinetics of the non-isothermal crystallization of poly(ethylene terephthalate) determined by D.S.C. *Polymer*, 19, 1142-1144.
- Kuo, M. C., Huang, J. C. & Chen, M. 2006. Non-isothermal crystallization kinetic behavior of alumina nanoparticle filled poly(ether ether ketone). *Materials Chemistry and Physics*, 99, 258-268.
- Lai, K. Y. 1996. *Liquid Detergents*, CRC Press.
- Lorenzo, A. T., Arnal, M. L., Albuerne, J. & Müller, A. J. 2007. DSC isothermal polymer crystallization kinetics measurements and the use of the Avrami equation to fit the data: guidelines to avoid common problems. *Polymer Testing*, 26, 222-231.
- Marangoni, A. G. 1998. On the use and misuse of the Avrami equation in characterization of the kinetics of fat crystallization. *Journal of the American Oil Chemists' Society*, 75, 1465-1467.

- Miller, R. M., Ces, O., Brooks, N. J., Robles, E. S. J. & Cabral, J. T. 2017. Crystallization of Sodium Dodecyl Sulfate-Water Micellar Solutions under Linear Cooling. *Crystal Growth & Design*, 17, 2428-2437.
- Miller, R. M., Poulos, A. S., Robles, E. S. J., Brooks, N. J., Ces, O. & Cabral, J. T. 2016. Isothermal Crystallization Kinetics of Sodium Dodecyl Sulfate–Water Micellar Solutions. *Crystal Growth and Design*, 16, 3379-3388.
- Monasse, B. & Haudin, J. 1986. Thermal dependence of nucleation and growth rate in polypropylene by non isothermal calorimetry. *Colloid & Polymer Science*, 264, 117-122.
- Mudalip, S. A., Adam, F., Parveen, J., Bakar, M. A., Amran, N., Sulaiman, S., Man, R. C., Arshad, Z. M. & Shaarani, S. M. Effect of Cooling Rates on Shape and Crystal Size Distributions of Mefenamic Acid Polymorph in Ethyl Acetate. IOP Conference Series: Materials Science and Engineering, 2017. IOP Publishing, 012025.
- Ozawa, T. 1971. Kinetics of non-isothermal crystallization. *Polymer*, 12, 150-158.
- Özcan, A., Ludwig Jr, K., Lavoie, C., Cabral Jr, C. & Harper, J. 2003. Time-resolved X-ray diffraction studies of the texture formation kinetics in the C49-C54 TiSi₂ phase transformation. *Journal of Research of the National Institute of Standards and Technology Diffraction Standards*, 46, 157-162
- Pei, A., Zhou, Q. & Berglund, L. A. 2010. Functionalized cellulose nanocrystals as biobased nucleation agents in poly(L-lactide) (PLLA) - Crystallization and mechanical property effects. *Composites Science and Technology*, 70, 815-821.
- Ratta, V., Ayambem, A., Young, R., Mcgrath, J. E. & Wilkes, G. L. 2000. Thermal stability, crystallization kinetics and morphology of a new semicrystalline polyimide based on 1,3-bis(4-aminophenoxy) benzene and 3,3',4,4'-biphenyltetracarboxylic dianhydride. *Polymer*, 41, 8121-8138.

- Shapaan, M. & Shaaban, E. R. 2010. Studying the crystallization behavior of the $\text{Se}_{85}\text{S}_{10}\text{Sb}_5$ chalcogenide semiconducting glass by DSC and X-ray diffraction. *Journal of Physics and Chemistry of Solids*, 71, 1301-1305.
- Supaphol, P., Dangseeyun, N. & Srimoan, P. 2004. Non-isothermal melt crystallization kinetics for poly(trimethylene terephthalate)/poly(butylene terephthalate) blends. *Polymer Testing*, 23, 175-185.
- Torrens-Serra, J., Venkataraman, S., Stoica, M., Kuehn, U., Roth, S. & Eckert, J. 2011. Non-isothermal kinetic analysis of the crystallization of metallic glasses using the master curve method. *Materials*, 4, 2231-2243.
- Van Der Veen, J. F. 2015. JSR - XFELs, DLSRs and beamline articles. *Journal of Synchrotron Radiation*, 22, 1-2.
- Vedantam, S. & Ranade, V. V. 2013. Crystallization: Key thermodynamic, kinetic and hydrodynamic aspects. *Sadhana-Academy Proceedings in Engineering Sciences*, 38, 1287-1337.
- Xu, Y., Huang, L.-M., Zhang, R.-C., Lu, A., Li, Z.-M. & Sun, J. 2009. Dependence of the avrami exponent on supercooling during nonisothermal crystallization of poly (phenylene sulfide). *Polymer-Plastics Technology and Engineering*, 48, 324-326.
- Zhang, F., Ilavsky, J., Long, G. G., Quintana, J. P. G., Allen, A. J. & Jemian, P. R. 2010. Glassy Carbon as an Absolute Intensity Calibration Standard for Small-Angle Scattering. *Metallurgical and Materials Transactions A*, 41, 1151-1158.
- Ziabicki, A. 1974. Theoretical analysis of oriented and non isothermal crystallization. *Colloid & Polymer Science*, 252, 207-221.
- Zoller, U. 2008. Handbook of Detergents, Part E. CRC Press.

CHAPTER 6

FACTORS AFFECTING THE LOW TEMPERATURE STABILITY OF COMPLEX DISH LIQUID SYSTEMS

6.1 Abstract

Building on the knowledge gained from studying mixed sodium dodecyl sulfate (SDS) and N,N-dimethyldodecylamine N-oxide (DDAO) systems, this chapter explores the crystallisation of unstable dish liquid products at low and sub-zero temperatures. Alkyl sulfates are found to be the major component of the crystals, composed of surfactant rich layers separated by layers of water. In addition, nuclear magnetic resonance (NMR) showed that the crystals do not contain any ethoxylated alkyl sulfates.

Product stability at low temperatures is extensively studied across many formulations. The occurrence of crystallisation is detected via time lapse photography and light transmission techniques. The amount of alkyl sulfate alcohol precursor, the alkyl sulfate to amine oxide ratio and chemical nature of the alkyl sulfate paste in the formulation are shown to have a strong influence on the stability of this homecare product at low temperatures. Increasing the amount of alkyl sulfate alcohol precursor increases the susceptibility of a formulation to crystallisation. Furthermore, a greater concentration of amine oxide improves the product stability at low and sub-zero temperatures. Ethoxylated variants in the alkyl sulfate paste also help to improve the stability of dish liquid products.

6.2 Introduction

As a result of a daily need for detergent formulations worldwide, these products must demonstrate chemical and physical stability across a wide range of temperatures and climates (Summerton *et al.*, 2017). With the constant move towards low-cost, greener raw materials, formulation of detergent products is an important part of research and development within industry. In dish liquid formulations, the major components are anionic surfactants (alkyl sulfates), amphoteric surfactants (amine oxides) and water (Lai, 1996). This combination forms

the basis of a model system previously presented in Chapters 2-5. Anionic surfactants are used in detergents because of their strong cleaning ability, foaming properties (Prud'homme, 2017; Subramanyan and Ananthapadmanabhan, 2007) and relatively low cost. Amine oxides are added, despite their greater cost, because of high compatibility with the other ingredients and their foaming capability (Schramm *et al.*, 2003). The finished product also contains other components such as preservatives, dyes, ethanol, propylene glycol, perfume and salt, albeit at much lower concentrations. It is vital that dish liquid products demonstrate a high level of foaming, optimal cleaning performance, minimal skin irritation as well as retaining chemical and physical stability across a range of conditions (Showell, 2016). This chapter focuses on understanding how changes in the composition of dish liquid formulations can affect the stability at low temperatures, when crystalline entities form in the solution.

Previous studies in Chapters 2-5 have focused on understanding the nature of this crystallisation process through the use of pure SDS and mixed sodium dodecyl sulfate (SDS) and N,N-dimethyldodecylamine N-oxide (DDAO) aqueous systems with the surfactants present at concentrations typical of those in commercial dish liquid. Through nuclear magnetic resonance (NMR) and small-angle X-ray scattering (SAXS) studies, the crystals were found to be mainly composed of SDS hydrates with no or little DDAO present. In these crystals, SDS-rich layers are separated by water layers. The same SDS hydrated crystals were detected upon cooling pure SDS and mixed SDS + DDAO surfactant systems. However, an intermediary crystal structure was only detected with the pure SDS system. The presence of DDAO was found to reduce the tendency for SDS to crystallise as a result of an increased viscosity (ZaNa, 2007) and more stable micelles. DDAO inserts into the SDS micelles and reduces the repulsion between the negatively charged headgroups. This increases the favourability to form micelles and, in doing so, lowers the monomer concentration available to form crystals. As a result, there is a decrease

in the drive for crystallisation and the Krafft temperature of the system reduces (Soontravanich and Scamehorn, 2009; Soontravanich, 2007).

In addition to the presence of DDAO, the alcohol precursor of SDS, 1-dodecanol, was also found to influence SDS crystallisation (Summerton *et al.*, 2016). 1-dodecanol promotes SDS crystallisation by acting as a seed for the phase transition, with SDS crystals forming around the alcohol globules.

In this work, knowledge gained from the simple model systems is applied to dish liquid systems. Previous studies on the model SDS and SDS + DDAO systems indicated factors which could influence stability. The effect of three variables on formulation stability at low temperatures are considered in this investigation. These include the degree of ethoxylation in the alkyl sulfate component, the ratio between anionic and amphoteric surfactants and the amount of the alkyl sulfate alcohol precursor present in the formulation. Compositional and structural studies are also performed on the crystals that form in dish liquid.

6.3 Materials and methods

6.3.1 Materials

Figure 6.1 shows a simplified flow diagram of dish liquid manufacture. The pastes of the anionic (alkyl sulfates) and the amphoteric (amine oxides) surfactants are combined to form a concentrated mixed surfactant paste. This is used to produce the final formulation.

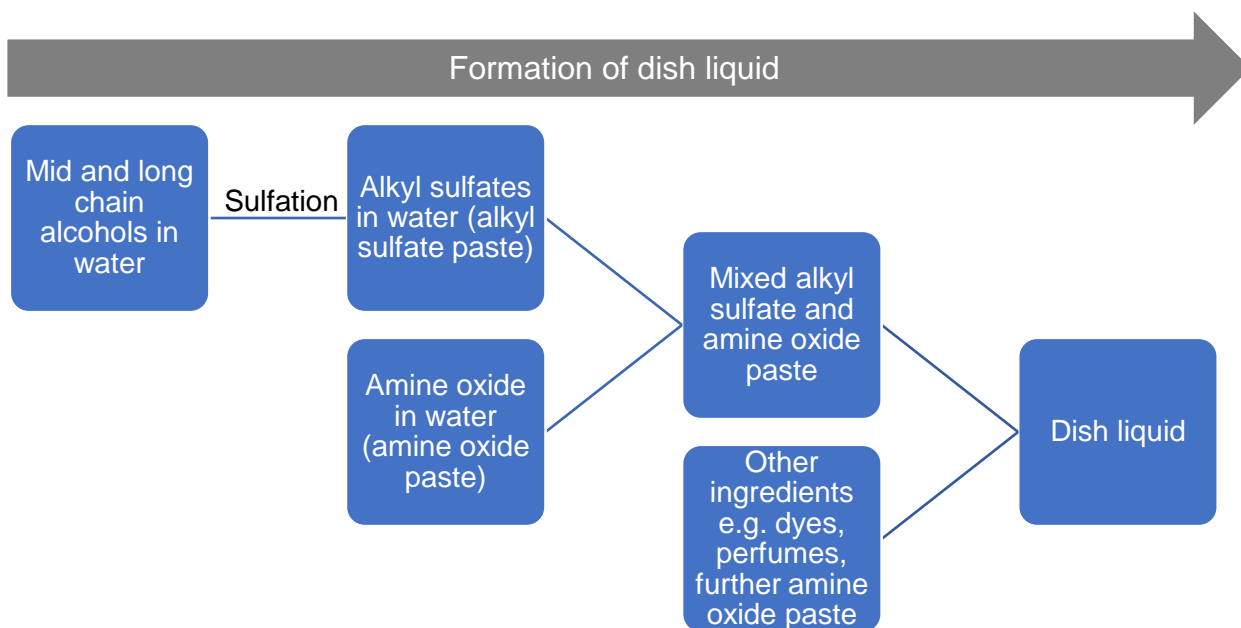


Figure 6.1. Simplified flow diagram for producing dish liquid (Bettiol et al., 2013).

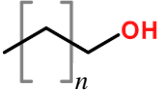
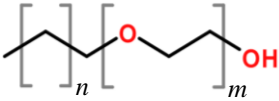
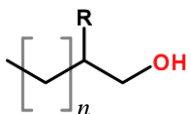
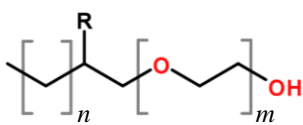
6.3.1.1 Surfactant pastes

The surfactants used in dish liquid products are supplied to P&G as concentrated aqueous pastes before the remaining ingredients are added. One paste comprising solely of the anionic (alkyl sulfates) and a second composed of the amphoteric (amine oxides) surfactants were analysed at concentrations of 20 wt. % and 3 wt. %, respectively. To attain the required surfactant concentration samples were diluted with D₂O, for NMR, or in distilled water, for DSC measurements, and subsequently mixed for 15 minutes at room temperature before being left for 24 hours so entrapped air could be released from the system.

The exact composition of the pastes was not available. However, the total carbon number of the alkyl sulfates was known to be a distribution of C12, C13, C14 and C16. This alkyl sulfate paste $C_xH_y(OCH_2CH_2)_mOSO_3^- Na^+$ also contained a distribution of ethoxylation degrees m . The average degree of ethoxylation in this paste was 0.6 indicating most of the alkyl sulfates exhibit $m = 0$ or 1. The amine oxide paste contained a distribution of C12, C14 and C16 linear chains.

As shown in Figure 6.1, the alkyl sulfate paste is formed from alcohol blends. For example, SDS is produced *in situ* from 1-dodecanol. The alcohol blends contain natural and synthetic alcohols. The total carbon number for natural alcohols is a distribution of C12, C14 and C16. Synthetic alcohols have a total carbon number of C12 or C13 and may contain branching at the C2 position. Both types may contain ethoxylated alcohols. The four different categories of alcohols are provided in Table 6.1. Many variations of each type are possible due to changes in the main carbon chain length, the branched carbon chain length and the number of ethoxy units.

Table 6.1. Four categories of alcohols present in blends used in the production of alkyl sulfates present in dish liquid formulations.

Category name	Origin	Structure
Linear alcohol LA	Natural and Synthetic	 $n = 10 - 14$
Linear alcohol ethoxylate LAE	Natural and Synthetic	 $n = 0 - 8$ $m = 1 - 7$
Branched alcohol BrA	Synthetic	 $n = 5 - 9$ $R = C_aH_b$ where $a = 1 - 5$
Branched alcohol ethoxylate BrAE	Synthetic	 $n = 0 - 7$ $m = 1 - 4$ $R = C_aH_b$ where $a = 1 - 5$

The amount of synthetic and natural alcohols in marketed formulations depends on their relative prices, which fluctuates with time. As a result, P&G follow a process known as ‘surflexing’ where they change the alcohol blend depending on the current market.

A mixed surfactant paste containing both alkyl sulfates and amine oxides was also utilised in NMR studies. The total surfactant concentration of the paste was 63.48 wt. %. The paste was

diluted with D₂O to obtain a surfactant concentration of 23 wt. %, which was used in the measurements.

6.3.1.2 Dish liquid formulations

Specific details of each formulation cannot be disclosed but a general overview of the production process is provided. The total surfactant concentration, active level, in a dish liquid formulation is typically 28.69 wt. %. Typically, they contain 20.76 wt. % sulfates, 6.95 wt. % amine oxide and 1.00 wt. % alcohol ethoxylate. The surfactants are dissolved in a solvent system composed of water, ethanol, phenxyethanol, sodium citrate, sodium chloride (NaCl), polypropylene glycol, sodium hydroxide (NaOH) and Acticide™. These additional ingredients are added to improve the consumer experience by altering the appearance, odour, viscosity and pH (Lai, 1996). The formulations and surfactant pastes used in this study were prepared by the sponsor company, P&G, at one of their manufacturing sites. During lab scale production, a portion of water was mixed with the solvent, NaCl and polymers. After addition of each ingredient, the solution was mixed with an overhead stirrer at 200 rpm for 2 minutes until the ingredient was completely dissolved. Then the surfactant pastes were added, and the mixing increased to 350 rpm for 10 minutes to compensate for the increased viscosity. Finally, the necessary amount of NaCl, and ethanol were added to attain a viscosity of 1000 cP and a pH of 8.9. Dyes, perfume and the remaining water were added.

6.3.1.2.1 Formulation A

One dish liquid product, Formulation A, was specifically formulated to be unstable at low temperatures and was used when investigating the composition and structure of the crystals. The degree of ethoxylation m of the alkyl sulfate component $C_xH_y(OCH_2CH_2)_mOSO_3^-Na^+$ in Formulation A averaged at 0.5 moles and the wt. % ratio of anionic to amphoteric surfactants was set as 4.4:1. The total surfactant active level for this formulation was 28.69 wt. %.

6.3.1.2.2 Formulations 1-32

32 different formulations were used to understand the impact of the composition on the stability at low temperatures. As mentioned in Section 6.3.1.1, the alkyl sulfates in dish liquid formulations are produced from alcohol blends via a sulfation process. The amount of alcohol remaining in the final formulation is termed the ‘unreacted alcohol’ and was investigated in the range 0 - 0.25 wt. %. The anionic to amphoteric surfactant wt. % ratio ranged from 3.0:1 to 4.4:1 across the 32 formulations. The amount of Na₂SO₄ also differed between the formulations. Although the exact composition of the formulations cannot be disclosed, the amounts or ratios of the key ingredients are shown in Appendix D, Table D.1. To minimise further variability, the surfactant concentration was 13.4 wt. % across all 32 formulations.

6.3.1.2.3 Formulations X1-X6

To explore how the nature of the alkyl sulfate component affects stability, two formulations were produced, X1 and X6, using a blend of the alcohols previously displayed in Table 6.1. X1 and X6 contained the same degree of total branching in the alcohol blend (Table 6.2).

However, the two formulations varied in the molar amounts of the linear (LA) and branched (BrA) alcohol contributions and linear (LAE) and branched (BrAE) ethoxylated alcohol contributions. These differences resulted in the formulations having very different Low T numbers (equation 6.1). The Low T number is a term developed by P&G to correlate formulation composition with low temperature stability. The lower the Low T number the more unstable the product is predicted to be. Currently this mathematical expression only considers the alkyl sulfate surfactant component and not the factors described previously such as the amounts of unreacted alcohol and amine oxide.

$$Low\ T\ \# = \left[\left(\frac{LAE}{LA} \right) * (BrA + BrAE) \right] \quad (6.1)$$

where LAE = mol. % of linear alcohol ethoxylates, LA = mol. % of linear alcohol, BrA = mol. % of branched alcohol and BrAE = mol. % of branched alcohol ethoxylates.

The blends were subsequently sulfated and the other ingredients added, while maintaining a comparable completeness level, the same alkyl sulfate to amine oxide ratio (3.0:1) and the same total surfactant concentration (35.8 wt. %) between the two products.

Completeness is related to the amount of alcohol remaining in the system (equation 6.2)

$$Completeness\ (\%) = \frac{\left(Act \frac{MW_{al}}{MW_{as}} \right)}{\left(Act \frac{MW_{al}}{MW_{as}} \right) + UnR} * 100\ \% \quad (6.2)$$

where *Act* is the active level (wt. %), *MW_{al}* and *MW_{as}* are the molecular weights of the alcohol and alkyl sulfate respectively and *UnR* is the amount of unreacted alcohol in wt. %.

Table 6.2. Composition of Formulations X1 and X6.

	LA/ mol. %	LAE/ mol. %	BrA/ mol. %	BrAE/ mol. %	Total branching / mol. %	Low T #	Completeness / %
X1	49.0	17.0	34.2	0.0	33	11.83	97.60
X6	56.8	7.1	26.4	9.9	33	4.54	97.77

The two formulations were then combined in various ratios to produce Formulations X2, X3, X4 and X5, as shown in Table 6.3. This was achieved by mixing the solutions at 25 °C with an overhead stirrer at 500 rpm for 30 minutes. The corresponding Low T number for each formulation was calculated.

Table 6.3. Composition and related Low T number for Formulations X1 – X6.

Nomenclature	Amount of X1 / wt.	Amount of X6 / wt.	Low T #
X1	100	0	11.83
X2	80	20	10.37
X3	60	40	8.91
X4	40	60	7.46
X5	20	80	6.05
X6	0	100	4.54

6.3.2 Methods

6.3.2.1 Time lapse photography

Crystallisation of dish liquid formulations was visually recorded with a Canon EOS 5D Mark II. 80 g of each formulation was added into a test bottle composed of polyethylene terephthalate (PET). Samples were placed in a Memmert ICP 450 chamber, set to 0 °C. Images were automatically captured every 10 seconds for a period of 7 days for each Formulation. A backlight panel was used to minimise any light reflections. For each test, three replicates were performed. One image set for each formulation was further analysed across the 7-day timescale using an image analysis software developed by P&G that detects changes in homogeneity.

The software functions by converting the images to greyscale and assigning each individual pixel a value from 0 to 255 depending on the greyscale intensity. Hence each image is a 2D-matrix filled with pixel values between 0 and 255. A greyscale co-occurrence matrix (GCOM) for the positional relation $x = 0$, $y = 1$ was made (Sebastian *et al.*, 2012). The matrix depends on how many times a certain difference in greyscale occurs between pixels with this chosen spatial relationship. The matrix was subsequently normalised and the homogeneity, a statistical property of the matrix (Rao *et al.*), was calculated (equation 6.3).

$$\text{Homogeneity} = \sum_{i,j} \frac{p(i,j)}{1+|i-j|} \quad (6.3)$$

where i and j refer to the greyscale intensity of the i^{th} and j^{th} pixels; $p(i,j)$ is the cooccurrence probability of pixels i and j . The area of analysis was selected such that it incorporated most of the bulk within the bottle. Graphical plots showing the change in homogeneity across the different formulations were produced in OriginPro (v.9.0).

6.3.2.2 Microplate method

The microplate method, a technique developed by P&G, was based on detecting the presence of crystals through a change in light intensity passing through the sample. The rig used was built from a camera (model IDS UI-5240RE-C-HQ PoE Rev.2), a servo motorised polarizer, a fixed polariser and a light source. 270 μ L of the product was pipetted into each well of a transparent bottomed 96-well microplate, and subsequently inserted into the rig. The sample tray was located between the camera and the light source. The polarisers were set parallel to one another. A simplified schematic of the setup is provided in Figure 6.2(a) and Figure 6.2(b) is a typical 96-well microplate.

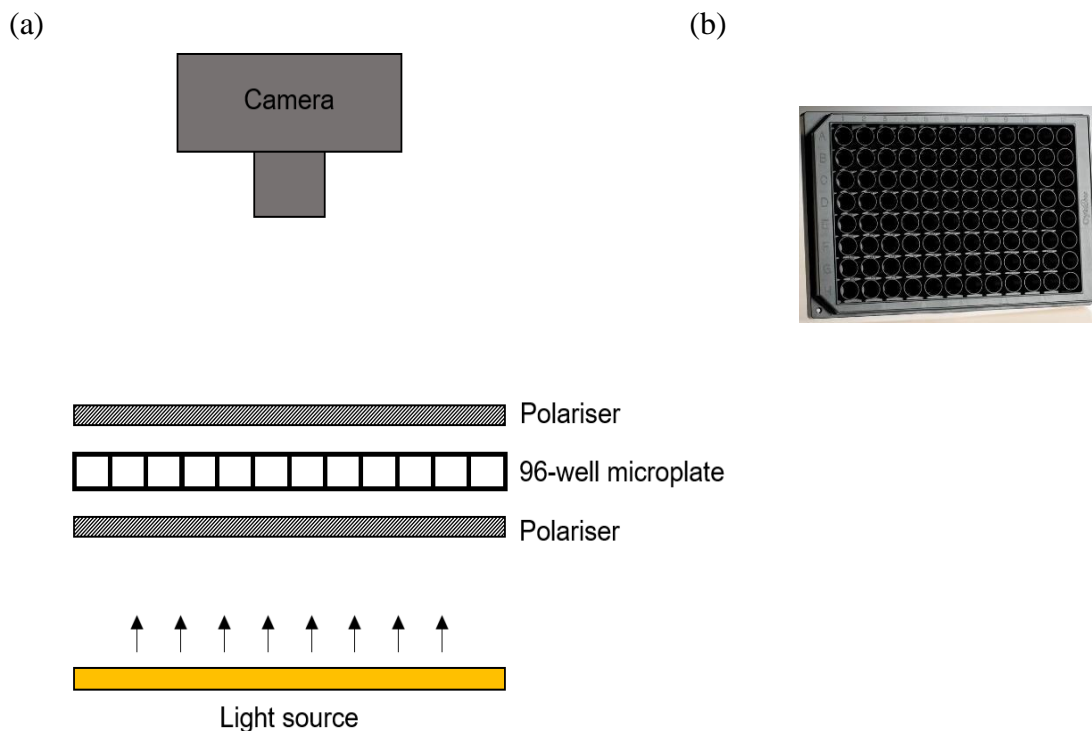


Figure 6.2. (a) Schematic of equipment setup where the polarisers can be set parallel or perpendicular; (b) A typical 96-well microplate.

Crystal formation was detected by a reduction in the light intensity transmitted from the source through the sample to the camera. Each test was performed four times. The recorded intensity lay in the greyscale range 0 to 255 where 255 was 100 % light transmittance through the sample. When the intensity falls below 150 P&G deem the sample failed. Plots showing the change in transmission over time for the different formulations were produced in MS Excel and OriginPro (v.9.0).

6.3.2.3 X-ray scattering

SAXS (small-angle X-ray scattering) and wide-angle X-ray scattering (WAXS) data were obtained using the I22 beamline at the Diamond Light Source, Oxfordshire, UK. Capillaries were securely fixed in a cooling bath at 0 °C for 64 hours. After this time, samples were loaded into 1.5 mm special glass capillaries and mounted in the beam within the Linkam DSC600

capillary stage, set to 0 °C. A 12.3989 keV ($\lambda = 0.099987$ nm) beam was used with a sample-detector distance of 6702.56 mm, providing a detectable Q -range on the SAXS detector of order 0.02 - 2.5 nm⁻¹ and 1.51 - 60.57 nm⁻¹ on the WAXS detector.

Data processing was performed as described in Chapters 3, 4 and 5 (Summerton *et al.*, 2018). The data at 25 °C and 0 °C was analysed using the SASfit software package (Bressler *et al.*, 2015) using a simple model comprising a power law, a spherical shell contribution and a contribution from background scattering. The profile at 0 °C also contained an additional Bragg peak contribution. The graphical package OriginPro (v.9.0) was used to plot the SAXS and WAXS profiles.

6.3.2.4 Nuclear Magnetic Resonance (NMR)

NMR measurements were performed on the surfactant pastes with Wilmad Precision 5 mm NMR tubes, using a Bruker AVANCE spectrometer equipped with a 9.6 T vertical bore magnet, operating at a ¹H resonance frequency of 400.13 MHz and fitted with a 5 mm BBO probe. The sample temperature was controlled using a BVT3200 unit. Samples were equilibrated at each temperature for a minimum of 30 minutes. Spectra at each temperature were acquired using a pulse acquire sequence, [90°-acq]. A spectral width of 8 kHz was used with 32k complex data points collected. 64 signal averages were acquired with a repetition time of 15 s, which was greater than 5 T_1 for the protons in the SDS and DDAO surfactants. ¹H NMR spectra were acquired at the following temperatures: 10 °C, 5 °C, 0 °C, -3 °C, -5 °C. At least two replicates were performed at each temperature. Spectra were processed using MestReNova software (v10.0.2), in which the triplet in SDS was set at 3.7 ppm for all temperature and pH environments, which is the value for this proton in DMSO-d₆ (SDBS).

6.3.2.5 Differential scanning calorimetry (DSC)

DSC thermograms were acquired using a Mettler Toledo DSC 2 fitted with a Huber TC100 bath. Approximately 20 mg of the solution was placed into a 100 μL aluminium pan and into the furnace of the instrument. A blank cell was used as the reference sample. The temperature cycle consisted of cooling the system from 25 $^{\circ}\text{C}$ to -10°C at the lowest available cooling rate, 1 $^{\circ}\text{C}/\text{min}$, and then holding at -10°C for 20 minutes. Initially a blank cell was exposed to the temperature cycle and then subtracted from subsequent measurements. Three replicates were acquired for each surfactant solution. The resultant data was plotted in OriginPro (v.9.0).

6.4 Results and discussion

6.4.1 Composition and structural attributes

Prior NMR and SAXS studies on the crystallisation of mixed 20 wt. % SDS + 3 wt. % DDAO surfactant solutions determined the crystals to be predominately composed of SDS (Chapter 3). However, it was also found, from confocal Raman studies, that the DDAO surfactant tends to surround the SDS crystals, rather than dispersing evenly through the solution (Chapter 4). Following the investigations of this simple SDS + DDAO system, a low temperature NMR study was performed on a surfactant paste comprising of alkyl sulfates, both ethoxylated and non-ethoxylated, amine oxides and water. Full details on the composition of this complex surfactant paste were not available so a full assignment could not be performed. However, certain regions of the room temperature ^1H NMR spectrum are assigned to the different surfactant types, as provided in Figure 6.3. As a result of the work performed on the SDS + DDAO system (see Chapter 3) it is possible to assign certain regions above 2.9 ppm to proton environments from non-ethoxylated alkyl sulfates and amine oxides. As a result, remaining

peaks above 2.9 ppm must result from proton environments present in ethoxylated alkyl sulfates.

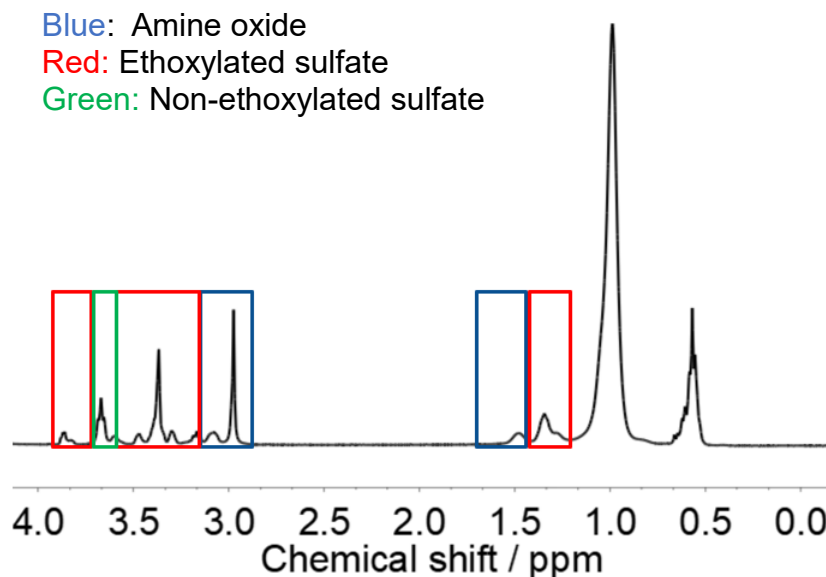


Figure 6.3. ^1H NMR spectrum for a typical dish liquid paste dissolved in D_2O at 25 °C.

The ^1H NMR spectra of this paste, acquired upon cooling to various temperatures, is shown in Figure 6.4. The regions between 2.9 and 4.0 ppm are of particular interest since this region allows for differentiation between the three types of surfactants.

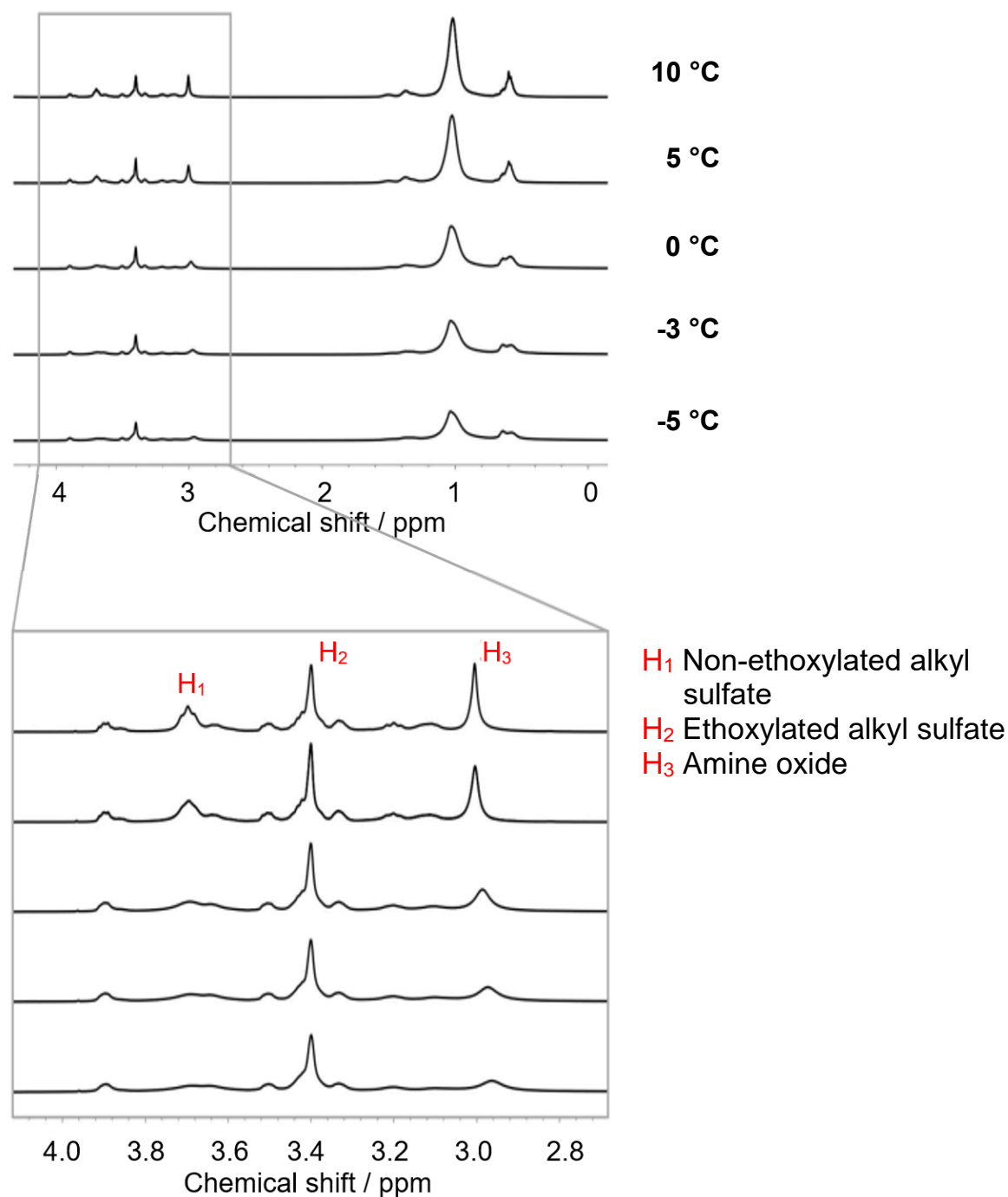


Figure 6.4. ^1H NMR spectra for dish liquid surfactant paste upon cooling.

The intensity of H_1 , located at 3.67 ppm in Figure 6.4, reduces upon cooling from 5 °C to 0 °C. This indicates that the non-ethoxylated alkyl sulfate component is undertaking a phase transition. It is also observed that H_3 , at 2.88 ppm, also broadens and reduces in intensity as the temperature is progressively lowered. A similar observation was previously reported with the SDS + DDAO system and was explained by association of the DDAO surfactant to the SDS

crystal (see Chapters 2 and 3). Conversely, peaks relating to protons from the ethoxylated alkyl sulfates, such as H_2 , do not display any significant decrease in signal intensity, with the relative peak intensities plotted in Figure 6.5. This observation suggests that ethoxylated alkyl sulfates do not comprise the crystals nor do they reside in the region of the crystals. The very slight decrease in H_2 is likely a result of the viscosity of the solution increasing upon cooling and impacting the molecular mobility.

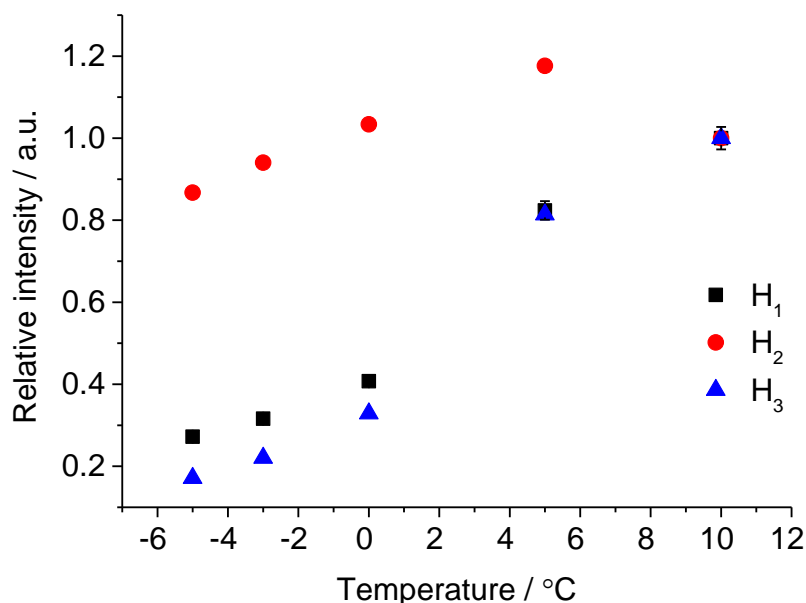


Figure 6.5. Change in NMR intensity for proton environments from the different surfactant structures upon cooling.

Further evidence for the composition of the crystals is provided upon comparing the cooling DSC thermograms of aqueous 20 wt. % samples of the alkyl sulfate paste, which contains a degree of ethoxy units, and SDS (Figure 6.6). The SDS solution displays a crystallisation peak, with a peak maximum residing at 1.1 °C. However, the ethoxylated alkyl sulfate sample does not display crystallisation above -10 °C.

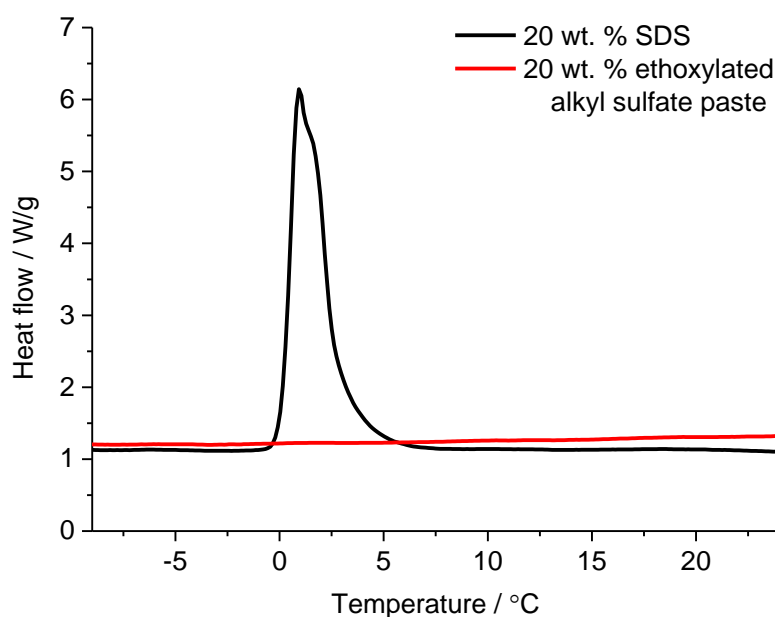


Figure 6.6. DSC thermograms for 20 wt. % SDS (black line) and 20 wt. % ethoxylated alkyl sulfate paste (red line) solutions acquired upon cooling from 25 °C to –5 °C.

The absence of a crystallisation peak upon cooling the ethoxylated alkyl sulfate solution illustrates the reduced tendency for crystallisation when ethoxy units are present in the surfactant structure and a resulting decrease in the Krafft temperature of the system (Weil *et al.*, 1959; Bel'skii, 2003; Farn, 2008). Similarly, a study into calcium and sodium dodecyl polyoxyethylene sulfates reported a decrease in the Krafft temperature upon an increase in the number of oxyethylene units (Hato and Shinoda, 1973). The Krafft temperature of a system depends on the capability of the surfactants to close pack in a crystal structure (Kronberg *et al.*, 2014). Factors such as branching, an increased distribution of chain lengths or the addition of large ethoxy groups therefore reduce the favourability to form crystals (Tadros, 2017).

Aside from understanding the composition, structural factors were also investigated. The SAXS profiles of a dish liquid product, Formulation A, acquired at both 25 °C and 0 °C, after 64 hours,

are displayed in Figure 6.7 where an appropriate model has been successfully fitted to both profiles.

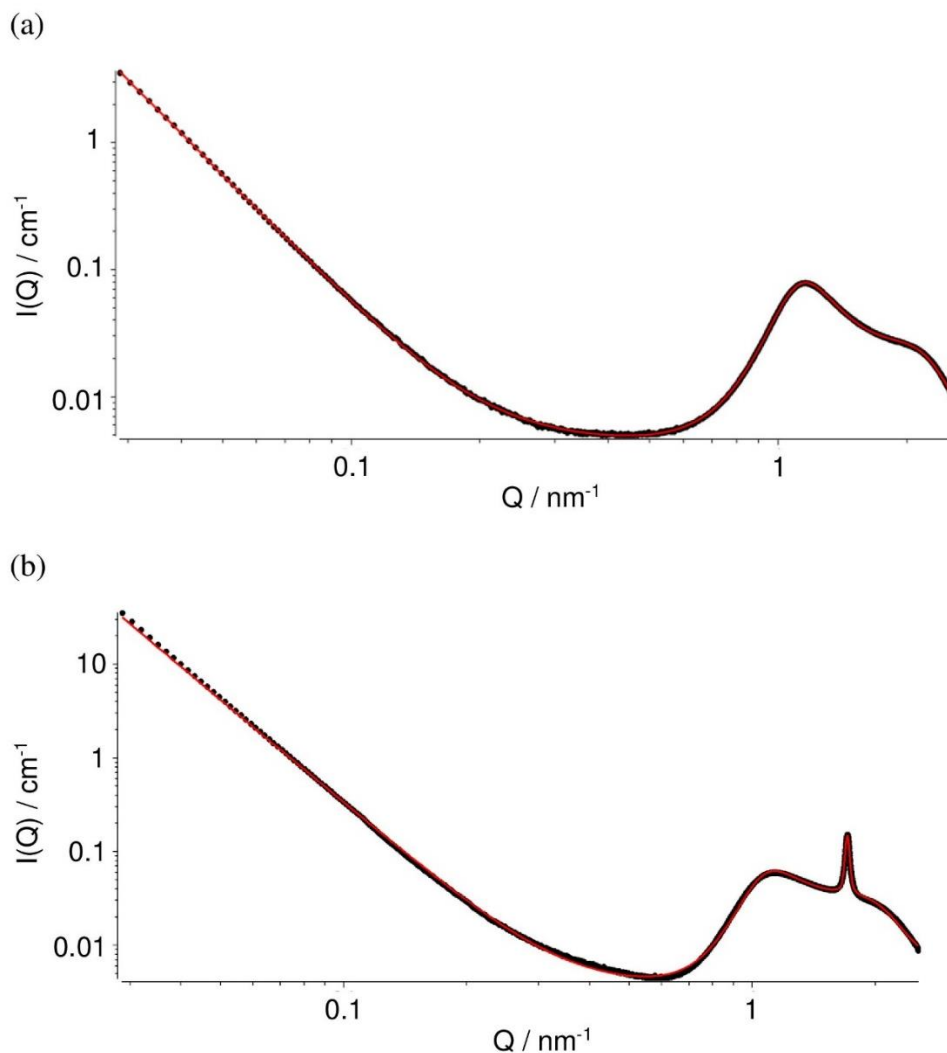


Figure 6.7. SAXS profiles for Formulation A at (a) 25 °C and (b) after 64 hours at 0 °C. The red lines correspond to fits to the data as described in the text and Appendix C.

The underlying double hump in both SAXS profiles results from contributions from a form factor $P(Q)$ and a structure factor $S(Q)$ and is characteristic of a micelle structure. The profiles have been fitted to spherical shell micelles, but it is likely that there is a wider distribution of micelles in the dish liquid including ellipsoids, rods and worm-like micelles. However, from a SAXS perspective, these aggregates are relatively similar providing they are of comparable

dimensions. The core radius increases from 1.79 nm at 25 °C to 1.95 nm at 0 °C and the shell radius decreases from 0.57 nm to 0.49 nm. Aside from the power law, background scattering and micelle contributions, the profile at 0 °C also displays a Bragg peak due to the formation of hydrated alkyl sulfate crystals. Further details of the fit parameters are provided in Appendix C. Two further equally spaced Bragg peaks are observed in the corresponding WAXS profile (Figure 6.8) which is typical of a lamellar-type phase. The spacing between these Bragg peaks relates to the d -spacing between the layers of alkyl sulfate within the crystals, which are separated by water (Hammouda, 2013). A similar profile was reported for SDS hydrated crystals formed from the model SDS + DDAO system (see Chapters 3 and 4).

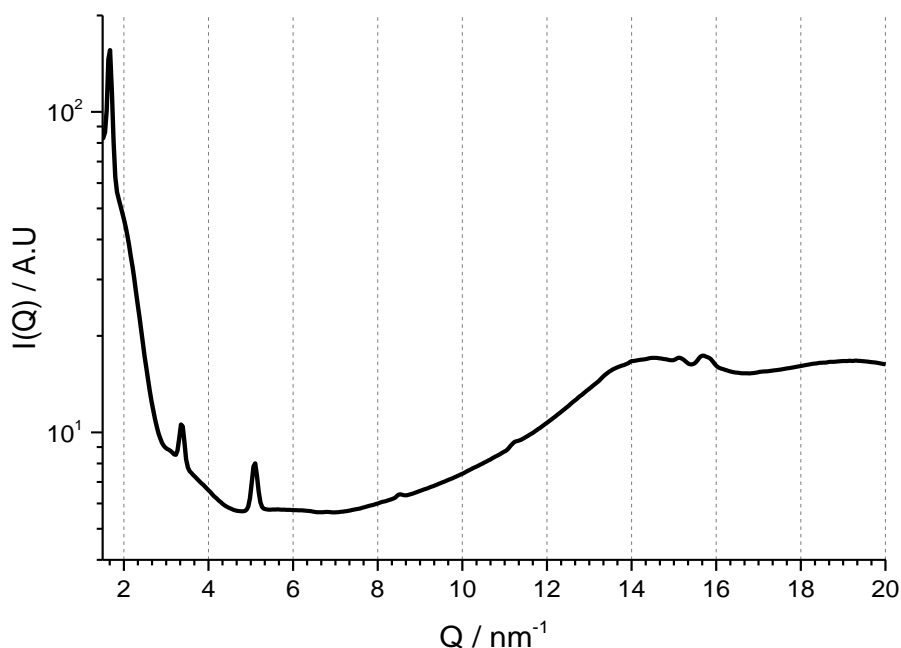


Figure 6.8. WAXS profile for Formulation A, acquired after 64 hours at 0 °C.

The first Bragg peak in the SAXS profile for the pure 20 wt. % SDS system, when exposed to the same temperature condition, initially appears at 1.65 nm^{-1} but, after approximately 400 s, it is replaced by a peak at 1.91 nm^{-1} as a result of the system transitioning to a different hydrate form (see Chapter 4). This matches the first Bragg peak that forms upon crystallisation of SDS from a 20 wt. % SDS + 3 wt. % DDAO system. However, in the case of dish liquid

crystallisation, the first Bragg peak appears at 1.71 nm^{-1} in the SAXS profile. A hypothesis for the peak deviation from the model SDS + DDAO system is based on the existence of the other components affecting the d -spacing of the system, moving it closer to the intermediary structure that a pure SDS system initially forms. The approximate size of the crystals was estimated as 574 nm via the Scherrer equation, which depends on the X-ray wavelength, line broadening at half peak maximum and the associated Bragg angle (Patterson, 1939).

From the NMR and SAXS studies, it can be deduced that the major component of the crystal, in agreement with model system findings, are the non-ethoxylated alkyl sulfates. These surfactants form a hydrated crystal structure composed of layers of alkyl sulfate separated by water layers. This layered structure gives rise to lamellar peaks in the WAXS profile (Figure 6.8). As evident from the DSC studies, crystals formed from the non-ethoxylated alkyl sulfates are more thermodynamically favoured than those formed from the ethoxylated alkyl sulfate surfactants. The presence of ethoxylation has been reported to lower the Krafft temperature (Jalali-Heravi and Knouz, 2002; Hato and Shinoda, 1973; Weil *et al.*, 1959). This is due to steric hindrance between the bulky ethoxy headgroups when close packed in a crystal structure.

6.4.2 Influences of formulation composition on low temperature stability

Many factors influence alkyl sulfate crystallisation in dish liquid at low temperatures. By monitoring a selection of formulations at 0°C , it was revealed that the ratio of alkyl sulfate (both linear and ethoxylated alkyl sulfates) to amine oxide and the amount of alkyl sulfate alcohol precursor ('unreacted alcohol') are key contributors to the stability, as depicted in Figure 6.9.

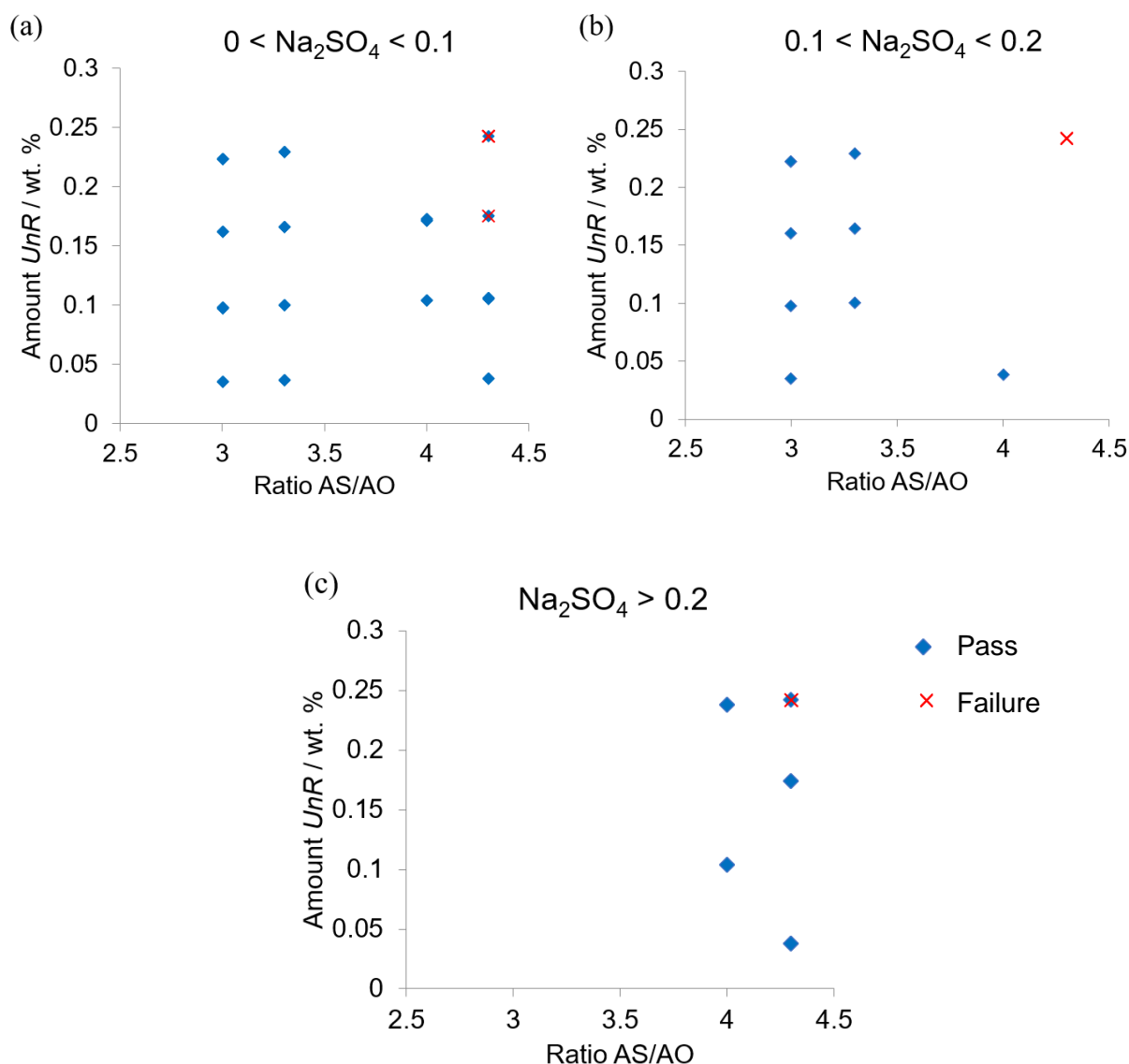


Figure 6.9. Screening for the presence of crystalline failures after 7 days at 0 °C across a formulation space varying by the ratio of amount of alkyl sulfate (AS) to amine oxide (AO) and the amount of unreacted alcohol (UnR) across a range of sodium sulfate concentrations (wt. %). A cross indicates at least one failure out of 4 replicates. A failure corresponds to a transmission intensity, detected via the microplate technique, below 150.

In Figure 6.9 it is evident that failures (red crosses) occur in formulations containing a high ‘unreacted alcohol’ content or a high ratio of alkyl sulfate to amine oxide. This is explored further in the following sub-sections.

6.4.2.1 Ratio of alkyl sulfate to amine oxide

DDAO exhibits non-ionic characteristics in dish liquid as it is an alkaline environment (Singh *et al.*, 2006). The presence of DDAO reduces the repulsive interaction between the SDS head groups in micelles (Sidim and Acar, 2013; Sidim and Arda, 2011). This reduced repulsion results in an increased tendency to form micellar aggregates so the SDS monomer concentration decreases. Since the crystalline entities are formed from SDS monomers, the drive for crystallisation also decreases (Rodriguez *et al.*, 2001). As a result, the Krafft temperature, below which there is a risk of crystallisation, reduces with an increase in DDAO concentration. In Chapter 4, the crystallisation temperature of SDS + DDAO systems, acquired by DSC, decreased with amount of DDAO (Summerton *et al.*, 2018). Figure 6.9 demonstrates that this trend also holds for the dish liquid systems since the formulations that display failure are those with the highest ratio of alkyl sulfate to amine oxide.

6.4.2.2 Completeness level

The stability of dish liquid formulations at low temperatures was also found to depend on the amount of alcohol precursor remaining in the solution, referred to as the amount of ‘unreacted alcohol’ in P&G terminology. The process of sulfation does not provide a 100 % yield and some alcohol precursor remains in the final formulation. The target completeness for dish liquid formulations is 98.5 %, with low completeness set at 97.5 % and high completeness set as above 99.25 %. The completeness is not targeted at 100 % because there is a risk of discolouration at the higher levels. It is reported in the literature that the existence of alcohols enhances the stability of micelles, which contain surfactants of matching hydrocarbon chain length, at ambient temperature and low surfactant concentrations (Patist *et al.*, 1998). However, at low temperatures the existence of the alcohol precursors can have a negative impact on the stability of dish liquid formulations. The crystallisation temperatures of alcohol precursors are higher

than their corresponding alkyl sulfates. The crystallisation temperatures of 1-dodecanol (5 wt. %) and SDS (20 wt. %) are 24 °C and 13 °C, respectively, when cooled at a rate of 0.1 °C/min (Summerton *et al.*, 2016). Although the alcohols are trapped in micelles, they are likely to crystallise out when the formulation is exposed to low and sub-zero temperatures. It is hypothesised that crystallised alcohol precursor seeds surfactant crystallisation. The most effective seeds are those that have the same structure or bear some degree of structural resemblance to the target crystal (Allahyarov *et al.*, 2015). In previous work (see Chapter 2), microscopy and differential scanning calorimetry (DSC) studies showed that 1-dodecanol is able to seed SDS crystallisation (Summerton *et al.*, 2016). The formulations in Figure 6.9 that contain highest amounts of ‘unreacted alcohol’ and a high alkyl sulfate to amine oxide ratio develop crystalline failures at 0 °C after 7 days. This illustrates the importance of these two parameters on low temperature stability of dish liquid formulations.

6.4.2.3 Alkyl sulfate paste

Aside from the completeness level and the ratio of alkyl sulfate to amine oxide, the chemical nature of the alkyl sulfate paste is important for low temperature stability. The Low T number (equation 6.1), introduced in Section 6.3.1.2.3, was proposed by P&G as a means predict the stability of dish liquid products from the composition of the alkyl sulfate surfactant paste. Further modification of this equation is required to incorporate amine oxide and the completeness level. However, for the purpose of this chapter, the relationship between the Low T number and the amount of crystallite material or time to failure is investigated.

Figure 6.10 indicates that the degree of crystalline entities after 7 days increases with a decrease in the Low T number of the formulation. From equation 6.1, a low value for the Low T number corresponds to high amount of linear alkyl sulfate. This is further evidence that these alkyl

sulfates are indeed the driving force for crystallisation. Such a finding also agrees with the NMR data which indicated ethoxylated alkyl sulfates are not present in the crystals.

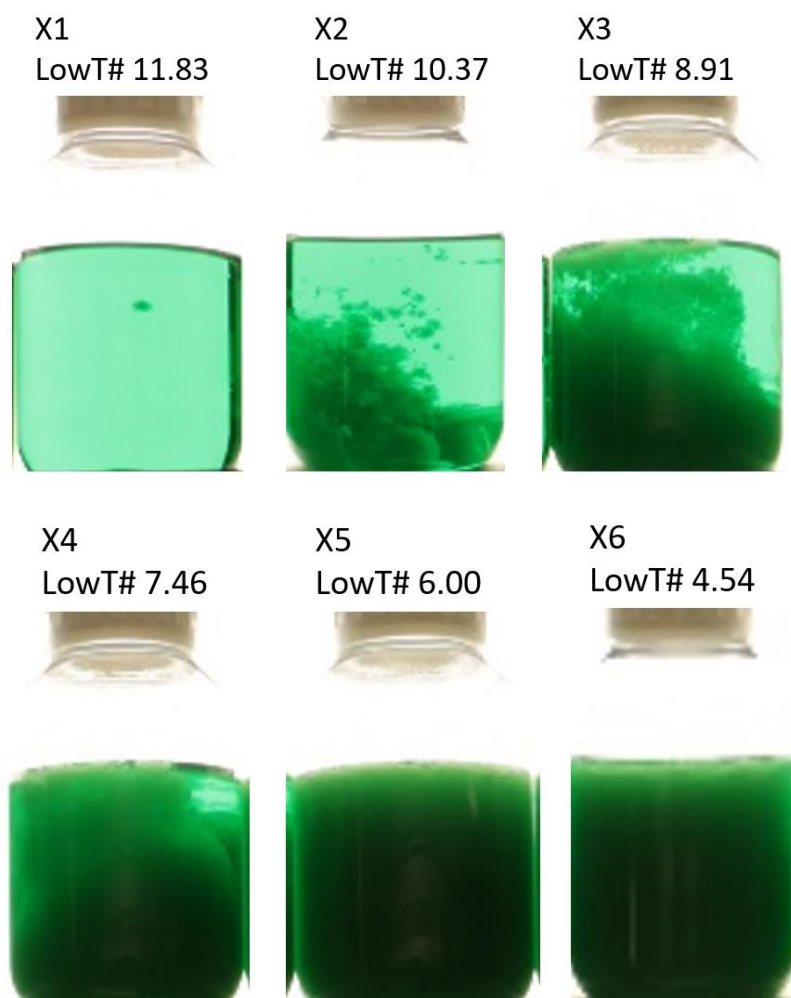


Figure 6.10. Images of formulations with differing Low *T* number after 7 days holding at 0 °C.

The induction time and rate of the crystal growth were investigated across the six formulations. This was achieved by monitoring the changes in the homogeneity, using an image analysis technique developed by P&G (see Section 6.3.2.1). The degree of greyscale homogeneity between neighbouring pixels decreases as crystals are formed. Once crystals comprise most of the system, the homogeneity starts to increase again. The time to the initial reduction in homogeneity can be used to predict the induction time and the gradient of slope can be used to estimate relative rates of crystallisation between the different formulations. Each test was

performed in triplicate but, due to limited time on the experimental setup, reflections from surrounding sources were unavoidable for some repeated measurements. However, reproducibility is demonstrated for one of the formulations, X6, in Figure 6.11, where all three replicates were suitable for analysis.

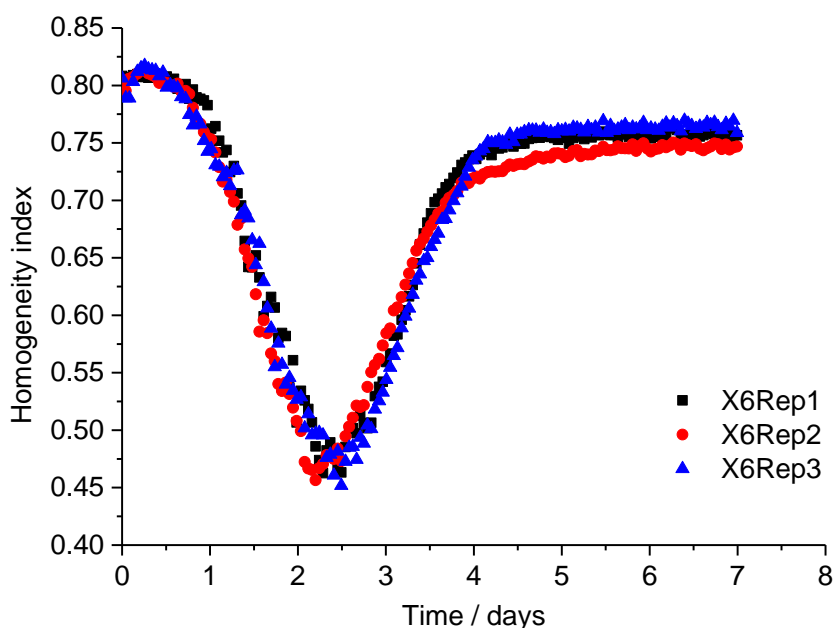


Figure 6.11. Change in homogeneity for the three X6 replicates across a 7-day period at 0 °C.

X2, X3, X4 and X5 also demonstrated reproducibility visually but the presence of light reflections had an effect on further analysis. For the most stable formulation, X1, only one of three samples developed a significant amount of crystals after 7 days. This demonstrates the variability that can occur with this test method, which is likely a result of factors difficult to control such as the presence of dust particles acting as seeds to crystallisation. For each formulation (X1-X6) the sample with minimal light reflections was used in the homogeneity analysis presented in Figure 6.12. Examples of the output greyscale images are provided in Figure 6.13 for Formulation X6.

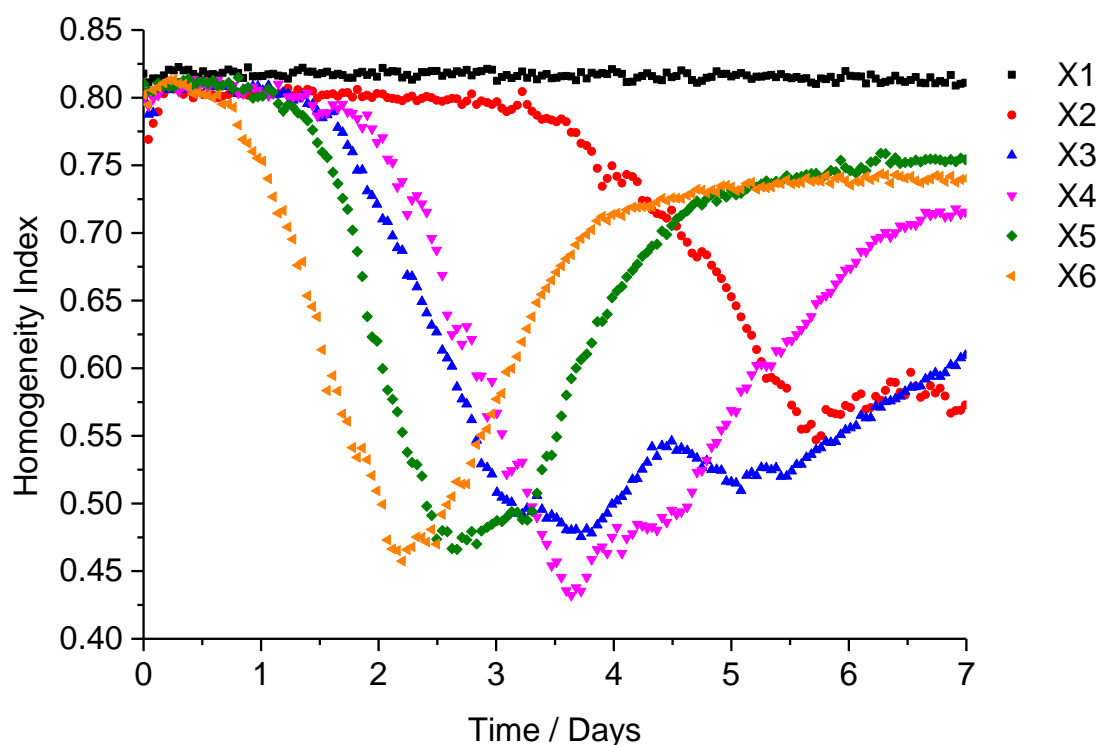


Figure 6.12. Homogeneity analysis of X1, X2, X3, X5 and X6 over a 7-day period at 0 °C.

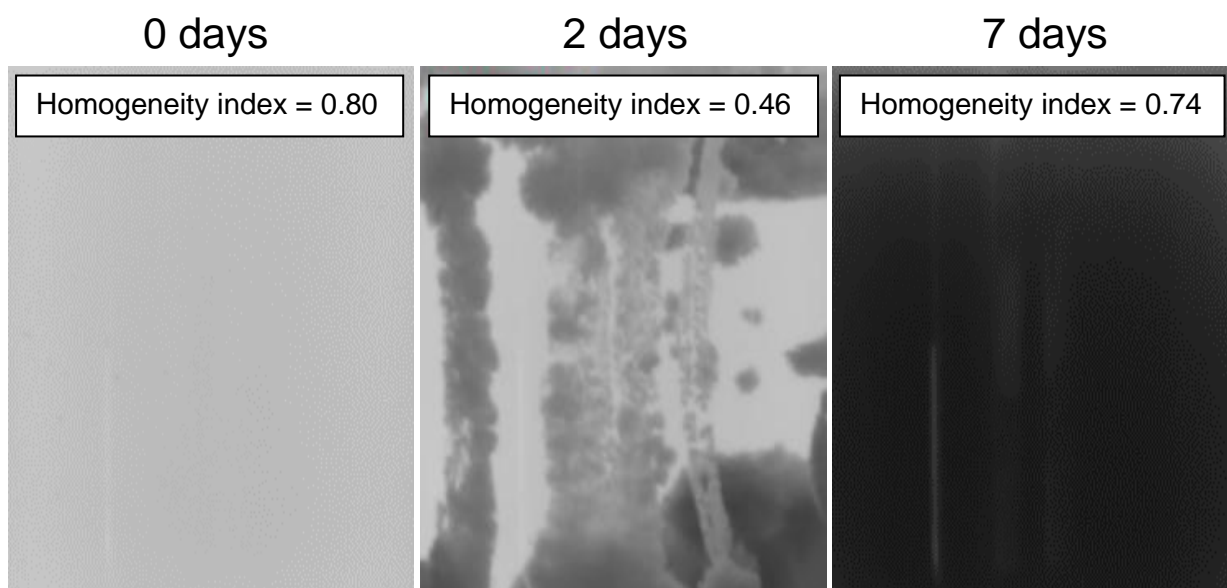


Figure 6.13. Greyscale images for Formulation X6 at various time points and their corresponding homogeneity index.

A decrease in the homogeneity index corresponds to the initial crystal formation. The subsequent increase is due to the crystallised area increasing and occupying most of the

analysed area. In X3 and X4 there are slight fluctuations in the increasing slope which is attributed to a shift in the crystal bulk when the accumulation of crystallite entities collapses and rearranges. The formulation with the highest Low T number, X1, displays a slight drop in homogeneity which is attributed to the appearance of one small group of crystals in the bulk. Furthermore, Formulation X2 (Low T number = 10.37) does not display any significant drop in homogeneity until the 3-day timepoint. The remaining formulations all fail within a relatively short time scale, with only slight differences between X3, X4 and X5. There are two variables to consider when comparing between formulations. Firstly, the time lag to the decrease in homogeneity and, secondly, the gradient of the decrease. The latter can be related to the rate of crystallisation and the former to the induction time. The gradient of the decrease is calculated by fitting a linear trendline to the relevant section of the plot. The variation in the rate of crystallisation and induction time across the formulations are plotted in in Figures 6.14(a) and (b), respectively.

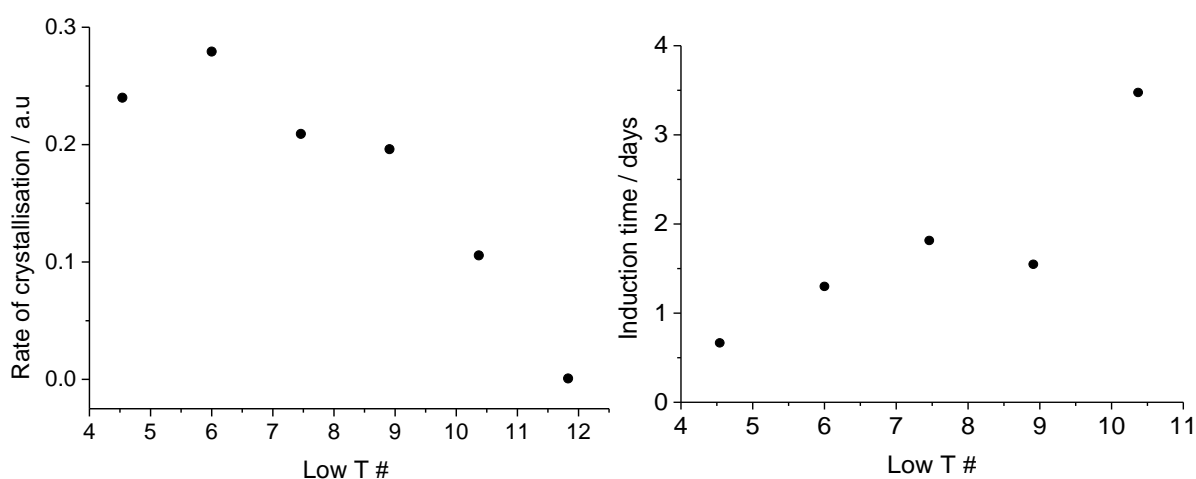


Figure 6.14. Plot of (a) rate of crystallisation and (b) induction time against the Low T number of the formulation.

For the most part, there tends to be a decrease in the rate of crystallisation as the Low T number increases. However, the three formulations with the lowest Low T numbers all crystallise

relatively fast with minor differences in their rates. The induction time, corresponding to the time taken to observe a change in gradient, also demonstrates an increase with Low T number. The most stable formulation, with a Low T number of 11.37, is not included on the graph because there is no notable change in gradient. For the remaining four formulations there tends to be a positive correlation between induction time and Low T number. However, X5 crystallises faster than expected. This may be due to the presence of dust particles seeding crystallisation. Such a factor is difficult to control between the different formulations. Despite this outlier, there is a clear trend displaying a general increase in induction time with an increase in Low T number.

The Low T number, and therefore the composition of the alkyl sulfate paste, has been shown to influence both the induction time and rate of crystallisation. The molar proportion of linear alkyl sulfate in the formulation and the Low T number have an inverse relationship. A higher proportion of linear alkyl sulfate results in high instability, whereas the inverse is true with the ethoxylated alkyl sulfate. This is to be expected since, from previous investigations, it is known that the crystals are primarily composed of non-ethoxylated alkyl sulfates due to their packing ability. Although these alkyl sulfates appear to be detrimental for low temperature stability, they are key for product performance, so it is necessary that formulations employ a balance between the two effects.

6.5 Conclusions

Crystals formed from unstable dish liquid products upon cooling was found to mainly comprise non-ethoxylated alkyl sulfates. The surfactants were present as hydrated crystals in a lamellar-type phase. From NMR studies, it is concluded that ethoxylated alkyl sulfates do not form part of the crystals, prior to complete freezing of the system. This is attributed to the larger headgroup of these sulfates resulting in a steric interaction when in a close packed crystal

arrangement. This consequently reduces the thermodynamic drive for crystallisation, compared to non-ethoxylated variants.

Monitoring the stability across a selection of formulations revealed the importance of the composition on the low temperature stability of the product. Some initial insight has previously been gained from the SDS + DDAO model systems, but the knowledge was applied to complex dish liquid systems in this chapter. A lower alkyl sulfate to amine oxide ratio improved the robustness of the formulation whereas an increased amount of alkyl sulfate alcohol precursor proved detrimental for stability. Furthermore, the structures of the alkyl sulfates were found to be of paramount importance for low temperature stability, with the linear alkyl sulfate being the main driving component for crystallisation. The presence of ethoxy groups in the alkyl sulfate component was found to improve stability of the formulation. This understanding will be valuable for P&G when designing new, or refining existing, dish liquid formulations.

6.6 References

- Allahyarov, E., Sandomirski, K., Egelhaaf, S. U. & Löwen, H. 2015. Crystallization seeds favour crystallization only during initial growth. *Nature Communications*, 6, 7110.
- Bel'skii, V. E. 2003. Influence of the structure of amphiphilic anions on the Krafft temperature of micellar solutions of anionic surfactants. *Russian Chemical Bulletin*, 52, 1347-1352.
- Bettioli, J. P., Morabet, S., Scialla, S. 2013. Alkaline liquid hand dish washing detergent composition. U.S Patent: 8343906.
- Bressler, I., Kohlbrecher, J. & Thunemann, A. F. 2015. SASfit: a tool for small-angle scattering data analysis using a library of analytical expressions. *Journal of Applied Crystallography*, 48, 1587-1598.
- Farn, R. J. 2008. *Chemistry and Technology of Surfactants*, Wiley.

- Hammouda, B. 2013. Temperature Effect on the Nanostructure of SDS Micelles in Water. *Journal of Research of the National Institute of Standards and Technology*, 118, 151-167.
- Hato, M. & Shinoda, K. 1973. Krafft points of calcium and sodium dodecylpoly(oxyethylene) sulfates and their mixtures. *The Journal of Physical Chemistry*, 77, 378-381.
- Jalali-Heravi, M. & Knouz, E. 2002. Use of quantitative structure-property relationships in predicting the Krafft point of anionic surfactants. *Electronic Journal of Molecular Design*, 1, 410-417.
- Kronberg, B., Holmberg, K. & Lindman, B. 2014. *Surface Chemistry of Surfactants and Polymers*, Wiley.
- Lai, K. Y. 1996. *Liquid Detergents*, CRC Press.
- Patist, A., Axelberd, T. & Shah, D. O. 1998. Effect of long chain alcohols on micellar relaxation time and foaming properties of sodium dodecyl sulfate solutions. *Journal of Colloid and Interface Science*, 208, 259-265.
- Patterson, A. L. 1939. The Scherrer Formula for X-Ray Particle Size Determination. *Physical Review*, 56, 978-982.
- Prud'homme, R. K. 2017. *Foams: Theory: Measurements: Applications*, CRC Press.
- Rao, C. N., Sastry, S. S., Mallika, K., Tiong, H. S. & Mahalakshmi, K. 2013. Co-occurrence matrix and its statistical features as an approach for identification of phase transitions of mesogens. *International Journal of Innovative Research in Science, Engineering & Technology*, 2, 4531-4538
- Rodriguez, C. H., Lowery, L. H., Scamehorn, J. F. & Harwell, J. H. 2001. Kinetics of precipitation of surfactants. I. Anionic surfactants with calcium and with cationic surfactants. *Journal of Surfactants and Detergents*, 4, 1-14.

- Schramm, L. L., Stasiuk, E. N. & Marangoni, D. G. 2003. 2 Surfactants and their applications. *Annual Reports Section "C" (Physical Chemistry)*, 99, 3-48.
- Spectral database for organic compounds SDBS* [Online]. Available: http://sdb.sdb.aist.go.jp/sdb/cgi-bin/direct_frame_top.cgi [Accessed 03/06/2018].
- Sebastian, V., Unnikrishnan, A. & Balakrishnan, K. 2012. Gray level co-occurrence matrices: generalisation and some new features. *International Journal of Computer Science, Engineering and Information Technology*, 2, 151-157.
- Showell, M. 2016. *Handbook of Detergents, Part D: Formulation*, CRC Press.
- Sidim, T. & Acar, G. 2013. Alcohols Effect on Critic Micelle Concentration of Polysorbate 20 and Cetyl Trimethyl Ammonium Bromine Mixed Solutions. *Journal of Surfactants and Detergents*, 16, 601-607.
- Sidim, T. & Arda, M. 2011. Some Surface Properties of Polysorbates and Cetyl Trimethyl Ammonium Bromine Mixed Systems. *Journal of Surfactants and Detergents*, 14, 409-414.
- Singh, S. K., Bajpai, M. & Tyagi, V. 2006. Amine oxides: a review. *Journal of Oleo Science*, 55, 99-119.
- Soontravanich, S. 2007. *Formation and Dissolution of Surfactant Precipitates*. PhD Thesis, University of Oklahoma.
- Soontravanich, S. & Scamehorn, J. F. 2009. Use of a Nonionic Surfactant to Inhibit Precipitation of Anionic Surfactants by Calcium. *Journal of Surfactants and Detergents*, 13, 13.
- Subramanyan, K. & Ananthapadmanabhan, K. P. 2007. C.1 - Personal Cleansing A2 - Johansson, *Handbook for Cleaning/Decontamination of Surfaces*. Amsterdam: Elsevier Science B.V.

- Summerton, E., Hollamby, M. J., Zimbitas, G., Snow, T., Smith, A. J., Sommertune, J., Bettiol, J., Jones, C., Britton, M. M. & Bakalis, S. 2018. The impact of N,N-dimethyldodecylamine N-oxide (DDAO) concentration on the crystallisation of sodium dodecyl sulfate (SDS) systems and the resulting changes to crystal structure, shape and the kinetics of crystal growth. *Journal of Colloid and Interface Science*, 527, 260-266.
- Summerton, E., Zimbitas, G., Britton, M. & Bakalis, S. 2016. Crystallisation of sodium dodecyl sulfate and the corresponding effect of 1-dodecanol addition. *Journal of Crystal Growth*, 455, 111-116.
- Summerton, E., Zimbitas, G., Britton, M. & Bakalis, S. 2017. Low temperature stability of surfactant systems. *Trends in Food Science & Technology*, 60, 23-30.
- Tadros, T. F. 2017. *Handbook of Colloid and Interface Science: Industrial Applications*, Walter de Gruyter GmbH.
- Weil, J. K., Stirton, A. J., Bistline, R. G. & Maurer, E. W. 1959. Tallow alcohol sulfates. Properties in relation to chemical modification. *Journal of the American Oil Chemists' Society*, 36, 241-244.
- Zana, R. K. E. 2007. *Giant Micelles: Properties and Applications*, CRC Press.

CHAPTER 7

INVESTIGATING METHODS FOR REDUCING THE TIME TO FAILURE

7.1 Abstract

Productivity is a key priority for fast-moving consumer goods (FMCG) companies such as P&G. Improving the stability tests performed on dish liquid products will contribute to increasing productivity for P&G. This can be achieved by reducing the timescale and variability of product failures resulting from crystallisation. This chapter introduces two methods explored in the initial screening process.

Seeding formulations with oven-dried dish liquid is the first approach to be investigated. Although initially found to be promising, it was not pursued beyond initial screening due to practical limitations. The rough surface topology of the seed and the similarity in composition between the seeds and target crystals are key to the success of this method. The second approach relies on using sonication to initiate crystallisation in bulk. With this method, issues arose due to a lack of reproducibility. A third method, the use of agitation, yielded success in the initial screening and is investigated in further detail, as described in Chapter 8.

7.2 Introduction

Fast moving consumer goods (FMCG) companies, such as P&G, strive for their products to be market-leading. During product development, formulations are assessed in terms of their cleaning performance, mildness, foaming properties and stability (Bajaj *et al.*, 2012; Falbe, 2012). The latter is particularly important when products are supplied to countries exhibiting extreme climates. Stability testing involves monitoring changes in formulation appearance upon exposure to varying temperatures and humidity levels (Williams and Schmitt, 2012). At P&G, the temperatures range from $-3\text{ }^{\circ}\text{C}$ to $50\text{ }^{\circ}\text{C}$ and the maximum humidity level is set at 60 % Relative Humidity (RH). Assessing product stability at $0\text{ }^{\circ}\text{C}$ is a widely used test condition at P&G and there is large chamber dedicated to this temperature. Formulations experience this

low temperature in some countries during winter months. In addition to assessing the appearance across a selection of controlled temperatures, the products are subjected to freeze-thaw cycles where the effect of continuous heating and cooling on sample stability is monitored. This type of testing is also important in other industries. For example, in the food sector, freezing is often used by consumers for preservation purposes (Degner *et al.*, 2014). When defrosting the product, it must retain all chemical and physical attributes.

In this research, the product of interest is dish liquid, where there is a risk of surfactant crystallisation at low and sub-zero temperatures in some formulations (Summerton *et al.*, 2017). The stability tests performed routinely on P&G dish liquid products at low temperatures can take 28 days and exhibit variability in failure times between samples. Providing the capability to reduce the timescale and associated variability will increase productivity.

The addition of a seed crystal has been reported to reduce the time to crystallisation in some systems since its presence increases the rate of heterogeneous nucleation (Summerton *et al.*, 2016; Okawa *et al.*, 2001). Seeds are often composed of the target crystals. However, other objects have been used as seeds, such as animal hair and hard spheres (Cacciuto *et al.*, 2004; Bergfors, 2003). Rough surfaces, impurities and dust particles can also act as bases for this type of nucleation (Allahyarov *et al.*, 2015; Maksimov *et al.*, 2013).

This chapter explores routes to improve the efficiency of the stability tests performed on dish liquid products at low temperatures. The three methods investigated include seeding with oven-dried dish liquid, sonication and mixing, with the latter being the focus of Chapter 8. With optimisation of this methodology, it is expected that the knowledge will be extended to other products that experience similar failure issues, such as fabric conditioners and shampoos.

7.3 Materials and methods

7.3.1 Materials

7.3.1.1 Formulations

32 formulations were prepared according to the P&G standard operating procedure previously outlined in Section 6.3. Properties of these 32 formulations are described in Section 6.3.1.2.2.

7.3.1.2 Oven-dried dish liquid seeds

For each formulation, oven-dried seed material was produced from the bulk by heating 20 g of the product in an oven at 70 °C for 20 hours. After this time, there was negligible change in the product mass (see Appendix E). The resultant white, sticky solid was moulded into spherical seeds with a diameter of 2 mm (for microplate studies) and 3 mm (for vial studies). These seed sizes were selected for ease of preparation. Seeds formed from a particular formulation were solely used to seed that product.

7.3.2 Methods

7.3.2.1 Scanning electron microscopy (SEM)

Scanning electron microscopy (SEM) was performed using a Hitachi TM3030 table top microscope. The oven-dried dish liquid samples were sputter coated with a thin gold conductive film prior to analysis by the instrument. Images were collected under low vacuum (100 Pa) using x800 magnification. The images were analysed using ImageJ.

7.3.2.2 Optical microscopy

An optical microscope, model Leica Z16 APOA, was coupled with a Linkam LTS120 Peltier stage and used to observe the topology of oven-dried dish liquid at different length scales. A

screenshot of the microscope settings is provided in Appendix A. Images were analysed using ImageJ.

7.3.2.3 Microplate method

The microplate method, a technique developed by P&G, was based on detecting the presence of crystals through changes in light transmission. The rig used was built from a camera (model IDS UI-5240RE-C-HQ PoE Rev.2), a servo motorised polarizer, a fixed polariser and a light source. 270 μ L of the product was pipetted into each well of a transparent bottomed 96-well microplate, and subsequently inserted into the rig. The sample tray was located between the camera and the light source. The polarisers were set parallel to one another. A simplified schematic of the setup is provided in Chapter 6, Figure 6.2.

Crystal formation was detected by a reduction in the light intensity transmitted from the source through the sample to the camera. Each test was performed four times. The recorded intensity lay in the greyscale range 0 to 255 where 255 was 100 % light transmittance through the sample. When this intensity falls below a value of 150, P&G deem the sample failed. Plots showing the change in transmission over time across the different formulations were produced in MS Excel and OriginPro (v.9.0).

7.3.2.4 Time lapse photography

Two vials containing 18 g of each formulation were placed in the 0 °C chamber; one with a seed and one without. Images were acquired after 48 hours using a Canon EOS 100D. A black background was used to minimise reflections from surrounding sources.

7.3.2.5 Sonication

Samples, each in quadruplicate, were pipetted into microplates and placed in a Polaris sonication bath within the 0 °C chamber. The bath was filled with a mixture of brine and water,

to prevent it freezing. Sonication was applied for 30 seconds followed by a 5 second break and then a further 30 seconds of sonication. The samples were then analysed with the microplate method (Section 7.3.2.3).

7.4 Results and discussion

7.4.1 Oven-dried dish liquid seeding

7.4.1.1 Nature of the seed

Seeds are most efficient when they are comprised of the target crystals (Bergfors, 2003). However, it proved challenging to separate the crystals formed in dish liquid at low temperatures from the bulk. This was due to the viscous solvent system and the tendency for the crystals to melt at room temperature. These factors meant that it was not possible to seed the formulation with the pure crystals themselves. As an alternative, oven-dried dish liquid was used as seed crystals (Cacciuto et al., 2004; Bergfors, 2003). Microscope images of the oven-dried dish liquid material at various length scales are displayed in Figures 7.1(a), (b) and (c), with the sharp crystalline surface especially evident from the latter image. The SEM image displayed in Figure 7.2 shows the rough surface of the material.

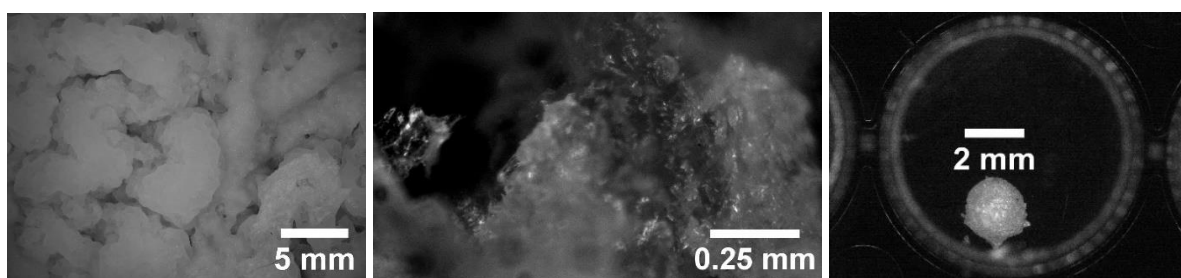


Figure 7.1. Microscope images of typical oven-dried dish liquid at varying length scales where (a) and (b) show a sample of oven-dried dish liquid before being moulded into seeds and (c) is a seed placed in the well of a 96-well microplate.

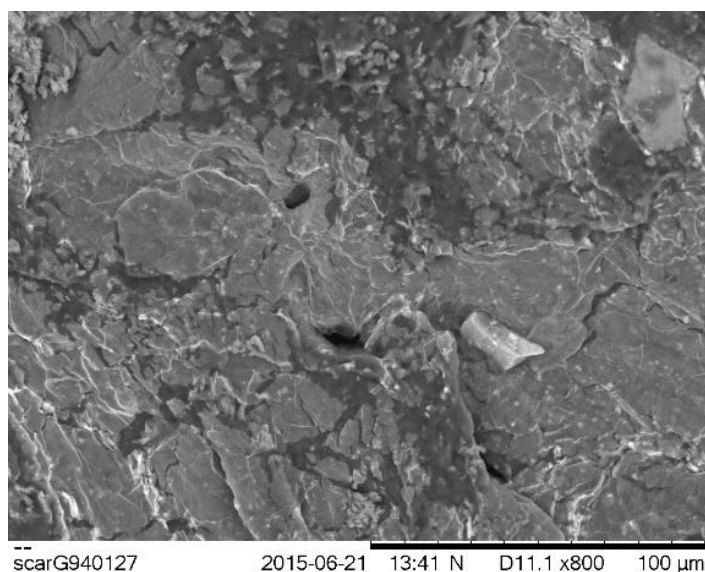


Figure 7.2. SEM image illustrating the rough surface of an oven-dried dish liquid seed.

It is hypothesised that the crystalline surface of oven-dried dish liquid seeds will act as a base for heterogeneous nucleation (Diao *et al.*, 2011). Additionally, these seeds have a similar chemical composition to the crystals. This factor will also promote crystal growth from the seed surface (Summerton *et al.*, 2016). Upon oven-drying dish liquid, water, ethanol, and perfume evaporate to leave a material primarily composed of the anionic, non-ionic surfactants and some remnant water. The crystals are known to be comprised of alkyl sulfate hydrates (see Chapter 6). Therefore, the seeds are expected to be similar in composition to the target crystals.

7.4.1.2 Seeding formulations with oven-dried dish liquid

Four of the 32 formulations (Samples 3, 7, 9, 32) contained crystalline entities after 48 hours at 0 °C. Figure 7.4 displays these four samples after this time, in the absence and presence of a 3 mm oven-dried dish liquid seed. In all four cases, the seeded sample contained more crystals than the control. A ‘tail structure’ was observed in the seeded samples, from which the crystals appeared to grow. This is possibly caused by the seed sinking through the bulk and leaving behind a trail of smaller seeds from which crystals can grow. The images show that seeding

with oven-dried dish liquid promotes crystallisation in unstable dish liquid samples that are susceptible to crystallisation.

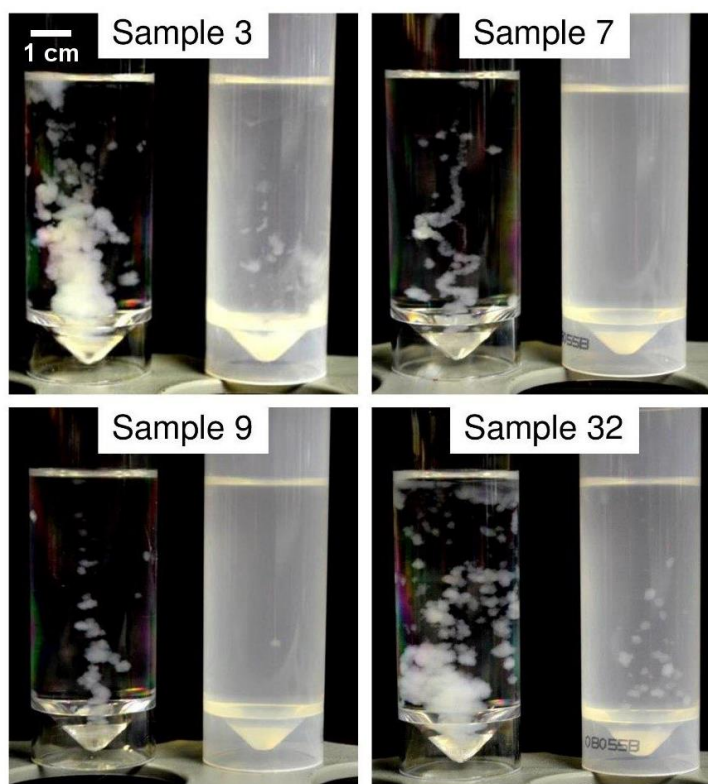
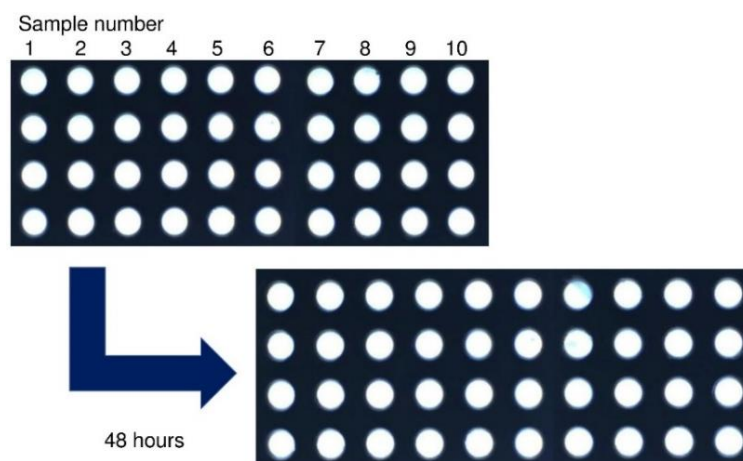


Figure 7.3. Seeded (left) and control (right) results for Samples 3, 7, 9 and 32 after 48 hours at 0 °C.

The first 10 samples of the 32-sample set contained both unstable and stable samples, where stable samples were not prone to crystallisation within the 28-day timescale. These 10 samples were monitored over 7 days at 0 °C using the microplate technique. This technique is used extensively in P&G because of its ability to test many replicates in a much smaller space than would otherwise be required. Images of the microplates containing the selected 10 samples are shown in Figure 7.4 with each column corresponding to a sample performed four times. Samples 3, 7 and 9 were known to fail within the 28-day specification limit. In the presence of a 2 mm oven-dried dish liquid seed, crystals formed in those three formulations after 48 hours. Conversely, in the absence of a seed, these formulations did not crystallise at such an early

stage, illustrating the capability of this seeding technique. These results also demonstrate that this technique is specific to unstable formulations. If it were to be implemented, the technique would need to be compared against the current test method to determine the time that corresponds to the 28-day specification limit.

(a)



(b)

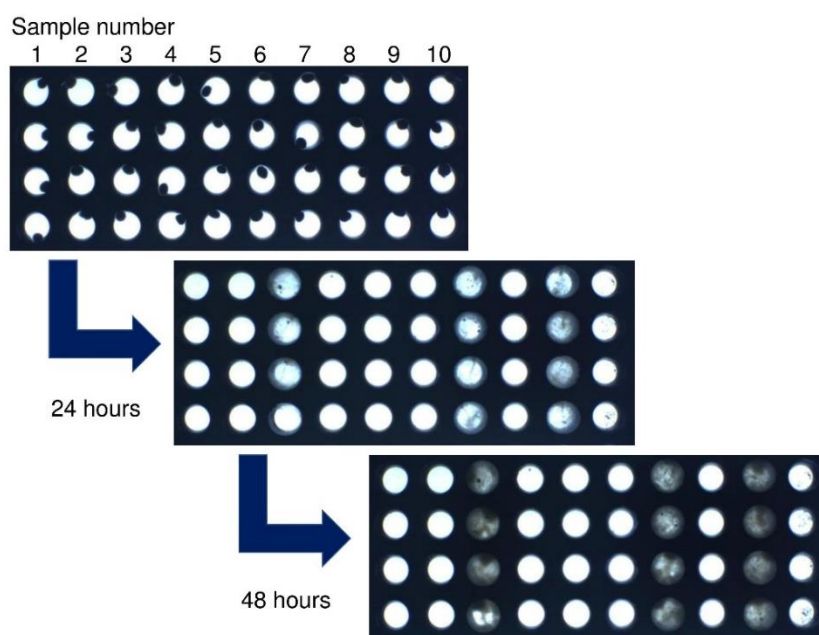


Figure 7.4. Microplate images for Samples 1-10 after 48 hours exposure to 0 °C (a) in the absence of any seeding and (b) in the presence of oven-dried dish liquid seeding.

P&G have previously investigated another seeding method involving the addition of 1 mm diameter metal balls into formulations, with crystallisation monitored via the microplate

technique. However, this route comes with the disadvantage that the resultant system might not be representative of a bottle sample since the addition of a ‘foreign object’ has the potential to alter properties of the bulk. Secondly, the timescale was not reduced to the same extent as oven-dried dish liquid seeding. The histogram in Figure 7.5 plots the transmission intensity for the first 10 samples at 0 °C after 7 days, with each sample performed in quadruplicate. In the absence of any crystal formation the transmission is high, with a maximum value of 255. As crystalline entities develop within the bulk, the transmission intensity reduces. Three of the 10 samples (Samples 3, 7 and 9) are known to fail. Therefore, there were a total of 12 unstable samples since each sample was repeated four times.

In the absence of any seed, only one sample (sample 9) displayed a reduction in light transmission after 7 days (Figure 7.5). However, in the presence of a seed, a higher sample frequency was obtained at lower transmission values. Comparing between the two seeding techniques in Figure 7.5, it can be concluded that oven-dried seeding reduces the transmission of the unstable samples to the largest extent. This implies an increased rate of crystallisation with this method, compared to metal-ball seeding. This is attributed to the similarity in the compositions of oven-dried dish liquid seeds and the target crystals. Furthermore, the rough surface of the oven-dried dish liquid seed can act as a base for heterogenous nucleation.

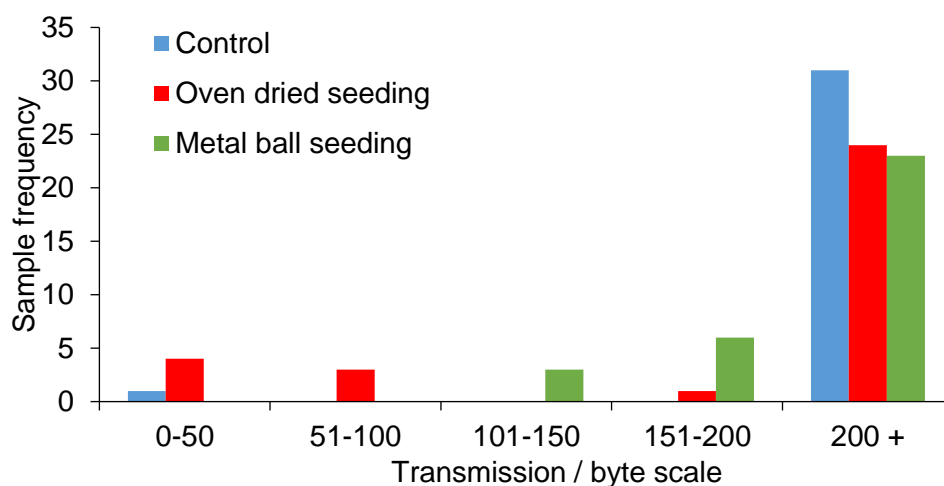


Figure 7.5. Histogram plots showing the transmission measured for Samples 1-10 (each performed in quadruplicate) after 7 days at 0 °C.

A further comparison between these two methods is displayed in Figure 7.6, in which the transmission is plotted at regular intervals over a 48-hour timescale. When seeded with metal balls, the transmission of the unstable samples (Samples 3, 7 and 9) does not drop significantly. However, upon the addition of an oven-dried dish liquid seed, the transmission of the unstable samples reduces after 48 hours. Crystals were found to only form over this timescale in the presence of an oven-dried dish liquid seed.

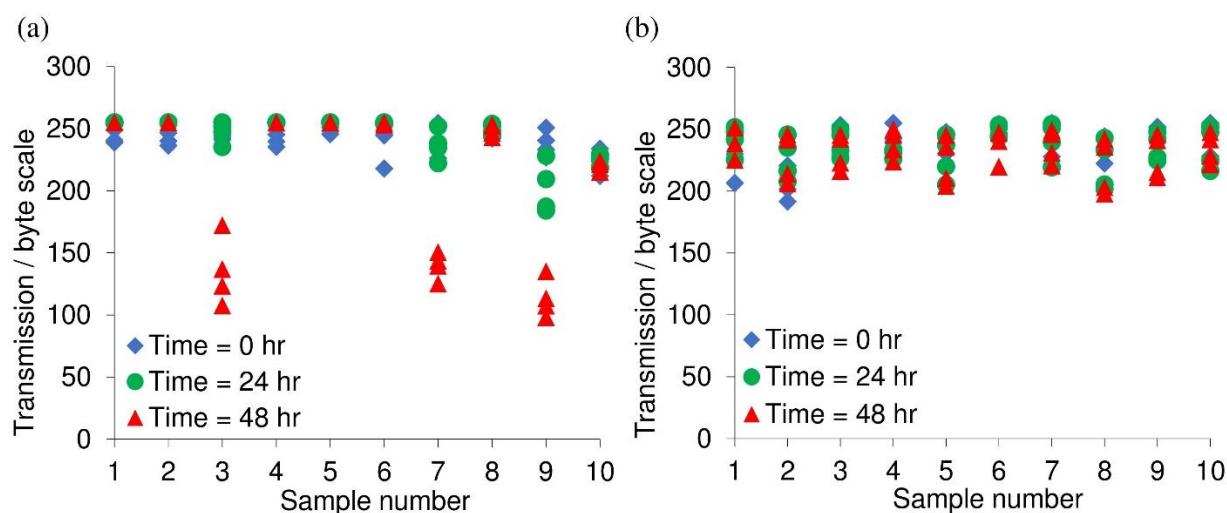


Figure 7.6. The effect of (a) oven-dried dish liquid seeding and (b) metal ball seeding on the light transmission measured at set intervals across Samples 1-10 when held at 0 °C for a total period of 48 hours. Each sample was performed in quadruplicate.

7.4.1.3 Method viability

The addition of an oven-dried dish liquid seed to a formulation at 0 °C was found to seed the crystallisation and be specific to unstable formulations. Oven-dried dish liquid seeds induced crystallisation within a shorter timescale compared to seeding with a metal ball. Increasing the number of seeds will promote surfactant crystallisation in multiple areas of the bulk and further increase the rate of crystallisation. The seed must also be above a defined critical size to promote crystallisation. Furthermore, a previous study used computer simulations to show that increasing the size of a spherical seed, beyond the critical size, impacts the energy barrier to nucleation (Cacciuto *et al.*, 2004). Larger seeds were found to lower the energy barrier to the greatest extent.

Production of the seeds and adding them to the respective formulations required considerable time and labour. The use of oven-dried dish liquid seeding is unlikely to be used to improve the testing timescales in industry so was not investigated further. As well as being a laborious

process, addition of an object can alter the properties of the system and result in the solution failing to be a true representation of the bulk. Although the oven-dried dish liquid seed may not be strictly considered as a ‘foreign object’, since it is produced from the bulk, it will increase the total surfactant concentration in the sample. In most of the samples shown in Figure 7.5 the seed appears to have at least partially dissolved. To minimise any changes to the formulation, the next method of screening focused on a technique not requiring the addition of a seed.

7.4.2 Sonication

The use of sonication was investigated as an alternate route to promote crystallisation in dish liquid products. In previous studies sonication has been used to control crystal growth and reduce the nucleation time of various systems (Lee *et al.*, 2014; Sander *et al.*, 2014; Dincer *et al.*, 2014). In the presence of sonication, a process known as cavitation occurs in the system that involves the formation of bubbles that collapse and form additional nucleation sites (Wu *et al.*, 2013).

Figure 7.7 shows optical images of unstable dish liquid samples contained in microplates for 6 days at 0 °C, in the absence and presence of sonication. The presence of crystals reduces light transmission. As can be seen from Figure 7.7, the average light transmission after 6 days for each sample set is lower when sonicated, compared to the control. This implies that there is an increased probability of crystallisation when samples are subjected to initial sonication.

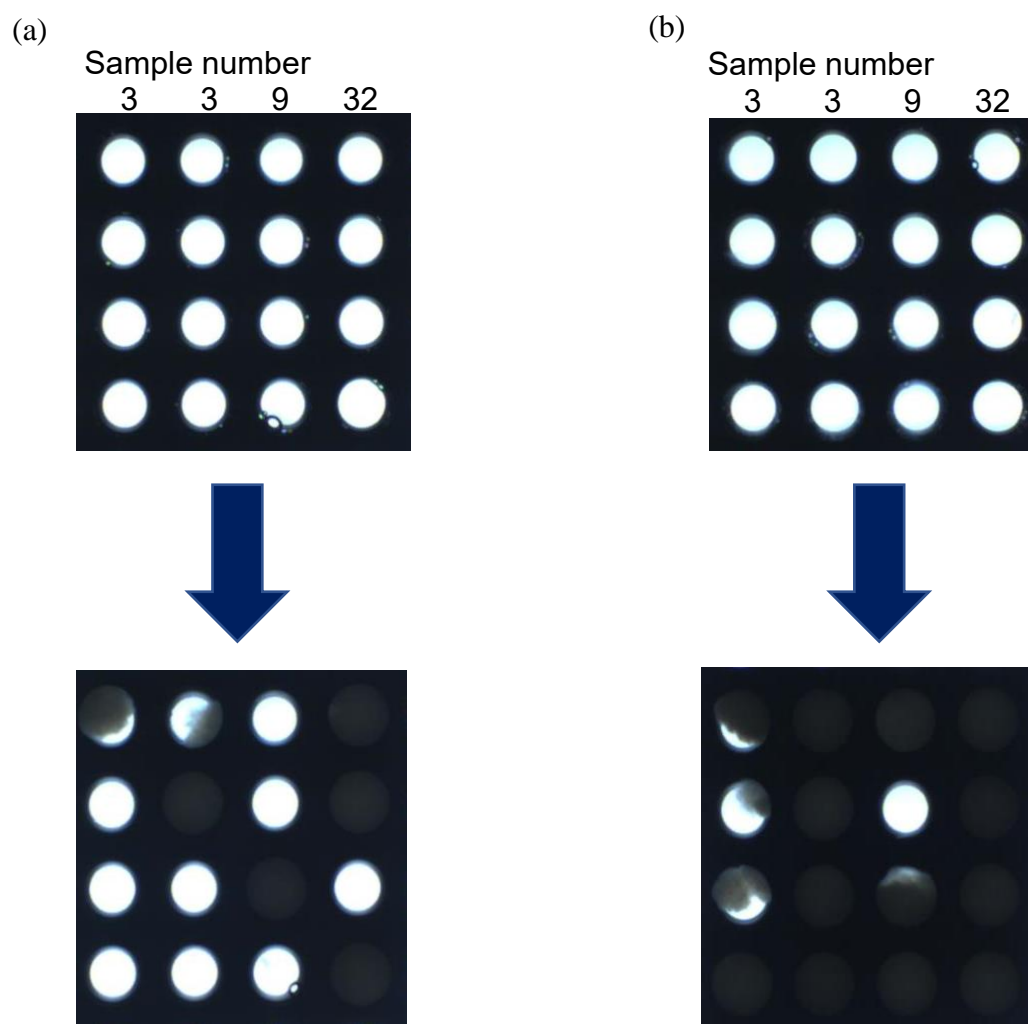


Figure 7.7. Microplate optical images for the (a) control and (b) sonicated samples at the initial time point (top) and after 6 days (bottom) at 0 °C for 3 samples that are prone to failure, namely Samples 3, 9 and 32 (columns), each performed 4 times (rows). A second set of Sample 3 was also performed.

The related plots that illustrate the changes in transmission across the 6 days are shown in in Figures 7.8(a), (b) and (c). When samples are exposed to sonication, the intensity reduces at a faster rate indicating an increased rate of crystallisation.

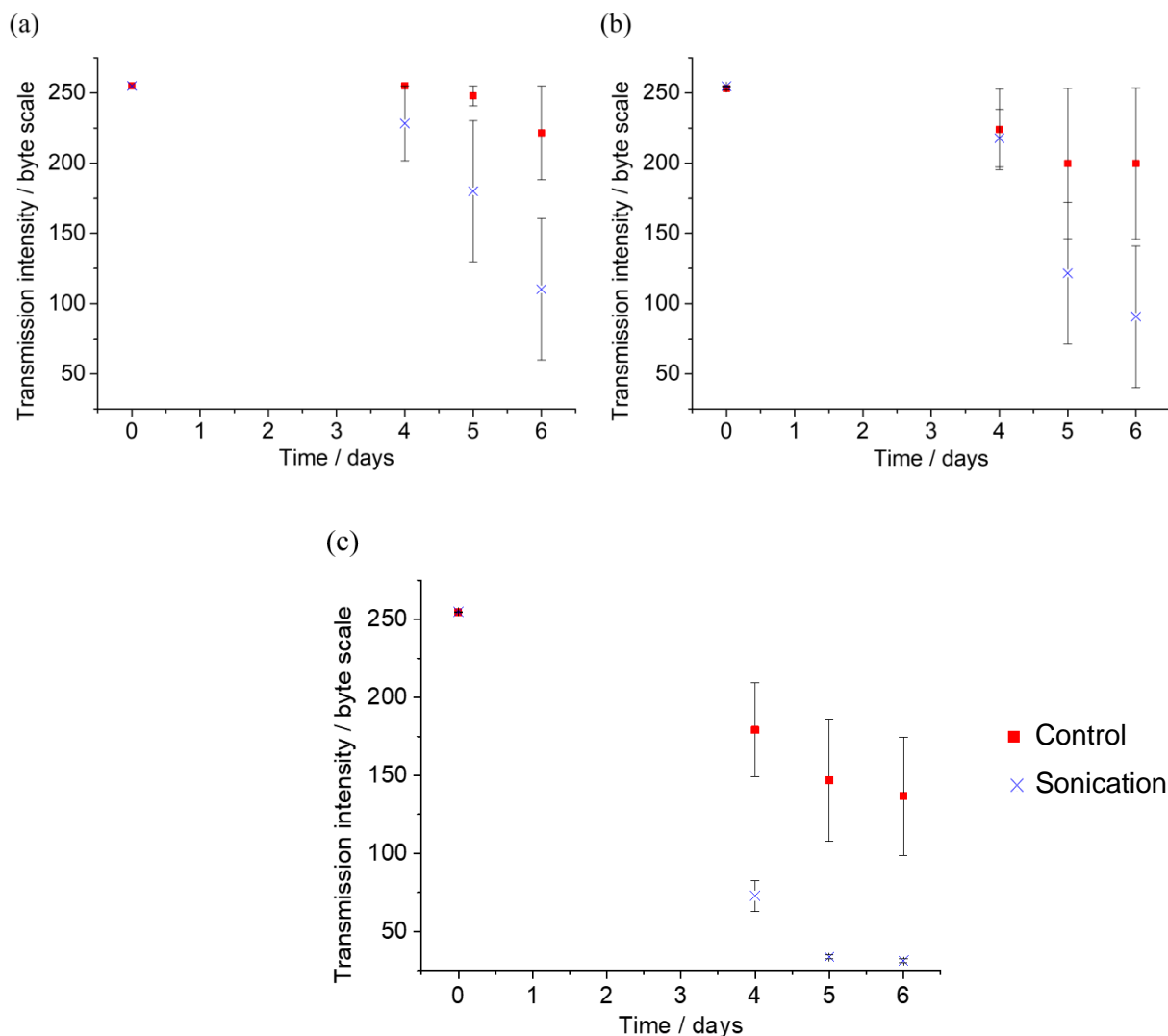


Figure 7.8. Change in the intensity of the detected light transmission for (a) Sample 3, (b) Sample 9 and (c) Sample 32 in the presence (red boxes) and absence (blue crosses) of sonication across a 6-day timescale at 0 °C.

These initial results appeared promising with sonication appearing to reduce the time to failure by at least a day. When repeating this experiment across all 32 samples, the times to failure exhibited a longer timescale and were also less reproducible. Contrary to the initial results, the time to crystal formation did not decrease significantly compared to control samples.

The possible reasoning for the lack of reproducibility was attributed to:

1. Contamination of the sample by the surrounding water if a seal was not completely airtight.

2. Variability of the position of the microplate within the sonication bath.

The use of a sonicating probe has potential to mitigate these problems and may form part of future work arising from this research project. With a probe there is the option to control power, positioning and, additionally, no water bath is required.

7.4.3 Mixing

A third route involving the application of mixing was considered. Chapter 8 details the reduction in time to crystallisation by this method.

7.5 Conclusions

A method that involved the addition of oven-dried dish liquids seeds of the respective formulations proved successful at instigating crystallisation. Across many formulations, the time to failure was reduced significantly compared to control samples, with the seeds providing a base for nucleation. Furthermore, the method was found to be specific for unstable formulations where it is thermodynamically favourable to form crystals. Despite reducing the timescale and variability of failure times, the method presented disadvantages. Producing the seeds was found to be time consuming and the seed size proved difficult to control accurately. Secondly, the bulk liquid in the test needed to be representative of the formulation found in a consumer bottle but, on addition of a seed, this may no longer be the case as the total surfactant concentration increases.

The potential of sonication to promote crystallisation was also investigated, since it does not require the addition of a seed. After initially testing the method across three unstable formulations, it appeared to be a viable option. However, upon further testing, the reproducibility was poor, possibly due to factors surrounding the water bath setup.

With limited access to other sonicating sources, the application of mixing was considered as an alternative route. This method proved more successful than seeding and sonication and is outlined in Chapter 8.

7.6 References

- Allahyarov, E., Sandomirski, K., Egelhaaf, S. U. & Löwen, H. 2015. Crystallization seeds favour crystallization only during initial growth. *Nature Communications*, 6, 7110.
- Bajaj, S., Singla, D. & Sakhuja, N. 2012. Stability Testing of Pharmaceutical Products.
- Bergfors, T. 2003. Seeds to crystals. *Journal of Structural Biology*, 142, 66-76.
- Cacciuto, A., Auer, S. & Frenkel, D. 2004. Onset of heterogeneous crystal nucleation in colloidal suspensions. *Nature*, 428, 404-406.
- Degner, B. M., Chung, C., Schlegel, V., Hutkins, R. & McClements, D. J. 2014. Factors Influencing the Freeze-Thaw Stability of Emulsion-Based Foods. *Comprehensive Reviews in Food Science and Food Safety*, 13, 98-113.
- Diao, Y., Harada, T., Myerson, A. S., Alan Hatton, T. & Trout, B. L. 2011. The role of nanopore shape in surface-induced crystallization. *Nature Materials*, 10, 867.
- Dincer, T. D., Zisu, B., Vallet, C., Jayasena, V., Palmer, M. & Weeks, M. 2014. Sonocrystallisation of lactose in an aqueous system. *International Dairy Journal*, 35, 43-48.
- Falbe, J. 2012. *Surfactants in Consumer Products: Theory, Technology and Application*, Springer Berlin Heidelberg.
- Lee, J., Ashokkumar, M. & Kentish, S. E. 2014. Influence of mixing and ultrasound frequency on antisolvent crystallisation of sodium chloride. *Ultrasonics Sonochemistry*, 21, 60-68.
- Maksimov, A. O., Kaverin, A. M. & Baidakov, V. G. 2013. Heterogeneous Vapor Bubble Nucleation on a Rough Surface. *Langmuir*, 29, 3924-3934.

- Okawa, S., Saito, A. & Minami, R. 2001. The solidification phenomenon of the supercooled water containing solid particles. *International Journal of Refrigeration*, 24, 108-117.
- Sander, J. R. G., Zeiger, B. W. & Suslick, K. S. 2014. Sonocrystallization and sonofragmentation. *Ultrasonics Sonochemistry*, 21, 1908-1915.
- Summerton, E., Zimbitas, G., Britton, M. & Bakalis, S. 2016. Crystallisation of sodium dodecyl sulfate and the corresponding effect of 1-dodecanol addition. *Journal of Crystal Growth*, 455, 111-116.
- Summerton, E., Zimbitas, G., Britton, M. & Bakalis, S. 2017. Low temperature stability of surfactant systems. *Trends in Food Science & Technology*, 60, 23-30.
- Williams, S. D. & Schmitt, W. H. 2012. *Chemistry and Technology of the Cosmetics and Toiletries Industry*, Springer Netherlands.
- Wu, T. Y., Guo, N., Teh, C. Y. & Hay, J. X. W. 2013. Theory and Fundamentals of Ultrasound. *Advances in Ultrasound Technology for Environmental Remediation*. Dordrecht: Springer Netherlands.

CHAPTER 8

UNDERSTANDING THE CRYSTALLISATION PROCESS IN DETERGENT FORMULATIONS IN THE ABSENCE AND PRESENCE OF AGITATION

Discussions contained in this chapter have been accepted for publication within:

Summerton, E., Bettiol, J., Jones, C., Britton, M. M., and Bakalis, S., 2018. Understanding the crystallisation process in detergent formulations in the absence and presence of agitation, *Industrial Engineering & Chemistry Research* (in press).

8.1 Abstract

Detergent formulations are used on a global scale and, therefore, are exposed to a wide range of temperatures and shear rates during distribution. At low and sub-zero temperatures, crystallisation may occur in the product. Manufacturers utilise a variety of methods to detect these crystal failures, typically involving the storage of formulations between $-3\text{ }^{\circ}\text{C}$ and $10\text{ }^{\circ}\text{C}$ for up to 28 days. This paper describes the application of agitation as a route to reduce the timescale of the stability tests, increasing productivity. Furthermore, agitation simulates vibrations that the formulations experience during distribution. In the absence of mixing, crystallisation was found to originate from the air-liquid interface, whereas, in the presence of mixing, the crystallisation began around the mixing blade. The times to failure as detected by the current and proposed methods correlated with each other, indicating the potential for this novel approach to be used in stability testing.

8.2 Introduction

The soap and detergent industry manufactures a wide range of products, such as shampoos, fabric conditioners and dish liquids, with an estimated net-worth of \$97.26 billion in 2016 (GrandViewResearch, 2018). Surfactants are the main components in these products, typically present at concentrations between 15 % and 40 % (Lai, 1996). The detergent industry is a major user of anionic surfactants (Scheibel, 2004). Sodium dodecyl sulfate (SDS) and N,N-dimethyldodecylamine N-oxide (DDAO) are examples of an anionic surfactant and amphoteric surfactant, respectively, present in detergent formulations. Under the alkaline conditions of dish liquid, amine oxides exhibits non-ionic behaviour (Singh *et al.*, 2006).

Since cleaning products are used worldwide, they must demonstrate chemical and physical stability across a wide range of environments. At high temperatures there is a risk of

discolouration, due to an increase in the reactivity and degradation of dyes in the formulation (Bechtold and Mussak, 2009), and at low and sub-zero temperatures surfactant crystallisation may occur, both of which are detrimental for physical stability.

Despite the industrial significance of surfactant crystallisation with respect to detergent products, there are limited studies into the crystallisation of mixed surfactant systems (Soontravanich and Scamehorn, 2009; Stellner and Scamehorn, 1986; Fan *et al.*, 1988; Shiau *et al.*, 1994; Soontravanich *et al.*, 2009; Summerton *et al.*, 2018). The tendency of an anionic surfactant system to crystallise is reduced on addition of a non-ionic surfactant, as has been reported for SDS + nonphenol polyethoxylate (Soontravanich and Scamehorn, 2009; Shiau *et al.*, 1994) and SDS + DDAO mixtures, performed as part of this thesis (Chapters 3-5) (Summerton *et al.*, 2018). In the presence of a non-ionic surfactant, micelle formation becomes increasingly favoured reducing the concentration of anionic surfactant monomers, from which crystals form.

In addition to the types of surfactants present in the mixture, it is also expected that physical factors such as agitation, presence of dust particles, temperature and air-liquid interfacial area also influence the mechanism of crystallisation in detergent products and associated stability tests. In this paper, the effect of agitation on the failure mechanism is discussed and compared to the behaviour observed in the absence of any agitation. The mechanism of crystallisation within detergents, both in the absence and presence of agitation, is yet to be addressed in the literature.

Understanding the effect of agitation on detergent crystallisation will provide insight into product stability during the supply chain. Formulations are exposed to high levels of agitation during road transport and the unloading and loading of goods, but less vibration when travelling via ferry or plane (Saunders, 1998). Depending on the condition of the road surface, the

background vibration during vehicle transportation has accelerations between 0.5 and 1 g, where g is the gravitational constant. In contrast, loading products into aircraft can result in shocks up to 10 times greater. When products are transported worldwide, they are also subjected to a selection of temperatures, typically ranging between $-3\text{ }^{\circ}\text{C}$ and $50\text{ }^{\circ}\text{C}$. The temperatures are prone to change, where a rate of $0.1\text{ }^{\circ}\text{C}/\text{min}$ is typical of environmental fluctuations (Miller *et al.*, 2017). When products are transferred between different environments, such as from inside to outside storage, the rate of thermal change ranges from 0.5 to $50\text{ }^{\circ}\text{C}/\text{min}$ (Miller *et al.*, 2017). In warehouses or production plants such changes are unavoidable. Products are typically held in warehouses for limited periods, between 2 and 4 hours, before onward transportation (Seiler, 2011). Following transportation, home and personal care products must remain stable for a 2 year shelf life period (Chantraine *et al.*, 2006).

To ensure product stability through the preparation, packaging, transportation and subsequent shelf life, manufacturers have methods in place. Typically, formulations are stored in temperature chambers ($50\text{ }^{\circ}\text{C}$ to $-3\text{ }^{\circ}\text{C}$) and their chemical properties, including viscosity, appearance and odour, are monitored at regular intervals (Falbe, 2012). In addition, the effect of continuous heating and cooling on sample stability must also be tested, to account for temperature fluctuations experienced during the supply chain. This type of test is also important in other industries. For example, in the food sector, freezing is often used by consumers for preservation purposes (Degner *et al.*, 2014). When defrosting the product, it must retain all chemical and physical attributes. The current tests for detergent products solely monitor the stability of quiescent formulations, which is not necessarily representative of the supply chain where background vibrations exist. Therefore, there is a requirement for a method which incorporates agitation and more closely simulates the distribution process.

The application of agitation may also improve the efficiency of the stability test methods at low temperatures. The timescales of stability tests can be long, requiring up to 28 days of storage at a variety of temperatures. With the present method, the time to crystallisation also varies between samples of the same formulation. This is attributed to factors that are difficult to control such as the existence of dust particles, temperature fluctuations or pressure differences. Dust or other foreign objects can provide nucleation sites for crystallisation (Hartel and Shastry, 1991; Hartel *et al.*, 2011). As a result, it is necessary to identify an alternative test method capable of determining whether a formulation remains physically stable within a shorter timescale and with reduced variability, resulting in an increase in productivity.

Using agitation to reduce the timescale of crystallisation in detergent products is an area of scientific research that has not previously been reported in the literature. However, agitation is known to influence the time to crystal formation in other systems through both secondary and primary nucleation effects (McLeod *et al.*, 2016). A study into the kinetics of alpha-lactose monohydrate crystallisation revealed an increase in the rate of primary nucleation upon agitation (McLeod *et al.*, 2016). From classical nucleation theory, the primary nucleation rate J is a sum of the heterogenous and homogenous nucleation contributions:

$$J_{\text{total}} = J_{\text{hom}} + J_{\text{het}} \quad (8.1)$$

Each J component can be provided by equation 8.2:

$$J = Ae^{-\frac{\Delta G}{kT}} \quad (8.2)$$

where A is the pre-exponential factor, ΔG is the energy of nucleation, k is the Boltzmann constant and T is the temperature (Mullin, 1997). Upon mixing (agitation), the increase in J is attributed to an increase in the pre-exponential factor A of both the heterogenous and homogeneous components. The energy barrier for heterogenous nucleation also decreases with mixing. This parameter also depends on the degree of supercooling. The increase in A is due to

increased Brownian motion of the molecules resulting in a higher probability of forming crystals (Mazzanti *et al.*, 2007; Rathee *et al.*, 2013). This has also been demonstrated for silica particle systems, in which only a small amount of shear was applied (Wu *et al.*, 2009). The rough surface of the stirrer provides additional nucleation sites for crystallisation, reducing the barrier to heterogenous nucleation (Maksimov *et al.*, 2013; McLeod *et al.*, 2016).

In addition to primary nucleation, the application of mixing also influences secondary nucleation. In a study focused on the crystallisation of glutamic acid (Liang *et al.*, 2004), it was found that mixing increased the rate of secondary nucleation in the bulk. The high shear at the stirrer blade diminishes the boundary layer surrounding the crystals and mixing blade thus promoting further crystal growth. Furthermore, crystals are broken apart by the mixer to yield additional nuclei sites throughout the system (Callahan and Ni, 2014).

This chapter explores the potential of mixing to reduce the time to crystallisation across a range of dish liquid products, with varying degrees of stability. Discussion and insight into the mechanism of the failure, both in the presence and absence of mixing, is also discussed. With this knowledge, it will enable industry to develop more robust formulations, improved packaging and more efficient stability tests. In particular, an insight into the origins of crystallisation is crucial for improving product stability.

8.3 Materials and methods

8.3.1 Materials

8.3.1.1 Model SDS + DDAO studies

Binary surfactant solutions were prepared with 20 wt. % SDS and 3 wt. % DDAO in distilled water and used for conductivity measurements. SDS (Fisher Scientific, 97.5 %) and DDAO (Sigma Aldrich, 30 wt. % in water) were used without further purification. The solutions were

made up 24 hours in advance to minimise hydrolysis. The solution was mixed for 15 minutes at 25 °C and then left for 12 hours to release any entrapped air.

8.3.1.2 Commercially relevant dish liquid formulations

When crystals appear in complex commercial products, the resulting appearance is unacceptable for consumers. By understanding the mechanism of the crystallisation process, it is expected that product stability at low temperatures, between 10 °C and –3 °C, and the efficiency of the stability tests can be improved. Therefore, to ensure the industrial relevance of this work, commercially relevant dish liquid products were used throughout the study. A typical dish liquid formulation consists of anionic surfactants (linear, branched and ethoxylated alkyl sulfates), amphoteric surfactants (linear amine oxides), water, preservatives, dyes, perfume, sodium chloride (NaCl), polypropylene glycol and ethanol. Remnant alcohol precursor of the alkylsulfate component may also be present. Completeness is related to the amount of alcohol remaining in the system (equation 8.3):

$$\text{Completeness (\%)} = \frac{\left(Act \frac{MW_{al}}{MW_{as}}\right)}{\left(Act \frac{MW_{al}}{MW_{as}}\right) + UnR} \times 100 \% \quad (8.3)$$

where *Act* is the active level (wt. %), *MW_{al}* and *MW_{as}* are the molecular weights of the alcohol and alkyl sulfate respectively and *UnR* is the amount of alcohol in wt. %.

8.3.1.2.1 Formulations A and B

Mechanistic studies, in the absence and presence of mixing, were performed using a dish liquid product, Formulation A, specifically formulated to be unstable at low temperatures. Prior stability tests revealed that Formulation A develops crystallites at 0 °C within 28 days. Conversely, Formulation B was formulated to be stable under the same conditions. In Formulation A, the degree of ethoxylation *m* of the alkyl sulfate component

$C_xH_y(OCH_2CH_2)_mOSO_3^- Na^+$ averaged at 0.5 moles and the wt. % ratio of alkyl sulfates to amine oxides was 4.4:1. The degree of ethoxylation m of the alkyl sulfate component $C_xH_y(OCH_2CH_2)_mOSO_3^- Na^+$ in Formulation B averaged at 0.6 moles and the wt. % ratio of alkyl sulfates to amine oxides was set as 3:1. Commercial grade sunflower oil was also used to explore the role of the air-liquid interface in the crystallisation process. Furthermore, the effect of mixing speed on the crystallisation process was investigated using Formulation A.

8.3.1.2.2 Formulations X1-X6

Whilst Formulations A and B were tailored to be stable and unstable at low temperatures, respectively, Formulation X1-X6 spanned a range of product stabilities as determined from standard stability tests at 0 °C. These were used to compare the times to crystallisation in the absence and presence of mixing for a selection of formulations to determine a correlation between the current and proposed methods.

The six formulations varied in the molar amounts of the linear (LA) and branched (BrA) alcohol contributions and linear (LAE) and branched ethoxylated (BrAE) alcohol contributions. The blends were subsequently sulfated and the other ingredients added, while maintaining the same alkyl sulfate to amine oxide ratio (3.0:1), the same total surfactant concentration (35.8 wt. %) and a comparable completeness level between the two products.

8.3.2 Methods

8.3.2.1 Conductivity

30 g of the surfactant solution was placed in a 50 mL glass beaker and inserted into a jacketed vessel. The temperature of the 50:50 (by vol. %) water:ethylene glycol mixture contained in the jacket was controlled by a Grant LTD 6G cooling bath. Upon cooling from 25 °C to 0 °C, the conductivity of the 20 wt. % SDS + 3 wt. % DDAO solution was measured every 30 seconds

via an Orion star A212 conductivity meter. A mini-stirrer was used to induce mixing in the system for the duration of the experiment. The conductivity probe and the stirrer were equally spaced across the diameter of the beaker. The distance between the stirrer and the probe was equal to the distance from each to the wall of the container. The stirrer and the probe were at the same vertical position in the solution, halfway between the bottom of the container and the solution surface. The stirrer paddle was supplied as an attachment to the Orion star A212 conductivity meter (Fisher Scientific), consisting of a double blade propeller, as presented in Figure 8.1 (a). A schematic of the overall setup is provided in Figure 8.1 (b).

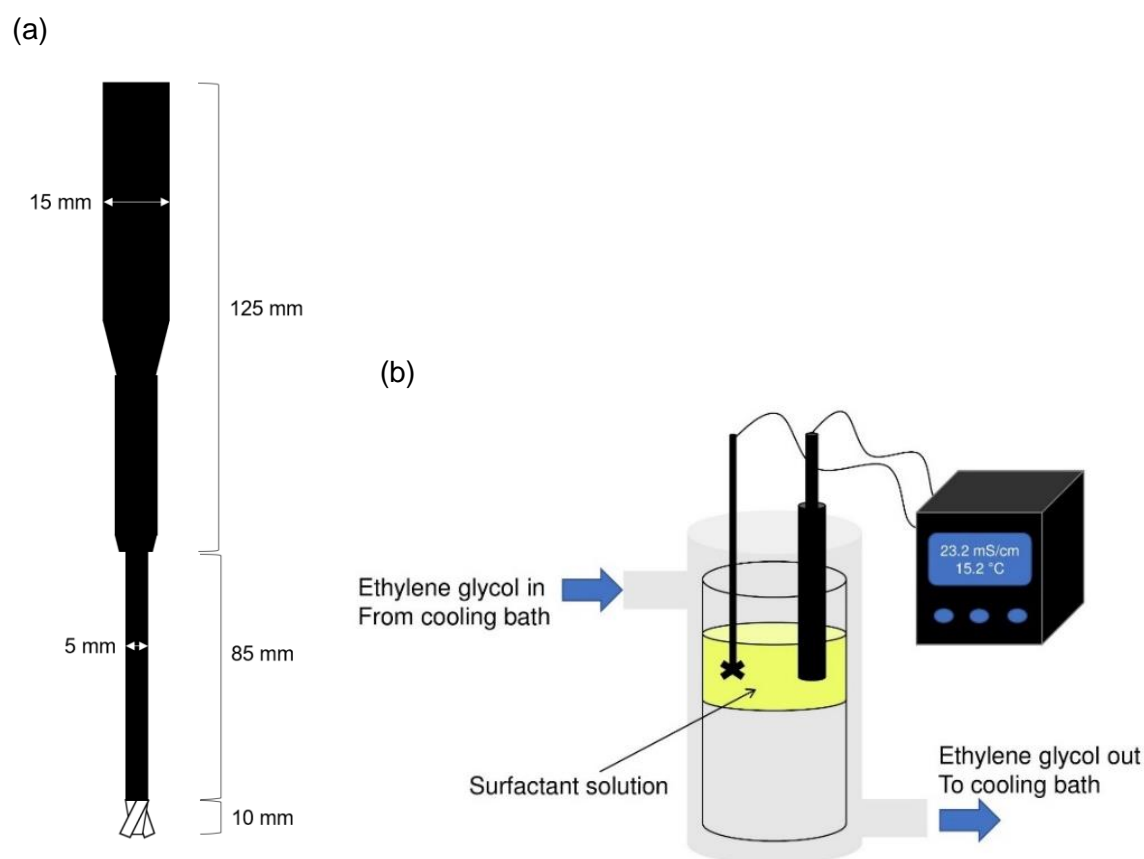


Figure 8.1. (a) Stirrer probe dimensions (b) Schematic diagram of the setup for conductivity measurements.

The rate of cooling was approximately 0.5 °C/min. Each measurement was performed in triplicate at the five different speeds (indicated in Table 8.1) and in the absence of any stirring.

Table 8.1. Speed levels and corresponding rpm values.

Stirrer speed setting	Speed of rotation / rpm
1	914
2	1385
3	1842
4	2310
5	3333

8.3.2.2 Time lapse photography

8.3.2.2.1 Cooling chamber experiments

Crystallisation of the dish liquid formulations was visually recorded using a Canon EOS 5D Mark II. 80 g of each formulation was added into a 100 mL test bottle composed of polyethylene terephthalate (PET). Samples were placed in a Memmert ICP 450 chamber, set to 0 °C. Images were automatically captured every 10 seconds for a period of 7 days for each formulation. A backlight panel was used to minimise any light reflections from the surroundings. For each test, three replicate measurements were performed. Image analysis was performed using a processing software developed by P&G.

This software functions by converting a selected area of each image set to greyscale and assigning each individual pixel a value from 0 to 255, depending on the greyscale intensity. For each test, the maximum area of the bulk absent from light reflections was used in the analysis. Each image can be envisaged as a 2D-matrix filled with pixel values between 0 and 255. A greyscale co-occurrence matrix (GCOM) was produced for the positional relation $x = 0, y = 1$, where each pixel was compared to the one vertically above (Sebastian *et al.*, 2012). The matrix depends on how many times a certain difference in greyscale occurs between pixels with this chosen spatial relationship. The matrix was subsequently normalised and the homogeneity, a statistical property of the matrix (Rao *et al.*, 2013), was calculated (equation 8.4).

$$\text{Homogeneity} = \sum_{i,j} \frac{p(i,j)}{1+|i-j|} \quad (8.4)$$

where i and j refer to the greyscale intensity of the i^{th} and j^{th} pixels; $p(i,j)$ is the cooccurrence probability of pixels i and j . The area of analysis was selected such that it incorporated most of the bulk within the bottle. Graphical plots showing the change in homogeneity across the different formulations were produced in OriginPro (v.9.0). From these plots, the time to failure for each quiescent formulation was estimated as the point at which the gradient changes indicating a decrease in homogeneity within the system.

In addition, 60 mm diameter and 100 mm diameter petri dishes containing 20 mL of Formulation A were placed in the chamber. 2D images of the petri dishes were captured at 24 hour and 48 hour time points using a Canon 100D positioned vertically above the sample. Thresholding in ImageJ was used to determine the area of the formulation which contained crystals.

A magnetic stirrer plate was also inserted in the chamber. To investigate the effect of mixing, a magnetic flea of 35 mm length and 6 mm diameter was added to a formulation contained in a 100 mL PET bottle and placed on the plate, with the flea rotating at approximately 10 rpm. However, the effect of mixing was investigated in detail with the jacketed vessel setup outlined below.

8.3.2.2.2 Jacketed vessel experiments

The vacuum jacketed glass vessel depicted in Figure 8.2 was used to observe the effect of mixing on dish liquid crystallisation at low temperatures. 400 mL of Formulation A was initially poured into the hemispherical vessel with an internal diameter of 75 mm. A Grant LTC4 cooling bath, filled with 50 % ethylene glycol and 50 % water by volume, was connected to the jacketed chamber. The bath was set to 0 °C and the vessel left to cool for 2.5 hours. This was the time

required for the centre of the vessel to reach 0 °C (see Appendix E). A temperature of 0 °C was selected for these investigations since the majority of low temperature stability tests within P&G are performed at this condition.

A Hei-TORQUE Precision 100 overhead stirrer was set to the chosen speed. A PTFE turbine stirrer blade was used with an 8 mm shaft diameter and a 400 mm shaft length. The impellor measured 40 mm in diameter and 15 mm in height. The blades were positioned at a 45 ° rotor angle with the length of each blade measuring 21 mm. The stirrer was positioned approximately 30 mm above the base of the vessel. Images were captured every 10 seconds for a total period of 60 minutes, or until crystallisation was complete, using a Cannon 100D mounted on a Velbon EF-61 tripod. A backlight panel was used to attain optimal images. Stirrer speeds of 20 rpm, 50 rpm, 150 rpm and 300 rpm were investigated, with three repeats performed at each speed.

The resulting time lapse images were analysed in MATLAB 2016b. Images were converted to 8-bit greyscale images with each pixel assigned a number from 0 to 255, corresponding to the intensity. Values of 255 and 0 relate to white and black pixels, respectively, with numbers between relating to differing amounts of greyscale. The change in average greyscale intensity for the pixels in each boxed area, A-D (Figure 8.2(b)), was determined. Using SigmaPlot, the results were plotted as percentages of greyscale intensity over time, with a value of 255 corresponding to 100 %. The time relating to a reduction in greyscale intensity is related to the onset of crystallisation.

This method was also used with Formulations X1-X6 to investigate the effect of mixing over a wider range of formulations. A stirrer speed of 20 rpm was used for these tests.

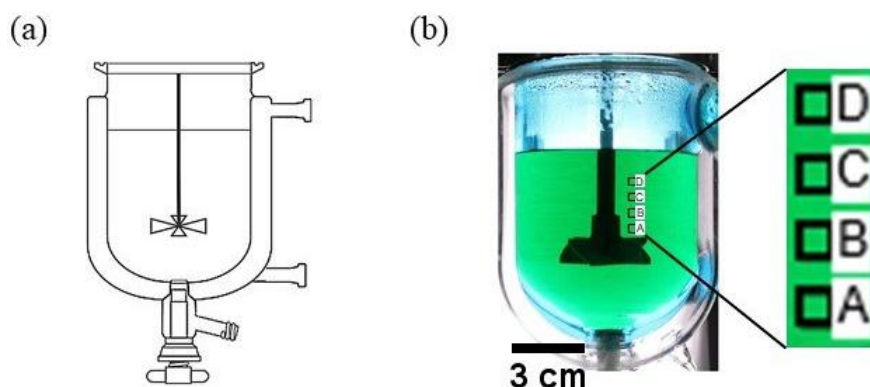


Figure 8.2. (a) Schematic diagram of vacuum jacketed vessel setup. Adapted from a figure supplied by Asynt Ltd. (b) Photograph of the vessel setup indicating the areas used in greyscale intensity analysis.

8.3.2.3 Transmissivity

The time to crystallisation in Formulation A was also detected using a Crystalline unit (Technobis, Netherlands), which was able to simultaneously record the temperature and turbidity of multiple samples. Crystal formation was detected by an increase in turbidity in the solution and a corresponding reduction in transmissivity. The instrument was connected to a Lauda Proline RP 845 cooling bath to attain the necessary low temperatures. For each measurement, 4 mL of Formulation A was pipetted into a vial and placed into the furnace of the instrument. To apply mixing, a mini overhead stirrer replaced the vial cap and the speed was set to 1000 rpm. The samples were exposed to temperature cycles from 20 °C to 0 °C at a maximum cooling rate of 15 °C/min and with a hold time of 1.5 hours at 0 °C and 30 minutes at 20 °C. Each experiment consisted of 13 consecutive temperature cycles, with every test performed in duplicate. The temperature and transmittivity were reported for the duration of each experiment. In comparison to experiments performed in test bottles or the jacketed vessel, this used smaller sample volumes.

8.4 Results and discussion

8.4.1 Mechanism without agitation

Time lapse images of Formulation A at 0 °C show crystal formation occurs at the air-liquid interface (Figure 8.3). In the absence of any physical forces or seeding, crystallisation is commonly observed to commence from the surface. The crystals subsequently sink to the bottom of the product over a time due to the higher density of crystals, with respect to the bulk.

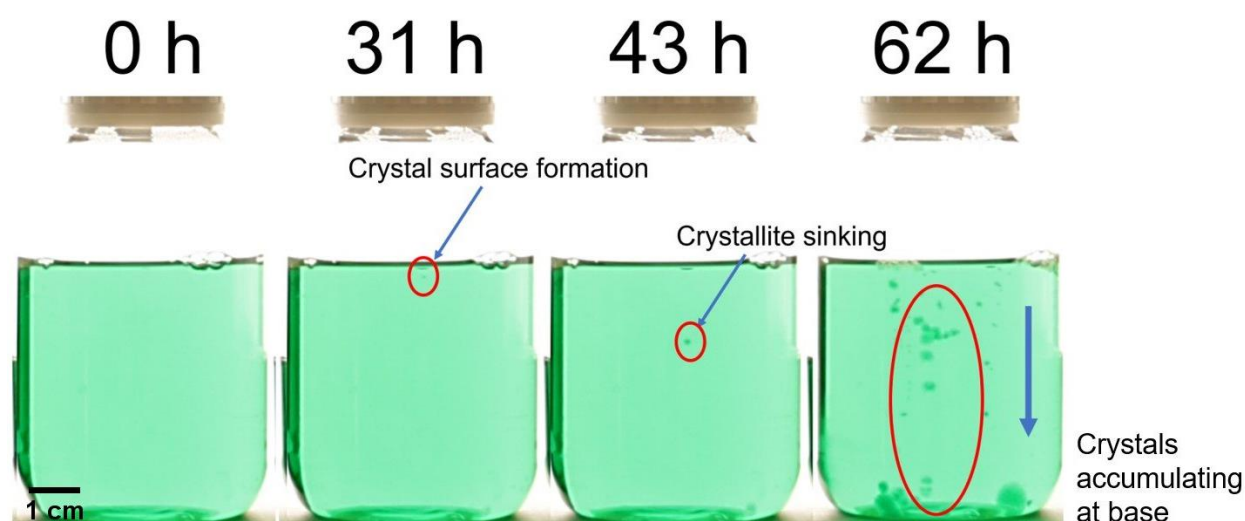


Figure 8.3. Time lapse images acquired during the crystallisation of Formulation A at 0 °C.

This observation can be explained by the segregation of surfactants at the air-liquid interface (Goodwin, 2004). Figure 8.4 shows a simplified schematic diagram of the different surfactant environments, before and after crystallisation. Surfactant molecules in the monolayer exist in a close packed arrangement and, therefore, bear a close structural resemblance to the crystals (Scaimehorn, 1986). The crystals are known to be alkyl sulfate hydrates, consisting of layers of alkyl sulfates separated by water layers (Summerton *et al.*, 2018). As result of this similarity, crystal formation from the interface is proposed to be the lowest energy pathway (Chen *et al.*, 2015). In addition, solvent evaporation may result in high local supersaturation at the surface,

compared to bulk, promoting crystallisation from this region (Hurle and Jakeman, 2014). However, at 0 °C, it is unlikely there will be significant evaporation from the formulation. The rate of evaporation depends on the air-liquid interfacial area and the vapour pressure of the formulation.

There is also evidence that the surfactants are organised in a bilayer just below the interface, rather than a monolayer at the surface (Shibata *et al.*, 2015; Moroi *et al.*, 2004). If this is the case, it is expected that crystallisation would originate from the close-packed bilayer.

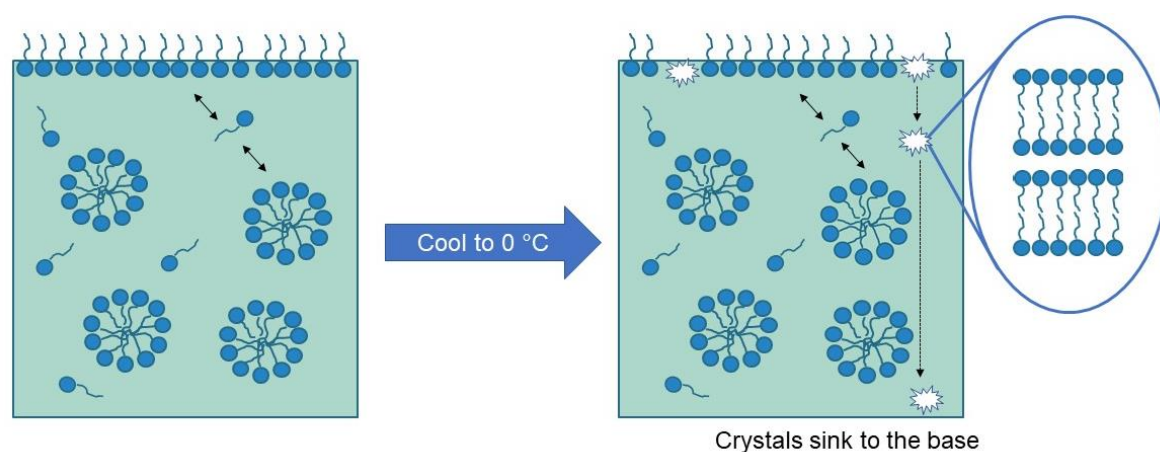


Figure 8.4. Simplified schematic diagram illustrating the different surfactant environments residing in a dish liquid sample at 25 °C and 0 °C.

A further test was performed in which an oil layer was added to Formulation A at 0 °C. On addition of the oil, no crystals were observed in Formulation A after 7 days at 0 °C (Figure 8.5). The presence of an oil layer on the surface was hypothesised to suppress crystallisation at the interface. The hydrophobic oil stabilises the surfactant hydrocarbon chains of the monolayer effectively ‘freezing’ the interface and reducing the drive for crystallisation. It is likely that the presence of the oil layer also reduces the degree of evaporation from the surface, minimising local supersaturation at the interface. Since supersaturation dictates whether a sample will crystallise, this effect may also contribute to a reduced tendency for crystallisation. In the

absence of an oil layer crystalline entities were observed after 2 days, as shown in Figure 8.5. Crystals sink to the bottom of the formulation, as indicated by the areas labelled 1, 2 and 3. These findings corroborate the proposed mechanism, where crystal formation occurs from the close-packed surfactant monolayer.

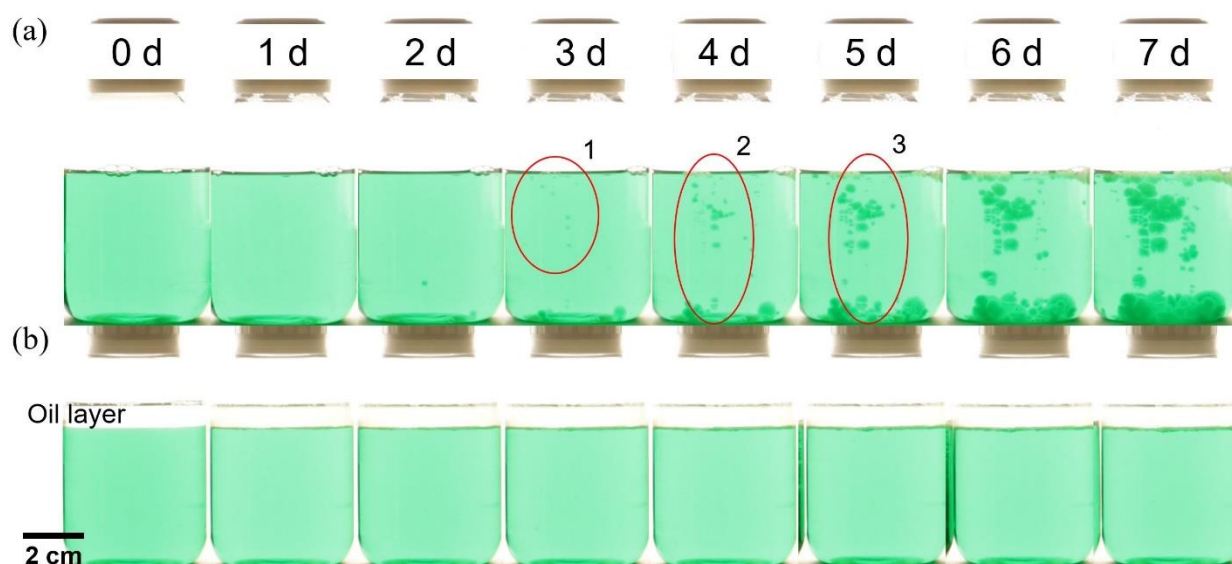


Figure 8.5. Time lapse images of an unstable dish liquid formulation held isothermally at 0 °C over 7 days **(a)** in the absence and **(b)** in the presence of a layer of sunflower oil.

Having established the importance of the air-liquid interface on crystallisation, the effect of the surface area of this interface was explored. Petri dishes of two different diameters were filled with the same volume of Formulation A and stored at 0 °C. After 24 hours, there was only a minor difference in the measured crystalline area (Figure 8.6). However, after 48 hours, the area containing crystals was larger for the 100 mm diameter dish. This is a result of this dish having a greater air-liquid interface, from which the crystals can begin to grow.

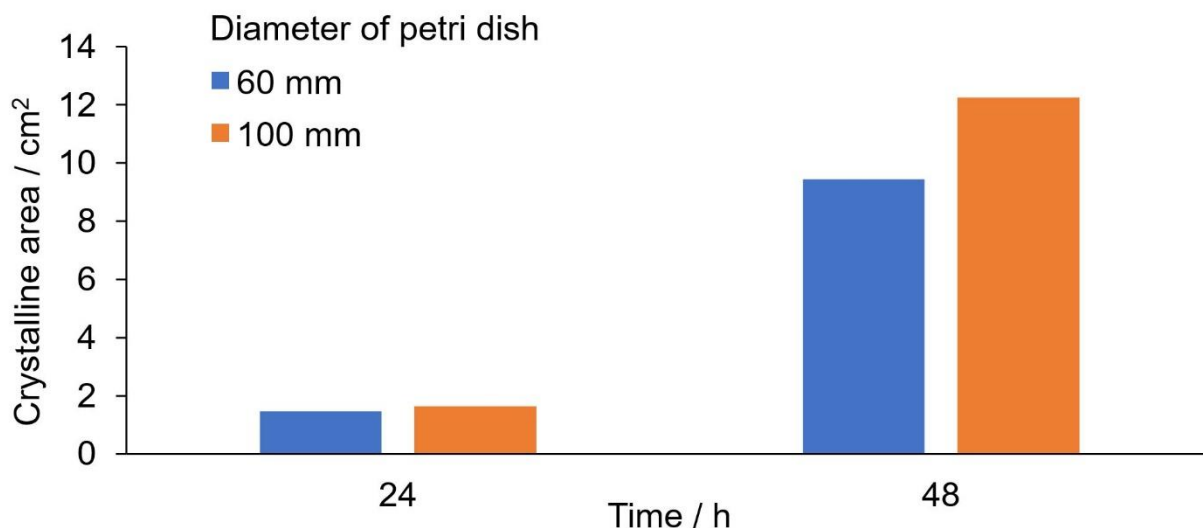


Figure 8.6. Relation of petri dish diameter to the crystallisation area, measured after 24 and 48 hours at 0 °C.

8.4.2 Effect of agitation

8.4.2.1 Application to the model SDS + DDAO system

The effect of mixing on the crystallisation kinetics was investigated, using conductivity measurements, on a model SDS + DDAO system. When the SDS + DDAO system crystallised, there was significant decrease in conductivity of the solution. The counterions in the solution bind to the crystal phase and become less available to transport charge (Sasaki, 2007). A typical conductivity profile is provided in Figure 8.7(a) which shows that crystallisation has occurred by the time the conductivity of the SDS + DDAO solution reaches 8 mS/cm. The time for crystallisation is indicated by the time for the conductivity to reach 8 mS/cm and is plotted across the different stirrer speeds in Figure 8.7(b). The average time for the quiescent sample to reach this value is 41 minutes longer than the time measured when stirring the solution at maximum speed. These results imply that mixing promotes the onset of SDS crystallisation.

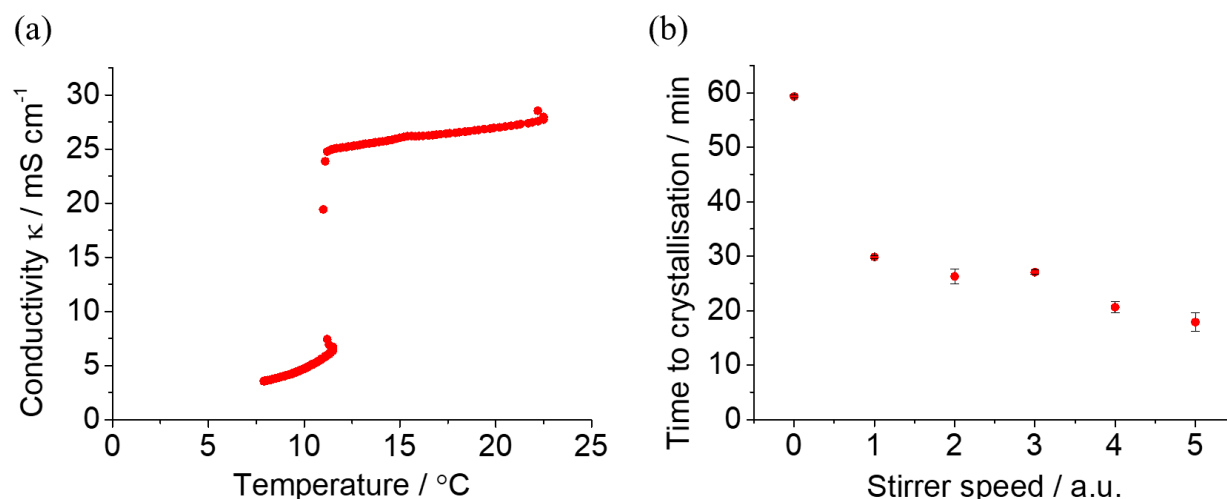


Figure 8.7. (a) Typical conductivity plot attained upon cooling a 20 wt. % SDS + 3 wt.% DDAO system at speed level 1 (949 rpm) (b) Plot of the time to crystallisation across the range of speed levels where the time for crystallisation is taken as the time for the conductivity of the surfactant solution to reduce to 8 mS cm^{-1} .

8.4.2.2 Application to dish liquid products

A representative time series of photos are shown in Figure 8.8 for Formulation A at 0°C , in the presence of mixing. Crystallisation was observed to begin around the stirrer bar rather than the air-liquid interface, as was the case for quiescent samples. Formulation B did not develop crystals even after mixing the formulation for 4 days at 0°C . This was expected since Formulation B did not fail current stability tests. The plot in Figure 8.9(a) shows the relative times to crystallisation for Formulation A under the influence and absence of mixing, determined by visual inspection. As expected from prior work on the SDS + DDAO model system (Section 8.4.2.1), the time to crystallisation reduces when the solution is stirred. Furthermore, the box plot in Figure 8.9(b) shows that the variability of failure times also reduces when mixed.

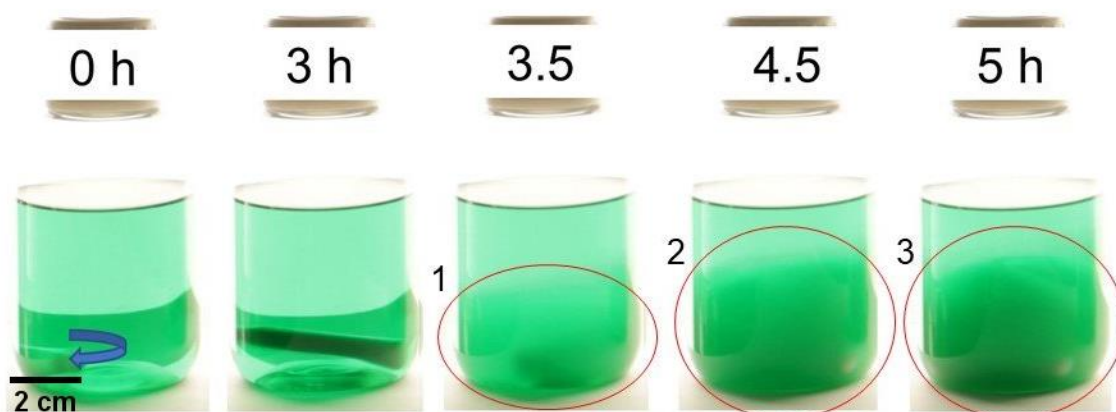


Figure 8.8. Time lapse images of the crystallisation of Formulation A in the presence of mixing. The initial colour differences in the solution are due to unavoidable light reflections from the surroundings. Circles 1, 2 and 3 indicate the growing crystalline area.

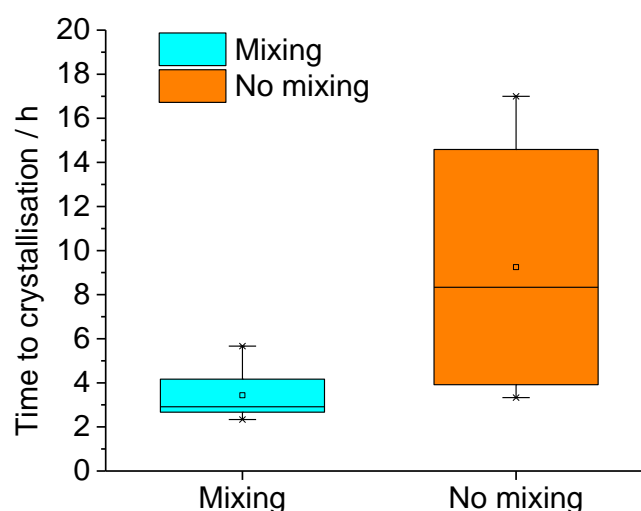


Figure 8.9. Box plot demonstrating the reduction in the timescale to crystallisation and statistical variability upon mixing at 0 °C, across 8 replicates of Formulation A.

The effect of mixing on dish liquid crystallisation was observed through a change in light transmission. In Figure 8.10 a snapshot is shown of the measured light transmission (blue line) across the fluctuating temperature cycles for the Formulation A, both in the absence and presence of mixing. A reduction in the transmissivity was only observed for the mixed sample.

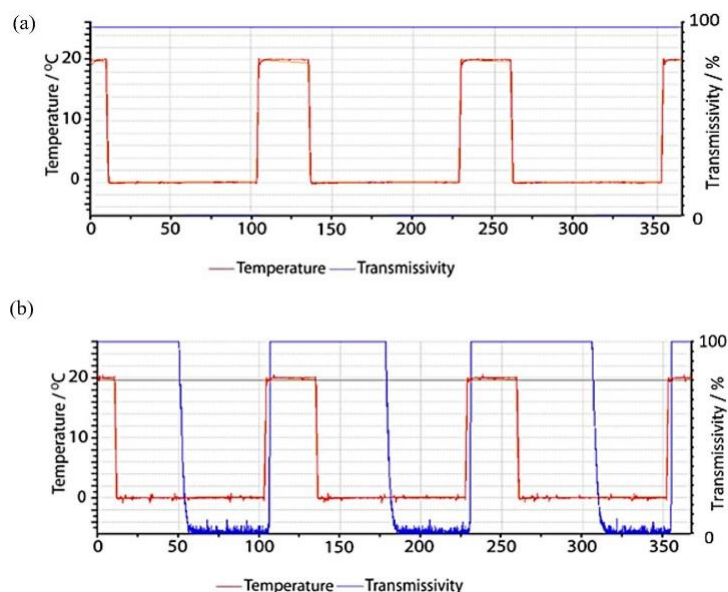


Figure 8.10. Snapshot of the light transmission measurements acquired for Formulation A across the displayed temperature cycle (a) in the absence of mixing and (b) in the presence of mixing.

Mixing not only reduces the time to crystallisation, and the associated variability, but appears to also affect the mechanism of crystal formation. When Formulation A was mixed at 0 °C, crystallisation originated from the stirrer blade (Figure 8.8) but, in the absence of mixing, crystals were initially observed at the air-liquid interface (Section 8.4.1). The reasons for this change in mechanism, and reduced timescale, are believed to be explained by secondary and primary nucleation effects (Callahan and Ni, 2014; McLeod *et al.*, 2016).

Secondary nucleation occurs when existing crystals are used to create further nucleation sites through the system. Possible mechanisms for secondary nucleation, when in the presence of mixing, include crystal breakage and dispersion, crystal-crystal and crystal-stirrer collisions or the replacement of crystal boundary layers with further solute molecules. The rate of secondary nucleation B_0 can be expressed by equation 8.5:

$$B_0 = kSM_T W \quad (8.5)$$

where k is a constant, S is supersaturation, M_T is crystal density and W is the agitation rate. Fluid movement is greatest for areas of the bulk closest to the mixing blade (Myerson, 2002; Paul *et al.*, 2004). Hence, the rate of secondary nucleation is also higher in these areas, which may explain why crystallisation is observed close to the stirrer.

The rate of primary nucleation is also affected by the presence of mixing (McLeod *et al.*, 2016; Liu *et al.*, 2015). The increased movement of the bulk, especially near the mixing blade, results in a higher collision frequency between the monomers and hence an increased probability of crystal nuclei formation (Liu and Rasmuson, 2013). This effect is more pronounced at the mixing blade, where the velocity of the fluid is highest. The rough stirrer surface provides additional nucleation sites for crystallisation. The energy barrier to heterogeneous nucleation reduces and crystallisation originates at the stirrer blade (Liang *et al.*, 2004).

8.4.3 Effect of mixing speed

Images were acquired during the crystallisation of Formulation A at 0 °C at various mixing speeds. Typical images are provided in Figure 8.11, at a speed of 20 rpm. These images provide further evidence for crystal formation starting around the stirrer, rather than the air-liquid interface. Images for 50 rpm, 150 rpm and 300 rpm can be found in Appendix E, Figure E.3.

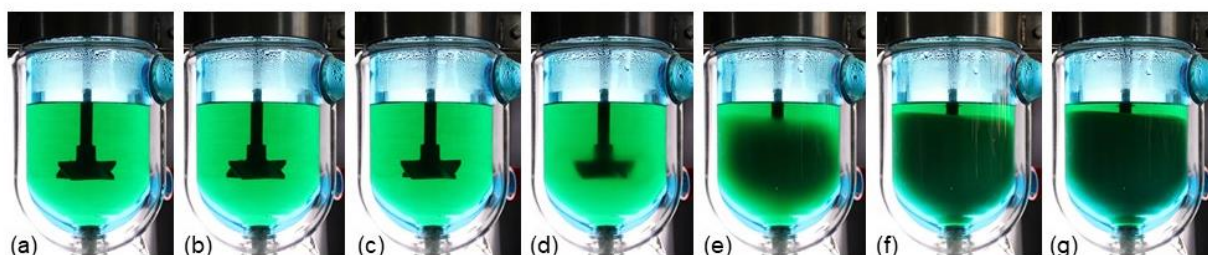


Figure 8.11. Time series of images, acquired at 10 minute intervals, during the crystallisation of Formulation A at a stirrer speed of 20 rpm, with the solution held at 0 °C.

Plots of the average greyscale intensity over time for the areas contained within boxes A-D (Figure 8.2(b)) are provided in Figure 8.12 across the different mixing speeds. Crystallisation is detected by a reduction in the greyscale intensity. Following an initial plateau, which corresponds to the induction time of the phase transition, crystallisation is observed by a reduction in the greyscale intensity, typically following a sigmoidal curve. On completion of crystallisation, a plateau at a lower greyscale intensity is visible in the plots.

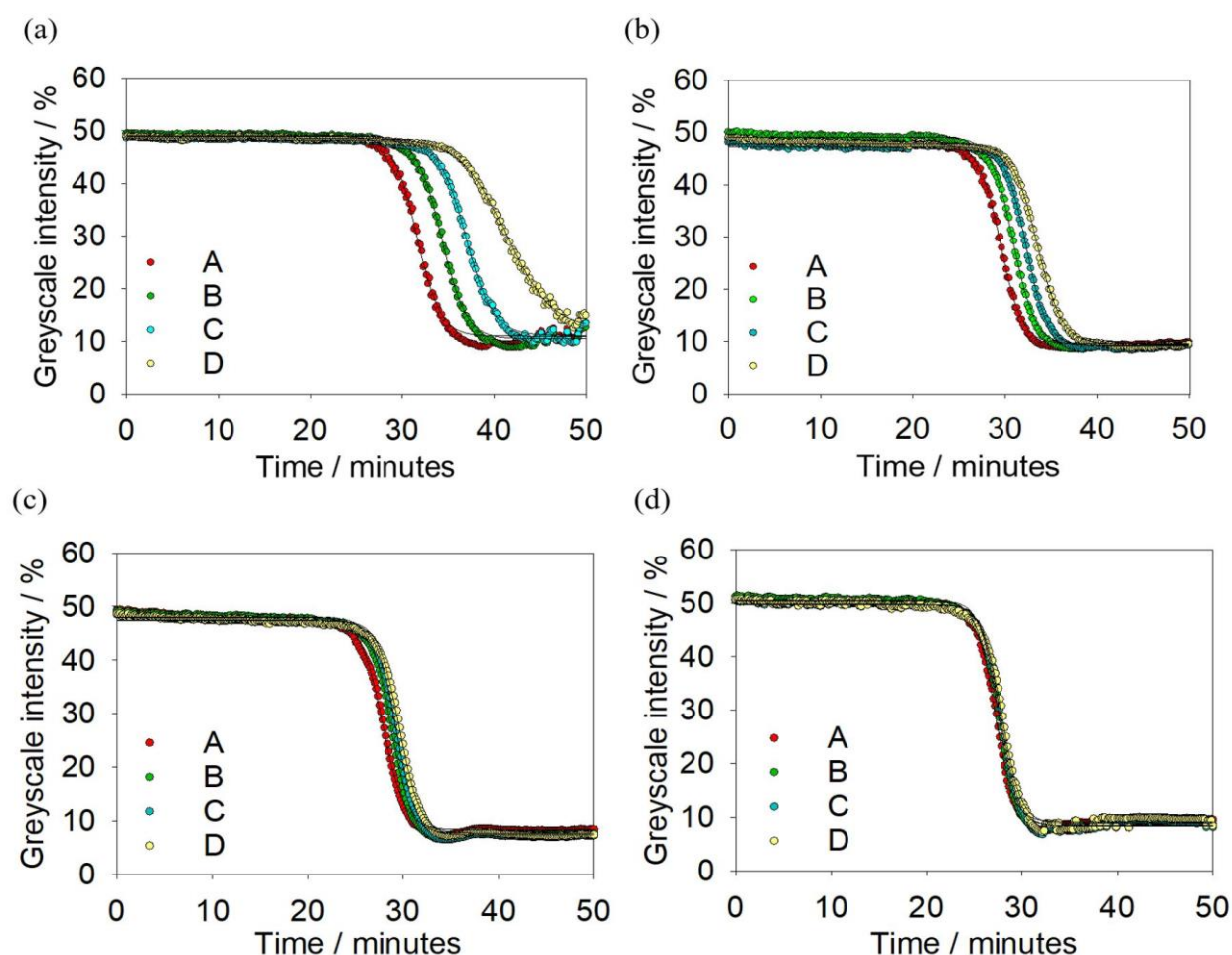


Figure 8.12. Time resolved plot of greyscale intensity for the 4 boxed areas (A-D) when mixed at (a) 20 rpm (b) 50 rpm (c) 150 rpm (d) 300 rpm. The black line for each profile corresponding to the fit of a 4 parameter sigmoidal curve to the data.

At the lower mixing speeds, there are notable differences between the profiles for regions A, B, C and D. The region closest to the mixing blade (A) is the first to exhibit a reduction in

greyscale intensity, as crystallisation starts around the stirrer. However, no differences are observed at the higher rpm, 300 rpm, when crystal growth propagates quickly through the system.

The plots are fitted to a 4-parameter sigmoidal curve:

$$f = y_0 + \frac{a}{\left(1 + e^{\frac{-(x-x_0)}{b}}\right)} \quad (8.6)$$

where x_0 is the midpoint, y_0 is the minimum value, a is the maximum value and $\frac{1}{b}$ relates to the slope of the curve which indicates the rate of crystallisation. In all cases, there is an acceptable fit with R^2 values greater than 0.98. The full fitting parameters, including the corresponding R^2 values, are provided in Appendix E.

The change in $\frac{1}{b}$ and x_0 across the regions A-D for the different mixing speeds are plotted in Figure 8.13, along with the change in induction time. The induction time is a sum of the relaxation time, collision time and time for the crystal to grow into a visible failure (Mullin, 1997). The induction times for the different speeds and areas were estimated, across all replicates, by determining the crossover points between linear trendlines fitted to the induction period and those fitted to the slope of crystallisation.

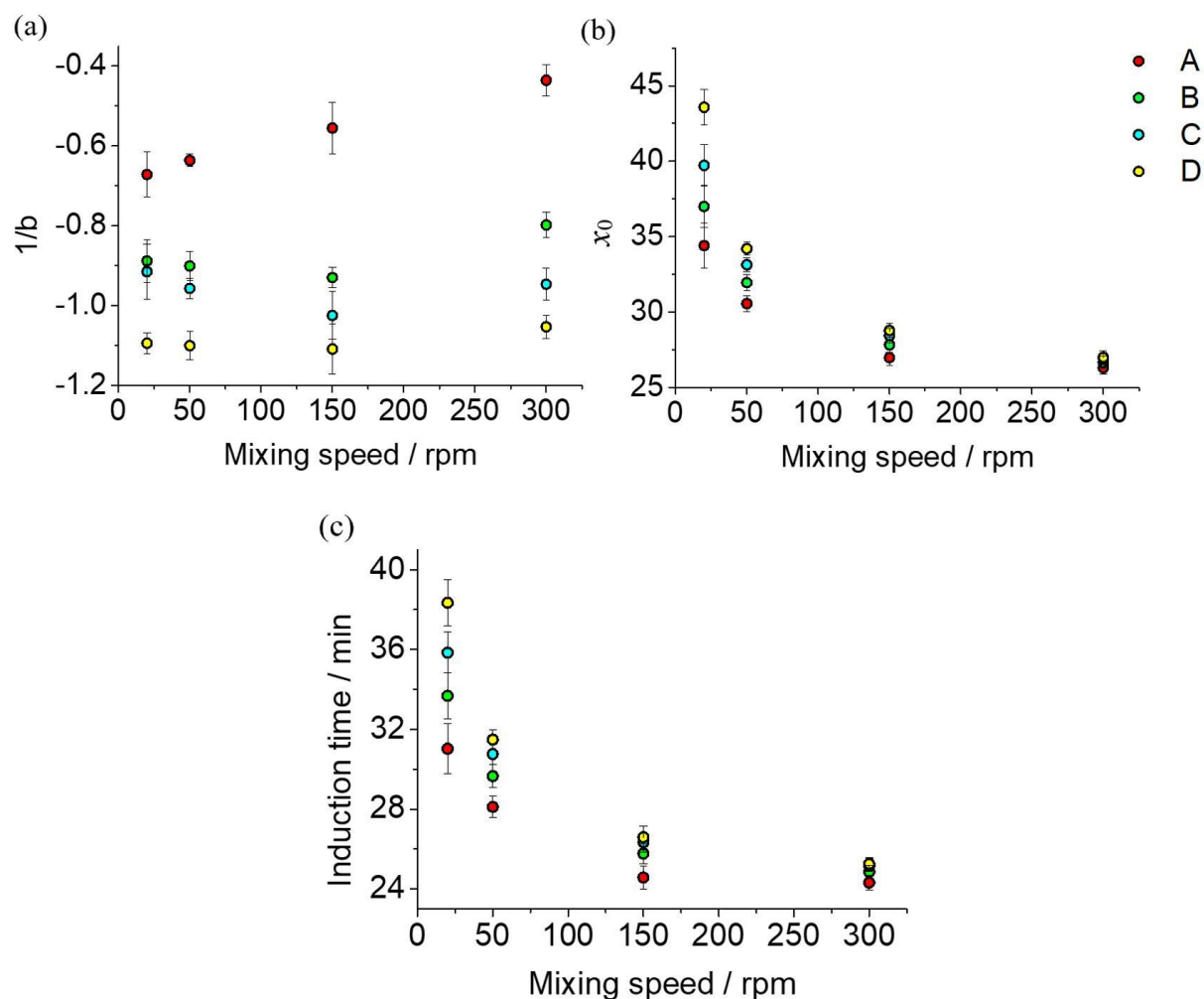


Figure 8.13. Variation of (a) $\frac{1}{b}$ (steepness), (b) x_0 (midpoint) and (c) induction time across the different mixing speeds and boxed areas (A-D).

The slope, related to the rate of crystallisation, does not vary significantly with mixing speed, with the exception of the area closest to the mixing blade (area A). Conversely, the induction time and midpoint, x_0 , are influenced by mixing speed with both displaying a similar trend. Both parameters decrease as the mixing speed is increased. This can be attributed to a higher monomer collision frequency at higher mixing speeds. Since crystals are formed from the surfactant monomers (Stellner and Scamehorn, 1986), an increased number of collisions results in a higher probability of nucleation. The time to crystallisation, and the midpoint, decrease as a result.

8.4.4 Comparison with the current test method

In the presence of mixing, the time to crystallisation for Formulations X1-X6 was estimated from the greyscale plots, as previously described for Formulation A. In the absence of mixing, time to crystallisation was estimated from plots of homogeneity over time, following the method described in Section 8.3.2.2.1. An example plot, for X6, is provided in Figure 8.14. After an average induction time of 0.63 days it is possible to observe a decrease in homogeneity, which relates to the onset of crystallisation.

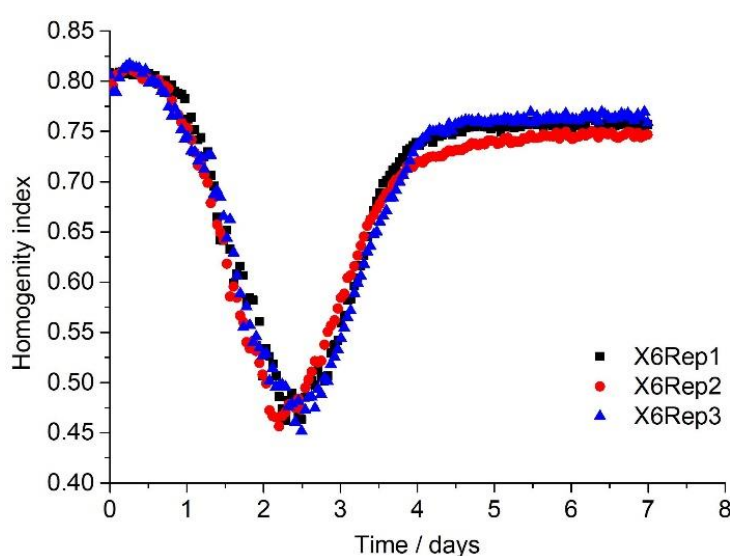


Figure 8.14. Change in homogeneity for the three X6 samples across a 7-day period at 0 °C.

For a selection of formulations, X2 – X6, the time to failure, in the absence and in the presence of mixing at 20 rpm, have been plotted against each other and shown in Figure 8.15. Using the current test method, X1 did not fail within the 7 day experimental run time, so this sample was omitted from the analysis.

Despite the high degree of variability with the current test method, the two methods were found to be positively correlated, as shown in in Figure 8.15. Despite the two methods appearing to exhibit different mechanisms, the same failure trend can be observed, which leaves scope for

further investigation. If the new proposed method is to be implemented, this correlation is important for determining new specification limits.

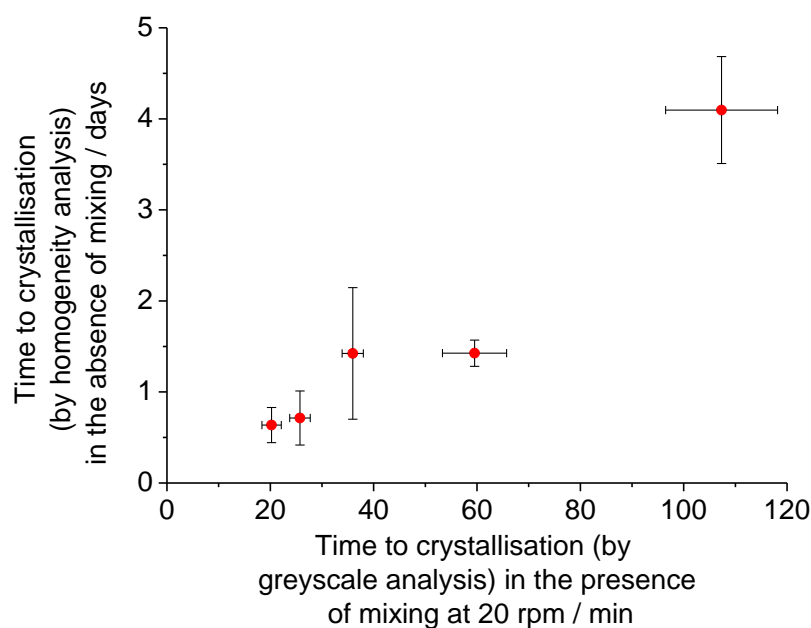


Figure 8.15. Correlation of failure times between the current and proposed low temperature stability test methods across a range of dish liquid formulations. Error bars refer to the standard errors calculated from triplicate measurements.

8.5 Conclusions

Agitation is known to initiate crystallisation in some systems, particularly in the consumer product and food sectors. In this study it has been shown, for the first time, that mixing can reduce the time to dish liquid crystallisation, due to primary and secondary nucleation effects. This insight is not only important for developing accelerated stability tests, but also when exploring the effect of transportation on stability. Detergent formulations are likely to experience movement and vibration during the supply chain.

In the absence of any mixing, crystallisation was found to originate from the air-liquid interface due to the close-packed nature of the monolayer. In the presence of mixing, the crystal growth

began from the mixing blade, the point of highest shear. An increase in mixing speed resulted in a decrease in both the induction time and the time to the midpoint of the crystallisation process. A higher mixing speed also resulted in faster dispersion of crystalline entities through the bulk. This was attributed to an increase in the degree of crystal breakage, dispersion and boundary layer removal.

In addition to reducing the timescale to crystallisation, the application of mixing also reduced the variability of the failure times. This is because, in the presence of mixing, the crystal growth was accelerated and spread in a cloud-like formation through the bulk whereas, in the absence of mixing, it proved difficult to notice the individual crystal entities forming. Two techniques were demonstrated as viable options to follow the crystallisation process whilst mixing. The first involved using an experimental setup consisting of a transparent jacketed vessel and an overhead stirrer. Time lapse photography, in combination with greyscale analysis, was used to determine the point of crystallisation. Alternatively, crystallisation was detected through a reduction in light transmission passing through the sample. The sample vial cap was replaced with a mini-overhead stirrer to induce mixing in the sample.

Extending the investigation to other formulations revealed that the time to crystallisation under the current and the proposed test methods were found to be positively correlated, despite proceeding via different mechanisms. These insights have a significant application to industry, with the potential for the acquired knowledge to be implemented in the stability test methods at P&G. By using agitation, the tests will have shorter timescales and be more representative of the supply chain process. Further work within P&G will include applying this new method to a larger number of formulations to further determine the suitability of this proposed route.

8.6 References

- Bechtold, T. & Mussak, R. 2009. *Handbook of Natural Colorants*, Wiley.
- Callahan, C. J. & Ni, X.-W. 2014. An investigation into the effect of mixing on the secondary nucleation of sodium chlorate in a stirred tank and an oscillatory baffled crystallizer. *CrystEngComm*, 16, 690-697.
- Chantraine, F., Viana, M., Brielles, N., Mondain-Monval, O., Pouget, C., Branlard, P., Rubinstenn, G. & Chulia, D. 2006. Parametric study of surfactant effect on mechanical and dissolution properties of detergent tablets. *Journal of Surfactants and Detergents*, 9, 267-277.
- Chen, Q., Yao, J., Hu, X., Shen, J., Sheng, Y. & Liu, H. 2015. Monolayer effect of a gemini surfactant with a rigid biphenyl spacer on its self-crystallization at the air/liquid interface. *Journal of Applied Crystallography*, 48, 728-735.
- Degner, B. M., Chung, C., Schlegel, V., Hutkins, R. & McClements, D. J. 2014. Factors Influencing the Freeze-Thaw Stability of Emulsion-Based Foods. *Comprehensive Reviews in Food Science and Food Safety*, 13, 98-113.
- Falbe, J. 2012. *Surfactants in Consumer Products: Theory, Technology and Application*, Springer Berlin Heidelberg.
- Fan, X. J., Stenius, P., Kallay, N. & Matijevic, E. 1988. Precipitation of surfactant salts. 2. The effect of nonionic surfactants on precipitation of calcium dodecyl-sulfate. *Journal of Colloid and Interface Science*, 121, 571-578.
- Goodwin, J. 2004. *Colloids and Interfaces with Surfactants and Polymers: An Introduction*, Wiley.
- Grandviewresearch. 2018. *Soap and Detergent Market Size, Share & Trends Analysis Report By Product (Household Detergents, Industrial Soaps & Detergents, Household Soaps), Competitive Landscape, And Segment Forecasts, 2018 – 2025* [Online]. Available:

<https://www.grandviewresearch.com/industry-analysis/soap-detergent-market>

[Accessed 21/05 2018].

- Hartel, R. W., Ergun, R. & Vogel, S. 2011. Phase/State Transitions of Confectionery Sweeteners: Thermodynamic and Kinetic Aspects. *Comprehensive Reviews in Food Science and Food Safety*, 10, 17-32.
- Hartel, R. W. & Shastry, A. V. 1991. Sugar crystallization in food products. *Critical Reviews in Food Science and Nutrition*, 30, 49-112.
- Hurle, D. T. J. & Jakeman, E. 2014. *The Role of Convection and Fluid Flow in Solidification and Crystal Growth: Physicochemical Hydrodynamics*, Vol. 2.4, Elsevier Science.
- Lai, K. Y. 1996. *Liquid Detergents*, CRC Press.
- Liang, K., White, G., Wilkinson, D., Ford, L. J., Roberts, K. J. & Wood, W. M. 2004. Examination of the process scale dependence of L-glutamic acid batch crystallized from supersaturated aqueous solutions in relation to reactor hydrodynamics. *Industrial & Engineering Chemistry Research*, 43, 1227-1234.
- Liang, K., White, G., Wilkinson, D., Ford, L. J., Roberts, K. J. & Wood, W. M. L. 2004. An Examination into the Effect of Stirrer Material and Agitation Rate on the Nucleation of l-Glutamic Acid Batch Crystallized from Supersaturated Aqueous Solutions. *Crystal Growth & Design*, 4, 1039-1044.
- Liu, J. & Rasmuson, Å. C. 2013. Influence of Agitation and Fluid Shear on Primary Nucleation in Solution. *Crystal Growth & Design*, 13, 4385-4394.
- Liu, J., Svärd, M. & Rasmuson, Å. C. 2015. Influence of Agitation on Primary Nucleation in Stirred Tank Crystallizers. *Crystal Growth & Design*, 15, 4177-4184.
- Maksimov, A. O., Kaverin, A. M. & Baidakov, V. G. 2013. Heterogeneous Vapor Bubble Nucleation on a Rough Surface. *Langmuir*, 29, 3924-3934.

- Mazzanti, G., Guthrie, S. E., Marangoni, A. G. & Idziak, S. H. J. 2007. A Conceptual Model for Shear-Induced Phase Behavior in Crystallizing Cocoa Butter. *Crystal Growth & Design*, 7, 1230-1241.
- Mcleod, J. S., Paterson, A. H. J., Bronlund, J. E. & Jones, J. R. 2016. The effect of agitation on the nucleation of α -lactose monohydrate. *International Dairy Journal*, 61, 114-119.
- Miller, R. M., Ces, O., Brooks, N. J., Robles, E. S. J. & Cabral, J. T. 2017. Crystallization of Sodium Dodecyl Sulfate-Water Micellar Solutions under Linear Cooling. *Crystal Growth & Design*, 17, 2428-2437.
- Moroi, Y., Rusdi, M. & Kubo, I. 2004. Difference in Surface Properties between Insoluble Monolayer and Adsorbed Film from Kinetics of Water Evaporation and BAM Image. *The Journal of Physical Chemistry B*, 108, 6351-6358.
- Mullin, J. W. 1997. *Crystallization*, Butterworth-Heinemann.
- Myerson, A. 2002. *Handbook of Industrial Crystallization*, Butterworth-Heinemann.
- Paul, E. L., Atiemo-Obeng, V. A. & Kresta, S. M. 2004. *Handbook of Industrial Mixing: Science and Practice*, Wiley.
- Rao, C. N., Sastry, S. S., Mallika, K., Tiong, H. S. & Mahalakshmi, K. 2013. Co-occurrence matrix and its statistical features as an approach for identification of phase transitions of mesogens. *International Journal of Innovation Research in Science, Engineering and Technology*. 2, 4531-4538
- Rathee, V., Krishnaswamy, R., Pal, A., Raghunathan, V. A., Imp  rator-Clerc, M., Pansu, B. & Sood, A. K. 2013. Reversible shear-induced crystallization above equilibrium freezing temperature in a lyotropic surfactant system. *Proceedings of the National Academy of Sciences of the United States of America*, 110, 14849-14854.
- Sasaki, S. 2007. Metastable Crystalline Lamella of Cetylpyridinium Chloride in the Krafft Transition. *The Journal of Physical Chemistry B*, 111, 2473-2476.

- Saunders, D. 1998. Monitoring Shock and Vibration during the Transportation of Paintings. *National Gallery Technical Bulletin*, 19, 64-73.
- Scamehorn, J. F. 1986. An Overview of Phenomena Involving Surfactant Mixtures. *ACS Symposium Series*, 311, 1-27.
- Scheibel, J. J. 2004. The evolution of anionic surfactant technology to meet the requirements of the laundry detergent industry. *Journal of Surfactants and Detergents*, 7, 319-328.
- Sebastian, V., Unnikrishnan, A. & Balakrishnan, K. 2012. Gray level co-occurrence matrices: generalisation and some new features. *International Journal of Computer Science, Engineering and Information Technology*, 2, 151-157.
- Seiler, T. 2011. *Transportation Services in the Consumer Goods Industry*.
- Shiau, B. J., Harwell, J. H. & Scamehorn, J. F. 1994. Precipitation of mixtures of anionic and cationic surfactants. 3. Effect of added nonionic surfactant. *Journal of Colloid and Interface Science*, 167, 332-345.
- Shibata, O., Nakahara, H. & Moroi, Y. 2015. New Adsorption Model—Theory, Phenomena and New Concept. *Journal of Oleo Science*, 64, 1-8.
- Singh, S. K., Bajpai, M. & Tyagi, V. 2006. Amine oxides: a review. *Journal of Oleo Science*, 55, 99-119.
- Soontravanich, S. & Scamehorn, J. F. 2009. Use of a Nonionic Surfactant to Inhibit Precipitation of Anionic Surfactants by Calcium. *Journal of Surfactants and Detergents*, 13, 13.
- Soontravanich, S., Walsh, S., Scamehorn, J. F., Harwell, J. H. & Sabatini, D. A. 2009. Interaction between an anionic and an amphoteric surfactant. Part II: Precipitation. *Journal of Surfactants and Detergents*, 12, 145-154.

- Stellner, K. L. & Scamehorn, J. F. 1986. Surfactant precipitation in aqueous-solutions containing mixtures of anionic and nonionic surfactants. *Journal of the American Oil Chemists' Society*, 63, 566-574.
- Summerton, E., Hollamby, M. J., Zimbitas, G., Snow, T., Smith, A. J., Sommertune, J., Bettiol, J., Jones, C., Britton, M. M. & Bakalis, S. 2018. The impact of N,N-dimethyldodecylamine N-oxide (DDAO) concentration on the crystallisation of sodium dodecyl sulfate (SDS) systems and the resulting changes to crystal structure, shape and the kinetics of crystal growth. *Journal of Colloid and Interface Science*, 527, 260-266.
- Wu, Y. L., Derks, D., Van Blaaderen, A. & Imhof, A. 2009. Melting and crystallization of colloidal hard-sphere suspensions under shear. *Proceedings of the National Academy of Sciences*, 106, 10564-10569.

CHAPTER 9

CONCLUSIONS AND FUTURE WORK

9.1 Fundamental understanding of the failure process

This thesis has explored the crystallisation process that can occur in dish liquid formulations upon exposure to low and sub-zero temperatures. Despite the occurrence of this phase transition in commercial products, this area of scientific research has received relatively little interest. Using a variety of techniques, a greater fundamental understanding of the failure process has been acquired. The resultant findings are particularly relevant for P&G since it will help to provide a pathway to more robust formulation designs. An understanding of the crystallisation process, including the crystal structure and composition, will provide valuable insights during the development of future dish liquid products.

A fundamental understanding of the phase transition was initially developed using a model system comprising of sodium dodecyl sulfate (SDS), N,N-dimethyldodecylamine N-oxide (DDAO) and water at concentrations typical of those in commercial products. These two surfactants are present in dish liquid, with further variants arising from branching, changes in chain length or the addition of ethoxy units. Differential scanning calorimetry (DSC) provided a means to determine changes in crystallisation temperatures and enthalpy upon a change in DDAO concentration. Nuclear magnetic resonance (NMR) and X-ray scattering techniques revealed the composition and structure of the crystalline entities. Confocal Raman microscopy and optical microscopy provided further insight into the crystal shape and location of the surfactants. Using the knowledge gained from studies on the model systems, a stability study was conducted across many dish liquid formulations to determine the effect of various parameters on the development of crystalline failures. Light transmission and time lapse photography were used to follow the phase transition in these systems.

9.1.1 Model system studies

With regards to experiments performed on pure SDS and SDS + DDAO systems, the following conclusions were reached:

1) The presence of 1-dodecanol promotes SDS crystallisation (Chapter 2)

20 wt. % SDS solutions were found to crystallise at a higher temperature when in the presence of its alcohol precursor. This can be attributed to the ability of 1-dodecanol to seed SDS crystallisation. 1-dodecanol crystallises and provides a base, with similar structural and compositional attributes to the alkyl sulfate, from which the SDS crystals can then form.

2) The crystals are composed of SDS hydrates (Chapter 3)

From NMR and X-ray scattering studies it was possible to determine that the crystals formed from SDS + DDAO systems comprise solely of SDS and water, termed SDS hydrates. The surfactants reside in a lamellar-type structure due to the appearance of equally spaced peaks in the corresponding wide-angle X-ray scattering (WAXS) profiles.

Although DDAO is not present in the crystals it was found, from NMR studies, that the DDAO surfactant mobility is affected by the surrounding SDS crystallisation. This can be attributed to the DDAO surfactant preferentially existing in the region of the crystal despite not being a component of the crystal itself. Further evidence was provided by confocal Raman spectroscopy where the DDAO contribution was matched to regions around the crystal.

3) The presence of DDAO reduces the tendency for crystallisation (Chapter 4)

DDAO was found to influence the crystallisation kinetics of an SDS system. As the concentration of DDAO increased, the system crystallised at a lower temperature when cooled at a constant rate. Isothermal studies were performed at the Diamond Light Source, Oxfordshire,

UK where the samples were held at 0 °C for prolonged periods and SAXS (small-angle X-ray scattering) profile periodically attained. Plots of the first Bragg peak intensity over time were attained for 20 wt. % SDS solutions with a range of DDAO concentrations (1 - 5 wt. %). The time to peak formation and the rate of peak growth both positively correlated with DDAO concentration. DDAO promotes the formation of mixed micelles within the system and, therefore, increases the tendency to form micelles. This results in a lower concentration of SDS monomers and, since SDS hydrates are formed from the monomer constituents, the corresponding drive for crystallisation is also reduced.

4) The presence of DDAO also affects structural changes occurring during crystal formation (Chapter 4)

Pure SDS and mixed SDS+ DDAO aqueous solutions displayed clear differences in their time-resolved WAXS profiles, acquired when samples were held at 0 °C. Although they formed the same hydrated crystal structure after a certain period of time, the SDS system was observed to proceed via an additional hydrate intermediary, which was not evident in the mixed system. When DDAO was present in the solution, the growth was more controlled and directly yielded the final structure. This can be attributed to the slower crystallisation kinetics, a higher solution viscosity and the DDAO residing in the region of the crystal and thus controlling the crystal growth.

5) Crystallisation of SDS and SDS + DDAO systems are described by the Avrami and Ozawa theories, under isothermal and non-isothermal conditions respectively (Chapter 5)

Upon crystallisation of a pure SDS system under isothermal conditions, with the holding temperature increasing from 12 °C to 14 °C, the Avrami exponent increased from 3 to 4. This indicates either a change in dimensionality, from 2D to 3D, or 3D growth with a change in nucleation mode from sporadic to instantaneous. The former is most likely since platelets (2D)

are known to exist at lower temperatures or higher cooling rates (Chapter 4). The SDS + DDAO system gave an Avrami exponent of 3 at 0 °C. This indicates 3D growth, which corroborates the findings from Chapter 4 where the crystals were observed to be ring-shaped by confocal Raman microscopy. An Ozawa exponent of 3 was attained from non-isothermal studies into the crystallisation of a pure SDS system, suggesting that 3D crystal growth occurs under these conditions.

6) Increasing the cooling rate of SDS + DDAO system results in an increased degree of polydispersity amongst the crystals (Chapter 5)

The oscillations in the slope of the SAXS profiles for the SDS + DDAO system depend on the polydispersity of the crystals in the system. The oscillations were found to be more prominent at lower cooling rates, indicating the crystals are increasingly monodispersed. This is attributed to a slow cooling rate allowing for a more controlled and even growth.

9.1.2 Application to commercially relevant dish liquid products

The knowledge gained from model SDS and SDS + DDAO systems was used as a basis for understanding the phase transition that can occur in commercial dish liquid products upon exposure to low temperatures. The following conclusions can be drawn:

1) The crystals are composed of alkyl sulfate hydrates (Chapter 6)

In line with the model SDS + DDAO system studies, alkyl sulfates were also the main component of the crystals formed from the surfactant paste which is used to produce dish liquid products. The paste was dissolved in D₂O and NMR spectra were acquired at set temperature intervals as the system was cooled. The intensity of peaks corresponding to proton environments in water, amine oxide and alkyl sulfate all decreased with temperature. Between two temperatures intervals, there was a significant drop in the intensity of a peaks relating to

the non-ethoxylated alkyl sulfate, which is indicative of this component undergoing a phase transition. However, the peaks corresponding to ethoxylated alkyl sulfates did not display any drop in NMR intensity, indicating that this surfactant is not present in the crystal nor does it reside in the region of the crystal.

SAXS and WAXS studies performed on the crystals formed from an unstable dish liquid formulation, after holding at 0 °C for 62 hours, indicated a lamellar-type crystal structure, as was previously observed for crystals formed from the model SDS + DDAO system. Using the Scherer equation, the crystal size was calculated to be 574 nm, although this is an approximation because this equation is not usually applicable at these length scales.

2) A higher concentration of alkyl sulfate alcohol precursor increases the susceptibility of the formulation to crystallisation (Chapter 6)

The time required for crystalline entities to develop was monitored across a wide number of formulations using the microplate method, a light transmission technique developed by P&G. As to be expected from the studies on the SDS system in the presence of 1-dodecanol, a low completeness resulted in poorer performance during stability tests. The completeness level corresponds to the amount of alkyl sulfate alcohol precursor remaining in the formulation after sulfation.

3) An increase in the alkyl sulfate to amine oxide ratio results in poorer product stability at low temperatures (Chapter 6)

The model system studies indicated that an increase in DDAO reduces the susceptibility of SDS solutions to crystallisation. In agreement with these findings, the dish liquid formulations with a higher alkyl sulfate to amine oxide ratio exhibited poorer stability when monitored at 0 °C across a duration of 7 days.

4) *The alkylsulfate paste is key for determining the stability of the formulation (Chapter 6)*

The stability of six formulations, varying by Low T number, was monitored for 7 days at 0 °C.

The Low T number depends on the alcohol blend, from which the alkyl sulfates are formed.

$$\text{Low T \#} = \left[\left(\frac{\text{LAE}}{\text{LA}} \right) * (\text{BrA} + \text{BrAE}) \right] \quad (9.1)$$

where LAE = mol. % of linear alcohol ethoxylates, LA = mol. % of linear alcohol, BrA = mol. % of branched alcohol, BrAE = mol. % of branched alcohol ethoxylates. There was a positive correlation between the Low T number and the degree of crystalline failure. The key determining parameter for the Low T number is the amount of linear alcohol and, in turn, the amount of linear alkyl sulfate, which is formed *in situ* from the linear alcohol. This is to be expected since the NMR studies indicated that crystals comprise alkyl sulfate hydrates.

5) *The crystals consistently form from the air-liquid interface (Chapter 8)*

Crystals began growing from the surface of the formulation before collecting on the bottom surface of the formulation. The close packed nature of the monomers at the interface causes the crystals to form from the surface of the bulk. The surfactant monolayer bears a distinct similarity to that of the crystal structure and, therefore, provides a lower energy pathway to crystal formation.

9.2 Improvements to low temperature stability test methods

Work within this thesis also tackled a topical issue at P&G regarding the efficiency of the low temperature stability tests performed on their dish liquid products. Therefore, a secondary aim of this research was to investigate routes to improve these test methods, which monitor formulation stability between –3 °C and 10 °C. Prior to this work, the method for detecting crystalline failures relied on daily observation of quiescent formulations across a 28-day period.

Using the fundamental understanding acquired on the model and complex systems, routes to reduce the variability and increase the efficiency of the test methods have been proposed within this manuscript. Furthermore, the test method aimed to be more representative of the supply chain, where formulations are subjected to agitation and vibrations. This additional scientific insight has initiated the next stage in the development of stability tests at P&G.

9.2.1 Screening potential methods

Two viable options, seeding and sonication, were the first to be investigated. However, they were not pursued past initial screening. An overview of the outcomes is outlined in the following points:

1) Seeding with oven-dried dish liquid reduces the timescale to crystallisation (Chapter 7)

Across a sample set of 32 formulations, seeding with oven-dried dish liquid successfully reduced the time to crystallisation. This can be attributed to the structural and compositional similarity between the crystal and the seed, as was also the case in the SDS + 1-dodecanol investigation. Despite the success, this method was not pursued past initial screening since it came with practical limitations due to preparation process being laborious and time consuming.

2) The presence of sonication results in limited success (Chapter 7)

The application of sonication was also met with some success but, upon repeating the experiments, the results displayed a significant degree of variability. This was a result of factors that proved too difficult to control with the available equipment.

9.2.2 Application of mixing

One method, the application of agitation, was investigated in further detail and the following conclusions were drawn:

1) Mixing is a successful route to reduce both the timescale and variability of the crystallisation process (Chapter 8)

Mixing the simple SDS + DDAO system at different speeds whilst cooling and recording the conductivity of the solution initially demonstrated the viability of the method. Subsequently, mixing was demonstrated to reduce the time to crystallisation in dish liquid samples as well as reducing the statistical variability between the failure times of samples from the same formulation batch. Time lapse photography and Crystalline8, a light transmission technique, were used to investigate the effect of mixing on the time to failure. The reasoning for the reduction in timescale in the presence of mixing can be attributed to a combination of primary and secondary nucleation effects. The former is affected by collision frequency of the monomers and the latter is a result of crystal breakage forming further nucleation sites and boundary layer removal enhancing subsequent growth.

2) Crystallisation consistently occurs from the point of mixing (Chapter 8)

In a mixed sample, the solid phase formed from the point of mixing. Monomers display a high velocity close to the mixing blade, which increases the probability of these molecules colliding and forming a crystal structure.

3) The speed of mixing affects the spread of crystal growth (Chapter 8)

The rate at which crystallisation spread through the sample was found to be greatly affected by the speed of the mixer. With increased mixing the entire system crystallised in a shorter period. The mechanisms by which secondary nucleation is enhanced become more prominent. The

induction time also decreased slightly with an increase in mixing speed. This can be explained by an increase in collision frequency of the monomers, from which crystals form. The rate of crystallisation at a selected point did not vary significantly, except for areas close to the stirrer blade.

4) Mixing time to failure correlates with quiescent time to failure (Chapter 8)

At a set temperature and mixing speed, the time to failure, in the absence and presence of mixing, was explored across a range of formulations. Although the errors with the quiescent samples were large, the two failure times tended to show a positive correlation.

9.3 Future recommendations

This section indicates how this work could be extended with the following recommendations:

1) Extend the fundamental understanding to incorporate different model systems

This study has focused on surfactants that are of interest in dish liquid products, but similar stability issues can also be observed in fabric conditioners and shampoos. As a result, further work could involve using similar techniques and experimental approach with other model systems and commercial products. Other surfactants could include linear alkylbenzene sulfonate, betaines or branched alkyl sulfates.

2) Further extend the mixing investigation to incorporate a wider range of conditions

An in depth investigation of the effect of mixing on the crystallisation across different temperatures and with a wider formulation space is required to determine the true application of this method within industry. In this study, this proposed method has been tested across a selection of products, but there is opportunity to test an extended number of formulations and include other temperature conditions in addition to 0 °C.

3) Optimisation of the detection technique

The majority of the stability testing contained in this manuscript relied on the use of time lapse photography. In addition, a small set of experiments were performed using a light transmission technique called Crystalline8. Advantages of this second technique include the ease of quantification and capability for monitoring samples simultaneously. This could be one route to incorporate mixing into sample testing on a large scale but requires further investigation.

4) Investigate the use of a vibrating table to perform mass stability testing

As a result of the findings from this project, P&G have acquired a vibrating table with a view to monitoring the stability of several agitated samples simultaneously. The parameters, amplitude and frequency, need to be optimised prior to implementation of this method.

5) Modelling as route to predict stability of formulations

Mixing has been proposed as a route to reduce the timescale of stability test methods at low temperatures, but subsequent improvements could remove the need to perform any testing completely. Future work could, therefore, focus on developing a modelling approach to predict the stability of formulations using the Low T number as an initial starting point. Currently the Low T number does not account for the amine oxide and unreacted alcohol in the formulation, so these variables that would need to be incorporated into the model. Mixing would allow the suitability of a model to be tested in a short space of the time. This project has opened the gateway to future test methods and, in combination with the increased fundamental understanding, a new low temperature stability test will be implemented on a large scale at P&G in the foreseeable future.

APPENDIX A

OPTICAL MICROSCOPE SETTINGS

A.1 Microscope setup

Parameters for the optical microscopy setup were selected using the software platform Micro-Manager. Figure A.1. below shows those selected for the purpose of experiments outlined in this thesis manuscript.

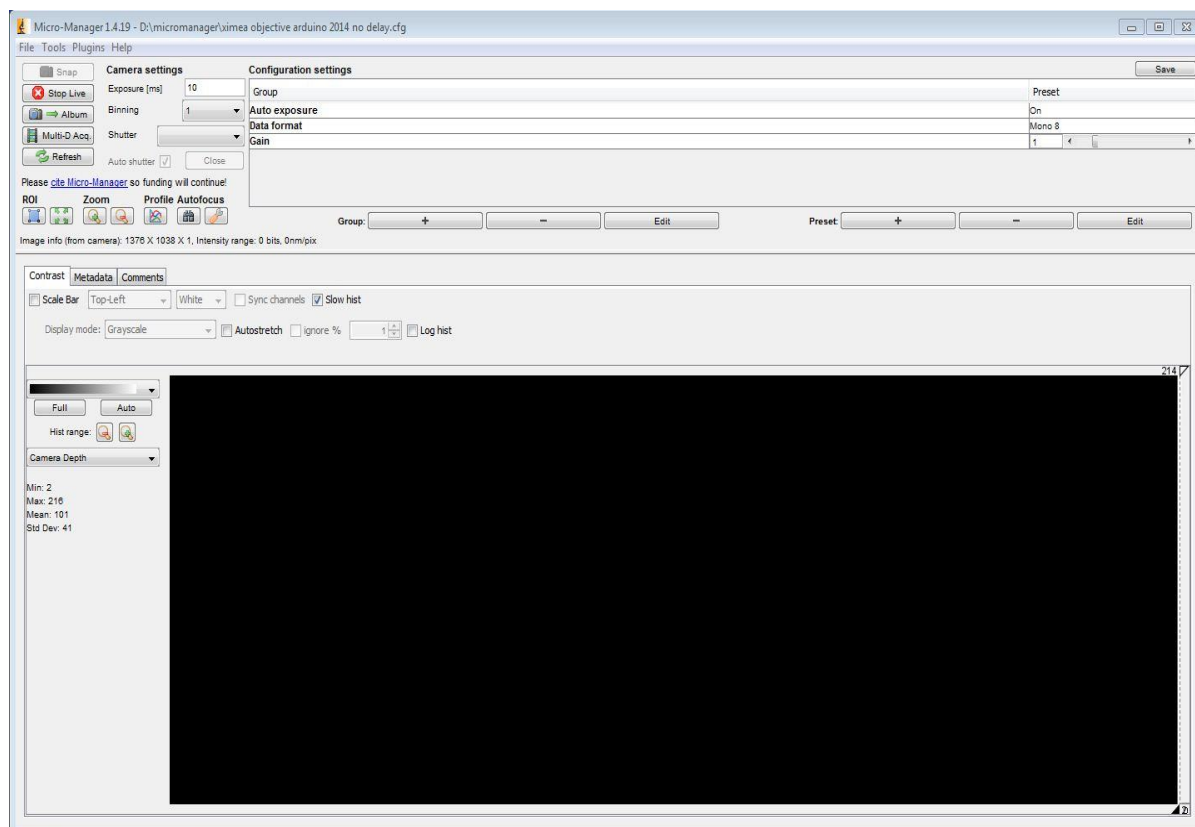


Figure A.1. Screenshot of the microscope settings.

APPENDIX B

^1H NMR ASSIGNMENTS

B.1 ^1H NMR assignments for the individual SDS and DDAO components

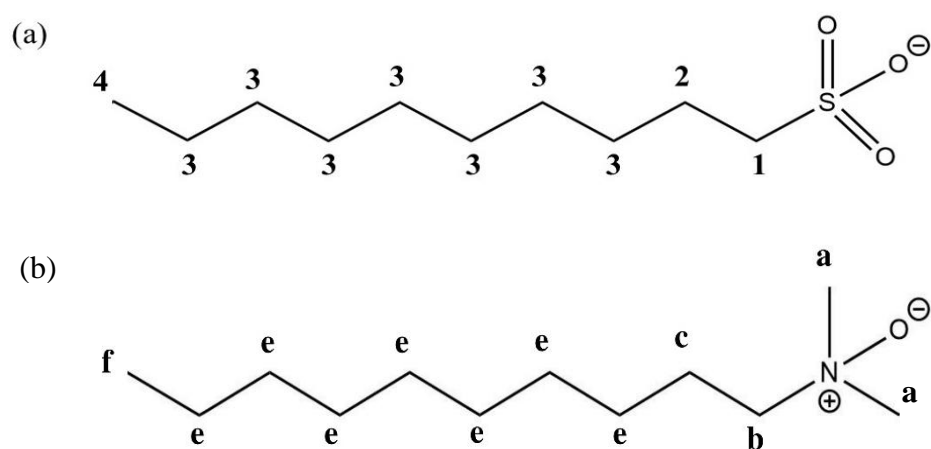
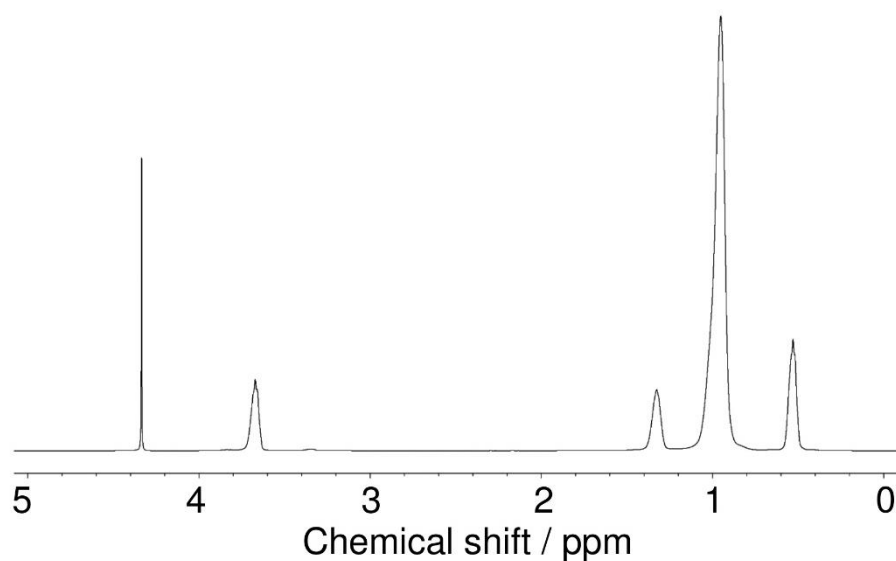


Figure B.1. Labelling scheme for the proton environments in (a) *N,N*-dimethyldodecylamine *N*-oxide (DDAO) and (b) sodium dodecyl sulfate (SDS).

(a)



(b)

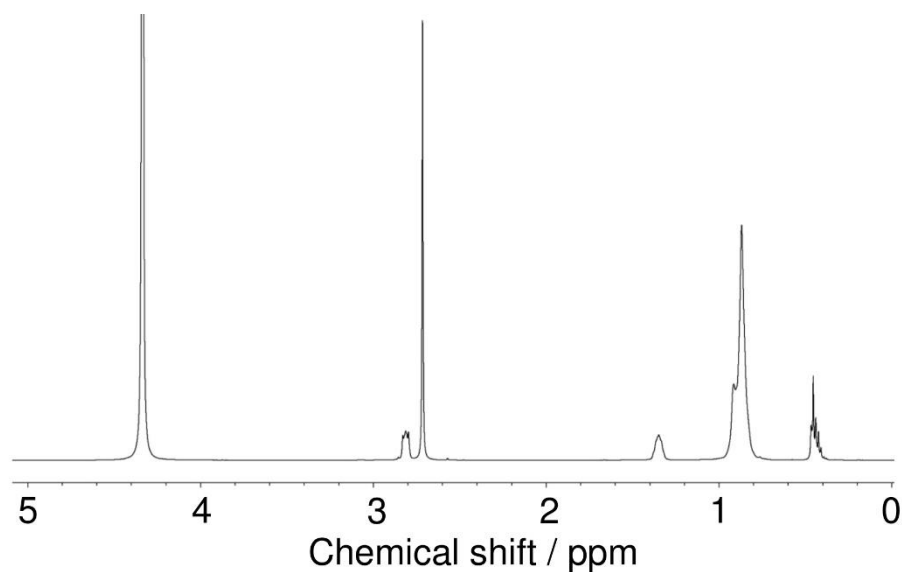


Figure B.2. (a) ^1H NMR spectrum for a 20 wt. % SDS system and (b) ^1H NMR spectrum for a 3 wt. % DDAO system dissolved in D_2O at 25 °C acquired at 500 MHz. As the NMR signals for protons H_a and H_1 are well resolved, and do not overlap with other peaks, they have been used to identify each surfactant when in a mixed system. H_1 is set to 3.67 ppm and both spectra have been adjusted relative to this calibration.

Table B.1. ^1H NMR assignments for the individual SDS and DDAO systems at 25 °C at 500 MHz.

Proton	Chemical shift / ppm
H₁	3.67
H₂	1.33
H₃	0.95
H₄	0.53
H_a	2.71
H_b	2.82
H_c	1.34
H_d	0.91
H_e	0.87
H_f	0.46
H₂O	4.35

Table B.2. T_1 values for select proton environments acquired at 300 MHz.

Proton environment	T_1 /s
H_a	0.27
H₁	0.81

APPENDIX C

THE FITTING OF SMALL-ANGLE X-RAY SCATTERING PROFILES AND FURTHER AVRAMI PLOTS

C.1 Model SDS and SDS + DDAO systems

C.1.1 Small-angle X-ray scattering (SAXS) model fitting

To model the data the following approaches were used. In all cases, except those where references are given, equations are based on those found in the comprehensive SASfit documentation, which is available as part of the SASfit package written by Kohlbrecher and Bressler that can be freely downloaded from the PSI website.

C.1.1.1 Data at 24 °C (charged ellipsoidal micelles)

The small-angle X-ray scattering (SAXS) data arising from both the 20 wt. % SDS and the 20 wt.% SDS + 3 wt.% DDAO samples was analysed using a model corresponding to a delta distribution of charged core-shell prolate ellipsoids.

Ellipsoidal $P(Q)$

The form factor, $P(Q)$ for core-shell ellipsoids is given by the following equations (Breßler *et al.*, 2015; Kakitani *et al.*, 1995):

$$P(Q)_{\text{ellipsoid}} = \int_0^1 [F(Q, \mu)_{\text{ellipsoid}}]^2 d\mu \quad (\text{C.1})$$

$$F(Q, \mu)_{\text{ellipsoid}} = (\rho_{\text{core}} - \rho_{\text{shell}}) \mathcal{V}_{\text{core}} \left[\frac{3J_1(x_c)}{x_c} \right] + (\rho_{\text{shell}} - \rho_{\text{solvent}}) \mathcal{V}_{\text{total}} \left[\frac{3J_1(x_t)}{x_t} \right] \quad (\text{C.2})$$

$$J_1(x) = \frac{\sin x - x \cos x}{x^2} \quad (\text{C.3})$$

$$x_c = Q \sqrt{a^2 \mu^2 + b^2 (1 - \mu^2)} \quad (\text{C.4})$$

$$x_t = Q \sqrt{(a+t)^2 \mu^2 + (b+t)^2 (1 - \mu^2)} \quad (\text{C.5})$$

$$\mathcal{V}_{\text{core}} = \frac{4}{3} \pi a b^2 \quad (\text{C.6})$$

$$V_{total} = \frac{4}{3} \pi (a+t)(b+t)^2 \quad (C.7)$$

In the above equations Q is the scattering vector and $\mu = \cos\theta$, where θ = an angle between the major axes and the Bragg wave vector. The required analysis parameters are the semi-principle axes of the core, a , the equatorial semi-axis axes of the core, b , the thickness of the shell, t and the scattering length densities of the core, ρ_{core} , shell, ρ_{shell} and solvent $\rho_{solvent}$. During analysis, ρ_{core} was fixed at $7.68 \times 10^{10} \text{ cm}^{-2}$ in line with previous SAXS analysis of SDS micelles in water. This was done for both samples, as the alkyl chain is the same length in both cases. The scattering length density of water, $\rho_{solvent} = 9.46 \times 10^{10} \text{ cm}^{-2}$, was calculated using the online NIST tool (Munter, 2014). ρ_{shell} was fixed at 1.25×10^{11} (Zemb and Charpin, 1985). All other parameters were allowed to float and the results are listed in Table C.1.

Table C.1. Fitting parameters for surfactant solutions at 24 °C.

Parameter	20 wt.% SDS	20 wt.% SDS + 3 wt.% DDAO
a / nm	3.1	3.6
b / nm	1.8	1.7
t / nm	0.44 ^I	0.45 ^I
N_{agg}^{II}	170	190
$\rho_{shell} / 10^{10} \text{ cm}^{-2}$	12.5	12.0
R_{HS} / nm	2.4	2.7
Z / electrons	20	20
I_{bkg} / cm^{-1}	0.00167	0.00144

^IValues taken from reference (Kakitani *et al.*, 1995) and fixed during the fitting process.

^{II}Calculated using 0.41 nm^3 as the volume of SDS.

Charged $S(Q)$

To describe the interparticle structure factor $S(Q)$ the rescaled mean spherical approximation (RMSA) approach introduced by Hayter and Penfold (Hayter and Penfold, 1981) was used, in accordance with many other studies that have modelled small-angle scattering of SDS micelles (Kakitani *et al.*, 1995; Garg *et al.*, 2005; Bergstrom and Pedersen, 1999). Parameters were the effective hard sphere radius, R_{HS} , the micelle charge, Z in units of the charge of an electron $e = 1.60 \times 10^{-19} \text{ C}$, the volume fraction of micelles, ϕ (held at 0.2 for 20 wt. % SDS and 0.23 for

20 wt. % SDS + 3 wt. % DDAO), the temperature, T in $^{\circ}\text{C}$ (24°C for the room temperature samples, 0°C for the cooled samples), the solution monovalent salt concentration (held at $1 \times 10^{-5}\text{ M}$), and the dielectric constant (held at 71.08). Two parameters, R_{HS} and Z , were allowed to float and the results are presented in Table C.1.

Overall modelled scattering law

The overall scattering law corresponding to a delta distribution of charged core-shell prolate ellipsoids is therefore given as follows:

$$I(Q)_{fit} = N \times P(Q)_{\text{ellipsoid}} \times S(Q)_{RMSA} + I_{BKG} \quad (\text{C.8})$$

In the above, I_{BKG} is a fitted Q -independent (flat) background scattering that was unable to be fully subtracted during the data reduction and normalisation routine. A breakdown of the fit contributions for the 20 wt.% SDS + 3 wt.% DDAO sample are shown in Figure C.1.

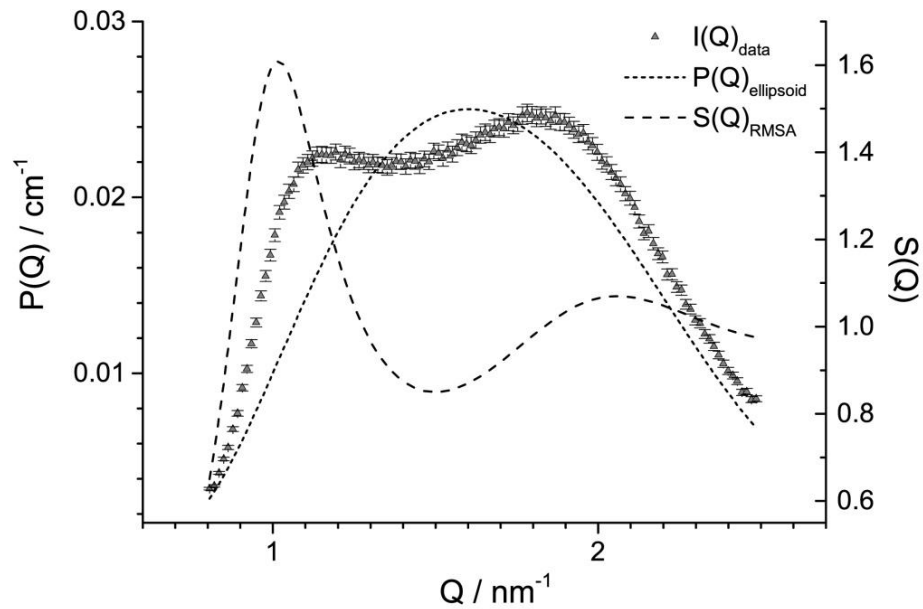


Figure C.1. Fit deconstruction for SAXS data for 20 wt. % SDS + 3 wt. % DDAO at 24°C , showing the contributions of the prolate ellipsoid micelle $P(Q)_{\text{ellipsoid}}$ and the charged $S(Q)_{RMSA}$. The total scattering, $I(Q)_{fit} = P(Q)_{\text{ellipsoid}} \times S(Q)_{RMSA} + I_{BKG}$, where $I_{BKG} = 0.00144$.

C.1.1.2 Data at 0 °C

The SAXS data arising from both the 20 wt.% SDS and the 20 wt. % SDS + 3 wt.% DDAO samples was analysed using a model comprising contributions from a power law, flat background (I_{BKG}) and a Bragg peak. For the 20 wt. % SDS + 3 wt.% DDAO sample an additional contribution to the scattering from a charged micelle population was included, using the same approach as explained above for the data at 24 °C.

The contributions from the power law and Q -independent background I_{BKG} is given as:

$$I(Q)_{PL+BKG} = I_{BKG} + \beta Q^{-\alpha} \quad (C.9)$$

To model the Bragg peak, a Gaussian-Lorentzian sum was used:

$$I(Q)_{Peak} = 2A \left[\frac{\nu}{|\sigma|} \sqrt{\frac{\ln 2}{\pi}} \exp \left(-4 \ln 2 \left(\frac{Q - Q_{max}}{|\sigma|} \right)^2 \right) + \frac{1 - \nu}{\pi |\sigma| \left(1 + 4 \left(\frac{Q - Q_{max}}{|\sigma|} \right)^2 \right)} \right] \quad (C.10)$$

In the above, A is the area below the peak, ν is the shape parameter (full Lorentzian if $\nu = 0$, full Gaussian if $\nu = 1$), Q_{max} is the peak centre and σ is the full width at half maximum. All of the above parameters were allowed to float and the results of model fitting are shown in Table S.2. A breakdown of the fit contributions for the 20 wt. % SDS + 3 wt. % DDAO sample are shown in Figure C.2.

Table C.2. Fitting parameters for surfactant solutions at 0 °C.

Parameter	20 wt.% SDS	20 wt.% SDS + 3 wt.% DDAO, pH 9	20% SDS + 3% DDAO, pH 2
a / nm	-	4.3	-
b / nm	-	1.8	-
t / nm	-	0.49 ^I	-
N_{agg}^{II}	-	240	-
ρ_{shell} / 10^{10} cm^{-2}	-	12.5	-
R_{HS} / nm	-	2.8	-
Z / electrons	-	10	-
I_{bkg} / cm^{-1}	0.00176	0.00133	0.00198
B	0.00054	0.00014	0.00055
A	3.986 ^{III}	3.895	3.964 ^{III}
A	0.0723	0.0339	0.0117; 0.0246
Q_{max}	1.89	1.90	1.83; 2.17
Σ	0.0377	0.0308	0.160; 0.0395
N	0.30	0.58	0; 0 ^{IV}

^IValues taken from reference (Kakitani *et al.*, 1995) and fixed during the fitting process.

^{II}Calculated using 0.41 nm^3 as the volume of SDS (Vo and Papavassiliou, 2016).

^{III}Fixed in overall analysis based on value found by fitting gradient at low Q .

^{IV}Fixed as allowing to float gave nonsensical values.

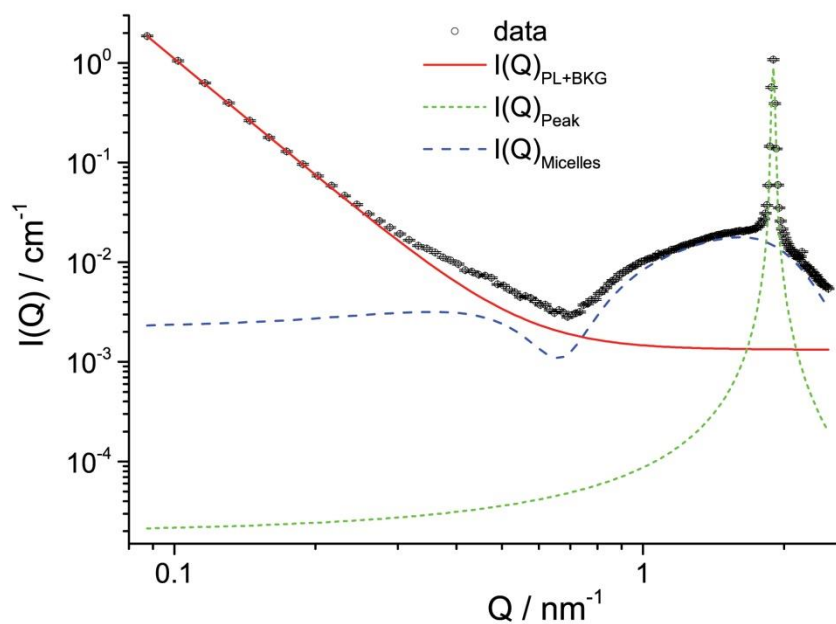
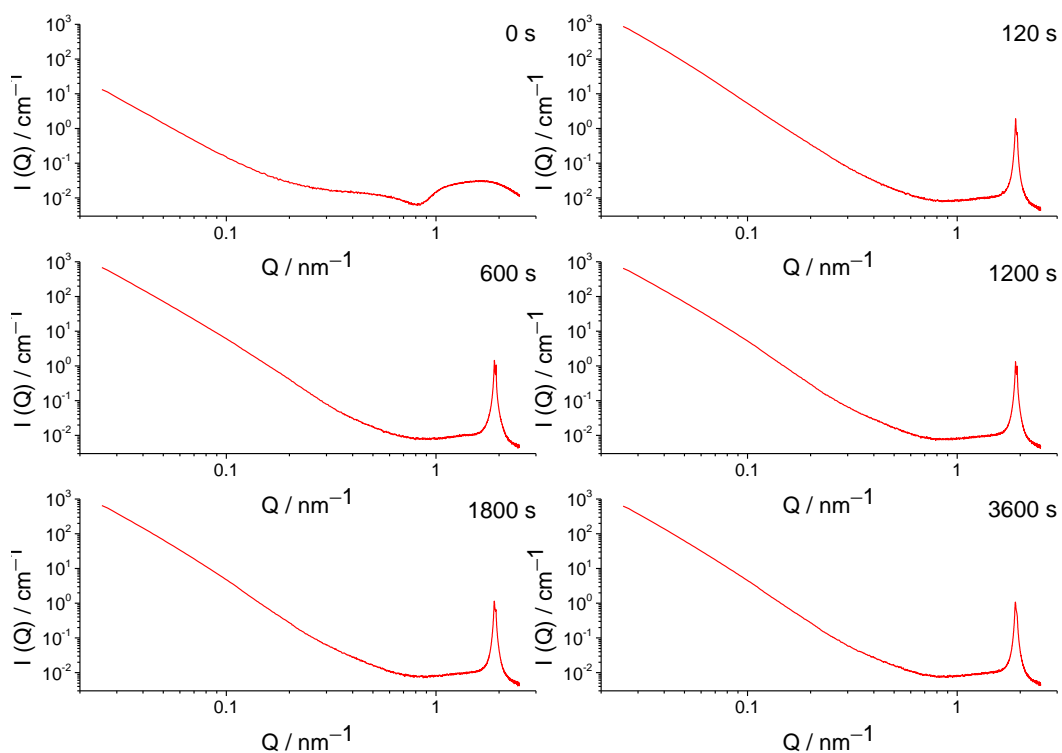


Figure C.2. Fit deconstruction for SAXS data for 20 wt. % SDS + 3 wt. % DDAO at 0 °C, showing the contributions of the power law (PL), background (BKG), micelle population and peak intensities to the overall fit. The total modelled scattering, $I(Q)_{fit} = I(Q)_{PL+BKG} + I(Q)_{Peak} + I(Q)_{Micelles}$.

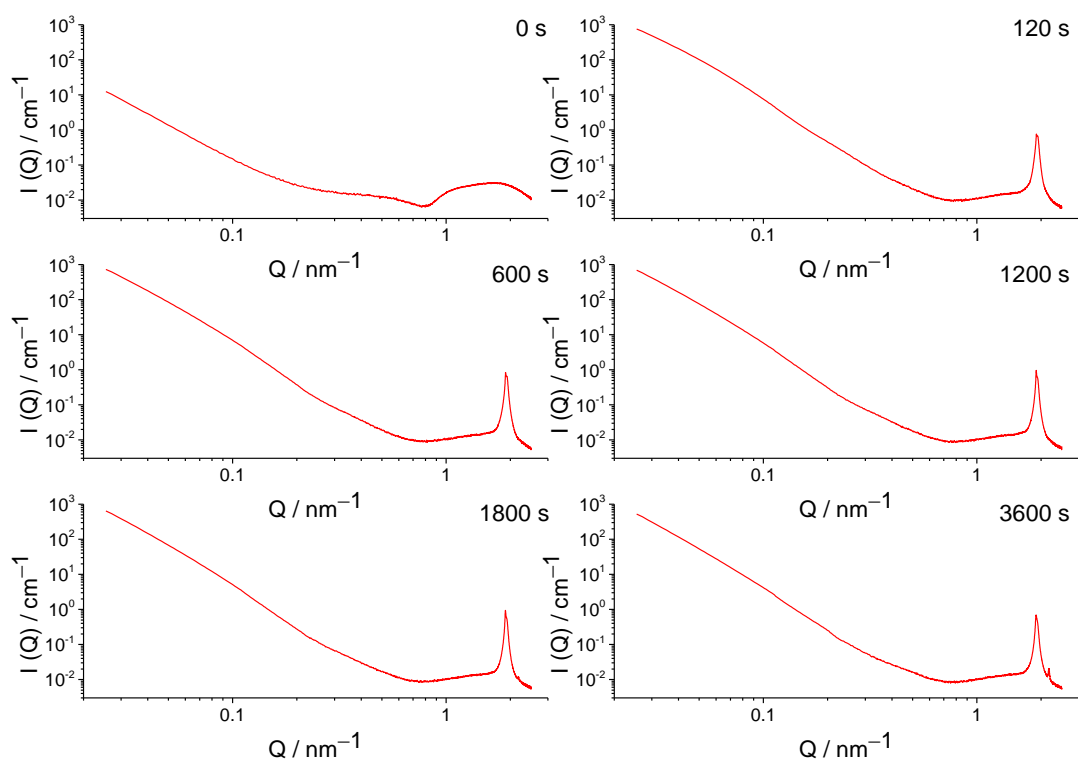
C.1.2 SAXS profiles at selected time points

Provided in the plots below are the SAXS profiles acquired for 20 wt. % SDS solutions containing (a) 1 wt. % DDAO, (b) 2 wt. % DDAO, (c) 3 wt. % DDAO, (d) 4 wt. % DDAO and (e) 5 wt. % DDAO when held at 0 °C.

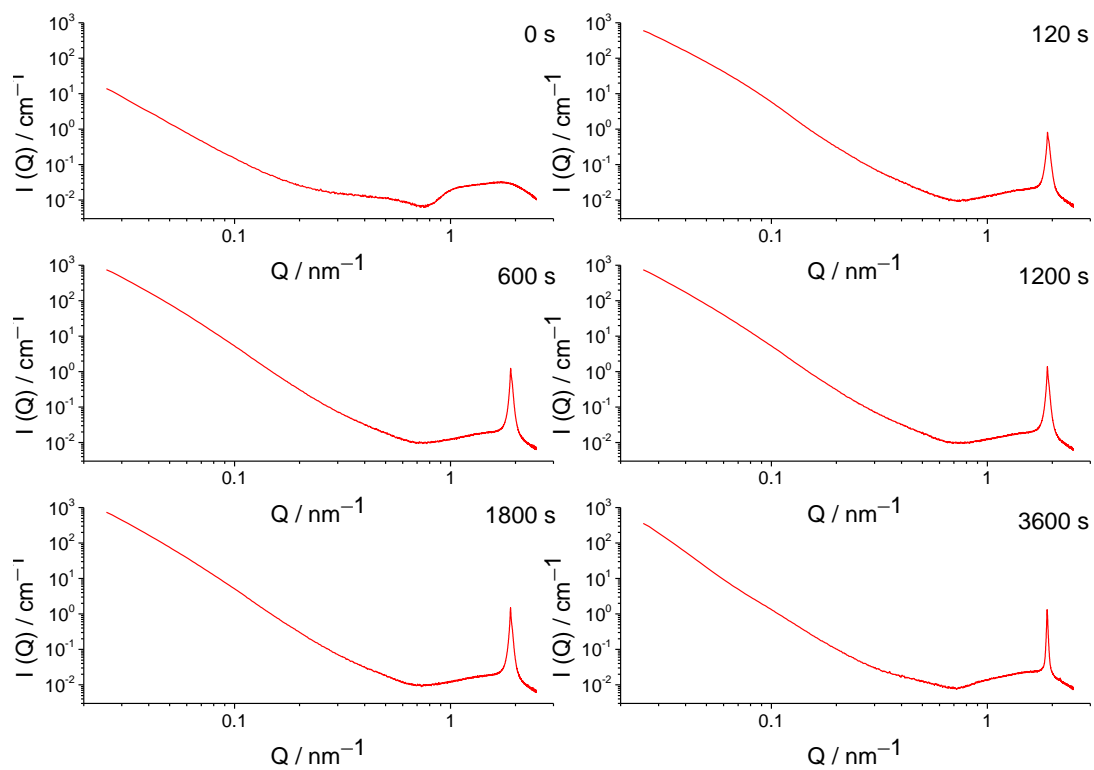
(a)



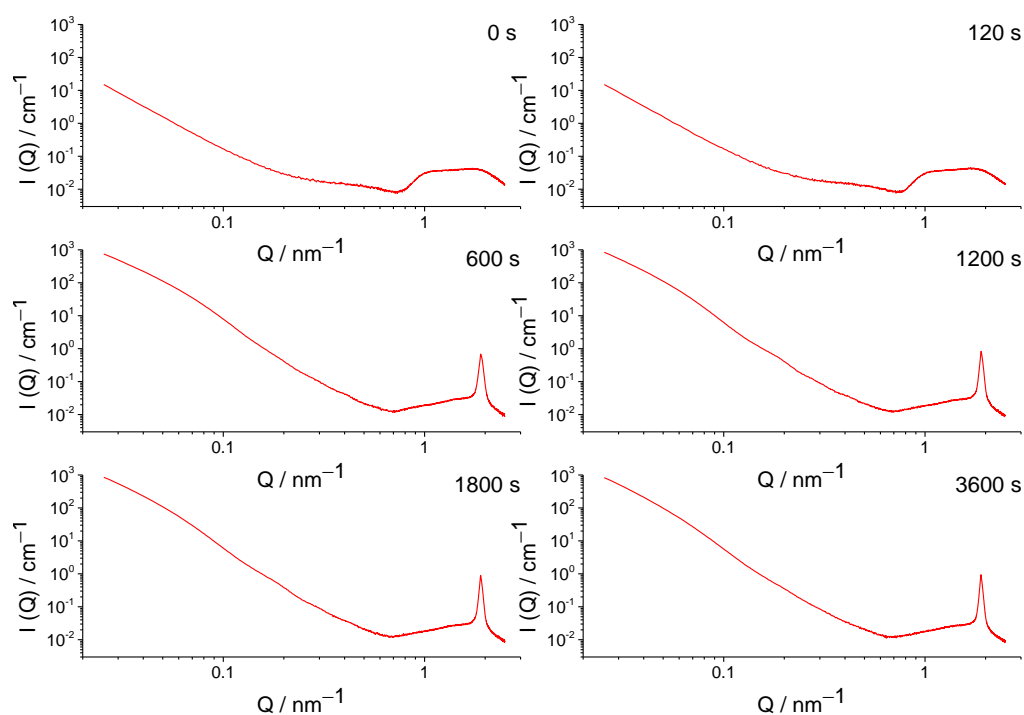
(b)



(c)



(d)



(e)

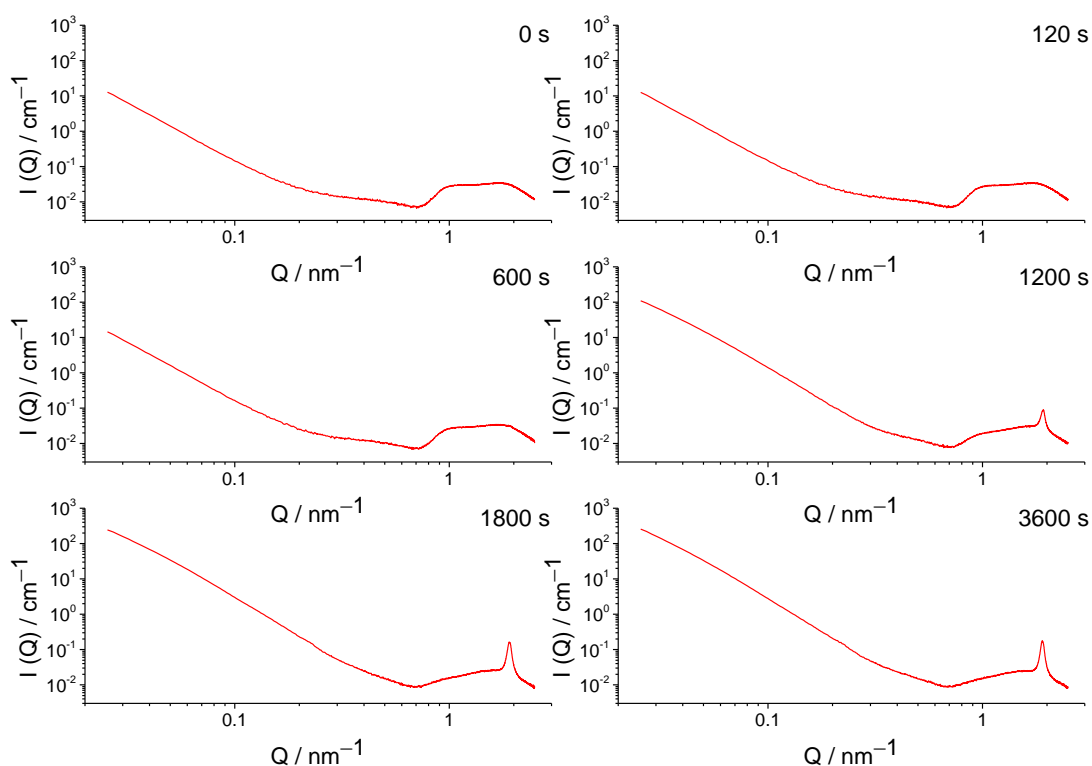
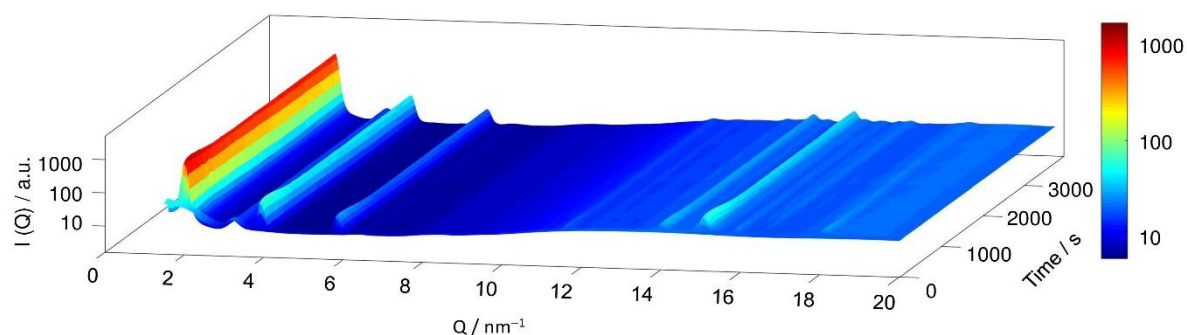


Figure C.3. SAXs profiles acquired at various timepoints (0 s, 120 s, 600 s, 1200 s, 1800 s, 3600 s) during crystallisation of SDS + DDAO systems containing 20 wt. % SDS and (a) 1 wt. % DDAO (b) 2 wt. % DDAO (c) 3 wt. % DDAO (c) 4 wt. % DDAO (d) 5 wt. % DDAO.

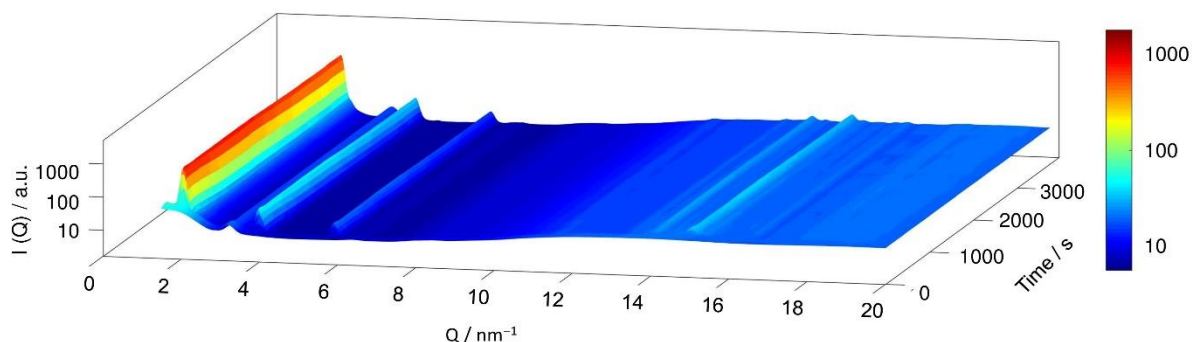
C.1.3 Time-resolved wide-angle X-ray scattering (WAXS) profiles

WAXS profiles attained upon holding 20 wt. % SDS solutions with various amounts of DDAO (1, 2, 4, 5 wt. %) at 0 °C are provided in the next figure. The 20 wt. % SDS and 20 wt. % SDS + 3 wt. % DDAO profiles are contained in the main text (Chapter 4). Peaks of interest are provided in Table C.3.

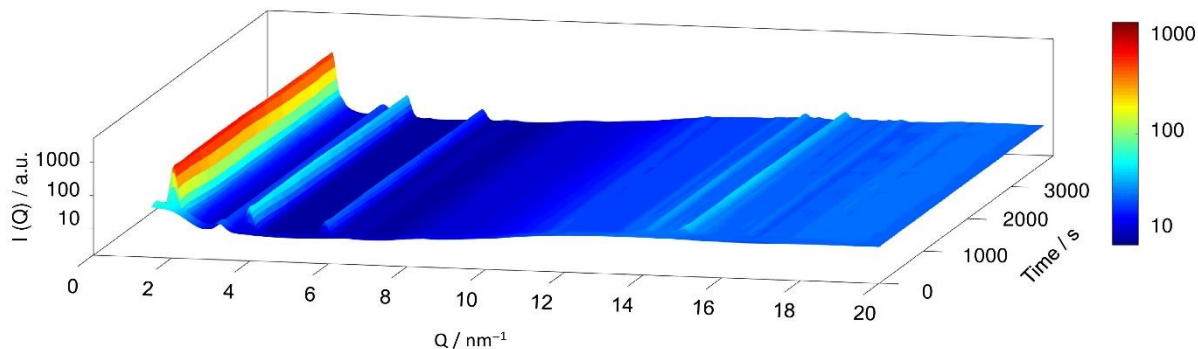
(a)



(b)



(c)



(d)

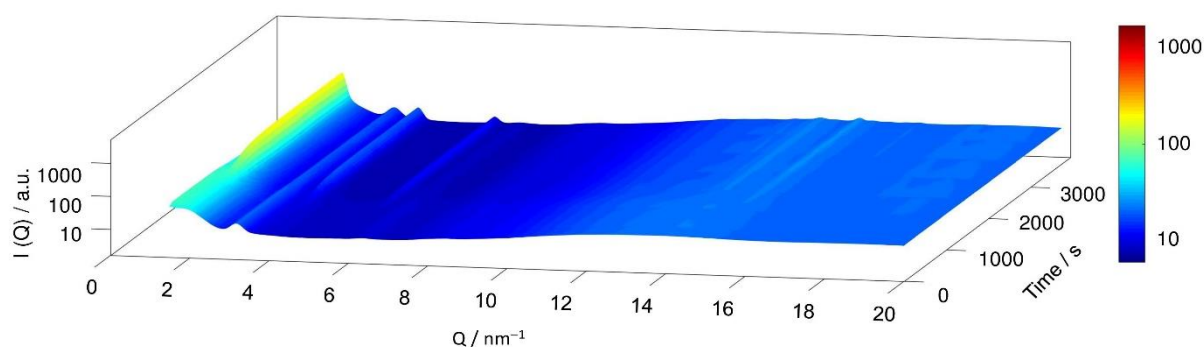


Figure C.4. 3D WAXS profiles acquired during the crystallisation of SDS + DDAO systems containing 20 wt. % SDS and; (a) 1 wt. % DDAO (b) 2 wt. % DDAO (c) 4 wt. % DDAO (d) 5 wt. % DDAO.

Table C.3. List of notable peaks in the WAXS data at 0 °C.

Peak centre / nm ⁻¹		
20 wt. % SDS	20 wt. % SDS + 3 wt. % DDAO, pH 9	20 wt. % SDS + 3 wt. % DDAO, pH 2
1.85	1.87	1.79
3.76	3.76	2.13
5.67	5.68	4.33
11.37	11.35	6.52
13.89	13.85	7.24
14.21	14.92	11.46
14.95	15.65	12.12
15.70	17.88	12.45
16.82		13.11
17.96		14.16
		15.92 ^V
		16.87

^VThis peak is likely to arise from two merged maxima, at approximately 15.8 and 16.0 nm⁻¹.

C.1.4 Avrami analysis

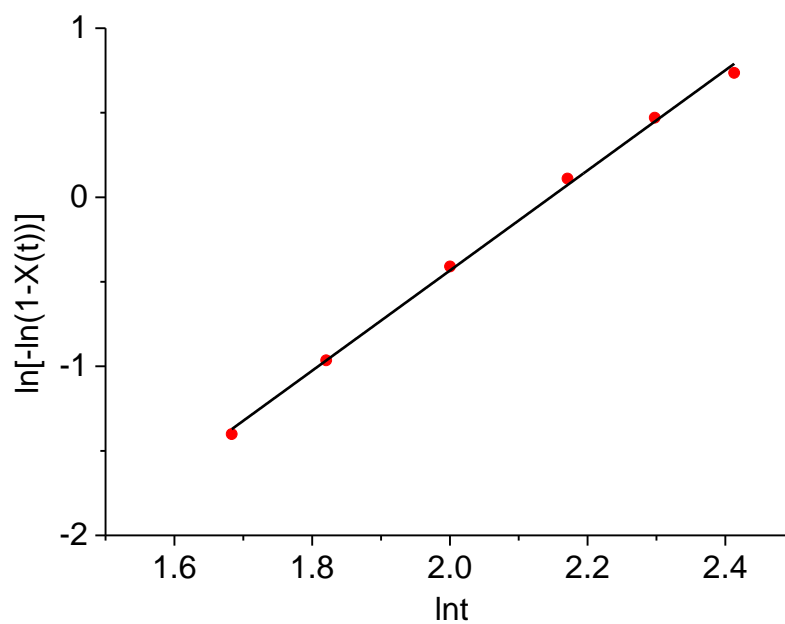
The fitting parameters acquired during Avrami analysis for the crystallisation of a 20 wt. % SDS + 3 wt. % DDAO system are shown in Table C.4.

Table C.4. SAXS fitting parameters for various scans during crystallisation of a 20 wt. % SDS + 3 wt. % DDAO system at 0 °C.

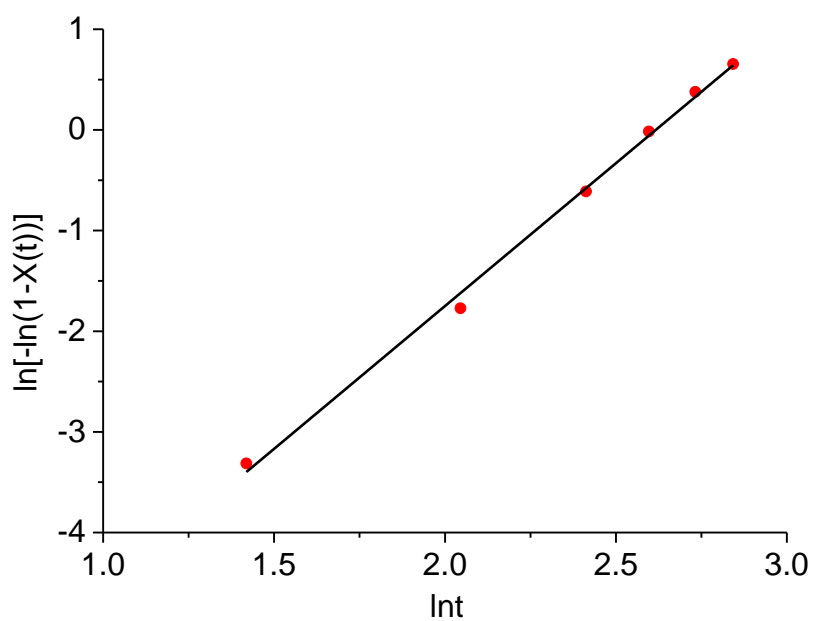
Scan number	Time	$c\theta$	$c\delta$	a	A / nm^2	Q_{max}	Width / nm	Shape	N	a / nm	b / nm	ϕ	$R_{\text{HS}} / \text{nm}$	χ^2
36	64	0.00116	0.0000738	2.99	0.000401	1.906	0.0333	0.5	3.18E-25	3.579	1.732	0.229	3.055	12.80
37	68	0.00121	0.0000693	3.57	0.00182	1.908	0.0468	0.212	3.09E-25	3.581	1.756	0.216	2.999	10.27
38	72	0.00121	0.000100	3.84	0.00542	1.909	0.0501	0.00257	2.92E-25	3.600	1.759	0.217	3.001	8.889
39	76	0.00149	0.000137	3.97	0.0112	1.910	0.0546	0.00350	2.58E-25	3.640	1.765	0.205	2.956	6.708
40	80	0.00154	0.000180	4	0.0170	1.910	0.0569	0.123	2.31E-25	3.703	1.768	0.205	3.007	7.261
41	84	0.00178	0.000228	4	0.0232	1.911	0.0608	0.190	1.98E-25	3.705	1.786	0.170	2.938	7.040
42	88	0.00196	0.000273	4	0.0295	1.912	0.0652	0.275	1.73E-25	3.719	1.801	0.16	2.940	7.794
43	92	0.00165	0.000345	4	0.0360	1.912	0.0695	0.345	1.45E-25	3.982	1.803	0.146	3.406	8.077
45	100	0.00174	0.000461	4	0.0459	1.913	0.0747	0.407	1.10E-25	3.981	1.844	0.112	3.463	8.544
50	120	0.00142	0.000572	3.92	0.0503	1.913	0.0761	0.474	1.01E-25	4.183	1.838	0.112	3.478	9.837
60	160	0.00126	0.000633	3.86	0.0516	1.913	0.0752	0.538	1.07E-25	4.121	1.825	0.15	3.419	10.44
80	240	0.00119	0.000641	3.84	0.0559	1.912	0.0685	0.501	9.67E-26	4.326	1.832	0.1175	3.429	8.631
100	320	0.00140	0.000626	3.85	0.0582	1.912	0.0659	0.496	9.44E-26	4.126	1.848	0.1157	3.377	8.699

Avrami plots for a pure 20 wt. % SDS system held at different isothermal temperatures are provided below. One of the plots for 12 °C is provided in the main text (Chapter 5).

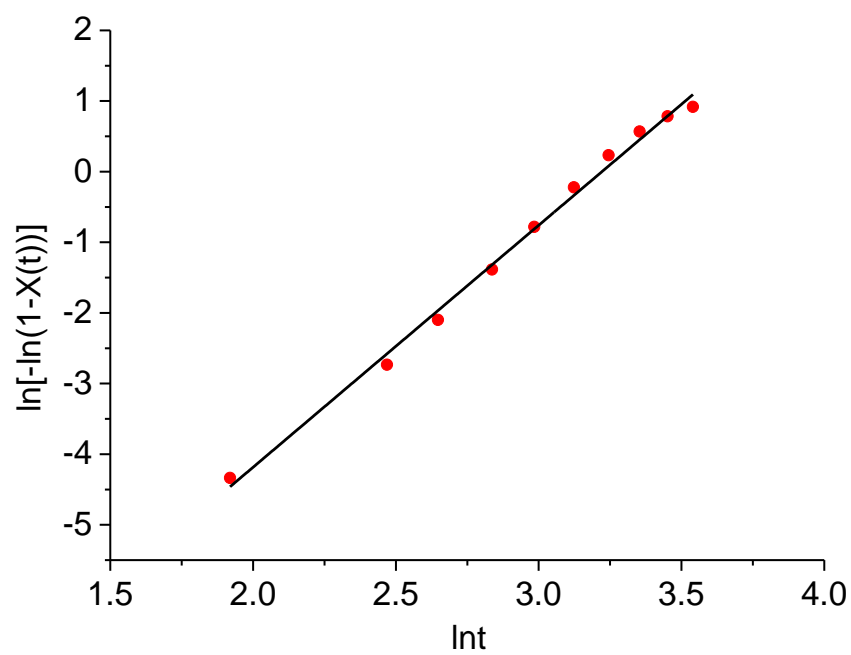
(a)



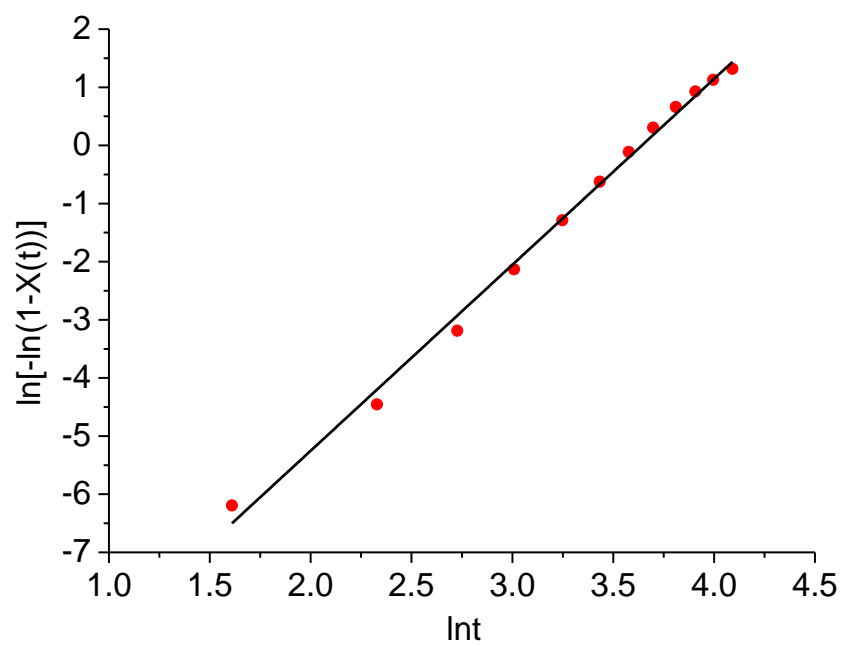
(b)



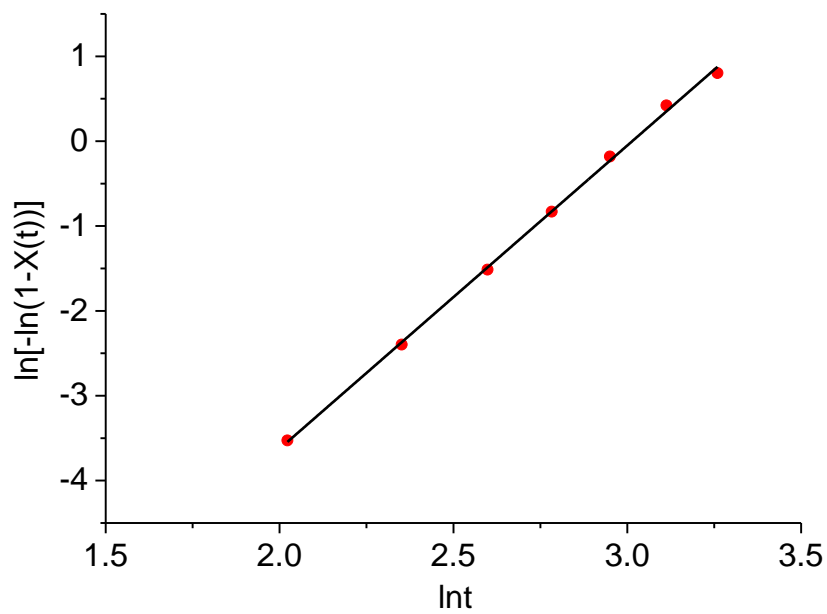
(c)



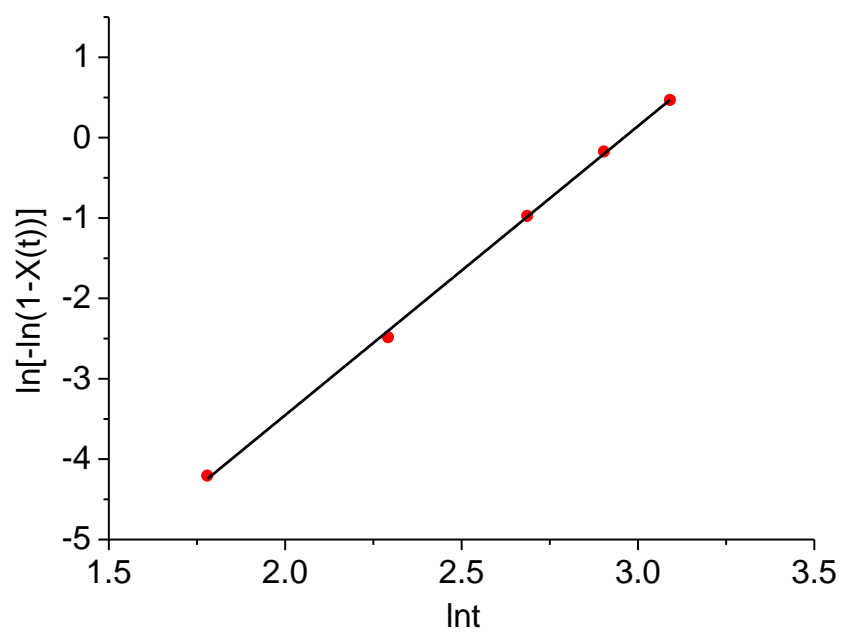
(d)



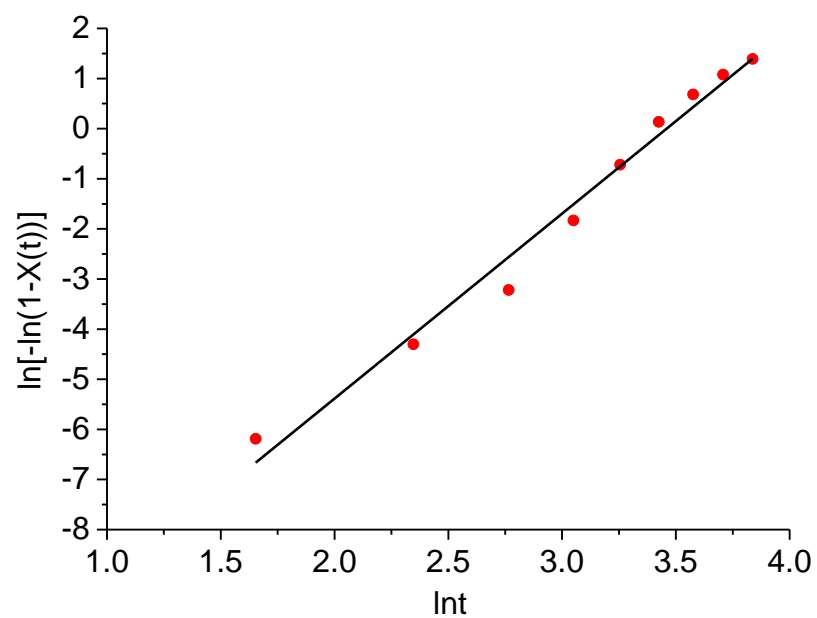
(e)



(f)



(g)



(h)

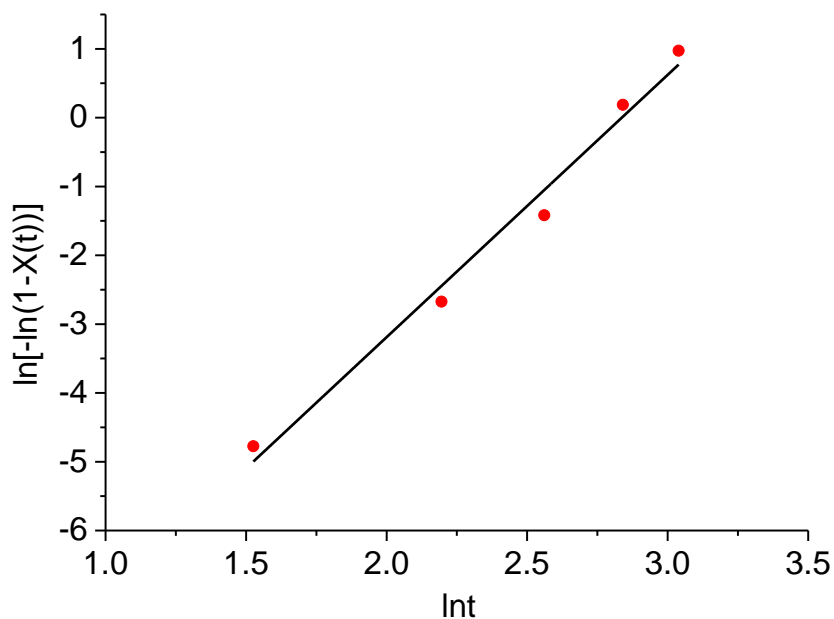


Figure C.5. Avrami plots corresponding to crystallisation of a 20 wt. % SDS solution at (a) 12 °C (rep 2). Fitted trendline has equation $y = (2.96 \pm 0.063)x - 6.36 \pm 0.131$ and $R^2 = 0.998$; (b) 12 °C (rep 3). Fitted trendline has equation $y = (2.84 \pm 0.079)x - 7.43 \pm 0.190$ and $R^2 = 0.997$; (c) 13 °C (rep 1): Fitted trendline has equation $y = (3.43 \pm 0.088)x - 11.04 \pm 0.263$ and $R^2 = 0.995$; (d) 13 °C (rep 2). Fitted trendline has equation $y = (3.20 \pm 0.070)x - 11.65 \pm 0.234$ and $R^2 = 0.995$; (e) 13 °C (rep 3). Fitted trendline has equation $y = (3.57 \pm 0.051)x - 10.77 \pm 0.140$ and $R^2 = 0.999$; (f) 14 °C (rep 1). Fitted trendline has equation $y = (3.60 \pm 0.053)x - 10.64 \pm 0.137$ and $R^2 = 0.999$; (g) 14 °C (rep 2). Fitted trendline has equation $y = (3.69 \pm 0.185)x - 12.77 \pm 0.580$ and $R^2 = 0.983$; (h) 14 °C (rep 3). Fitted trendline has equation $y = (3.81 \pm 0.267)x - 10.81 \pm 0.666$ and $R^2 = 0.986$.

Table C.5. Avrami exponents attained for the crystallisation of a 20 wt. % SDS solution at different isothermal temperatures: 12 °C, 13 °C and 14 °C.

Temperature	Avrami exponent			Average	Standard error
	1	2	3		
12	2.71	2.96	2.84	2.84	0.0721
13	3.43	3.2	3.57	3.4	0.1079
14	3.81	3.69	3.6	3.7	0.0608

C.2 P&G dish liquid sample

SAXS profiles for the unstable formulation, Formulation A, at 24 °C and after 64 hours at 0 °C, are provided in the main text (Chapter 6). The fitting parameters for the two profiles are shown below. This data was found to be optimally fitted with contributions from background scattering, a spherical shell contribution. There is an additional Bragg peak contribution for the data at 0 °C.

Table C.6. SAXS Fitting parameters for Formulation A at 24 °C and 0 °C.

Parameter	Formulation A, 24 °C	Formulation A, 0 °C
N (scaling factor)	8.03495E-25	7.42765E-25
Core radius R / nm	1.79293	1.95315
Dispersity of R	0.2846	0.209121
Shell thickness / nm	0.568688	0.494293
$\rho_{\text{core}} / 10^{10} \text{ cm}^{-2}$	1.609	1.609
$\rho_{\text{shell}} / 10^{10} \text{ cm}^{-2}$	-3.031	-3.031
Micelle Radius /nm	2.3616	2.447
S(Q) radius	2.4106	2.54194
Charge per micelles	0.00133	0.00133
Volume fraction	0.23	0.23
[salt] / M	0.12	0.12
ϵ_r	71.08	71.08
c_0	-0.0616841	-0.00191102
c_1	0	0
c_4	2.19167E-5	7.50329E-5
α	3.38343	3.6437
A	-	0.00672443
Peak centre	-	1.71
Peak width	-	0.0463421

C.3 References

- Bergstrom, M. & Pedersen, J. S. 1999. Structure of pure SDS and DTAB micelles in brine determined by small-angle neutron scattering (SANS). *Physical Chemistry Chemical Physics*, 1, 4437-4446.
- Breßler, I., Kohlbrecher, J. & Thünemann, A. F. 2015. SASfit: a tool for small-angle scattering data analysis using a library of analytical expressions. *Journal of Applied Crystallography*, 48, 1587-1598.
- Garg, G., Hassan, P. A., Aswal, V. K. & Kulshreshtha, S. K. 2005. Tuning the Structure of SDS Micelles by Substituted Anilinium Ions. *The Journal of Physical Chemistry B*, 109, 1340-1346.
- Hayter, J. B. & Penfold, J. 1981. An analytic structure factor for macroion solutions. *Molecular Physics*, 42, 109-118.
- Kakitani, M., Imae, T. & Furusaka, M. 1995. Investigation of Mixed Micelles of Dodecyldimethylamine Oxide and Sodium Dodecyl Sulfate by SANS: Shape, Size, Charge, and Interaction. *Journal of Physical Chemistry*, 99, 16018-16023.
- Munter, A. 2014. *Scattering Length Density Calculator* [Online]. Available: <http://www.ncnr.nist.gov/resources/sldcalc.html> [Accessed 01/07/2018].
- Vo, M. D. & Papavassiliou, D. V. 2016. Effect of sodium dodecyl sulfate adsorption on the behavior of water inside single walled carbon nanotubes with dissipative particle dynamics simulation. *Molecules*, 21, 500 - 515.
- Zemb, T. & Charpin, P. 1985. Micellar structure from comparison of X-ray and neutron small-angle scattering. *Journal de Physique*, 46, 249-256.

APPENDIX D

FURTHER INFORMATION ON THE COMPOSITION OF DISH LIQUID FORMULATIONS SAMPLES 1-32

D.1. Samples 1-32

Table D.1. Compositional information for Samples 1-32

Sample number	Ratio AS/AO	Na ₂ SO ₄ / wt. %	‘Unreacted alcohol’ / wt. %
1	3.0	0.193	0.035
2	3.0	0.079	0.223
3	4.3	0.086	0.242
4	4.3	0.086	0.038
5	3.0	0.079	0.098
6	4.0	0.085	0.171
7	4.3	0.209	0.242
8	3.0	0.136	0.223
9	4.3	0.147	0.242
10	4.3	0.086	0.106
11	3.3	0.081	0.229
12	3.3	0.198	0.229
13	3.0	0.136	0.098
14	3.0	0.193	0.161
15	4.3	0.209	0.174
16	3.0	0.079	0.035
17	4.0	0.206	0.104
18	4.0	0.206	0.238
19	4.0	0.145	0.038
20	3.0	0.193	0.223
21	3.3	0.140	0.165
22	4.3	0.209	0.038
23	3.3	0.081	0.036
24	3.3	0.198	0.100
25	3.3	0.098	0.100
26	4.0	0.101	0.100
27	3.3	0.067	0.170
28	4.0	0.070	0.170
29	3.0	0.096	0.100
30	4.3	0.103	0.100
31	3.0	0.066	0.160
32	4.3	0.071	0.180

AS = alkyl sulfate

AO = amine oxide

‘Unreacted alcohol’ is remnant alkyl sulfate alcohol precursor

APPENDIX E

TEST METHOD IMPROVEMENTS – FURTHER EXPERIMENTAL DATA

E.1 Oven-dried dish liquid seeding

E.1.1. Seed formation

To form the oven-dried dish liquid seeds, the dish liquid is placed in the oven at 70 °C for 20 hours. As mentioned in the main thesis manuscript, the reasoning for this is a result of minimal mass loss after this time. This is shown in the scatter plot in Figure E.1.

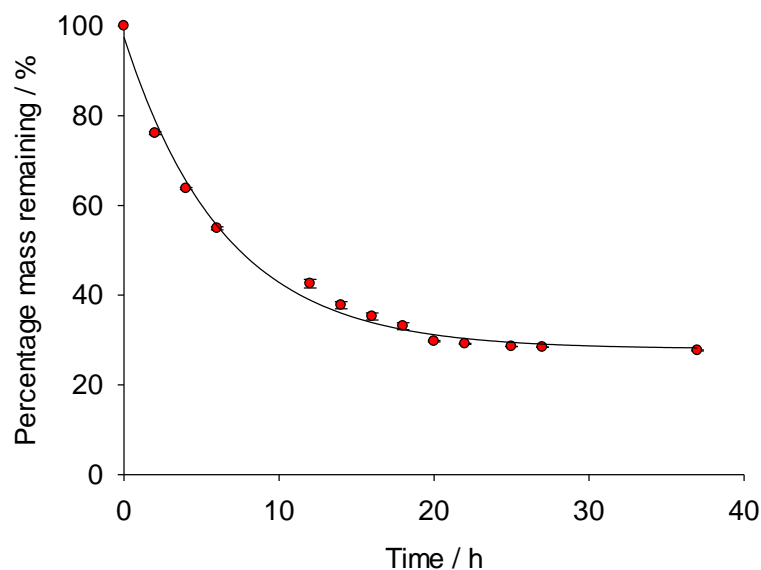


Figure E.1. Relative change in the mass of a 20 g sample of dish liquid placed in an oven at 70 °C.

E.2 Application of Mixing

E.2.1 Cooling time

In the Methods section in Chapter 8 (Section 8.3.2.2), a hold time of 2.5 hours was introduced to allow the formulation in the vessel to attain the required temperature throughout the system. Figure E.2 displays the related data that was used to select initial cooling time. After 2.5 hours, there was negligible change in the temperature of the system.

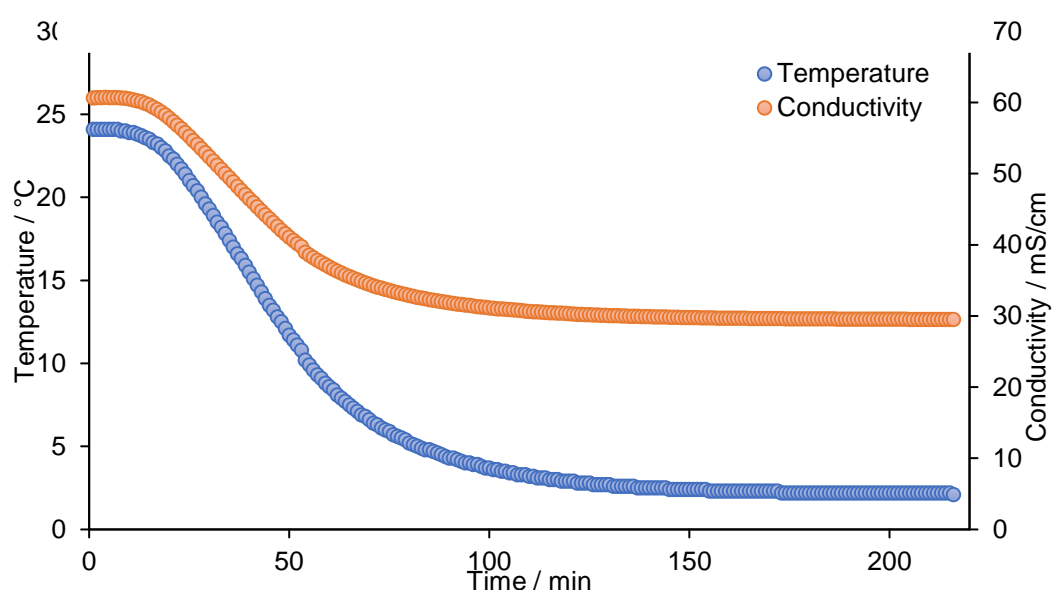


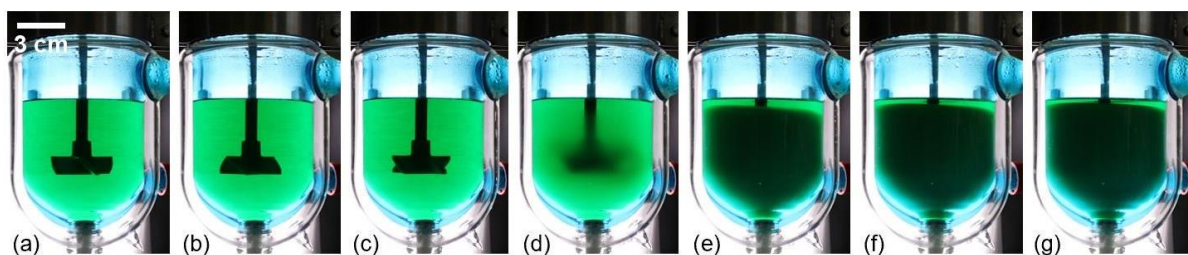
Figure E.2. Change in temperature and conductivity over time for a typical dish liquid product (Formulation A) contained within the jacketed vessel. The water bath set to 0 °C with measurements taken at the central point of the vessel.

E.2.2 Further time lapse images

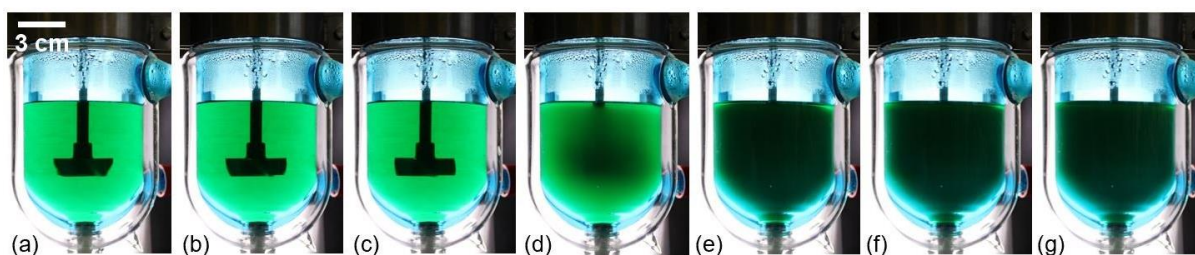
The time lapse images of Formulation A at 0 °C were acquired at various mixing speeds.

Examples of these images (taken every 10 minutes) are provided in Figure E.3 for 50, 150 and 300 rpm. 20 rpm is provided in the main manuscript (Chapter 8).

(a) 50 rpm



(b) 150 rpm



(c) 300 rpm

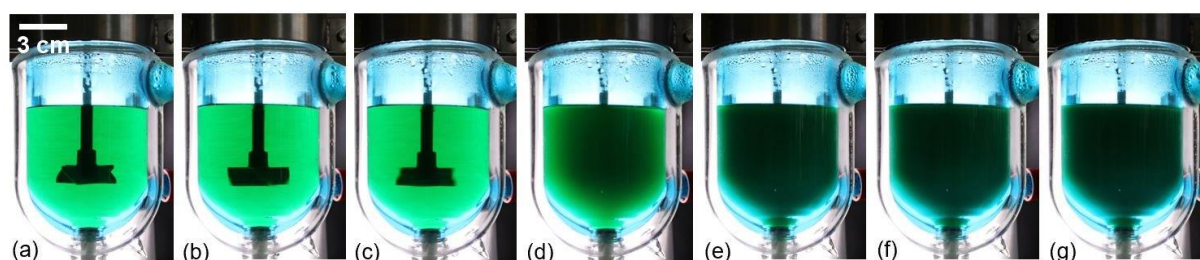


Figure E.3. Time lapse images taken at 10 minute intervals (a)-(g) upon holding Formulation A at 0 °C and with an applied mixing speed of (a) 50 rpm (b) 150 rpm (c) 300 rpm.

E.2.3 MATLAB code for greyscale intensity

The MATLAB code included on the next pages was written with the help of Dr. Thomas Moxon. This was used to attain time-resolved greyscale intensity plots during the crystallisation of Formulation A .

```
% Script call all images in a folder, first image is opened and allows for
% the used to crop picture for desired area, this will be repeated the
% the desired number of times moving the cropped area up 2 times the height
% of the original cropped area. The script will then loop over all images
% for each of the cropped area, convert them to grey scale and take mean of
% the 8bit colour number (0-255), this will be plotted for each area against
% time. Along with this the first image will be plotted with rectangles
% showing the areas which were analyses labelled alphabetically starting with
% the initial cropping point.
% All data will be saved in a .mat file, and the time and intensity data
% will be saved in an excel file.

%=====
%=====
%=====Change these things as appropriate=====
%=====
%=====

% location of folder containing the images required for processing
M_folder = 'E:\ExperimentX'; % location of folder containing the images required
for processing

% set times
time_0 = 0; % time of first image
time_f = 60; % time of last image

% The initial area which to sample:
% - If left blank ( [];) square brackets with nothing inside, when the
% script is run you will have to set an area to crop on the first
% image when it pops up, click and drag to set the area, then right
% click on the crop boarder and select 'crop image', at which point
% the script will run
% - If filled with a position vector, this value will be used for the
% initial crop area and simulation will run with no user input
% required
%
% position vector will be 4 numbers in the following form:
% [left position, bottom position, width, height]
Crop_in
=[5.835100000000000e+02,6.545100000000000e+02,31.98000000000000,30.98000000000000]
;
```



```
% number of areas to analyse
N_area = 4;

% gets all files from the folder specified as M_folder. all files of the
% type specified will be found:
%
%
%
%     e.g., .JPG files will be found if '/*.JPG' is added after the
%     folder, .png files if '/*.png' is added
% N.B. its case sensitive make sure hence .jpg is treated differently from .JPG

F = dir([M_folder, '/*.JPG']); % gets list of all files in folder with extension
.JPG

                                % check extension before hand and change as
                                % needed ( check case aswell) e.g., '/*.jpg'
                                % or '/*.JPG'

%=====
%=====
%=====Should not require changes after this point=====
%=====Except for figures if required (aesthetically)=====
%=====

% gets string containing the name of the folder-- this is used to name the
% files produced from the script
file_names =fliplr(strtok(fliplr(M_folder),'\'));

% some files are found, im unsure why but they begin with '._' or '_' hence
% these will be removed if they are present
%remove any files starting with '._' or '_'
pat1 = '._';
pat2 = '_';

files = sort_nat({F.name}'); % get names of images

files(startsWith(files,pat1))=[];
files(startsWith(files,pat2))=[];

% set memory for Intensity and Crop_dimension-
%           we produce a matrix of zeros as this speeds up the for
%           loop
Intensity = zeros(numel(files),N_area);
Crop_dim_all = zeros(N_area,4);

% begin timer
tic

%loop counter- initially set to zero
ii=0;

for files =files' % cropping & intensity loop - goes through each file found in
order
```

```

ii = ii+1 % counts number of files through loop

Img = imread([M_folder '/' files{1}]); % reads each image in folder
if ii == 1
    [Img, resize_Crop] = imcrop(Img);
else
    Img = imcrop(Img,resize_Crop);
end
Img = imresize(Img,[1250,890]);
for ij = 1:N_area % loops over the different sampling positions

    % first image
    if ii ==1 && ij==1 && isempty(Crop_in) % if no initial cropping dimensions
are provided
        figure(1)
        [Img_c, Crop_dim] = imcrop(Img); % Opens up a figure of the first image
which can be cropped
        Crop_dim_all(ij,:)= Crop_dim; % Crop dimension
[x-pos y-pos width height]
        close(ffigure(1))
        % set cropping for extra points
        for jj = 2:N_area
            Crop_dim_all(jj,:) = [Crop_dim(1) (Crop_dim(2)-(2*jj-
2)*Crop_dim(4)) Crop_dim(3) Crop_dim(4)];
        end
        figure(2);
        imshow(Img); % re-open first image as figure 2 for further editing
later
        elseif ii ==1 && ij==1 && ~isempty(Crop_in) % If initial cropping
dimensions are provided
            Crop_dim_all(ij,:) = Crop_in;
            for jj = 2:N_area
                Crop_dim_all(jj,:) = [Crop_in(1) (Crop_in(2)-(2*jj-2)*Crop_in(4))
Crop_in(3) Crop_in(4)];
            end
            Img_c = imcrop(Img,Crop_dim_all(ij,:));
            figure(2);
            imshow(Img);
        else % cropping for all other images after the first image
            Img_c = imcrop(Img,Crop_dim_all(ij,:));
        end
        % measures mean intensity of cropped area (should be a number between 0
(black) and 255 (white))
        Intensity(ii,ij) = mean2(rgb2gray(Img_c));
    end
end % end loop

% end timer and provide output to command window in seconds
toc

% assumes each image is taken with the same time spacing
time = linspace(time_0,time_f,numel(Intensity(:,1)));

```

```
% convert intensity to a percentage of white
PercentageIntensity = Intensity/255*100;

% create array of letters for labelling
alph =char('A'+(1:26)-1);
%=====
%=====
%=====Change figures as appropriate=====
%=====
%=====
```

figures

```
figure(1)

% plot(x-axis, y-axis, options)
% options in quotations '', can set color, linestyle, point marker etc.
% color k = black
%       r = red
%       b = blue
%       etc.
% linestyle - = solid line
%           -- = dashed line
%           -. = dashed & dotted line
%           : = dotted line
% So, 'k-' produces a black solid line
plot(time,PercentageIntensity)
xlabel('Time [min]') % label for x-axis
ylabel('Intensity (%)') % y-axis label
title('Intensity plot') % title of graph
if N_area ==1
    legend(alph(1),'location','eastoutside')
elseif N_area ==2
    legend(alph(1),alph(2),'location','eastoutside')
elseif N_area ==3
    legend(alph(1),alph(2),alph(3),'location','eastoutside')
elseif N_area ==4
    legend(alph(1),alph(2),alph(3),alph(4),'location','eastoutside')
elseif N_area ==5
    legend(alph(1),alph(2),alph(3),alph(4),alph(5),'location','eastoutside')
end
```

E.2.4 Fitting parameters

The greyscale plots were fitted to a 4-parameter sigmoidal function (see Chapter 8). The values for the different parameters are provided in Table E.1.

Table E.1 Fitting parameters for the sigmoidal plots of greyscale intensity over time, performed in triplicate at a mixing speed of (a) 20 rpm (b) 50 rpm (c) 150 rpm and (d) 300 rpm. For each replicate, 4 greyscale plots were attained corresponding to areas A-D (provided in Figure 8.2(b)).

(a)

	20-1				20-2				20-3			
	A	B	C	D	A	B	C	D	A	B	C	D
y_0	11.02	10.49	11.15	12.40	10.06	9.113	9.812	20.14	7.769	6.261	6.792	8.661
A	37.88	38.46	37.01	36.13	41.75	40.798	40.71	30.15	43.10	45.04	44.17	42.07
x_0	31.59	34.26	36.95	41.22	34.86	37.942	41.14	44.94	36.75	38.77	41.08	44.57
B	-1.278	-1.348	-1.466	-2.449	-1.68	-1.664	-2.247	-2.049	-1.572	-1.765	-1.853	-2.436
R^2	0.9972	0.9981	0.9983	0.998	0.9995	0.9996	0.9991	0.9983	0.9997	0.9998	0.9997	0.9986

(b)

	50-1				50-2				50-3			
	A	B	C	D	A	B	C	D	A	B	C	D
y_0	9.664	9.348	9.251	9.542	12.58	11.92	14.19	14.54	10.95	XX	10.88	11.28
A	38.24	39.76	38.06	38.34	37.54	38.55	35.64	35.79	36.23	36.77	35.58	35.20
x_0	29.50	30.88	32.29	33.50	31.11	32.66	33.90	34.99	31.06	32.30	33.18	34.08
B	-1.165	-1.208	-1.135	-1.351	-1.098	-1.080	-1.060	-1.262	-1.117	-1.054	-1.036	-1.160
R^2	0.9991	0.9991	0.9994	0.9993	0.9974	0.9979	0.9986	0.999	0.9948	0.9955	0.9938	0.9953

(c)

	150-1				150-2				150-3			
	A	B	C	D	A	B	C	D	A	B	C	D
y_0	8.370	7.719	7.404	7.684	7.420	6.766	6.322	6.4962	10.96	10.22	10.94	11.56
A	39.73	40.23	39.91	39.75	39.27	40.19	39.01	39.52	36.11	38.20	35.56	35.46
x_0	27.80	28.68	29.22	29.57	25.96	26.92	27.62	27.98	27.17	27.88	28.45	28.77
B	-1.171	-1.048	-1.032	-1.096	-1.179	-1.094	-1.041	-1.163	-0.959	-0.997	-0.874	-0.937
R^2	0.9988	0.999	0.999	0.999	0.9994	0.9995	0.9998	0.9997	0.9955	0.996	0.9934	0.9927

(d)

	300-4				300-5				300-6			
	A	B	C	D	A	B	C	D	A	B	C	D
y_0	9.217	8.458	8.417	8.886	12.32	11.46	12.17	12.85	12.46	11.60	12.39	13.34
A	41.19	41.98	41.23	40.88	37.90	39.06	37.57	37.25	37.81	39.17	37.39	37.00
x_0	27.13	27.51	27.72	27.84	25.85	26.24	26.46	26.56	25.91	26.27	26.50	26.58
B	-0.984	-0.965	-0.971	-1.006	-0.890	-0.883	-0.877	-0.927	-0.876	-0.883	-0.864	-0.921
R^2	0.999	0.9991	0.9989	0.9984	0.9941	0.9947	0.9909	0.9894	0.994	0.9946	0.9905	0.9872